ACS OMEGA

http://pubs.acs.org/journal/acsodf

Perspective

Metrics for Evaluation and Screening of Metal−Organic Frameworks for Applications in Mixture Separations

Rajamani Krishna*

Cite This: *ACS Omega* 2020, 5, 16987−17004

Read Online

ACCESS | Metrics & More | Article Recommendations | Supporting Information

ABSTRACT: For mixture separations, metal−organic frameworks (MOFs) are of practical interest. Such separations are carried out in fixed bed adsorption devices that are commonly operated in a transient mode, utilizing the pressure swing adsorption (PSA) technology, consisting of adsorption and desorption cycles. The primary objective of this article is to provide an assessment of the variety of metrics that are appropriate for screening and ranking MOFs for use in fixed bed adsorbers. By detailed analysis of several mixture separations of industrial significance, it is demonstrated that besides the adsorption selectivity, the performance of a specific MOF in PSA separation technologies is also dictated by a number of factors that include uptake capacities, intracrystalline diffusion influences, and regenerability. Low uptake capacities often reduce the efficacy of separations of MOFs with high selectivities. A combined selectivity−capacity metric, Δq, termed as the separation potential and calculable from ideal adsorbed solution theory, quantifies the maximum productivity of a component that can be recovered in either the adsorption or desorption cycle of transient fixed bed operations. As a result of intracrystalline diffusion limitations, the transient breakthroughs have distended characteristics, leading to diminished productivities in a number of cases. This article also highlights the possibility of harnessing intracrystalline diffusion limitations to reverse the adsorption selectivity; this strategy is useful for selective capture of nitrogen from natural gas.

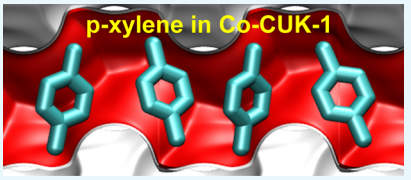

1. INTRODUCTION

During the last 2 decades, there has been a substantial increase in the development and synthesis of novel microporous crystalline materials for use as selective adsorbents in a variety of industrially important separation applications; examples of such materials include metal−organic frameworks (MOFs), zeolitic imidazolate frameworks (ZIFs), porous organic cages, porous aromatic frameworks, covalent organic frameworks, and polymers with intrinsic microporosity. Such separations are normally carried out in fixed bed devices that are operated in a transient mode, consisting of adsorption and desorption cycles. In one class of applications, the motivation has been to afford energy-efficient and environmentally benign alternatives to conventional separations such as absorption, distillation, extraction, or crystallization. In other cases, there are incentives for enhancing the separation performance by replacing the currently used microporous adsorbents such as cation-exchanged zeolites and activated carbon (AC) with tailor-made MOFs. To set the scene and define the objectives of this article, we consider a number of mixture separations that may be targeted for the development of novel MOFs.

Arguably, the most important and successful industrial application of adsorption separations is for H_2 purification. The catalytic reforming of natural gas, when combined with a water gas shift reaction step, yields a hydrogen-rich product stream containing a number of impurities such as H_2O vapor, CO_2, CH_4, CO, and N_2.[1−3] These impurities must be removed in order to attain the 99.95%+ H_2 purity that is normally demanded.[1] In fuel cell applications, the purity demands are as high as 99.99%+.[2,4] Large-scale production of hydrogen, with the desired purity, is carried out in pressure swing adsorption (PSA) units that are operated at pressures reaching about 7 MPa using the Skarstrom cycle, involving multiple steps or stages; see the schematic in Figure 1. In the simplest case, the four steps in the sequence are as follows.[5−7]

(a) Pressurization (with the feed or raffinate product)
(b) High-pressure adsorption separation with the feed, with withdrawal of the purified raffinate product
(c) Depressurization, or "blowdown", countercurrent to the feed
(d) Desorption at the lower operating pressure. This is accomplished by evacuation or purging the bed with a portion of the purified raffinate product.

The use of layered beds, consisting of three different adsorbents, is an important characteristic of the currently employed PSA technology for H_2 purification.[2,8] In order to rationalize and understand the use of multilayer adsorbent beds, Figure 2a,b presents simulations of transient breakthroughs of 73/4/3/4/16 $H_2/N_2/CO/CH_4/CO_2$ mixture, typical of steam methane reformer off-gas,[3] in fixed bed adsorbers packed with

Received: May 13, 2020
Accepted: July 1, 2020
Published: July 10, 2020

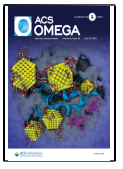

https://dx.doi.org/10.1021/acsomega.0c02218
ACS Omega 2020, 5, 16987−17004

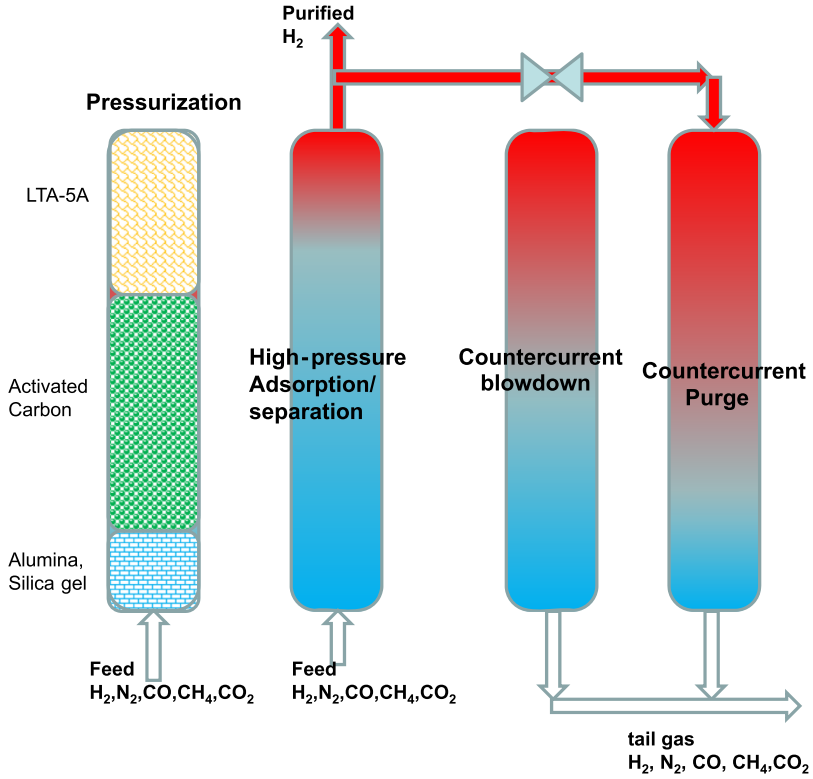

Figure 1. Sequential steps in the operation of a fixed bed adsorber in the Skarstrom cycle for H_2 purification.[2,5−7]

(a) AC and (b) LTA-5A zeolite[8−10] operating at 2 MPa total pressure and temperature T = 313 K. Purified H_2 can be recovered during the time intervals between the breakthroughs of H_2 and N_2, as indicated by the arrows. The stronger binding of N_2 in LTA-5A, as compared to AC, is due to the contribution of the quadrupole moment of N_2 and its interaction with the charges of extraframework cations Na^+ and Ca^{2+}.[5,11] The quadrupole moment of CO_2 also leads to stronger binding in LTA-5A, causing significantly higher CO_2 capture capacity, as evidenced by the strongly delayed breakthrough of CO_2 with LTA-5A as compared to AC.[5,11] The strong binding of CO_2 in LTA-5A is disadvantageous because deep vacuum will be required to reduce the CO_2 loading to the desired level during the purge step (d) in Figure 1. Consequently, despite the superior separation performance of LTA-5A, resulting in higher productivity of pure H_2 per kilogram of adsorbent, LTA-5A is not used on its own in the currently used PSA schemes.[2,3] Commonly, the first layer is either alumina or silica that retains the water vapor. Then, an AC layer is used to selectively adsorb CO_2. The main task of the alumina and AC layers is to prevent the H_2O vapor and CO_2 from reaching the zeolite layer.[2] The last layer is a cation-exchanged zeolite [such as LTA-5A, and NaX (=13X),[12] with Na^+ cations] with enhanced capacity for CO and N_2. For H_2 purification applications,[3,13−15] it is evident that CO_2/H_2 adsorption selectivity is not the "key" determinant of the achieved purity of H_2.

For CO_2 capture from flue gases from power plants, and from natural gas streams, MOFs offer energy-efficient alternatives to conventionally used amine absorption technologies.[16−21] In CO_2/flue gas and CO_2/natural gas separations, the process economics would demand high CO_2 capture capacity and concomitant ease of regeneration.[22]

For the production of alkene feedstocks of 99.95%+ purity required for polymerization reactors, cryogenic distillation columns, operated at high pressures and high reflux ratios, are commonly employed for large-scale separations of C_2H_4/C_2H_6 and C_3H_6/C_3H_8 mixtures. Many MOF developments have targeted alkene/alkane separations with the objective of eventually supplanting the energy-intensive distillation technologies.[23−29] Process economics would also demand high alkene productivities per kilogram adsorbent.

In steam cracking of ethane to produce ethene (C_2H_4), one of the byproducts is ethyne (C_2H_2). Typically, the C_2H_2 content of C_2H_2/C_2H_4 feed mixtures is 1%. Ethyne has a deleterious effect on the polymer products of ethene, such as polyethene. The impurity level of C_2H_2 in the C_2H_4 feed streams should be below 40 ppm in order to prevent the poisoning of catalysts used in the polymerization of C_2H_4. MOFs offer potential improvements to absorption technologies using dimethyl formamide as a solvent.[23,30−37] For 1/99 C_2H_2/C_2H_4 mixture separations, we would require that the MOF would have high productivity of pure alkene (<40 ppm C_2H_2) per kilogram of adsorbent.

Ethyne (C_2H_2) is an important building block in industrial chemical synthesis and is also widely used as a fuel in welding equipment. C_2H_2 is commonly manufactured by the partial combustion of CH_4 or comes from cracking of hydrocarbons. In the reactor product, C_2H_2 coexists with CO_2 or C_2H_4. Because of the similarity of molecular sizes and shapes (C_2H_2: 3.32 × 3.34 × 5.7 Å^3 and CO_2: 3.18 × 3.33 × 5.36 Å^3), the separation of C_2H_2/CO_2 mixtures is particularly challenging.[38,39] Because the boiling points of C_2H_2 (189.3 K) and CO_2 (194.7 K) are close, distillation separations need to operate at cryogenic temperatures and high pressures. A number of recently developed MOFs offer the potential of use in adsorptive separations of C_2H_2/CO_2 mixtures.[40−53]

The selective capture of CO_2 from the reactor effluents from the process for oxidative coupling of methane essentially requires for CO_2-selective separation of $CO_2/CH_4/C_2H_4/$

https://dx.doi.org/10.1021/acsomega.0c02218
ACS Omega 2020, 5, 16987−17004

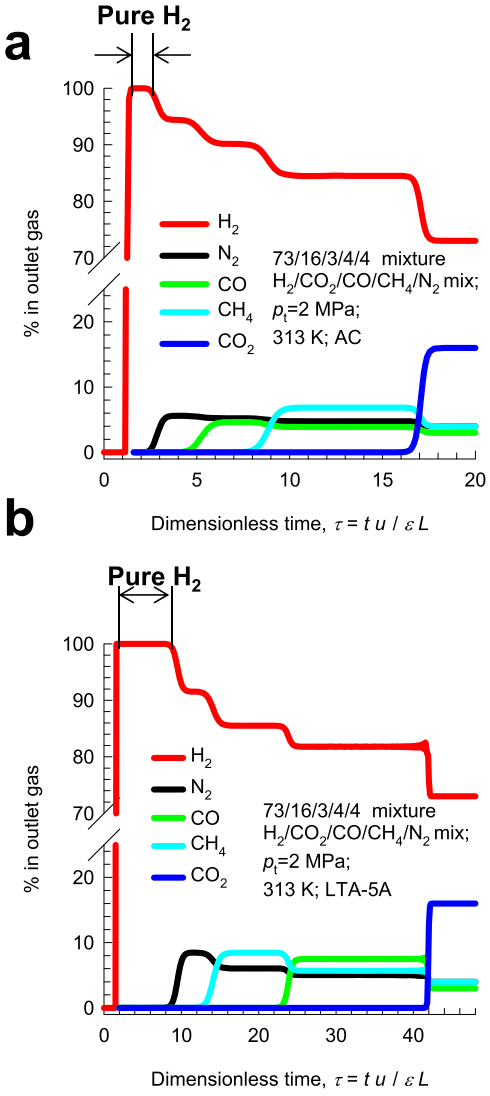

Figure 2. Transient breakthrough of 73/4/3/4/16 $H_2/N_2/CO/CH_4/CO_2$ mixtures in a fixed bed adsorber packed with (a) AC and (b) LTA-5A zeolite operating at a total pressure of 2 MPa and T = 313 K. For presenting the breakthrough simulation results, we use as x-axis the dimensionless time, $\tau = tv/L$, where L is the length of the adsorber and v is the interstitial gas velocity.[63,122] Further information on input data and simulation details are provided in the Supporting Information.

C_2H_6 mixtures; the number of candidate adsorbent materials is surprisingly limited.[54−56]

Noble gases such as He, Ne, Ar, Kr, and Xe find a variety of applications.[57] For example, heliox (a mixture of He and O_2) is used for patients with respiratory difficulties and in deep-sea diving,[58] Ne is used in the familiar "neon sign" for advertisements. Kr and Xe are used in flash bulbs and lasers. Ar is used in filament bulbs and in electric arc welding as a shielding gas. Based on the differences in the boiling points, Ne (27 K), Ar (87 K), Kr (120 K), and Xe (165 K) are commercially produced by liquefaction of air, followed by cryogenic distillation. Alternatively, adsorptive separations, relying essentially on the differences in polarizabilities (cf. Figure 3), are realizable with a number of MOFs.[57,59,60]

The process demands in each of the aforementioned examples of mixture separations are different. The primary objective of this article is to provide a comparative assessment of the variety of metrics that are appropriate for screening and ranking

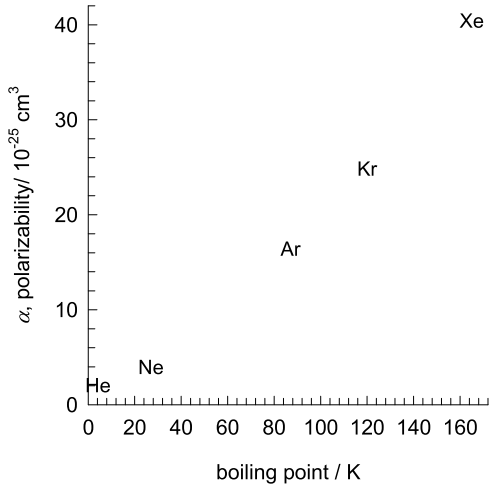

Figure 3. Boiling points and polarizabilities of noble gases culled from web sources.

candidate MOFs that are appropriate for the specific separation task in hand. The Supporting Information provides detailed structural information on the MOFs investigated, along with a detailed description of the methodology used for transient breakthrough simulations. For each of the chosen mixtures, the comparisons of the separation performance of various MOFs are on the basis of experimental data on the unary isotherms from published sources; the data sources are provided in the Supporting Information.

2. ADSORPTION SELECTIVITIES, UPTAKE CAPACITIES, AND TRANSIENT BREAKTHROUGHS

2.1. Xe/Kr Separations. To develop an understanding of the various metrics that determine the effectiveness of separations, let us consider the separation of 20/80 Xe(1)/Kr(2) mixtures in a fixed bed packed with CoFormate (=$Co_3(HCOO)_6$); the objective is to produce Kr with less

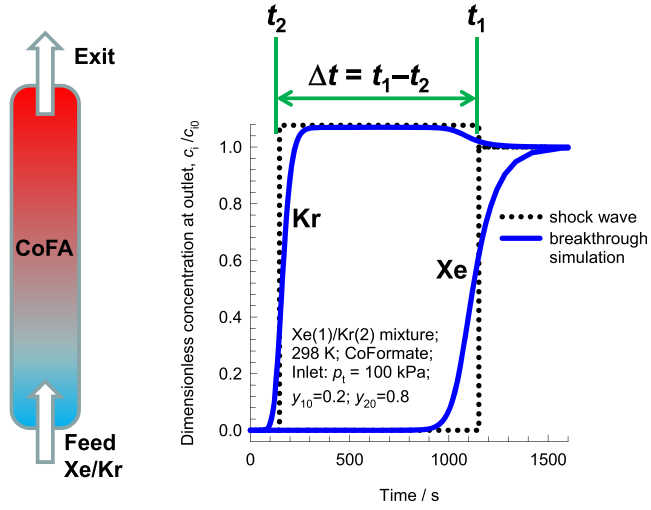

Figure 4. Transient breakthrough simulations (indicated by the solid blue line) for separation of 20/80 Xe/Kr mixtures at 298 K and 100 kPa in a fixed bed packed with CoFormate; these simulations include intracrystalline diffusion limitations. The dotted lines represent the shock wave model approximation.[63] The input data and calculation details are available in earlier works.[57,63,121]

https://dx.doi.org/10.1021/acsomega.0c02218
ACS Omega 2020, 5, 16987−17004

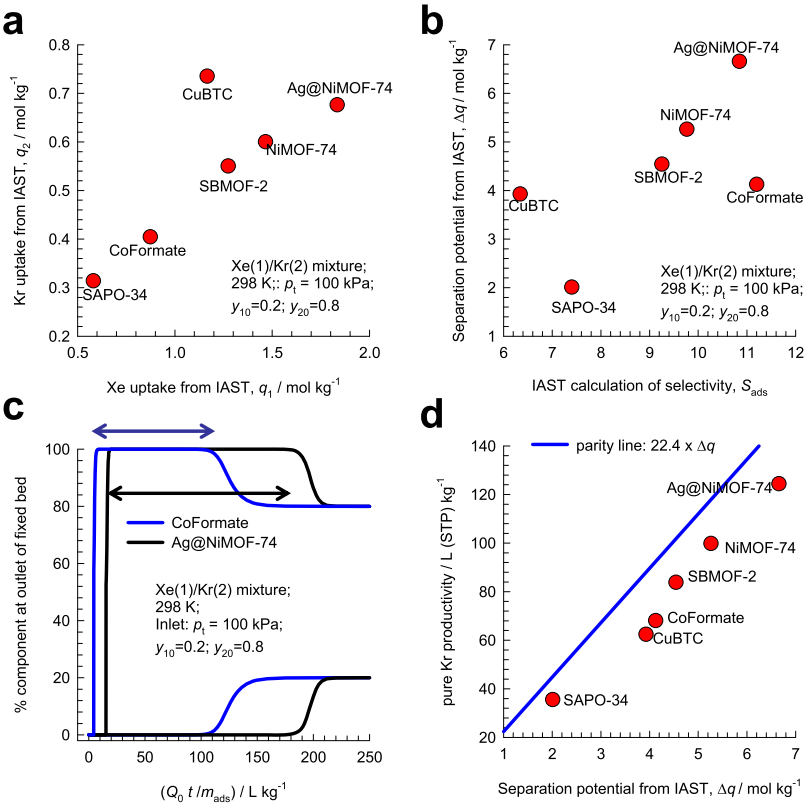

Figure 5. IAST calculations of (a) component loadings q_2 vs q_1 and (b) separation potential $\Delta q = q_1\frac{y_{20}}{y_{10}} - q_2$ vs adsorption selectivity S_{ads} for 20/80 Xe(1)/Kr(2) mixture adsorption at 298 K and 100 kPa in six different MOFs: NiMOF-74[65,66] Ag@NiMOF-74,[66] CuBTC,[65,67] SBMOF-2,[59] CoFormate[61] (=$Co_3(HCOO)_6$), and SAPO-34.[60] (c) Comparison of the transient breakthrough simulations for separation of 20/80 Xe/Kr mixtures at 298 K and 100 kPa in fixed beds packed with CoFormate and Ag@NiMOF-74. The dimensionless concentrations at the exit of the fixed bed are plotted as a function of Q_0t/m_{ads}, where Q_0 is the volumetric flow rate of the gas mixture at the inlet to the fixed bed, expressed in L s^{-1}, at STP conditions. (d) Plot of the productivity of pure Kr, determined from breakthrough simulations, vs the IAST calculations of $\Delta q = q_1\frac{y_{20}}{y_{10}} - q_2$ for six different MOFs with y_{10} = 0.2; y_{20} = 0.8. Further information on input data and simulation details are provided in earlier works.[57,63,121]

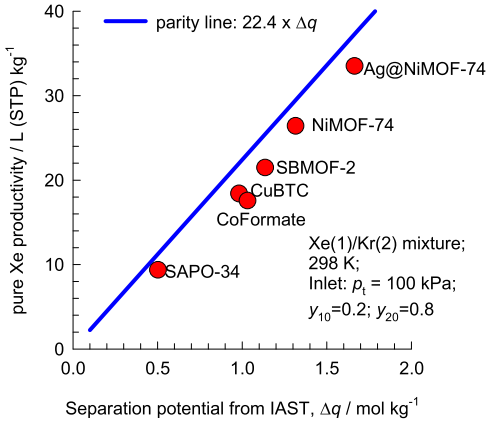

Figure 6. Plot of the productivity of pure Xe determined from transient desorption simulations for 20/80 Xe(1)/Kr(2) mixtures vs the IAST calculations of separation potential $\Delta q = q_1 - q_2\frac{y_{10}}{y_{20}}$ for six different MOFs with y_{10} = 0.2; y_{20} = 0.8. Further information on input data and simulation details are provided in earlier works.[57,63,121]

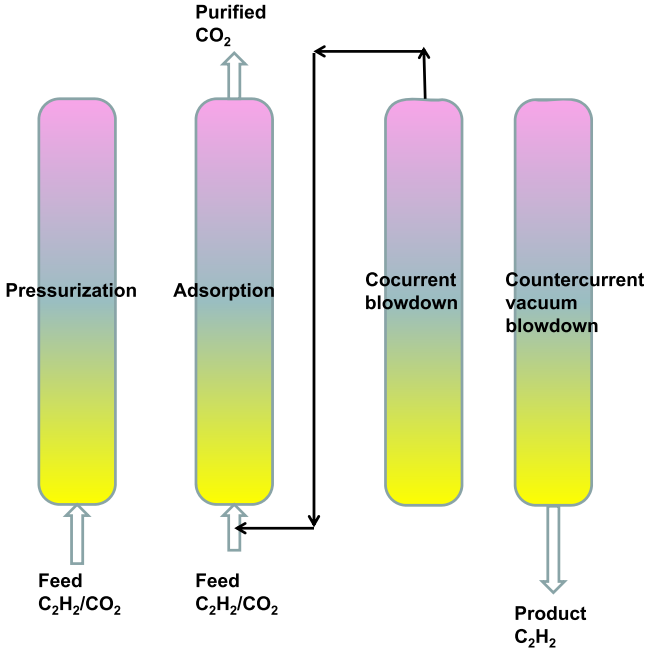

Figure 7. Sequential steps in the operation of a fixed bed adsorber in the Skarstrom cycle for $C_2H_2(1)/CO_2(2)$ separation.

than say 1000 ppm Xe. Because of the commensurate positioning of Xe within its cages, CoFormate displays high Xe/Kr selectivity.[61] The continuous solid lines in Figure 4 represent transient breakthrough simulation results for the dimensionless concentrations c_i/c_{i0} at the exit of the fixed bed.

https://dx.doi.org/10.1021/acsomega.0c02218
ACS Omega 2020, 5, 16987−17004

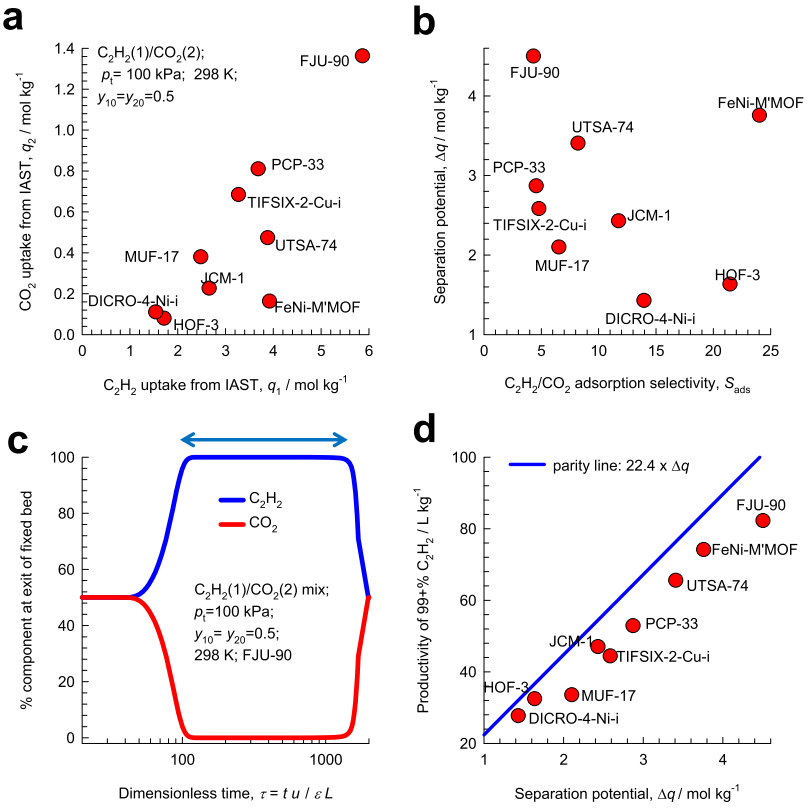

Figure 8. IAST calculations of (a) component loadings q_2 vs q_1 and (b) separation potential $\Delta q = q_1 - q_2\frac{y_{10}}{y_{20}}$ vs adsorption selectivity S_{ads} for the adsorption of $C_2H_2(1)/CO_2(2)$ mixtures in nine different MOFs operating at 298 K and 100 kPa. (c) Simulations of transient desorption (blowdown) under deep vacuum (0.2 Pa total pressure and 298 K). During the time interval indicated by the arrow, the C_2H_2 product containing <1% CO_2 can be recovered. (d) Productivity of 99%+ pure C_2H_2 product determined by transient desorption simulations for PCP-33, HOF-3, TIFSIX-2-Cu-i, JCM-1, DICRO-4-Cu-i, MUF-17, UTSA-74, FJU-90, and FeNi-M′MOF at 298 K and 100 kPa, plotted as a function of the separation potential $\Delta q = q_1 - q_2\frac{y_{10}}{y_{20}}$ with $y_{10} = y_{20} = 0.5$. Further information on input data and simulation details are provided in earlier works.[41,43,63,121]

The breakthroughs have distended characteristics that are caused by intracrystalline diffusional limitations. For subsequent discussions, it is useful to also consider the limiting scenario in which the concentration fronts traverse the fixed bed in the form of shock waves;[62,63] the shock wave model approximation is shown by the dotted lines in Figure 4; further details of the shock wave model are provided in the Supporting Information. Because the shock wave model has sharp fronts, the separation performance is the maximum achievable, and this simplified model helps to derive simple expressions for the metrics that describe the performance of fixed bed adsorbers.

In the shock wave model, the traversal velocity for the more strongly adsorbed Xe is significantly lower than that of the poorly adsorbed Kr.[6,7] The Xe capture capacity of CoFormate, q_1, expressed as moles captured per kilogram of adsorbent in the fixed bed can be calculated from a material balance

$$q_1 = \frac{y_{10} c_t Q_0}{m_{ads}} t_1 \tag{1}$$

In eq 1, y_{10} is the mole fraction of Xe at the inlet to the bed, Q_0 is the volumetric flow of the feed gas mixture with total molar concentration, $c_t = p_t/RT$, t_1 is the breakthrough time for Xe, and m_{ads} is the mass of the adsorbent. We define the displacement time interval $\Delta t = t_1 - t_2$ as the difference between the breakthrough times of Xe(1) and Kr(2); during this interval, pure Kr can be recovered. The productivity of purified Kr, Δq, that is collected during the displacement interval can be determined from the shock wave model[63]

$$\Delta q = \frac{c_t Q_0}{m_{ads}} \Delta t = q_1 \frac{y_{20}}{y_{10}} - q_2 \tag{2}$$

where q_2 is the uptake of Kr in the bed

$$q_2 = \frac{y_{20} c_t Q_0}{m_{ads}} t_1 - \Delta q \tag{3}$$

Because its derivation is based on the idealized shock wave model, the quantity Δq, dubbed the separation potential, represents the maximum productivity of the less strongly adsorbed component that can be recovered.

The adsorption selectivity, S_{ads}, defined by

$$S_{ads} = \frac{q_1/q_2}{y_{10}/y_{20}} \tag{4}$$

can be related to the breakthrough times by combining eqs 1−4

$$S_{ads} = \frac{1}{1 - \frac{\Delta t}{y_{20} t_1}}; \qquad \frac{\Delta t}{t_1} = \frac{\Delta q}{q_1/y_{10}} = y_{20}\left(1 - \frac{1}{S_{ads}}\right) \tag{5}$$

Increasing values of adsorption selectivities, S_{ads}, results in an increase in the values of $\Delta t/t_1$ and $\frac{\Delta q}{q_1/y_{10}}$. This implies that as the

https://dx.doi.org/10.1021/acsomega.0c02218
ACS Omega 2020, 5, 16987−17004

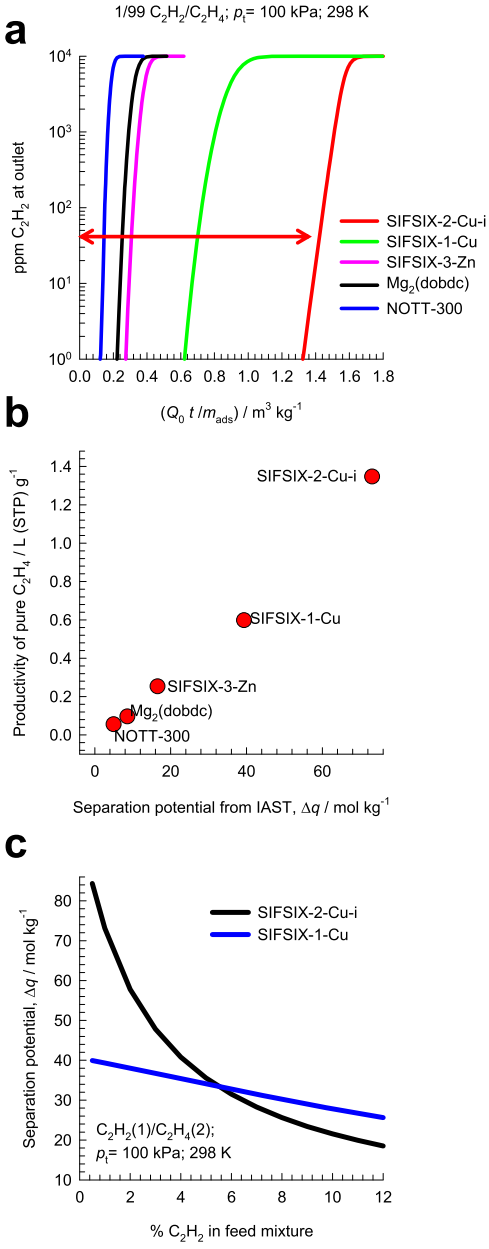

Figure 9. (a) Transient breakthrough simulations for 1/99 C_2H_2/C_2H_4 mixture adsorption at 298 K and 100 kPa in a fixed bed packed with five different MOFs. The ppm C_2H_2 in the gas mixture at the outlet of the fixed bed is plotted as a function of Q_0t/m_{ads}, where Q_0 is the volumetric flow rate of the gas mixture at the inlet to the fixed bed, expressed in m^3 s^{-1}, at STP conditions. (b) Productivity of pure C_2H_4, containing less than 40 ppm C_2H_2, plotted as a function of the separation potential $\Delta q = q_1\frac{y_{20}}{y_{10}} - q_2$ determined from IAST with $y_{10} = 0.01$; $y_{20} = 0.99$. (c) Separation potential, Δq, of SIFSIX-2-Cu-i and SIFSIX-1-Cu, plotted as a function of the % C_2H_2 in the feed mixture. Further information on input data and simulation details are provided in the Supporting Information.

selectivity increases, the breakthrough of Kr occurs increasingly earlier

$$S_{ads} \to \infty; \qquad t_2 \to 0; \qquad \Delta t \to y_{20}t_1 \tag{6}$$

Although a high value of S_{ads} is always a desirable characteristic, this metric does not guarantee a high productivity of pure Kr that is required of the "best" MOF. The highest

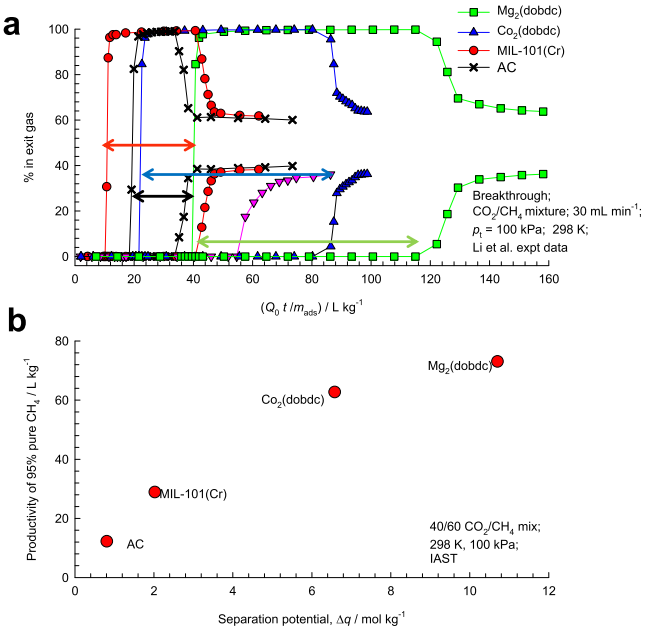

Figure 10. (a) Experimental breakthroughs for CO_2/CH_4 mixtures in a packed bed with Mg_2(dobdc), Co_2(dobdc), MIL-100(Cr), and AC at 298 K. The partial pressures at the inlet are $p_1 = 40$ kPa, $p_2 = 60$ kPa, and $p_t = 100$ kPa. The experimental data, indicated by the symbols, are from Li et al.[68] The % CO_2 and % CH_4 in the exit gas phase are plotted as a function of Q_0t/m_{ads}. (b) Productivity of 95% pure CH_4 plotted as a function of separation potential.

productivity of Kr will be offered by the MOF that has the highest value of separation potential $\Delta q = q_1y_{20}/y_{10} - q_2$, which should be regarded as a combined selectivity−capacity metric.[63] In order to underscore this observation, Figure 5a,b presents the ideal adsorbed solution theory[64] (IAST) calculations of (a) component loadings q_2 versus q_1 and (b) separation potential $\Delta q = q_1\frac{y_{20}}{y_{10}} - q_2$ versus adsorption selectivity S_{ads} for adsorption of 20/80 Xe(1)/Kr(2) mixtures in NiMOF-74,[65,66] Ag@NiMOF-74,[66] CuBTC,[65,67] SBMOF-2,[59] CoFormate,[61] and SAPO-34.[60] The MOF with the highest value of S_{ads} is CoFormate; however, the highest Δq is achieved by Ag@NiMOF-74. The presence of well-dispersed Ag nanoparticles in Ag@NiMOF-74 causes stronger van der Waals interactions of the polarizable Xe atoms; this results in the higher uptakes and the highest Δq.

Because the productivity of pure Kr, Δq, is proportional to the displacement time interval, $\Delta t = t_1 - t_2$, an alternative procedure for screening MOFs for Xe/Kr separations would be on the basis of the displacement intervals, determined by comparing transient breakthroughs in fixed beds, that are determined from experimental data or transient breakthrough simulations. Figure 5c compares the transient breakthrough simulations for Ag@NiMOF-74 and CoFormate on this basis. The transient breakthrough simulation methodology is described in detail in the Supporting Information. Briefly, the assumptions made in the simulations are as follows: (1) axial dispersion effects are considered to be negligible, (2) the mixture adsorption equilibrium can be described using IAST, (3) the column pressure drop is of negligible importance, and (4) the total pressure remains constant during the operation. Because the breakthrough times are dependent on the mass of the adsorbent, m_{ads}, and the volumetric flow rate, Q_0, the appropriate comparison of transient breakthroughs for different MOFs is

https://dx.doi.org/10.1021/acsomega.0c02218
ACS Omega 2020, 5, 16987−17004

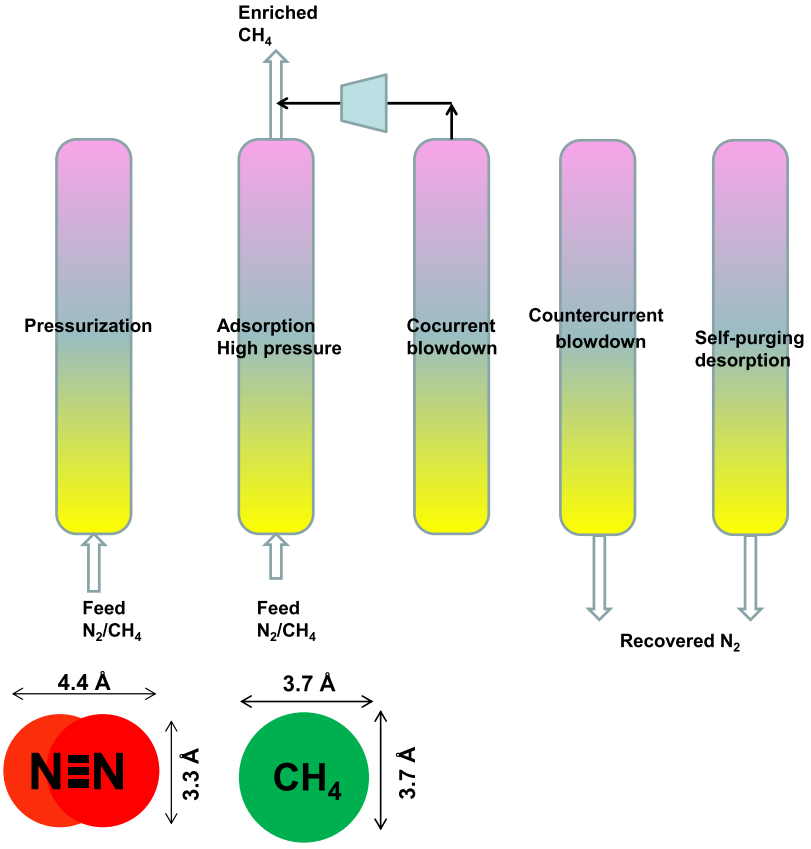

Figure 11. Different steps in the production of purified CH_4 using an adsorbent such as LTA-4A zeolite, Ba-ETS-4, and clinoptilolites, which rely on kinetic selectivity. The scheme shows the sequence of processing of a single bed in a multibed PSA scheme. Adapted from Bhadra and Farooq[70] and Jayaraman et al.[72]

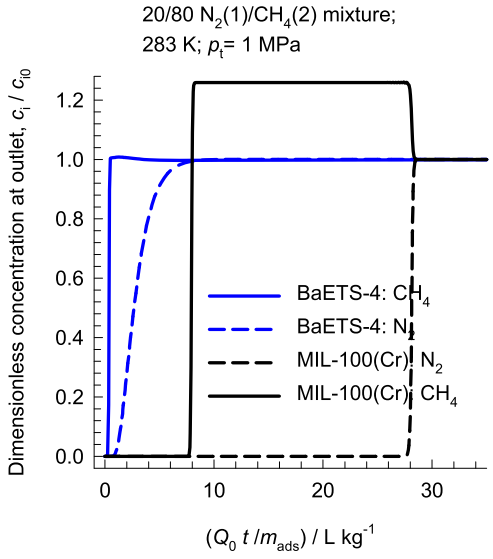

Figure 12. Comparison of the transient breakthroughs of 20/80 $N_2(1)$/$CH_4(2)$ mixtures in a fixed bed adsorber packed with MIL-100(Cr) and Ba-ETS-4 operating at 283 K and total pressure p_t = 1 MPa. Further information on input data and simulation details are provided in the Supporting Information.

to use the parameter Q_0t/m_{ads} as the x-axis in place of time; indeed, this parameter may be viewed as a "corrected" time. It is also a common practice to use the value of Q_0 at STP conditions. Noteworthily, the breakthroughs of both Ag@NiMOF-74 and CoFormate have distended characteristics. Because of intracrystalline diffusion limitations, the breakthrough characteristics of CoFormate are more distended than that of Ag@NiMOF-74. In the industry, the process requirement would demand the production of Kr containing <1000 ppm Xe. During the displacement intervals indicated by the arrows, the industrial process requirements may be met.[57] To determine the actual amount of Kr of desired purity that may be recovered, the total amount of Kr that exits the fixed bed during the displacement interval is determined by sampling of the exit gas from the fixed bed; from such sampling, the productivities of pure Kr are 125 L (STP) kg^{-1} for Ag@NiMOF-74 and 68 L (STP) kg^{-1} for CoFormate. Despite having the highest S_{ads} value, the significantly poorer productivity of CoFormate is directly ascribable to its lower uptake capacity (cf. Figure 5a). Figure 5d plots the productivities of pure Kr from transient breakthroughs of six different MOFs as a function of the corresponding IAST calculations of Δq. The near-linear relation between the two sets confirms that IAST calculations of the separation potential Δq may be used for screening purposes. Also shown by the continuous solid line in Figure 5d is the parity line 22.4 × Δq for the productivities. Because of the distended nature of the transient breakthroughs in Figure 5c, the actual productivities are lower than 22.4 × Δq.

The MOF crystallites in the fixed bed at the end of the adsorption cycle are predominantly rich in the more strongly adsorbing Xe. Pure Xe can be recovered during the desorption cycle by the application of deep vacuum. The maximum productivity of pure Xe can also be derived from the use of the shock wave model[63]

https://dx.doi.org/10.1021/acsomega.0c02218
ACS Omega 2020, 5, 16987−17004

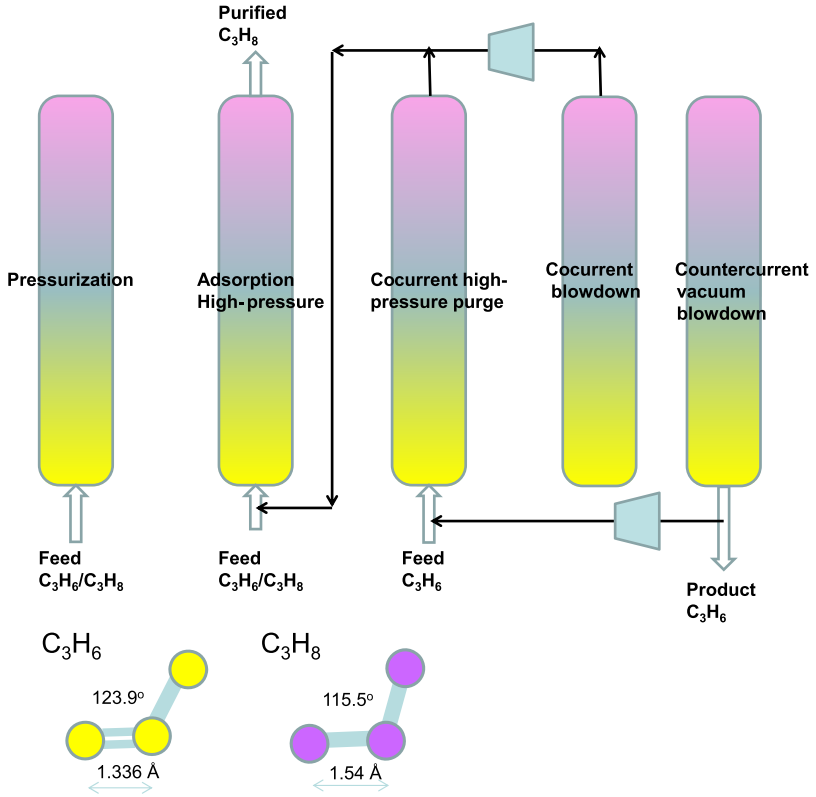

Figure 13. Five-step PSA process for separating C_3H_6/C_3H_8 mixtures.[77,78,81]

$$\Delta q = q_1 - q_2 \frac{y_{10}}{y_{20}}; \qquad \text{desorption cycle} \tag{7}$$

Figure 6 plots the productivities of pure Xe, containing <1000 ppm Kr, from transient desorption simulations using six different MOFs, against the corresponding IAST calculations of Δq, calculated using eq 7 with y_{10} = 0.2; y_{20} = 0.8. The relation between the actual productivities (symbols) and Δq is not perfectly linear. For example, the Xe productivity of CoFormate is slightly lower than that of CuBTC, despite the fact that the separation potential Δq of CoFormate is higher than that of CuBTC. IAST calculations of the separation potential Δq, from eq 7, for screening of MOFs will be of inadequate accuracy in cases of strong diffusional influences.

2.2. C_2H_2/CO_2 Mixture Separations. For separation of $C_2H_2(1)/CO_2(2)$ mixtures, most of the suggested MOFs such as PCP-33,[47] HOF-3,[48] TIFSIX-2-Cu-i,[49] JCM-1,[50] DICRO-4-Cu-i,[51] MUF-17,[52] UTSA-74,[46] FJU-90,[43] and FeNi-M′MOF[41] are selective to C_2H_2. Consequently, the desired ethyne product is available in the blowdown phase of the Skarstrom cycle of fixed bed operations, as shown in the schematic in Figure 7.

For the nine selected MOFs, Figure 8a,b presents the IAST calculations of (a) component loadings q_2 versus q_1 and (b) separation potential $\Delta q = q_1 - q_2 \frac{y_{10}}{y_{20}}$ versus adsorption selectivity S_{ads}. It is noteworthy that FJU-90 has the highest uptake capacity for ethyne, whereas the highest selectivity is afforded by FeNi-M′MOF. The separation performance in fixed bed adsorbers is dictated by a combination of selectivity and uptake capacities. Figure 8c presents the simulations of the vacuum blowdown cycle in which the equilibrated fixed bed of FJU-90 crystallites at the end of the adsorption cycle is subject to deep vacuum. During the time interval indicated by the arrow, C_2H_2 of the desired purity can be recovered from the gas mixture exiting the fixed bed. For a desired purity of 99%+, the amount of C_2H_2 that is recoverable can be determined from a material balance on the adsorber. These productivity values, expressed as L of the desired product (at STP) per kilogram of adsorbent in the packed bed, for the nine different MOFs are plotted in Figure 8d as the y-axis. The x-axis in Figure 8d is the separation potential, Δq, calculated using eq 7 with $y_{10} = y_{20}$ = 0.5, which represents the maximum C_2H_2 productivity that is achievable if the concentration "fronts" traversed the column in the form of shock waves during the desorption cycle. We note that the productivities determined from the transient breakthrough simulations (denoted as symbols) are near linearly related to Δq. Also shown by the continuous solid line in Figure 8d is the parity line 22.4 × Δq for the productivities. Because of the distended nature of the transient desorption breakthroughs, the actual productivities are lower than the parity values. The important conclusion to emerge is that separation potential, Δq, is the appropriate metric to use in the screening of MOFs for C_2H_2/CO_2 mixture separations. The MOF with the highest C_2H_2 productivity is FJU-90, which does not possess the highest selectivity but the highest Δq.

2.3. C_2H_2/C_2H_4 Mixture Separations. With great potential for separation of C_2H_2/C_2H_4 mixtures are a series of three-dimensional (3D) coordination networks composed of inorganic anions of $(SiF_6)^{2-}$ (hexafluorosilicate, SIFSIX).[30] The pore sizes within this family of SIFSIX materials can be systematically tuned by changing the length of the organic (=pyridine) linkers, the metal (=Cu, Ni, or Zn) node, and/or the framework interpenetration. Figure 9a compares the transient breakthroughs for 1/99 $C_2H_2(1)/C_2H_4(2)$ mixtures using SIFSIX-1-Cu, SIFSIX-2-Cu-i, SIFSIX-3-Zn, Mg_2(dobdc), and NOTT-300; the ppm C_2H_2 in the gas mixture at the outlet of the

https://dx.doi.org/10.1021/acsomega.0c02218
ACS Omega 2020, 5, 16987−17004

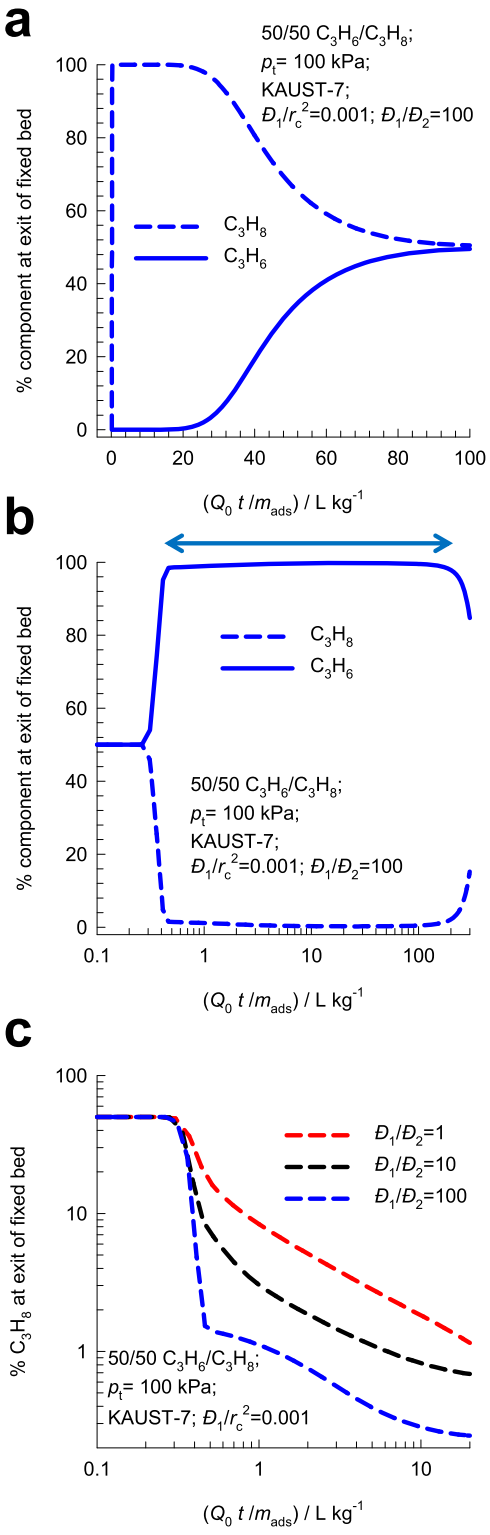

Figure 14. Transient breakthrough simulations for (a) adsorption and (b,c) desorption cycles for the separation of C_3H_6/C_3H_8 mixtures in a fixed bed adsorber packed with KAUST-7 operating at 298 K and 100 kPa; the feed compositions are $y_{10} = y_{20} = 0.5$. (c) Three different scenarios for the ratios of diffusivities $Đ_1/Đ_2$ = 1, 10, and 100 are compared, while maintaining $Đ_1/r_c^2 = 1 \times 10^{-3}\ s^{-1}$. Further information on input data and simulation details are provided in the Supporting Information.

fixed bed is plotted as a function of Q_0t/m_{ads}, where Q_0 is the volumetric flow rate of the gas mixture at the inlet to the fixed bed at STP conditions. From a material balance on the adsorber, we can determine the productivity of purified C_2H_4, containing less than 40 ppm. The productivity of pure C_2H_4 is found to be a near-linear function of the separation potential Δq determined from IAST; see Figure 9b. The highest productivity is obtained with SIFSIX-2-Cu-i (2 = 4,4′-dipyridylacetylene and i = interpenetrated);[30] in this case, each C_2H_2 molecule is bound by two F atoms from different nets. The binding of C_2H_4 with the F atoms is weaker because it is far less acidic than C_2H_2. This confirms that the separation potential Δq is the appropriate metric for screening MOFs for C_2H_2/C_2H_4 mixture separations.

Figure 9c compares the separation potentials of SIFSIX-2-Cu-i and SIFSIX-1-Cu as a function of the % C_2H_2 in the feed mixture. While the interpenetrated SIFSIX-2-Cu-i has the superior performance for feed compositions below 5% C_2H_2, SIFSIX-1-Cu, with a more open structure, has the better separation capability at higher % C_2H_2 in feed; this trend is verified in the experiments reported by Cui et al.[30]

2.4. CO_2 Capture from Natural Gas. For CO_2 capture from natural gas streams, the process economics would demand the high capture capacity, concomitant with high productivity of pure CH_4. Li et al.[68] report on the experimental results of transient breakthroughs for 40/60 $CO_2(1)/CH_4(2)$ mixtures in a packed bed with Mg_2(dobdc), Co_2(dobdc), MIL-100(Cr), and AC at 298 K temperature and 100 kPa total pressure. The masses of the adsorbents in the packed tube are not the same for each MOF, and therefore, their experimental data have been replotted in Figure 10a using Q_0t/m_{ads} as the x-axis. For each of the five materials, there is a displacement interval (indicated by the arrows) during which purified CH_4 can be recovered. The CH_4 productivities follow the hierarchy Mg_2(dobdc) > Co_2(dobdc) > MIL-100(Cr) > AC. Figure 10b presents a plot of productivity of 95%+ pure CH_4 as a function of the separation potential $\Delta q = q_1 y_{20}/y_{10} - q_2$. The 95%+ pure CH_4 productivities follow the same hierarchy as the Δq values, indicating that the separation potential can be used for screening purposes.

2.5. N_2/CH_4 Mixture Separations. Although natural gas reserves may contain N_2 in concentrations ranging to about 20%,[69] the nitrogen content must be reduced to below 4% in order to meet pipeline specifications.[70] For large capacity wells, it is most economical to employ cryogenic distillation for nitrogen removal. However, for smaller natural gas reserves, PSA separations become more cost-effective, especially because the feed mixtures are available at high pressures.[69,70] The adsorbent materials in the PSA units need to be selective to N_2, which is present in smaller concentrations than CH_4. For most known adsorbents, the adsorption selectivity for separation of N_2/CH_4 mixtures is in favor of CH_4 because of its higher polarizability.

One practical solution is to rely on diffusion selectivities by using microporous materials, such as LTA-4A zeolite, ETS-4 (ETS = Engelhard Titano-Silicate; ETS-4 is also named as CTS-1 = Contracted Titano Silicate-1), and clinoptilolites, which have significantly higher diffusivities of N_2 compared to that of CH_4.[5,70−73] The "spherical" CH_4 (3.7 Å) is much more severely constrained inside the narrow pores of such materials, whereas the "pencil-like" nitrogen molecule (4.4 Å × 3.3 Å) hops lengthwise with higher diffusivity. By tuning the size of the microporous channels of cation-exchanged ETS-4, such as Ba-ETS-4, CH_4 can be practically excluded from the pores.

Bhadra[70,74] have developed a detailed mathematical model for a PSA scheme for purification of natural gas using Ba-ETS-4, using the steps shown in Figure 11. In this scheme, the inclusion

https://dx.doi.org/10.1021/acsomega.0c02218
ACS Omega 2020, 5, 16987−17004

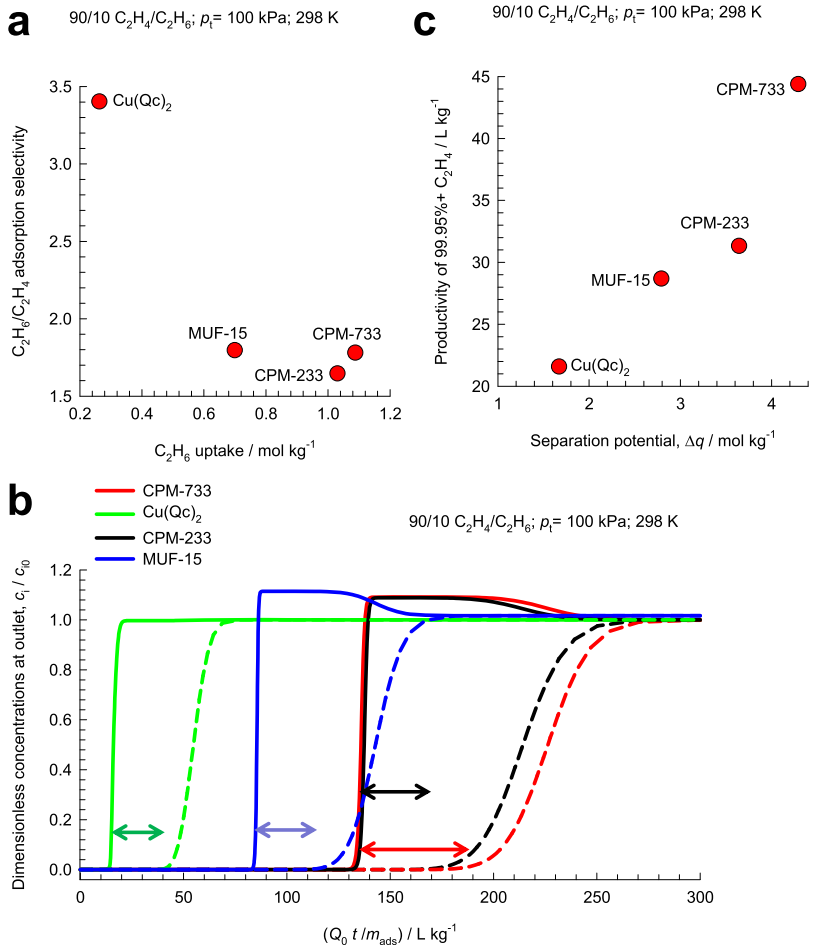

Figure 15. (a) IAST calculations of the C_2H_6 uptake q_2 vs the separation selectivity S_{ads} of 90/10 C_2H_4/C_2H_6 mixture adsorption at 298 K and 100 kPa in four different MOFs. (b) Transient breakthrough simulations for the separation of 90/10 C_2H_4/C_2H_6 mixture adsorption at 298 K and 100 kPa in fixed beds packed with $Cu(Qc)_2$, MUF-15, CPM-233, and CPM-733. (c) Productivity of 99.95%+ pure C_2H_4 product recovered during the displacement intervals, plotted as function of the separation potential Δq. Further information on input data and simulation details are provided in the Supporting Information.

of the cocurrent blowdown step (suggested by Jayaraman et al.[72] for N_2/CH_4 mixture separations with clinoptilolites) increases the CH_4 recovery. At the end of the countercurrent blowdown step, the bed contains both nitrogen (fast diffusing) and methane (slow diffusing). Thus, if the bed is simply closed at one end and left for a period of time, the nitrogen will diffuse out first, followed by methane, so the system is, in effect, self-purging (fifth step in the sequence).

In a recent article, Yoon et al.[75] have reported that MIL-100(Cr), activated at 523 K, shows adsorption selectivity in favor of N_2. However, an important disadvantage of this material for use in natural gas purification is that CH_4 is not completely excluded. Figure 12 compares the transient breakthrough of 20/80 $N_2(1)/CH_4(2)$ mixtures in a fixed bed adsorber packed with MIL-100(Cr) and Ba-ETS-4, operating at 283 K and total pressure p_t = 1 MPa. We note that the breakthrough of CH_4 occurs significantly later than that with BaETS-4, implying that a significant amount of CH_4 gets adsorbed. Consequently, even after cocurrent blowdown, a significant proportion of CH_4 will remain in the void spaces of the fixed bed packed with MIL-100(Cr) and will be "lost" along with N_2 in the final blowdown step; this implies that recovery of 96%+ pure CH_4 is likely to be unacceptably low with MIL-100(Cr). Candidate adsorbents for N_2/CH_4 separations must disallow the ingress of CH_4 inside the pores.

2.6. Separation of C_2H_4/C_2H_6 and C_3H_6/C_3H_8 Mixtures.

Both ethene (C_2H_4) and propene (C_3H_6) are important precursors for the manufacture of a variety of polymers. Propene is a byproduct from the steam cracking of liquid feedstocks such as naphtha and liquefied petroleum gas, as well as off-gases produced in fluid catalytic cracking units in refineries. The key processing steps for preparing feedstocks for polymer production are the separations of C_2H_4/C_2H_6 and C_3H_6/C_3H_8 mixtures, which are traditionally carried out in distillation columns. Because of small differences in the boiling points, the relative volatilities of C_2H_4/C_2H_6 and C_3H_6/C_3H_8 separations are in the range 1.1−1.2. In order to satisfy the 99.95%+ purity requirement of alkene feedstocks to polymerization reactors, the distillation columns are tall (150−200 trays) and operate at cryogenic temperatures, high pressures, and high reflux ratios (≈15). Use of adsorptive separations may result in reduced energy consumption.

Each of the unsaturated alkenes C_2H_4 and C_3H_6 possesses a π-bond, and the preferential adsorption of alkene from the corresponding alkane with the same number of C atoms can be achieved by choosing zeolitic adsorbents with extraframework cations [e.g., LTA-4A zeolite[76,77] and NaX (=13X) zeolite[76,78]]

https://dx.doi.org/10.1021/acsomega.0c02218
ACS Omega 2020, 5, 16987−17004

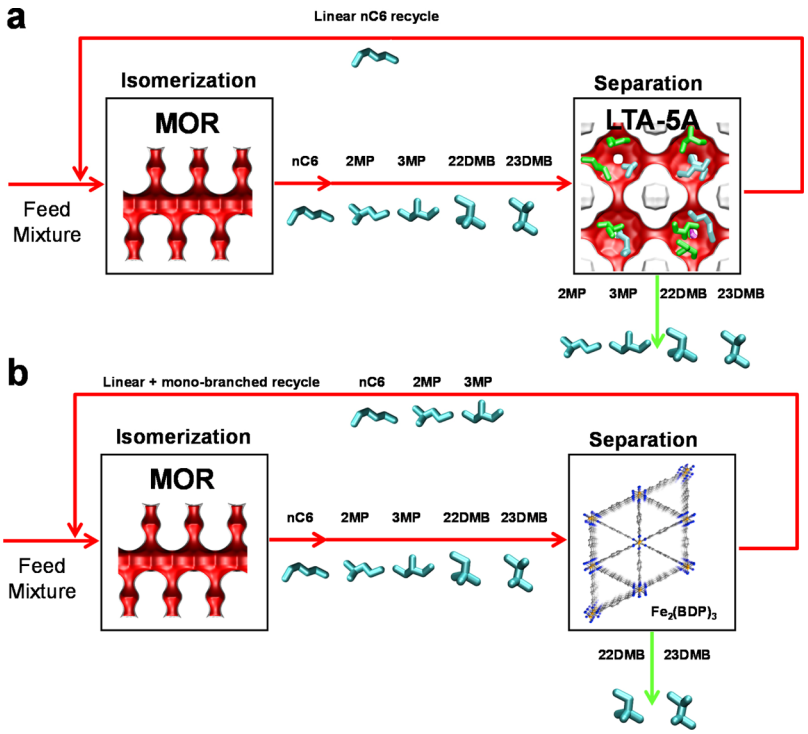

Figure 16. (a) Currently employed processing scheme for *n*C6 isomerization and a subsequent separation step using LTA-5A zeolite. (b) Improved processing scheme for the *n*C6 isomerization process. Further process background details are provided in the Supporting Information.

or MOFs with unsaturated "open" metal sites[23,79] (e.g., M_2(dobdc)[23,79] [M = Mg, Mn, Co, Ni, Zn, and Fe; dobdc^{4-} = 2,5-dioxido-1,4-benzenedicarboxylate] and CuBTC[80]). All of the atoms of C_2H_4 lie on the same plane, and its dipole moment is zero; however, it does possess a quadrupole moment. It is to be noted that the polarizability of the alkane (C_2H_6, C_3H_8) is slightly higher than that of the corresponding alkene (C_2H_4 and C_3H_6).

An important disadvantage of the alkene/alkane separations with the adsorbents listed above is that the desired alkene product, required for the production of polymer-grade feedstock, can only be recovered in the desorption phase. In practice, it becomes necessary to operate with multiple beds involving five different steps, as schematized in Figure 13; the C_3H_6 product of the desired purity is recovered in the final step by countercurrent vacuum blowdown.[77,78,81] The recovery of high-purity C_3H_6 product in the final vacuum blowdown step is expected to be enhanced if C_3H_8 is (almost) excluded during the high-pressure adsorption cycle. Near-total exclusion of C_3H_8 is achievable by kinetically based separations using cage-type zeolites with eight-ring windows such as CHA and LTA-4A zeolites.[81,82] An alternative is to employ a customized MOF such as NbOFFIVE-1-Ni (=KAUST-7) with pyrazine as the organic linker.[24] The use of bulkier $(NbOF_5)^{2-}$ pillars causes tilting of the pyrazine molecule on the linker, resulting in an effective aperture of 0.30 nm. This reduced aperture permits ingress of the smaller C_3H_6 molecules but practically excludes C_3H_8, relying on subtle differences in bond lengths and bond angles.

Figure 14a,b presents the simulations of the transient breakthroughs for the (a) adsorption and (b) desorption cycles for separation of equimolar $C_3H_6(1)/C_3H_8(2)$ mixtures in a fixed bed adsorber packed with KAUST-7 operating at 298 K and 100 kPa. During the time interval indicated by the arrow in Figure 14b, the C_3H_6 product of desired purity can be recovered. Because of the significantly lower diffusivity of C_3H_8, the desorption process is self-purging.[7,83] In the last step shown in Figure 13, if the bed is simply closed at the one end and left for a period of time, C_3H_6 will diffuse out first, followed by C_3H_8. Figure 14c presents a comparison of the transient desorption using three different ratios of intracrystalline diffusivities $Đ_1/Đ_2$ = 1, 10, and 100. From a material balance on the adsorber, the productivities of 99%+ pure C_3H_6 can be determined; the values are, respectively, 15.7, 18.9, and 24.3 L kg^{-1} at STP for the three scenarios. Because of the sensitivity of the C_3H_6 productivity to the values of intracrystalline diffusivities, a detailed process design exercise, such as that reported by Khalighi et al.,[81,82] will be required in order to compare the C_3H_6 productivities of KAUST-7, with other MOFs; simple IAST calculations of Δq and S_{ads} are unlikely to be sufficiently accurate for reliable screening.

For C_2H_4/C_2H_6 separations, near-total exclusion of C_2H_6 is achieved by use of ultramicroporous MOF [$Ca(C_4O_4)(H_2O)$] that possesses rigid one-dimensional (1D) channels.[25] The 1D channels are of similar size to C_2H_4 molecules (all atoms of which lie on the same plane), but owing to the size, shape, and rigidity of the pores, they practically exclude C_2H_6.

For C_2H_4/C_2H_6 separations, a number of microporous adsorbents such as $Fe_2(O_2)$(dobdc),[28] $Cu(Qc)_2$,[84] MUF-15,[85] PCN-250,[86] ZIF-7,[87,88] ZIF-8,[89,90] IRMOF-8,[91] Ni(bdc)-$(ted)_{0.5}$,[92] MAF-49,[91] CPM-233,[26] and CPM-733[26] adsorb the saturated alkane selectively exploiting the differences in van der Waals interactions, resulting from the higher polarizability of C_2H_6. Figure 15a presents the IAST calculations of the C_2H_6 uptake q_2 versus the separation selectivity S_{ads} of 90/10 C_2H_4/C_2H_6 mixture adsorption at 298 K and 100 kPa in four different MOFs. The hierarchy of separation selectivities is $Cu(Qc)_2$ > CPM-733 ≈ MUF-15 > CPM-233. However, because of the higher C_2H_6 uptake capacity of CPM-733, the separation

https://dx.doi.org/10.1021/acsomega.0c02218
ACS Omega 2020, 5, 16987−17004

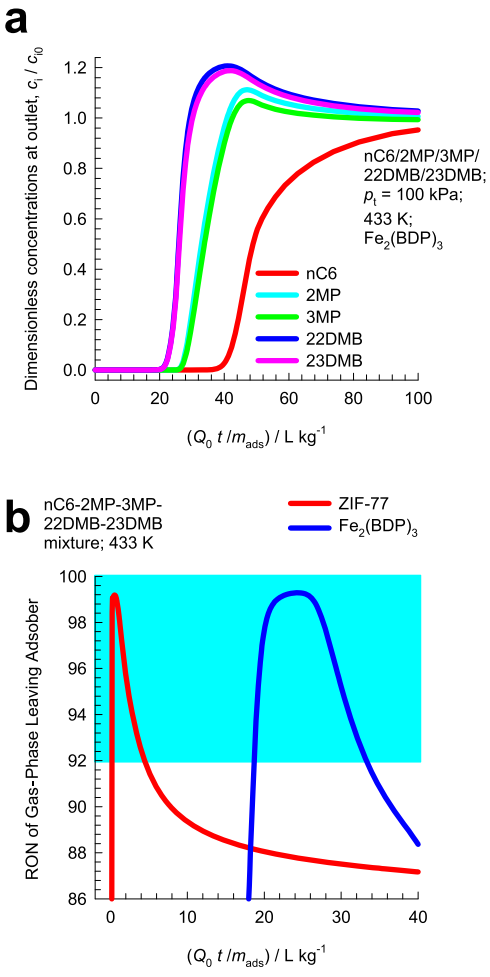

Figure 17. (a) Simulations of transient breakthrough characteristics for a five-component *n*C6/2MP/3MP/22DMB/23DMB mixture in a fixed bed adsorber packed with $Fe_2(BDP)_3$ operating at a total pressure of 100 kPa and 433 K. The partial pressures of the components in the bulk gas phase at the inlet are $p_1 = p_2 = p_3 = p_4 = p_5 = 20$ kPa. (b) Plot of RON of product gas mixture exiting the fixed bed adsorber packed with ZIF-77 and $Fe_2(BDP)_3$, plotted as a function of $Q_0 t/m_{ads}$. Further information on input data and simulation details are provided in the Supporting Information.

potential, Δq, follows the hierarchy CPM-733 > CPM-233 > MUF-15 > $Cu(Qc)_2$. The separation potential of $Cu(Qc)_2$ is the lowest because it has the smallest C_2H_6 uptake. In order to verify the hierarchy of Δq determined from IAST, transient breakthrough simulations were carried out for CPM-733, CPM-233, MUF-15, and $Cu(Qc)_2$; see Figure 15b. The dimensionless concentrations at the exit of the packed bed are plotted as a function of $Q_0 t/m_{ads}$. During the interval indicated by the arrows, purified C_2H_4 can be recovered. The productivities follow the hierarchy CPM-733 > CPM-233 > MUF-15 > $Cu(Qc)_2$, that is in line with the hierarchy of Δq values. From the transient breakthrough simulations, the amount of 99.95%+ pure C_2H_4 product recovered during the displacement intervals can be determined. The productivity values show a near-linear dependence on Δq; see Figure 15c. This implies that the IAST calculations of $\Delta q = q_1 y_{20}/y_{10} - q_2$ are appropriate metrics for screening and ranking MOFs.

2.7. Separation of Hexane Isomers. The values of the research octane number (RON) of alkane isomers increase with the degree of branching. For hexane isomers, for example, the RON values are *n*-hexane (*n*C6) = 30; 2-methylpentane (2MP) = 74.5; 3-methylpentane (3MP) = 75.5; 2,2 dimethylbutane (22DMB) = 94; and 2,3 dimethylbutane (23DMB) = 105. Consequently, dibranched alkane isomers are preferred blending components in high-octane gasoline.[90,93,94] As shown in the process scheme in Figure 16a, alkane isomers are currently separated on the basis of molecular sieving using LTA-5A zeolite. Linear alkanes can hop from one cage to the adjacent cage through the 4 Å windows of LTA-5A, but monobranched and dibranched alkanes are largely excluded. From an industrial perspective, it is desirable to adopt an alternative separation scheme (see Figure 16b) using an adsorbent that has the capability of separating the dibranched isomers from the linear and monobranched isomers that may be recycled back to the isomerization reactor.

One candidate MOF that can be employed as an adsorbent in Figure 16b is $Fe_2(BDP)_3$ [BDP^{2-} = benzenedipyrazolate] that possesses one-dimensional triangular shape channels of 4.9 Å.[93] Simulations of transient breakthroughs of hexane isomers using $Fe_2(BDP)_3$ are shown in Figure 17a; the hierarchy of breakthroughs is dibranched, monobranched, and linear isomers; this hierarchy is dictated by a combination of adsorption strengths, dictated essentially by van der Waals interactions (*n*C6 ≫ 2MP ≈ 3MP ≫ 22DMB ≈ 23DMB), and diffusivities (*n*C6 > 2MP ≈ 3MP > 22DMB ≈ 23DMB). The RON of the product gas mixture exiting the adsorber is plotted in Figure 17b. During a certain time interval, the 92+ RON product can be recovered for incorporation into the gasoline pool. This requirement of 92+ RON implies that the product stream will contain predominantly the dibranched isomers 22DMB and 23DMB, while allowing a small proportion of 2MP and 3MP to be incorporated into the product stream. Also shown in Figure 17b, for comparison purposes, is the corresponding breakthrough simulation data for ZIF-77[94] that has a characteristic pore dimension of 4.5 Å. Because of stronger diffusional limitations in ZIF-77, the 92+ RON productivity of ZIF-77 is significantly lower than that of $Fe_2(BDP)_3$; this is evidenced by the significantly shorter time interval during which 92+ RON product can be recovered.

2.8. Separation of C8 Aromatics. The xylene isomers, *o*-xylene, *m*-xylene, and in particular *p*-xylene, are important chemical intermediates. Xylenes, along with other aromatic hydrocarbons, are commonly obtained from catalytic reforming of naphtha, as illustrated in the process scheme in Figure 18.[63,95,96] The products of catalytic reformer are fed to a distillation column called the reformate splitter. The bottom product of the reformate splitter, rich in xylenes, is further distilled in the xylene splitter, whose bottom product consists of C9+ aromatics. The recovery of *p*-xylene from the mixture of C8 aromatics (typically composition: 20% *o*-xylene, 44% *m*-xylene, 17% *p*-xylene, and 19% ethylbenzene) in the overhead product of the xylene splitter is the focus of attention in this section.

Because of the very small differences in boiling points (cf. Figure 19), *p*-xylene recovery by use of distillation technology is not feasible. Two different technologies are currently in use for recovery of *p*-xylene: (a) fractional crystallization and (b) selective adsorption. Fractional crystallization relies on the differences in freezing points (cf. Figure 19). The freezing point of *p*-xylene is significantly higher than that of other C8 aromatics; on cooling, therefore, pure *p*-xylene crystals are the first to emerge from the solution. Selective adsorption of *p*-xylene from liquid-phase mixtures of C8 aromatics is achieved with cation-exchange FAU zeolite adsorbent, such as BaX, in a

https://dx.doi.org/10.1021/acsomega.0c02218
ACS Omega 2020, 5, 16987−17004

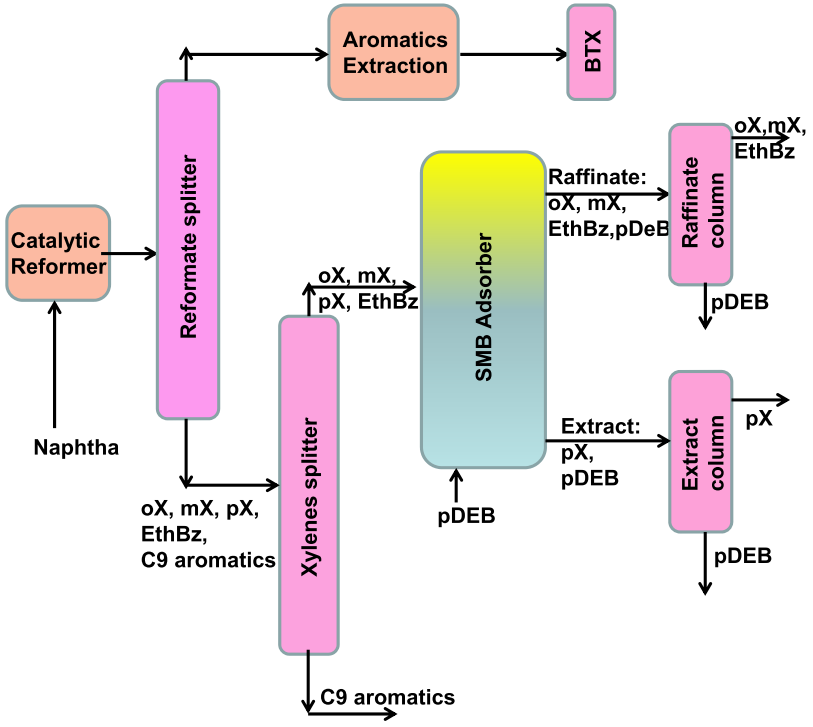

Figure 18. Schematic showing the separations of the products from a catalytic reforming unit. Further process background details are provided in the Supporting Information.

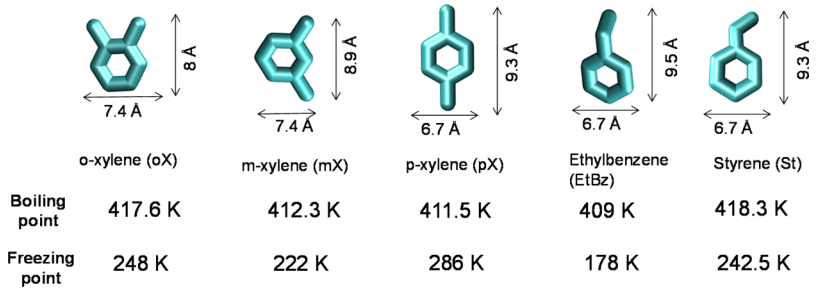

Figure 19. Boiling points and freezing points of C8 hydrocarbons, along with molecular dimensions, culled from Torres-Knoop et al.[107]

simulated moving bed (SMB) adsorption device.[97−99] The hierarchy of adsorption strengths in BaX is dictated by molecular packing, or entropy, effects that prevail under pore saturation conditions in liquid-phase SMB separations.[95,97−100] Unlike PSA technologies for gaseous separations, the SMB process operates continuously under steady-state conditions; see the schematic in Figure 20.

The C8 aromatic feed is introduced at a port near the middle of the SMB unit.[101,102] The desorbent *p*-diethylbenzene (boiling point 450 K) is introduced at the bottom.[103] Figure 20 also indicates typical liquid phase concentrations of *o*-xylene, *m*-xylene, *p*-xylene, and ethylbenzene along the adsorber height. The extract phase, containing the more strongly adsorbed *p*-xylene, is recovered below the feed injection port in the bottom section of the column. The raffinate phase, containing the more weakly adsorbed *o*-xylene, *m*-xylene, and ethylbenzene, is tapped off above the feed injection port in the upper section of the column.

For realizing improvements in the SMB units, there is considerable scope for the development of MOFs that have both higher uptake capacity and selectivity to *p*-xylene as compared to BaX zeolite. Improved MOF adsorbents will result in lower recirculation flows of eluent, and microporous adsorbent in the SMB unit, and this will result in significant economic advantages. There are several MOFs such as DynaMOF-100,[104,105] Co-CUK-1,[106] MAF-X8,[107] JUC-77,[108] Co(BDP),[21] and MIL-125[109−111] that have the potential for use in SMB units.

For preferential adsorption of *p*-xylene, and rejection of *o*-xylene, *m*-xylene, and ethylbenzene, the appropriate metric for comparing these MOFs is the separation potential Δq that is derived using the shock wave model for fixed bed adsorbers[63]

$$\Delta q = (q_{pX})\frac{y_{oX} + y_{mX} + y_{EthBz}}{1 - y_{oX} - y_{mX} - y_{EthBz}} - (q_{oX} + q_{mX} + q_{EthBz}) \quad (8)$$

In eq 8, the molar loadings of each of the four C8 aromatics, q_i, expressed in mol per kilogram of crystalline adsorbent are calculated using the IAST for mixture adsorption equilibrium. Figure 21 presents the plot of Δq versus *p*-xylene uptake for a few selected MOFs. The highest value of the separation potential is offered by DynaMOF-100 that is a Zn(II)-based dynamic coordination framework that undergoes guest-induced structural changes so as to allow selective uptake of *p*-xylene

https://dx.doi.org/10.1021/acsomega.0c02218
ACS Omega 2020, 5, 16987−17004

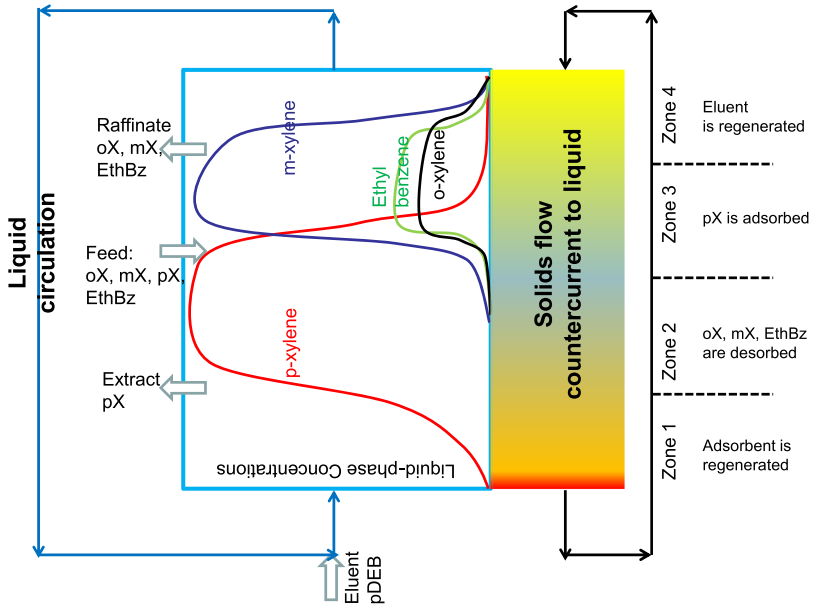

Figure 20. SMB adsorption technology for the separation of a feed mixture containing *o*-xylene/*m*-xylene/*p*-xylene/ethylbenzene. The SMB technology is depicted here with countercurrent contacting between the down-flowing adsorbent material and up-flowing desorbent (eluent) liquid. Also indicated are the liquid-phase concentrations of a mixture of *o*-xylene/*m*-xylene/*p*-xylene/ethylbenzene using the information presented by Minceva and Rodrigues.[101]

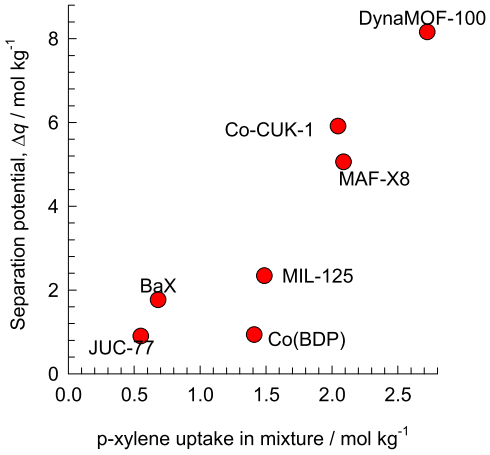

Figure 21. Plot of the separation potential, Δq, vs the gravimetric uptake of *p*-xylene. Further information on input data and simulation details are provided in the Supporting Information.

within the cavities. A slightly lower separation potential is offered by Co-CUK-1 that is composed of cobalt(II) cations and the dianion of dicarboxylic acid; the 1D zigzag-shaped channels of Co-CUK-1 allow optimal vertical stacking of *p*-xylene. Both these MOFs offer separation potentials about three to four times that achievable by BaX; there is a need for experimental verification of this expectation.

2.9. Influence of Thermodynamic Nonidealities in Mixture Adsorption. In many cases, the IAST fails to provide a quantitatively correct description of mixture adsorption equilibrium and thus thermodynamic nonidealities come into play. Thermodynamic nonidealities are evidenced for water/alcohol mixtures because of molecular clustering engendered by hydrogen bonding.[112−117] Thermodynamic nonidealities also arise because of preferential location of CO_2 molecules at the window regions of eight-ring zeolites such as DDR, CHA, ERI, LTA-4A, and LTA-5A.[55,56,117−119] For CO_2 capture with NaX zeolite, there is congregation of CO_2 around the cations, resulting in failure of IAST.[117,119] Thermodynamic nonidealities can be strong enough to cause selectivity reversals for CO_2/hydrocarbon mixture adsorption in cation-exchanged zeolites.[55,56,117] Framework flexibility and gate-opening behaviors may lead to failure of IAST.[120] In all the aforementioned cases, we need to use the real adsorbed solution theory (RAST) for quantitative description of mixture adsorption in transient breakthrough simulations. RAST calculations of Δq may be used for screening purposes.[116,119]

3. CONCLUSIONS

The following major conclusions emerge from this study.

(1) The separation performance in fixed bed devices is governed by a combination of adsorption selectivity, S_{ads}, and uptake capacities, q_1, q_2; low uptake capacities diminish the separation performance of MOFs with high values of S_{ads}.

(2) The separation potential Δq, which is calculable on the basis of IAST, provides a simple and convenient metric to screen and rank the separation capability of MOFs. For a component that is recovered in pure form during the adsorption cycle, Δq can be calculated using eq 2, which is derived using the shock wave model. For a component that is recovered in pure form during the blowdown cycle, the separation potential Δq is defined by eq 7. The value of Δq defines the upper limit to the achievable separations in fixed bed units. The actual separations in fixed bed adsorbers will be lower than the IAST-calculated Δq values because of distended breakthroughs.

(3) The composition of the feed mixture may have a significant influence on the separation potential of the MOF; this is illustrated in Figure 9c for C_2H_2/C_2H_4 mixtures.

(4) Broadly speaking, high product purities are more difficult to achieve if the desired product is recovered in the

https://dx.doi.org/10.1021/acsomega.0c02218
ACS Omega 2020, 5, 16987−17004

blowdown cycle of PSA schemes, as presented in Figures 7, 11, and 13. In such cases, it is advantageous to have MOF adsorbents that virtually exclude the less strongly adsorbing component because this facilitates the achievement of high-purity products. The productivity calculations are very sensitive to intracrystalline diffusion limitations, as illustrated in Figure 14 for C_3H_6/C_3H_8 mixture separations using KAUST-7.

(5) The concept of separation potential is particularly advantageous for multicomponent separations; several selectivities and uptake capacities are incorporated into one combined metric that quantifies the desired separation task. For example, eq 8 is the appropriate expression for Δq for separation of four-component mixture of C8 aromatics

(6) As illustrated in Figures 5, 9, 10, 12, 15, and 17, transient breakthrough experiments or simulations can be directly used to compare the separation effectiveness of MOFs. In such cases, the appropriate x-axis for plotting purposes is Q_0t/m_{ads}; this parameter may be viewed as "corrected" time. Such comparisons are indispensable for comparison and screening of MOFs that are subject to severe diffusion limitations,[90,121]

(7) For situations in which the intracrystalline influences are strong, the separation performance will be significantly lowered and IAST calculations of Δq will not be adequate for screening purposes.

(8) For kinetically driven separation, as used industrially for N_2/CH_4 and N_2/O_2 mixtures, some authors have suggested the use of $\sqrt{Đ_1/Đ_2}$ as a metric to quantify kinetic influences.[71,81] The concept of the separation potential Δq is not of relevance in such cases.

■ ASSOCIATED CONTENT

Supporting Information

The Supporting Information is available free of charge at https://pubs.acs.org/doi/10.1021/acsomega.0c02218.

Methodology used for transient breakthrough simulations, analytic solutions to the shock wave model for fixed bed transient operations, structural information on the MOFs investigated, unary isotherm data sources for each guest/host combination, and data inputs of simulation results for each of the investigated mixture separations (PDF)

■ AUTHOR INFORMATION

Corresponding Author

Rajamani Krishna − *Van 't Hoff Institute for Molecular Sciences, University of Amsterdam, 1098 XH Amsterdam, The Netherlands;* orcid.org/0000-0002-4784-8530; Email: r.krishna@contact.uva.nl

Complete contact information is available at: https://pubs.acs.org/10.1021/acsomega.0c02218

Notes

The author declares no competing financial interest.

■ ACKNOWLEDGMENTS

The simulation code for transient breakthroughs was developed by Dr. Richard Baur and Dr. Jasper van Baten; their assistance and help are gratefully acknowledged.

■ NOMENCLATURE

Latin Alphabet

c_i molar concentration of species i, mol m^{-3}
c_{i0} molar concentration of species i in fluid mixture at inlet, mol m^{-3}
c_t total molar concentration of mixture, mol m^{-3}
$Đ_i$ Maxwell−Stefan diffusivity for molecule−wall interaction, m^2 s^{-1}
L length of packed bed adsorber, m
m_{ads} mass of adsorbent in packed bed, kg
p_i partial pressure of species i in mixture, Pa
p_t total system pressure, Pa
q_i component molar loading of species i, mol kg^{-1}
q_t total molar loading in mixture, mol kg^{-1}
Q volumetric flow rate of gas mixture, m^3 s^{-1}
r_c radius of crystallite, m
S_{ads} adsorption selectivity, dimensionless
t time, s
T absolute temperature, K
u superficial gas velocity in packed bed, m s^{-1}
v interstitial gas velocity in packed bed, m s^{-1}
y_i mole fraction of species i in the bulk fluid phase, dimensionless
z distance along the adsorber, m

Greek Alphabet

ε voidage of packed bed, dimensionless
ρ framework density, kg m^{-3}
τ time, dimensionless

■ REFERENCES

(1) Sircar, S.; Golden, T. C. Purification of Hydrogen by Pressure Swing Adsorption. *Separ. Sci. Technol.* **2000**, *35*, 667−687.

(2) Ribeiro, A. M.; Grande, C. A.; Lopes, F. V. S.; Loureiro, J. M.; Rodrigues, A. E. A parametric study of layered bed PSA for hydrogen purification. *Chem. Eng. Sci.* **2008**, *63*, 5258−5273.

(3) Banu, A.-M.; Friedrich, D.; Brandani, S.; Düren, T. A Multiscale Study of MOFs as Adsorbents in H_2 PSA Purification. *Ind. Eng. Chem. Res.* **2013**, *52*, 9946−9957.

(4) Majlan, E. H.; Wan Daud, W. R.; Iyuke, S. E.; Mohamad, A. B.; Kadhum, A. A. H.; Mohammad, A. W.; Takriff, M. S.; Bahaman, N. Hydrogen purification using compact pressure swing adsorption system for fuel cell. *Int. J. Hydrogen Energy* **2009**, *34*, 2771−2777.

(5) Yang, R. T. *Adsorbents: Fundamentals and Applications*; John Wiley & Sons, Inc.: Hoboken, New Jersey, 2003.

(6) Ruthven, D. M. *Principles of Adsorption and Adsorption Processes*; John Wiley: New York, 1984.

(7) Ruthven, D. M.; Farooq, S.; Knaebel, K. S. *Pressure Swing Adsorption*; VCH Publishers: New York, 1994.

(8) Ahn, S.; You, Y.-W.; Lee, D.-G.; Kim, K.-H.; Oh, M.; Lee, C.-H. Layered Two- and Four-bed PSA Processes for H2 Recovery from Coal Gas. *Chem. Eng. Sci.* **2012**, *68*, 413−423.

(9) Pakseresht, S.; Kazemeini, M.; Akbarnejad, M. M. Equilibrium isotherms for CO, CO_2, CH_4 and C_2H_4 on the 5A molecular sieve by a simple volumetric apparatus. *Sep. Purif. Technol.* **2002**, *28*, 53−60.

(10) Sircar, S. Basic research needs for design of adsorptive gas separation processes. *Ind. Eng. Chem. Res.* **2006**, *45*, 5435−5448.

(11) Yang, R. T. *Gas Separation by Adsorption Processes*; Butterworth: Boston, 1987.

(12) Belmabkhout, Y.; Pirngruber, G.; Jolimaitre, E.; Methivier, A. A complete experimental approach for synthesis gas separation studies using static gravimetric and column breakthrough experiments. *Adsorption* **2007**, *13*, 341−349.

(13) Wu, H.; Yao, K.; Zhu, Y.; Li, B.; Shi, Z.; Krishna, R.; Li, J. Cu-TDPAT, an rht-type Dual-Functional Metal−Organic Framework Offering Significant Potential for Use in H_2 and Natural Gas

Purification Processes Operating at High Pressures. *J. Phys. Chem. C* **2012**, *116*, 16609−16618.
(14) Herm, Z. R.; Krishna, R.; Long, J. R. CO_2/CH_4, CH_4/H_2 and $CO_2/CH_4/H_2$ separations at high pressures using Mg_2(dobdc). *Microporous Mesoporous Mater.* **2012**, *151*, 481−487.
(15) Herm, Z. R.; Swisher, J. A.; Smit, B.; Krishna, R.; Long, J. R. Metal-Organic Frameworks as Adsorbents for Hydrogen Purification and Pre-Combustion Carbon Dioxide Capture. *J. Am. Chem. Soc.* **2011**, *133*, 5664−5667.
(16) Mason, J. A.; Sumida, K.; Herm, Z. R.; Krishna, R.; Long, J. R. Evaluating Metal-Organic Frameworks for Post-Combustion Carbon Dioxide Capture via Temperature Swing Adsorption. *Energy Environ. Sci.* **2011**, *4*, 3030−3040.
(17) Xiang, S.; He, Y.; Zhang, Z.; Wu, H.; Zhou, W.; Krishna, R.; Chen, B. Microporous Metal-Organic Framework with Potential for Carbon Dioxide Capture at Ambient Conditions. *Nat. Commun.* **2012**, *3*, 954.
(18) Asgari, M.; Semino, R.; Schouwink, P. A.; Kochetygov, I.; Tarver, J.; Trukhina, O.; Krishna, R.; Brown, C. M.; Ceriotti, M.; Queen, W. L. Understanding how Ligand Functionalization influences CO_2 and N2 Adsorption in a Sodalite MOF. *Chem. Mater.* **2020**, *32*, 1526−1536.
(19) Krishna, R.; van Baten, J. M. A comparison of the CO_2 capture characteristics of zeolites and metal-organic frameworks. *Sep. Purif. Technol.* **2012**, *87*, 120−126.
(20) Krishna, R. Adsorptive separation of $CO_2/CH_4/CO$ gas mixtures at high pressures. *Microporous Mesoporous Mater.* **2012**, *156*, 217−223.
(21) Krishna, R.; van Baten, J. M. In silico screening of metal-organic frameworks in separation applications. *Phys. Chem. Chem. Phys.* **2011**, *13*, 10593−10616.
(22) Rajagopalan, A. K.; Avila, A. M.; Rajendran, A. Do adsorbent screening metrics predict process performance? Aprocess optimisation based study for post-combustion capture of CO_2. *Int. J. Greenhouse Gas Control* **2016**, *46*, 76−85.
(23) Bloch, E. D.; Queen, W. L.; Krishna, R.; Zadrozny, J. M.; Brown, C. M.; Long, J. R. Hydrocarbon Separations in a Metal-Organic Framework with Open Iron(II) Coordination Sites. *Science* **2012**, *335*, 1606−1610.
(24) Cadiau, A.; Adil, K.; Bhatt, P. M.; Belmabkhout, Y.; Eddaoudi, M. A Metal-Organic Framework−Based Splitter for Separating Propylene from Propane. *Science* **2016**, *353*, 137−140.
(25) Lin, R.-B.; Li, L.; Zhou, H.-L.; Wu, H.; He, C.; Li, S.; Krishna, R.; Li, J.; Zhou, W.; Chen, B. Molecular Sieving of Ethylene from Ethane using a Rigid Metal-Organic Framework. *Nat. Mater.* **2018**, *17*, 1128−1133.
(26) Yang, H.; Wang, Y.; Krishna, R.; Jia, X.; Wang, Y.; Hong, A. N.; Dang, C.; Castillo, H. E.; Bu, X.; Feng, P. Pore-Space-Partition-Enabled Exceptional Ethane Uptake and Ethane-Selective Ethane−Ethylene Separation. *J. Am. Chem. Soc.* **2020**, *142*, 2222−2227.
(27) Bao, Z.; Wang, J.; Zhang, Z.; Xing, H.; Yang, Q.; Yang, Y.; Wu, H.; Krishna, R.; Zhou, W.; Chen, B.; Ren, Q. Molecular Sieving of Ethane from Ethylene through the molecular Cross-section Size Differentiation in Gallate-based Metal-Organic Frameworks. *Angew. Chem., Int. Ed.* **2018**, *57*, 16020−16025.
(28) Li, L.; Lin, R.-B.; Krishna, R.; Li, H.; Xiang, S.; Wu, H.; Li, J.; Zhou, W.; Chen, B. Ethane/ethylene Separation in a Metal-Organic Framework with Iron-Peroxo Sites. *Science* **2018**, *362*, 443−446.
(29) Zhang, X.; Li, L.; Wang, J.-X.; Wen, H.-M.; Krishna, R.; Wu, H.; Zhou, W.; Chen, Z.-N.; Li, B.; Qian, G.; Chen, B. Selective Ethane/Ethylene Separation in a Robust Microporous Hydrogen-Bonded Organic Framework. *J. Am. Chem. Soc.* **2020**, *142*, 633−640.
(30) Cui, X.; Chen, K.; Xing, H.; Yang, Q.; Krishna, R.; Bao, Z.; Wu, H.; Zhou, W.; Dong, X.; Han, Y.; Li, B.; Ren, Q.; Zaworotko, M. J.; Chen, B. Pore Chemistry and Size Control in Hybrid Porous Materials for Acetylene Capture from Ethylene. *Science* **2016**, *353*, 141−144.
(31) Peng, Y. L.; He, C.; Pham, T.; Wang, T.; Li, P.; Krishna, R.; Forrest, K. A.; Hogan, A.; Suepaul, S.; Space, B.; Fang, M.; Chen, Y.; Zaworotko, M. J.; Li, J.; Li, L.; Zhang, Z.; Cheng, P.; Chen, B. Robust Microporous Metal-Organic Frameworks for Highly Efficient and Simultaneous Removal of Propyne and Propadiene from Propylene. *Angew. Chem., Int. Ed.* **2019**, *58*, 10209−10214.
(32) Tao, Y.; Krishna, R.; Yang, L. X.; Fan, Y. L.; Wang, L.; Gao, Z.; Xiong, J. B.; Sun, L. J.; Luo, F. Enhancing C_2H_2/C_2H_4 separation by incorporating low-content sodium in covalent organic framework. *Inorg. Chem. Front.* **2019**, *6*, 2921−2926.
(33) Li, L.; Wen, H. M.; He, C.; Lin, R. B.; Krishna, R.; Wu, H.; Zhou, W.; Li, J.; Li, B.; Chen, B. A Metal−Organic Framework with Suitable Pore Size and Specific Functional Site for Removal of Trace Propyne from Propylene. *Angew. Chem., Int. Ed.* **2018**, *57*, 15183−15188.
(34) Li, L.; Lin, R.-B.; Krishna, R.; Wang, X.; Li, B.; Wu, H.; Li, J.; Zhou, W.; Chen, B. Efficient Separation of Ethylene from Acetylene/Ethylene Mixtures by a Flexible-Robust Metal−Organic Framework. *J. Mater. Chem. A* **2017**, *5*, 18984−18988.
(35) Li, L.; Lin, R.-B.; Krishna, R.; Wang, X.; Li, B.; Wu, H.; Li, J.; Zhou, W.; Chen, B. Flexible−Robust Metal−Organic Framework for Efficient Removal of Propyne from Propylene. *J. Am. Chem. Soc.* **2017**, *139*, 7733−7736.
(36) Li, L.; Krishna, R.; Wang, Y.; Wang, X.; Yang, J.; Li, J. Flexible metal−organic frameworks with discriminatory gate-opening effect for separation of acetylene from ethylene/acetylene mixtures. *Eur. J. Inorg. Chem.* **2016**, 4457−4462.
(37) Wen, H.-M.; Li, B.; Wang, H.; Wu, C.; Alfooty, K.; Krishna, R.; Chen, B. A Microporous Metal−Organic Framework with Rare lvt Topology for Highly Selective C_2H_2/C_2H_4 Separation at Room Temperature. *Chem. Commun.* **2015**, *51*, 5610−5613.
(38) Matsuda, R.; Kitaura, R.; Kitagawa, S.; Kubota, Y.; Belosludov, R. V.; Kobayashi, T. C.; Sakamoto, H.; Chiba, T.; Takata, M.; Kawazoe, Y.; Mita, Y. Highly controlled acetylene accommodation in a metal−organic microporous material. *Nature* **2005**, *436*, 238−241.
(39) Fischer, M.; Hoffmann, F.; Fröba, M. New Microporous Materials for Acetylene Storage and C_2H_2/CO_2 Separation: Insights from Molecular Simulations. *ChemPhysChem* **2010**, *11*, 2220−2229.
(40) Wang, L.; Yang, L.; Gong, L.; Krishna, R.; Gao, Z.; Tao, Y.; Yin, W.; Xu, Z.; Luo, F. Constructing redox-active microporous hydrogen-bonded organic framework by imide-functionalization: photochromism, electrochromism, and selective adsorption of C_2H_2 over CO_2. *Chem. Eng. J.* **2020**, *383*, 123117.
(41) Gao, J.; Qian, X.; Lin, R. B.; Krishna, R.; Wu, H.; Zhou, W.; Chen, B. Mixed Metal-Organic Framework with Multiple Binding Sites for Efficient C_2H_2/CO_2 Separation. *Angew. Chem., Int. Ed.* **2020**, *59*, 4396−4400.
(42) Liu, R.; Liu, Q.-Y.; Krishna, R.; Wang, W.; He, C.-T.; Wang, Y.-L. Water-stable Europium-1,3,6,8-tetrakis(4-carboxylphenyl)pyrene Framework for Efficient C_2H_2/CO_2 Separation. *Inorg. Chem.* **2019**, *58*, 5089−5095.
(43) Ye, Y.; Ma, Z.; Lin, R.-B.; Krishna, R.; Zhou, W.; Lin, Q.; Zhang, Z.; Xiang, S.; Chen, B. Pore Space Partition within a Metal-Organic Framework for Highly Efficient C_2H_2/CO_2 Separation. *J. Am. Chem. Soc.* **2019**, *141*, 4130−4136.
(44) Wu, H. Q.; Yan, C. S.; Luo, F.; Krishna, R. Beyond Crystal Engineering: Significant Enhancement of C_2H_2/CO_2 Separation by Constructing Composite Material. *Inorg. Chem.* **2018**, *57*, 3679−3682.
(45) Foo, M. L.; Matsuda, R.; Hijikata, Y.; Krishna, R.; Sato, H.; Horike, S.; Hori, A.; Duan, J.; Sato, Y.; Kubota, Y.; Takata, M.; Kitagawa, S. An Adsorbate Discriminatory Gate Effect in a Flexible Porous Coordination Polymer for Selective Adsorption of CO_2 over C_2H_2. *J. Am. Chem. Soc.* **2016**, *138*, 3022−3030.
(46) Luo, F.; Yan, C.; Dang, L.; Krishna, R.; Zhou, W.; Wu, H.; Dong, X.; Han, Y.; Hu, T.-L.; O'Keeffe, M.; Wang, L.; Luo, M.; Lin, R.-B.; Chen, B. UTSA-74: A MOF-74 Isomer with Two Accessible Binding Sites per Metal Center for Highly Selective Gas Separation. *J. Am. Chem. Soc.* **2016**, *138*, 5678−5684.
(47) Duan, J.; Jin, W.; Krishna, R. Natural Gas Purification Using a Porous Coordination Polymer with Water and Chemical Stability. *Inorg. Chem.* **2015**, *54*, 4279−4284.
(48) Li, P.; He, Y.; Zhao, Y.; Weng, L.; Wang, H.; Krishna, R.; Wu, H.; Zhou, W.; O'Keeffe, M.; Han, Y.; Chen, B. A Rod-Packing Microporous Hydrogen-Bonded Organic Framework for Highly Selective Separation

https://dx.doi.org/10.1021/acsomega.0c02218
ACS Omega 2020, 5, 16987−17004

of C_2H_2/CO_2 at Room Temperature. *Angew. Chem., Int. Ed.* **2015**, *54*, 574−577.
(49) Chen, K.-J.; Scott, H. S.; Madden, D. G.; Pham, T.; Kumar, A.; Bajpai, A.; Lusi, M.; Forrest, K. A.; Space, B.; Perry, J. J.; Zaworotko, M. J. Benchmark C_2H_2/CO_2 and CO_2/C_2H_2 Separation by Two Closely Related Hybrid Ultramicroporous Materials. *Chem* **2016**, *1*, 753−765.
(50) Lee, J.; Chuah, C. Y.; Kim, J.; Kim, Y.; Ko, N.; Seo, Y.; Kim, K.; Bae, T. H.; Lee, E. Separation of Acetylene from Carbon Dioxide and Ethylene by a Water-Stable Microporous Metal−Organic Framework with Aligned Imidazolium Groups inside the Channels. *Angew. Chem., Int. Ed.* **2018**, *130*, 7995−7999.
(51) Scott, H. S.; Shivanna, M.; Bajpai, A.; Madden, D. G.; Chen, K.-J.; Pham, T.; Forrest, K. A.; Hogan, A.; Space, B.; Perry, J. J., IV; Zaworotko, M. J. Highly Selective Separation of C2H2 from CO2 by a New Dichromate-Based Hybrid Ultramicroporous Material. *ACS Appl. Mater. Interfaces* **2017**, *9*, 33395−33400.
(52) Qazvini, O. T.; Babarao, R.; Telfer, S. G. Multipurpose Metal−Organic Framework for the Adsorption of Acetylene: Ethylene Purification and Carbon Dioxide Removal. *Chem. Mater.* **2019**, *31*, 4919−4926.
(53) Pei, J.; Shao, K.; Wang, J. X.; Wen, H. M.; Yang, Y.; Cui, Y.; Krishna, R.; Li, B.; Qian, G. A Chemically Stable Hofmann-Type Metal−Organic Framework with Sandwich-Like Binding Sites for Benchmark Acetylene Capture. *Adv. Mater.* **2020**, *32*, 1908275.
(54) Bachman, J. E.; Reed, D. A.; Kapelewski, M. T.; Chachra, G.; Jonnavittula, D.; Radaelli, G.; Long, J. R. Enabling alternative ethylene production through its selective adsorption in the metal−organic framework Mn_2(m-dobdc). *Energy Environ. Sci.* **2018**, *11*, 2423−2431.
(55) van Zandvoort, I.; Ras, E.-J.; Graaf, R. d.; Krishna, R. Using Transient Breakthrough Experiments for Screening of Adsorbents for Separation of C_2H_4/CO_2 Mixtures. *Sep. Purif. Technol.* **2020**, *241*, 116706.
(56) van Zandvoort, I.; van der Waal, J. K.; Ras, E.-J.; de Graaf, R.; Krishna, R. Highlighting non-idealities in C_2H_4/CO_2 mixture adsorption in 5A zeolite. *Sep. Purif. Technol.* **2019**, *227*, 115730.
(57) Banerjee, D.; Cairns, A. J.; Liu, J.; Motkuri, R. K.; Nune, S. K.; Fernandez, C. A.; Krishna, R.; Strachan, D. M.; Thallapally, P. K. Potential of Metal-Organic Frameworks for Capture of Noble Gases. *Acc. Chem. Res.* **2015**, *48*, 211−219.
(58) Krishna, R. Diffusing Uphill with James Clerk Maxwell and Josef Stefan. *Chem. Eng. Sci.* **2019**, *195*, 851−880.
(59) Chen, X.; Plonka, A. M.; Banerjee, D.; Krishna, R.; Schaef, H. T.; Ghose, S.; Thallapally, P. K.; Parise, J. B. Direct Observation of Xe and Kr Adsorption in a Xe-selective Microporous Metal Organic Framework. *J. Am. Chem. Soc.* **2015**, *137*, 7007−7010.
(60) Feng, X.; Zong, Z.; Elsaidi, S. K.; Jasinski, J. B.; Krishna, R.; Thallapally, P. K.; Carreon, M. A. Kr/Xe Separation over a Chabazite Zeolite Membrane. *J. Am. Chem. Soc.* **2016**, *138*, 9791−9794.
(61) Wang, H.; Yao, K.; Zhang, Z.; Jagiello, J.; Gong, Q.; Han, Y.; Li, J. The First Example of Commensurate Adsorption of Atomic Gas in a MOF and Effective Separation of Xenon from Other Noble Gases. *Chem. Sci.* **2014**, *5*, 620−624.
(62) Kluge, G.; Franke, T.; Schöllner, R.; Nagel, G. Estimation of Component Loadings in Fixed-Bed Adsorption from Breakthrough Curves of Binary Gas Mixtures in Nontrace Systems. *Chem. Eng. Sci.* **1991**, *46*, 368−371.
(63) Krishna, R. Screening Metal-Organic Frameworks for Mixture Separations in Fixed-Bed Adsorbers using a Combined Selectivity/Capacity Metric. *RSC Adv.* **2017**, *7*, 35724−35737.
(64) Myers, A. L.; Prausnitz, J. M. Thermodynamics of Mixed Gas Adsorption. *AIChE J.* **1965**, *11*, 121−127.
(65) Liu, J.; Thallapally, P. K.; Strachan, D. Metal−Organic Frameworks for Removal of Xe and Kr from Nuclear Fuel Reprocessing Plants. *Langmuir* **2012**, *28*, 11584−11589.
(66) Liu, J.; Strachan, D. M.; Thallapally, P. K. Enhanced noble gas adsorption in Ag@MOF-74Ni. *Chem. Commun.* **2014**, *50*, 466−468.
(67) Gurdal, Y.; Keskin, S. Atomically Detailed Modeling of Metal Organic Frameworks for Adsorption, Diffusion, and Separation of Noble Gas Mixtures. *Ind. Eng. Chem. Res.* **2012**, *51*, 7373−7382.
(68) Li, L.; Yang, J.; Li, J.; Chen, Y.; Li, J. Separation of CO_2/CH_4 and CH_4/N_2 Mixtures by M/DOBDC: a Detailed Dynamic Comparison with MIL-100(Cr) and Activated Carbon. *Microporous Mesoporous Mater.* **2014**, *198*, 236−246.
(69) Tagliabue, M.; Farrusseng, D.; Valencia, S.; Aguado, S.; Ravon, U.; Rizzo, C.; Corma, A.; Mirodatos, C. Natural gas treating by selective adsorption: Material science and chemical engineering interplay. *Chem. Eng. J.* **2009**, *155*, 553−566.
(70) Bhadra, S. J.; Farooq, S. Separation of MethaneNitrogen Mixture by Pressure Swing Adsorption for Natural Gas Upgrading. *Ind. Eng. Chem. Res.* **2011**, *50*, 14030−14045.
(71) Majumdar, B.; Bhadra, S. J.; Marathe, R. P.; Farooq, S. Adsorption and Diffusion of Methane and Nitrogen in Barium Exchanged ETS-4. *Ind. Eng. Chem. Res.* **2011**, *50*, 3021−3034.
(72) Jayaraman, A.; Hernandez-Maldonado, A. J.; Yang, R. T.; Chinn, D.; Munson, C. L.; Mohr, D. H. Clinoptilolites for Nitrogen/Methane Separation. *Chem. Eng. Sci.* **2004**, *59*, 2407−2417.
(73) Habgood, H. W. The Kinetics of Molecular Sieve Action. Sorption of Nitrogen-Methane Mixtures by Linde Molecular Sieve 4A. *Can. J. Chem.* **1958**, *36*, 1384−1397.
(74) Bhadra, S. J. Methane-Nitrogen Separation by Pressure Swing Adsorption. Ph.D. Dissertation, National University of Singapore, Singapore, 2007.
(75) Yoon, J. W.; Chang, H.; Lee, S.-J.; Hwang, Y. K.; Hong, D.-Y.; Lee, S.-K.; Lee, J. S.; Jang, S.; Yoon, T.-U.; Kwac, K.; Jung, Y.; Pillai, R. S.; Faucher, F.; Vimont, A.; Daturi, M.; Férey, G.; Serre, C.; Maurin, G.; Bae, Y.-S.; Chang, J.-S. Selective Nitrogen Capture by Porous Hybrid Materials Containing Accessible Transition Metal Ion Sites. *Nat. Mater.* **2017**, *16*, 526−531.
(76) Da Silva, F. A.; Rodrigues, A. E. Vacuum swing adsorption for propylene/propane separation with 4A zeolite. *Ind. Eng. Chem. Res.* **2001**, *40*, 5758−5774.
(77) Grande, C. A.; Poplow, F.; Rodrigues, A. E. Vacuum pressure swing adsorption to produce polymer-grade polypropylene. *Separ. Sci. Technol.* **2010**, *45*, 1252−1259.
(78) Silva, F. A. D.; Rodrigues, A. E. PropylenePropane Separation by Vacuum Swing Adsorption Using 13X Zeolite. *AIChE J.* **2001**, *47*, 341−357.
(79) Geier, S. J.; Mason, J. A.; Bloch, E. D.; Queen, W. L.; Hudson, M. R.; Brown, C. M.; Long, J. R. Selective adsorption of ethylene over ethane and propylene over propane in the metal−organic frameworks M_2(dobdc) (M = Mg, Mn, Fe, Co, Ni, Zn). *Chem. Sci.* **2013**, *4*, 2054−2061.
(80) Yoon, J.-W.; Jang, I.-T.; Lee, K.-Y.; Hwang, Y.-K.; Chang, J.-S. Adsorptive Separation of Propylene and Propane on a Porous Metal-Organic Framework, Copper Trimesate. *Bull. Korean Chem. Soc.* **2010**, *31*, 220−223.
(81) Khalighi, M.; Karimi, I. A.; Farooq, S. Comparing SiCHA and 4A Zeolite for Propylene/Propane Separation using a Surrogate-Based Simulation/Optimization Approach. *Ind. Eng. Chem. Res.* **2014**, *53*, 16973−16983.
(82) Khalighi, M.; Chen, Y. F.; Farooq, S.; Karimi, I. A.; Jiang, J. W. Propylene/Propane Separation Using SiCHA. *Ind. Eng. Chem. Res.* **2013**, *52*, 3877−3892.
(83) Ruthven, D. M.; Farooq, S. Air Separation by Pressure Swing Adsorption. *Gas Sep. Purif.* **1990**, *4*, 141−148.
(84) Lin, R.-B.; Wu, H.; Li, L.; Tang, X.-L.; Li, Z.; Gao, J.; Cui, H.; Zhou, W.; Chen, B. Boosting Ethane/Ethylene Separation within Isoreticular Ultramicroporous Metal−Organic Frameworks. *J. Am. Chem. Soc.* **2018**, *140*, 12940−12946.
(85) Qazvini, O. T.; Babarao, R.; Shi, Z.-L.; Zhang, Y.-B.; Telfer, S. G. A Robust Ethane-Trapping Metal−Organic Framework with a High Capacity for Ethylene Purification. *J. Am. Chem. Soc.* **2019**, *141*, 5014−5020.
(86) Chen, Y.; Qiao, Z.; Wu, H.; Lv, D.; Shi, R.; Xia, Q.; Zhou, J.; Li, Z. An Ethane-trapping MOF PCN-250 for Highly Selective Adsorption of Ethane over Ethylene. *Chem. Eng. Sci.* **2018**, *175*, 110−117.
(87) Gücüyener, C.; van den Bergh, J.; Gascon, J.; Kapteijn, F. Ethane/Ethene Separation Turned on Its Head: Selective Ethane

https://dx.doi.org/10.1021/acsomega.0c02218
ACS Omega 2020, 5, 16987−17004

Adsorption on the Metal-Organic Framework ZIF-7 through a Gate-Opening Mechanism. *J. Am. Chem. Soc.* **2010**, *132*, 17704−17706.
(88) Chen, D.-L.; Wang, N.; Xu, C.; Tu, G.; Zhu, W.; Krishna, R. A combined theoretical and experimental analysis on transient breakthroughs of C2H6/C2H4 in fixed beds packed with ZIF-7. *Microporous Mesoporous Mater.* **2015**, *208*, 55−65.
(89) Böhme, U.; Barth, B.; Paula, C.; Kuhnt, A.; Schwieger, W.; Mundstock, A.; Caro, J.; Hartmann, M. Ethene/Ethane and Propene/Propane Separation via the Olefin and Paraffin Selective Metal−Organic Framework Adsorbents CPO-27 and ZIF-8. *Langmuir* **2013**, *29*, 8592−8600.
(90) Krishna, R. The Maxwell-Stefan Description of Mixture Diffusion in Nanoporous Crystalline Materials. *Microporous Mesoporous Mater.* **2014**, *185*, 30−50.
(91) Liao, P.-Q.; Zhang, W.-X.; Zhang, J.-P.; Chen, X.-M. Efficient purification of ethene by an ethane-trapping metal-organic framework. *Nat. Commun.* **2015**, *36*, 8697.
(92) Liang, W.; Xu, F.; Zhou, X.; Xiao, J.; Xia, Q.; Li, Y.; Li, Z. Ethane Selective Adsorbent Ni(bdc)(ted)0.5 with High Uptake and its Significance in Adsorption Separation of Ethane and Ethylene. *Chem. Eng. Sci.* **2016**, *148*, 275−281.
(93) Herm, Z. R.; Wiers, B. M.; Mason, J. A.; van Baten, J. M.; Hudson, M. R.; Zajdel, P.; Brown, C. M.; Masciocchi, N.; Krishna, R.; Long, J. R. Separation of Hexane Isomers in a Metal-Organic Framework with Triangular Channels. *Science* **2013**, *340*, 960−964.
(94) Dubbeldam, D.; Krishna, R.; Calero, S.; Yazaydın, A. Ö. Computer-Assisted Screening of Ordered Crystalline Nanoporous Adsorbents for Separation of Alkane Isomers. *Angew. Chem., Int. Ed.* **2012**, *51*, 11867−11871.
(95) Krishna, R. Separating Mixtures by Exploiting Molecular Packing Effects in Microporous Materials. *Phys. Chem. Chem. Phys.* **2015**, *17*, 39−59.
(96) Krishna, R. Methodologies for Screening and Selection of Crystalline Microporous Materials in Mixture Separations. *Sep. Purif. Technol.* **2018**, *194*, 281−300.
(97) Khabzina, Y.; Laroche, C.; Perez-Pellitero, J.; Farrusseng, D. Xylene Separation on a Diverse Library of Exchanged Faujasite Zeolites. *Microporous Mesoporous Mater.* **2017**, *247*, 52−59.
(98) Khabzina, Y.; Laroche, C.; Pérez-Pellitero, J.; Farrusseng, D. Quantitative Structure−property Relationship Approach to Predicting Xylene Separation with Diverse Exchanged Faujasites. *Phys. Chem. Chem. Phys.* **2018**, *20*, 23773−23782.
(99) Costa, I. C. M. Adsorption/diffusion Interplay in Hierarchical Zeolites: Understanding the role of External Surface and Additional Porosity. Ph.D. Thesis, l'Université Claude Bernard Lyon 1, Lyon, 2019.
(100) Krishna, R.; van Baten, J. M. Commensurate-Incommensurate Adsorption and Diffusion in Ordered Crystalline Microporous Materials. *Phys. Chem. Chem. Phys.* **2017**, *19*, 20320−20337.
(101) Minceva, M.; Rodrigues, A. E. Modeling and Simulation of a Simulated Moving Bed for the Separation of p-Xylene. *Ind. Eng. Chem. Res.* **2002**, *41*, 3454−3461.
(102) Minceva, M.; Rodrigues, A. E. Understanding and Revamping of Industrial Scale SMB Units for p-Xylene Separation. *AIChE J.* **2007**, *53*, 138−149.
(103) Kulprathipanja, S. *Zeolites in Industrial Separation and Catalysis*; Wiley-VCH: Weinheim, 2010.
(104) Mukherjee, S.; Joarder, B.; Manna, B.; Desai, A. V.; Chaudhari, A. K.; Ghosh, S. K. Framework-Flexibility Driven Selective Sorption of p-Xylene over Other Isomers by a Dynamic Metal-Organic Framework. *Sci. Rep.* **2015**, *4*, 5761.
(105) Mukherjee, S.; Joarder, B.; Desai, A. V.; Manna, B.; Krishna, R.; Ghosh, S. K. Exploiting Framework Flexibility of a Metal-Organic Framework for Selective Adsorption of Styrene over Ethylbenzene. *Inorg. Chem.* **2015**, *54*, 4403−4408.
(106) Yoon, J. W.; Lee, J. S.; Piburn, G. W.; Cho, K. H.; Jeon, K.; Lim, H.-K.; Kim, H.; Jun, C.-H.; Humphrey, S. M.; Krishna, R.; Chang, J.-S. Highly Selective Adsorption of p-Xylene over other C8 Aromatic Hydrocarbons by Co-CUK-1: A Combined Experimental and Theoretical Assessment. *Dalton Trans.* **2017**, *46*, 16096−16101.
(107) Torres-Knoop, A.; Krishna, R.; Dubbeldam, D. Separating Xylene Isomers by Commensurate Stacking of p-Xylene within Channels of MAF-X8. *Angew. Chem., Int. Ed.* **2014**, *53*, 7774−7778.
(108) Jin, Z.; Zhao, H.-Y.; Zhao, X.-J.; Fang, Q.-R.; Long, J. R.; Zhu, G.-S. A novel microporous MOF with the capability of selective adsorption of xylenes. *Chem. Commun.* **2010**, *46*, 8612−8614.
(109) Moreira, M. A.; Santos, J. C.; Ferreira, A. F. P.; Loureiro, J. M.; Ragon, F.; Horcajada, P.; Yot, P. G.; Serre, C.; Rodrigues, A. E. Toward Understanding the Influence of Ethylbenzene in p-Xylene Selectivity of the Porous Titanium Amino Terephthalate MIL-125(Ti): Adsorption Equilibrium and Separation of Xylene Isomers. *Langmuir* **2012**, *28*, 3494−3502.
(110) Moreira, M. A.; Santos, J. C.; Ferreira, A. F. P.; Loureiro, J. M.; Ragon, F.; Horcajada, P.; Yot, P. G.; Serre, C.; Rodrigues, A. E. Effect of ethylbenzene in p-xylene selectivity of the porous titanium amino terephthalate MIL-125(Ti)_NH2. *Microporous Mesoporous Mater.* **2012**, *158*, 229−234.
(111) Vermoortele, F.; Maes, M.; Moghadam, P. Z.; Lennox, M. J.; Ragon, F.; Boulhout, M.; Biswas, S.; Laurier, K. G. M.; Beurroies, I.; Denoyel, R.; Roeffaers, M.; Stock, N.; Düren, T.; Serre, C.; De Vos, D. E. p-Xylene-Selective MetalOrganic Frameworks: A Case of Topology-Directed Selectivity. *J. Am. Chem. Soc.* **2011**, *133*, 18526−18529.
(112) Krishna, R.; van Baten, J. M. Highlighting a variety of unusual characteristics of adsorption and diffusion in microporous materials induced by clustering of guest molecules. *Langmuir* **2010**, *26*, 8450−8463.
(113) Krishna, R.; van Baten, J. M. Hydrogen Bonding Effects in Adsorption of Water-alcohol Mixtures in Zeolites and the Consequences for the Characteristics of the Maxwell-Stefan Diffusivities. *Langmuir* **2010**, *26*, 10854−10867.
(114) Gutiérrez-Sevillano, J. J.; Calero, S.; Krishna, R. Selective Adsorption of Water from Mixtures with 1-Alcohols by Exploitation of Molecular Packing Effects in CuBTC. *J. Phys. Chem. C* **2015**, *119*, 3658−3666.
(115) Gutiérrez-Sevillano, J. J.; Calero, S.; Krishna, R. Separation of Benzene from Mixtures with Water, Methanol, Ethanol, and Acetone: Highlighting Hydrogen Bonding and Molecular Clustering Influences in CuBTC. *Phys. Chem. Chem. Phys.* **2015**, *17*, 20114−20124.
(116) Krishna, R.; van Baten, J. M.; Baur, R. Highlighting the Origins and Consequences of Thermodynamic Nonidealities in Mixture Separations using Zeolites and Metal-Organic Frameworks. *Microporous Mesoporous Mater.* **2018**, *267*, 274−292.
(117) Krishna, R.; Van Baten, J. M. Elucidation of Selectivity Reversals for Binary Mixture Adsorption in Microporous Adsorbents. *ACS Omega* **2020**, *5*, 9031−9040.
(118) Krishna, R.; van Baten, J. M. Segregation effects in adsorption of CO_2 containing mixtures and their consequences for separation selectivities in cage-type zeolites. *Sep. Purif. Technol.* **2008**, *61*, 414−423.
(119) Krishna, R.; Van Baten, J. M. Investigating the Non-idealities in Adsorption of CO_2-bearing Mixtures in Cation-exchanged Zeolites. *Sep. Purif. Technol.* **2018**, *206*, 208−217.
(120) Fraux, G.; Boutin, A.; Fuchs, A. H.; Coudert, F.-X. On the Use of the IAST Method for Gas Separation Studies in Porous Materials with Gate-opening Behavior. *Adsorption* **2018**, *24*, 233−241.
(121) Krishna, R. Methodologies for Evaluation of Metal-Organic Frameworks in Separation Applications. *RSC Adv.* **2015**, *5*, 52269−52295.
(122) Krishna, R.; Long, J. R. Screening metal-organic frameworks by analysis of transient breakthrough of gas mixtures in a fixed bed adsorber. *J. Phys. Chem. C* **2011**, *115*, 12941−12950.

https://dx.doi.org/10.1021/acsomega.0c02218
ACS Omega 2020, 5, 16987−17004

Supporting Information

Metrics for Evaluation and Screening of Metal-Organic Frameworks for Applications in Mixture Separations

Rajamani Krishna*

Van 't Hoff Institute for Molecular Sciences

University of Amsterdam

Science Park 904

1098 XH Amsterdam, The Netherlands

email: r.krishna@contact.uva.nl

Table of Contents

1 Preamble

This Supporting Information accompanying the article *Metrics for Evaluation and Screening of Metal-Organic Frameworks for Applications in Mixture Separations* provides: provides:

(a) Brief review of adsorption fundamentals

(b) Brief summary of the Ideal Adsorbed Solution theory for calculation of mixture adsorption equilibrium,

(c) Methodology used for transient breakthroughs in fixed bed adsorbers

(d) Shock wave model for fixed bed adsorbers

(e) Structural information on the MOFs investigated

(f) Unary isotherm data sources for each guest/host combination

(g) Details simulation data inputs and results for each of the investigated mixture separations..

For ease of reading, the Supplementary Material is written as a stand-alone document.

2 “Equilibrium” vs “Kinetic” Separations

Separation technologies such as distillation, absorption, and extraction are energy intensive because of vapor/liquid phase transformations in condensers, reboilers and solvent recovery sections. The energy consumption for distillation accounts for about 50% of the total energy consumption for all separations.[1] The largest opportunities for energy reduction are offered by replacing distillation with (a) low-energy demanding separation systems such as adsorption or membranes, or (b) hybrid systems that combine distillation with adsorption or membranes.[1] In many cases, the hybrid processing option is easier to implement technically because adsorption and membrane separations often cannot produce products with the purity levels that are achievable with distillation. The success of such replacement strategies is crucially dependent on development of suitable porous materials that can be used in fixed bed adsorption devices or as thin layers in membrane permeation units.

Basically, there are two broad strategies for separations in fixed bed adsorption devices and membrane units:

(a) “Equilibrium Separations” that rely on selectivities dictated by mixture adsorption equilibrium, and

(b) “Kinetic Separations” that are rely on differences in the rates of diffusion of guest molecules within the framework of the microporous materials.

Even for “Equilibrium Separations”, diffusional influences may alter the separation performance, often leading to diminished separation effectiveness. For “Kinetic Separations”, the mixture adsorption equilibrium often lowers the separation performance. For the proper understanding, and modelling of separations in fixed bed adsorption devices and membrane units it is important to have an understanding of both mixture adsorption equilibrium and intra-particle diffusion.

We first summarize the various factors that govern the adsorption strength of a guest molecule; the treatment essentially follows that of Yang,[2] and Ruthven.[3]

2.1 Potential energies for adsorption

The total potential between the adsorbate molecules and the adsorbent is the sum of the adsorbate-adsorbate and adsorbate-adsorbent interaction potentials. Let us focus on the factors that govern the adsorbate-adsorbent interaction potential, ϕ. If we ignore π-complexation and chemical bonding,[2] the two contributions to the adsorbate-adsorbent interaction potential, ϕ, are dispersion interactions and electrostatic interactions. The adsorbate-adsorbent interaction potential, ϕ, is the sum of various contributions

$$\phi = \phi_D + \phi_R + \phi_{Ind} + \phi_{F\mu} + \phi_{\dot{F}Q} \tag{S1}$$

In Equation (S1):

$\phi_D = -\frac{A}{r^6}$ = dispersion energy

$\phi_R = \frac{B}{r^{12}}$ = close-range repulsion energy

where r is the distance between the centres of the interacting pairs of atoms/molecules

ϕ_{Ind} = induction energy (interaction between electric field and an induced dipole)

$\phi_{F\mu}$ = interaction between an electric field F and a permanent dipole μ

$\phi_{\dot{F}Q}$ = interaction between an electric field gradient $\dot{F}$ and a quadrupole (with quadrupole moment Q)

The dispersion and repulsion interactions form the Lennard-Jones potential

$$\phi_D + \phi_R = 4\varepsilon\left(\left(\frac{\sigma}{r}\right)^{12} - \left(\frac{\sigma}{r}\right)^{6}\right) \tag{S2}$$

At the equilibrium distance r_0 we have $\phi_D + \phi_R = 0$; $\frac{d\phi}{dr} = 0$ and $B = -\frac{Ar_0^6}{2}$.

"Equilibrium" vs "Kinetic" Separations

The most commonly used expression for calculating A is the Kirkwood-Müller formula for interaction between atoms and molecules (denoted by subscripts i and j)

$$A = \frac{6mc^2\alpha_i\alpha_j}{\frac{\alpha_i}{\chi_i} + \frac{\alpha_j}{\chi_j}} \tag{S3}$$

The potential for interaction between electric field and an induced dipole is

$$\phi_{Ind} = -\frac{1}{2}\alpha F^2 = -\frac{1}{2}\alpha\frac{q^2}{r^4(4\pi\varepsilon_0)^2} \tag{S4}$$

The potential for interaction between electric field F (of an ion) and point dipole is

$$\phi_{F\mu} = -\mu F\cos\theta = -\mu\frac{q}{r^2(4\pi\varepsilon_0)}\cos\theta \tag{S5}$$

The potential for interaction between electric field gradient $\dot{F}$ and linear point quadrupole is

$$\phi_{\dot{F}Q} = \frac{1}{2}Q\dot{F} = -\frac{1}{2}Q\frac{q}{2r^3(4\pi\varepsilon_0)}(3\cos^2\theta - 1) \tag{S6}$$

where

m = mass of electron

c = speed of light

α = polarizability

χ = magnetic susceptibility

α = polarizability

F = electric field

q = electronic charge of ion on surface

ε_0 = permittivity of a vacuum

μ = permanent dipole moment

θ = angle between the direction of the field or field gradient and the axis of the dipole or linear quadrupole

Q = linear quadrupole moment (+ or -)

r = distance between the centers of the interacting pairs

For a given sorbent, the sorbate-sorbent interaction potential depends on the properties of the sorbate. Among the five different types of interactions, the first two contributions $\phi_D + \phi_R$ are non-specific, which are operative in all sorbate-sorbent systems; the non-specific interactions $\phi_D + \phi_R$ are non-electrostatic. The London – van der Waals dispersion interaction energies are largely dictated by the polarizabilities of the guest molecules and surfaces atoms of the adsorbent materials. The polarizabilities of a wide variety of guest molecules are tabulated by Sircar and Myers.[4] Broadly speaking, the polarizabilites of molecules increase with increasing molar masses, as illustrated for noble gases He, Ne, Ar, Kr, and Xe in Figure S1, and for homologous series of hydrocarbons in Figure S2(a,b). The value of α generally increases with the molecular weight because more electrons are available for polarization.

The last three contributions $\phi_{Ind} + \phi_{F\mu} + \phi_{\cdot_{FQ}}$ arise from charges (which create electric fields) on the solid surface. For activated carbon, the non-specific interactions dominate. On a surface without charges, such as graphite, ϕ_{Ind} = 0. For metal oxides, zeolites, and ionic solids, the electrostatic interactions often dominate, depending on the adsorbate. For adsorbate with a quadrupole, the net interaction between a uniform field and the quadrupole is zero. However, the quadrupole interacts strongly with the field gradient, thus the term $\phi_{\cdot_{FQ}}$.

Figure S3(a,b) compare the polarizabilities, dipole moments, and quadrupole moments of H_2, Ar, O_2, N_2, CO, CH_4, and CO_2. Of these sorbates, only CO has a permanent dipole moment. The four guest sorbates O_2, N_2, CO, and CO_2 all possess finite quadrupole moments, with the hierarchy of magnitudes $O_2 < N_2 < CO < CO_2$. Interestingly, the polarizability of CH_4 is higher than that of CO, but does not possess either dipole or significant quadrupole moments. Therefore, in a non-charged adsorbent such as activated the adsorption strength of CH_4 is higher than that of CO. However, in cation-exchanged zeolites, CO may have a higher adsorption strength than CH_4.

"Equilibrium" vs "Kinetic" Separations

We also note that each of the three electrostatic contributions $\phi_{Ind}, \phi_{F\mu}, \phi_{\underset{FQ}{.}}$ are proportion to the ionic charges of the sorbent, q: $\phi_{Ind} \propto \alpha \frac{q^2}{r^4}$; $\phi_{F\mu} \propto \mu \frac{q}{r^2}$; $\phi_{\underset{FQ}{.}} \propto Q \frac{q}{r^3}$ Therefore Ca^{++} should be yield stronger interaction potential that Na^+, with say CO_2, on the basis of this consideration; note that these two cations have nearly the same ionic radius; see Figure S4. The electrostatic contributions are also inversely proportional to a power of the distance between the centers of the interacting pairs: $\phi_{Ind} \propto \alpha \frac{q^2}{r^4}$; $\phi_{F\mu} \propto \mu \frac{q}{r^2}$; $\phi_{\underset{FQ}{.}} \propto Q \frac{q}{r^3}$, we should expect the interaction potentials to be larger for Li^+ than for Na^+, because of the significantly smaller ionic radius of Li^+. This explains, albeit qualitatively, why LiLSX is the favored sorbent for selective adsorption of N_2 for O_2/N_2 mixtures.[2]

2.2 List of Figures for “Equilibrium” vs “Kinetic” Separations

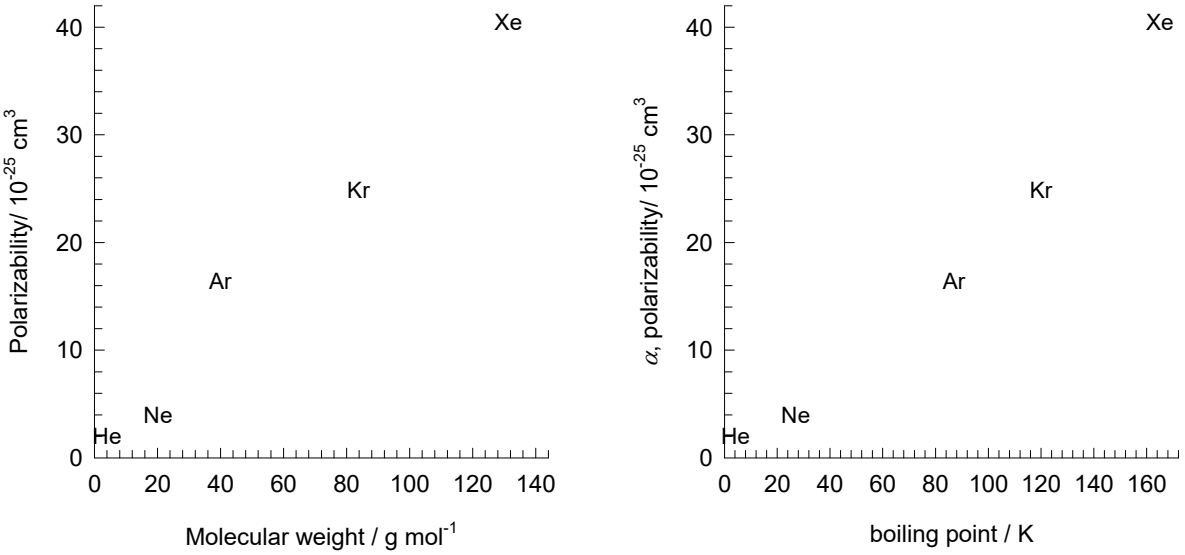

Figure S1. Polarizabilities and boiling points of noble gases. The data on polarizabilities are taken from Sircar and Myers.[4]

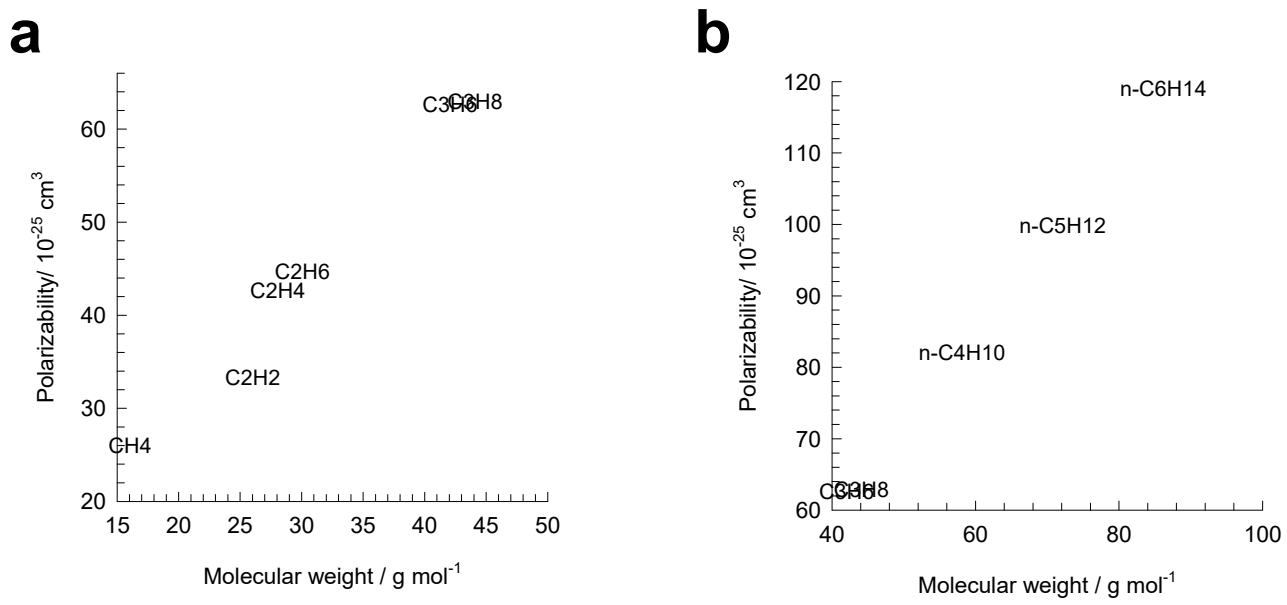

Figure S2. Polarizabilities of (a) light hydrocarbons, and (b) heavier hydrocarbons. The data on polarizabilities are taken from Sircar and Myers.[4]

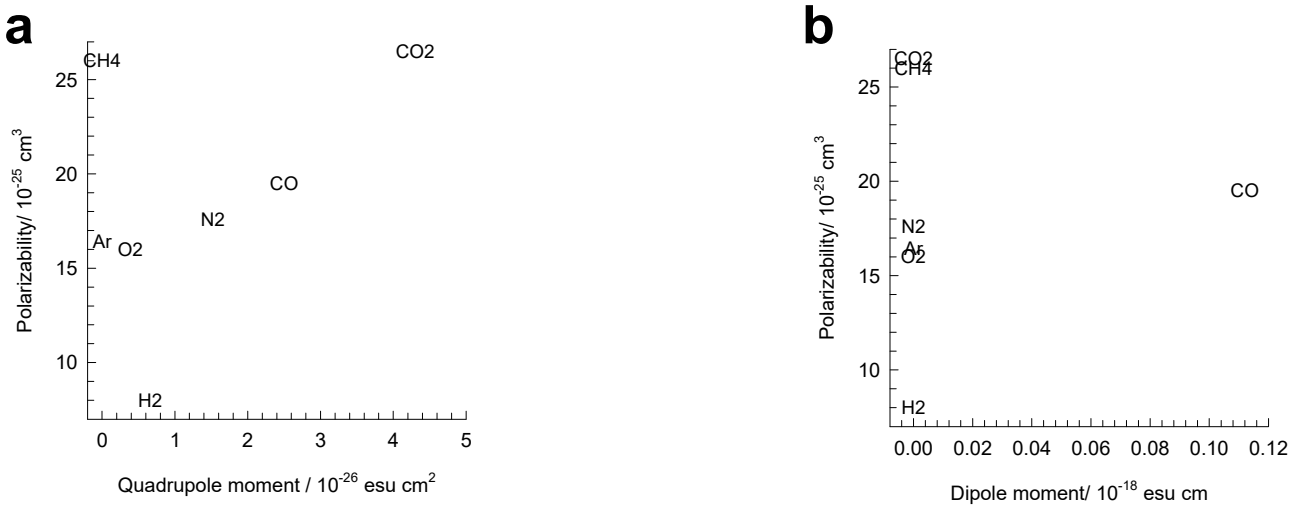

Figure S3. (a, b) Polarizabilities, dipole moments, and quadrupole moments of H_2, Ar, N_2, O_2, CO, CH_4, and CO_2. The data are taken from Sircar and Myers.[4]

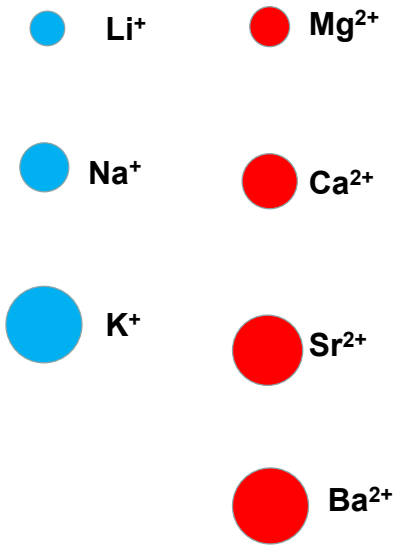

Figure S4. Relative sizes of cations.

3 IAST calculations of mixture adsorption

3.1 Brief outline of theory

Within microporous crystalline materials such as zeolites and metal-organic frameworks (MOFs), the guest molecules exist in the adsorbed phase. The Gibbs adsorption equation[3] in differential form is

$$Ad\pi = \sum_{i=1}^{n} q_i d\mu_i \tag{S7}$$

The quantity A is the surface area per kg of framework, with units of m^2 per kg of the framework of the crystalline material; q_i is the molar loading of component i in the adsorbed phase with units moles per kg of framework; μ_i is the molar chemical potential of component i. The spreading pressure π has the same units as surface tension, i.e. N m^{-1}.

The chemical potential of any component in the adsorbed phase, μ_i, equals that in the bulk fluid phase. If the partial fugacities in the bulk fluid phase are f_i, we have

$$d\mu_i = RTd \ln f_i \tag{S8}$$

where R is the gas constant (= 8.314 J mol^{-1} K^{-1}).

Briefly, the basic equation of Ideal Adsorbed Solution Theory (IAST) theory of Myers and Prausnitz[5] is the analogue of Raoult's law for vapor-liquid equilibrium, i.e.

$$f_i = P_i^0 x_i; \quad i = 1,2,..n \tag{S9}$$

where x_i is the mole fraction in the adsorbed phase

$$x_i = \frac{q_i}{q_1 + q_2 + ...q_n} \tag{S10}$$

and P_i^0 is the pressure for sorption of every component i, which yields the same spreading pressure, π for each of the pure components, as that for the mixture:

IAST calculations of mixture adsorption

$$\frac{\pi A}{RT} = \int_0^{P_1^0} \frac{q_1^0(f)}{f} df = \int_0^{P_2^0} \frac{q_2^0(f)}{f} df = \int_0^{P_3^0} \frac{q_3^0(f)}{f} df = \ldots \tag{S11}$$

where $q_i^0(f)$ is the *pure* component adsorption isotherm. The units of $\frac{\pi A}{RT}$, also called the adsorption potential,[6] are mol kg^{-1}.

The unary isotherm may be described by say the 1-site Langmuir isotherm

$$q^0(f) = q_{sat} \frac{bf}{1+bf}; \quad \theta = \frac{bf}{1+bf} \tag{S12}$$

where we define the fractional *occupancy* of the adsorbate molecules, $\theta = q^0(f)/q_{sat}$. The superscript 0 is used to emphasize that $q^0(f)$ relates the *pure component* loading to the bulk fluid fugacity. More generally, the unary isotherms may need to be described by, say, the dual-site Langmuir-Freundlich model

$$q^0(f) = q_{A,sat} \frac{b_A f^{\nu_A}}{1+b_A f^{\nu_A}} + q_{B,sat} \frac{b_B f^{\nu_B}}{1+b_B f^{\nu_B}} \tag{S13}$$

Each of the integrals in Equation (S11) can be evaluated analytically:

$$\begin{aligned} \int_{f=0}^{P_i^0} \frac{q^0(f)}{f} df &= \frac{q_{A,sat}}{\nu_A} \ln\left(1+b_A\left(P_i^0\right)^{\nu_A}\right) + \frac{q_{B,sat}}{\nu_B} \ln\left(1+b_B\left(P_i^0\right)^{\nu_B}\right) \\ \int_{f=0}^{P_i^0} \frac{q^0(f)}{f} df &= \frac{q_{A,sat}}{\nu_A} \ln\left(1+b_A\left(\frac{f_i}{x_i}\right)^{\nu_A}\right) + \frac{q_{B,sat}}{\nu_B} \ln\left(1+b_B\left(\frac{f_i}{x_i}\right)^{\nu_B}\right) \end{aligned} \tag{S14}$$

The right hand side of eq (S14) is a function of P_i^0. For multicomponent mixture adsorption, each of the equalities on the right hand side of eq (S11) must be satisfied. These constraints may be solved using a suitable equation solver, to yield the set of values of P_1^0, P_2^0, P_3^0,.. P_n^0, all of which satisfy eq (S11). The corresponding values of the integrals using these as upper limits of integration must yield the same value of $\frac{\pi A}{RT}$ for each component; this ensures that the obtained solution is the correct one.

The adsorbed phase mole fractions x_i are then determined from

IAST calculations of mixture adsorption

$$x_i = \frac{f_i}{P_i^0}; \quad i = 1,2,...n \tag{S15}$$

A key assumption of the IAST is that the enthalpies and surface areas of the adsorbed molecules do not change upon mixing. If the total mixture loading is q_t, the area covered by the adsorbed mixture is $\frac{A}{q_t}$ with units of m^2 (mol mixture)$^{-1}$. Therefore, the assumption of no surface area change due to mixture adsorption translates as $\frac{A}{q_t} = \frac{Ax_1}{q_1^0\left(P_1^0\right)} + \frac{Ax_2}{q_2^0\left(P_2^0\right)} + \cdots \frac{Ax_n}{q_n^0\left(P_n^0\right)}$; the total mixture loading is q_t is calculated from

$$q_t = q_1 + q_2 ... + q_n = \frac{1}{\frac{x_1}{q_1^0(P_1^0)} + \frac{x_2}{q_2^0(P_2^0)} + ... + \frac{x_n}{q_n^0(P_n^0)}} \tag{S16}$$

in which $q_1^0(P_1^0)$, $q_2^0(P_2^0)$,… $q_n^0(P_n^0)$ are determined from the unary isotherm fits, using the sorption pressures for each component P_1^0, P_2^0, P_3^0,.. P_n^0 that are available from the solutions to equations Equations (S11), and (S14).

The entire set of equations (S9) to (S16) need to be solved numerically to obtain the loadings, q_i of the individual components in the mixture.

4 Methodology for transient breakthrough simulations

We describe below the simulation methodology used to perform transient breakthrough calculations for fixed bed adsorbers (see schematics in Figure S5, and Figure S6). The simulation methodology is the same as used in our earlier publications.[7-10] For an *n*-component gas mixture flowing through a fixed bed maintained under isothermal, isobaric, conditions, the molar concentrations in the gas phase at any position and instant of time are obtained by solving the following set of partial differential equations for each of the species *i* in the gas mixture[9, 11-13]

$$-D_{ax}\frac{\partial^2 c_i(t,z)}{\partial z^2}+\frac{\partial c_i(t,z)}{\partial t}+\frac{\partial\left(v(t,z)c_i(t,z)\right)}{\partial z}+\frac{(1-\varepsilon)}{\varepsilon}\rho\frac{\partial \bar{q}_i(t,z)}{\partial t}=0;\quad i=1,2,...n \tag{S17}$$

In eq (S17), t is the time, z is the distance along the adsorber, ρ is the framework density, ε is the bed voidage, D_{ax} is the axial dispersion coefficient, v is the interstitial gas velocity, and $\bar{q}_i(t,z)$ is the *spatially averaged* molar loading within the crystallites of radius r_c, monitored at position z, and at time t. The time $t = 0$, corresponds to the time at which the feed mixture is injected at the inlet to the fixed bed. Prior to injection of the feed mixture, N_2 gas flows through the fixed bed. In this model described by eq (S17), the effects of all mechanisms that contribute to axial mixing are lumped into a single effect axial dispersion coefficient D_{ax}. Ruthven et al.[13] state that more detailed models that include radial dispersion are generally not necessary. They also make the following remark "when mass transfer resistance is significantly greater than axial dispersion, one may neglect the axial dispersion term and assume plug flow". All of the analysis and breakthrough simulations were carried out using the plug flow assumption.

The radial distribution of molar loadings, q_i, within a spherical crystallite, of radius r_c, is obtained from a solution of a set of differential equations describing the uptake

$$\rho\frac{\partial q_i(r,t)}{\partial t}=-\frac{1}{r^2}\frac{\partial}{\partial r}\left(r^2 N_i\right) \tag{S18}$$

The intra-crystalline fluxes N_i, in turn, are related to the radial gradients in the molar loadings by the Maxwell-Stefan (M-S) diffusion equations.[17, 19] For the scenario in which correlation effects are considered to be of negligible importance, the M-S equations simplify to yield

$$N_i = -\rho Đ_i \sum_{j=1}^{n} \Gamma_{ij} \frac{\partial q_j}{\partial r}; \qquad i = 1, 2..n \tag{S19}$$

The thermodynamic correction factors Γ_{ij} can be calculated by differentiation of the model describing mixture adsorption equilibrium.[17, 19] In previous works[9, 14] it has been established that the inclusion of the thermodynamic correction factors Γ_{ij} is important in the analysis of transient uptakes inside MOF crystallites, and transient breakthroughs in fixed-bed adsorbers. For the cases in which intra-crystalline diffusion effects are important, we use eqs (S19) in modelling of transient breakthrough in fixed bed adsorbers.

For all times $t \geq 0$, the exterior of the crystal is brought into contact with a bulk gas mixture at partial pressures p_{i0} that is maintained constant till the crystal reaches thermodynamic equilibrium with the surrounding gas mixture. At any time t, the component loadings at the surface of the particle $q_i(r_c, t) = q_i^*$ is in equilibrium with the bulk phase gas mixture with partial pressures p_{i0}. In the general case, the component loadings are calculated using the Ideal Adsorbed Solution Theory (IAST) of Myers and Prausnitz.[5] In some cases, of strong non-idealities in mixture adsorption equilibrium, we need to use the Real Adsorbed Solution Theory (RAST) as described in our previous works.[15-19]

At any time t, during the transient approach to thermodynamic equilibrium, the spatial-averaged component loading within the crystallites of radius r_c is calculated using

$$\bar{q}_i(t) = \frac{3}{r_c^3} \int_0^{r_c} q_i(r,t) r^2 dr \tag{S20}$$

Summing equation (S20) over all n species in the mixture allows calculation of the *total average* molar loading of the mixture within the crystallite

$$\bar{q}_t(t,z) = \sum_{i=1}^{n} \bar{q}_i(t,z) \tag{S21}$$

The term $\frac{\partial \bar{q}_i(t,z)}{\partial t}$ in equation (S17) is determined by solving the set of equations (S18), and (S20), and (S21). At any time *t*, and position *z*, the component loadings at the outer surface of the particle $q_i(r_c,t,z)$ is in equilibrium with the bulk phase gas mixture with partial pressures $p_i(t,z)$ in the bulk gas mixture. In the general case, the component loadings $q_i(r_c,t,z)$ are calculated using the Ideal Adsorbed Solution Theory (IAST) of Myers and Prausnitz.[5]

If the value of $\frac{Đ_i}{r_c^2}$ is large enough to ensure that intra-crystalline gradients are absent and the entire crystallite particle can be considered to be in thermodynamic equilibrium with the surrounding bulk gas phase at that time *t*, and position *z* of the adsorber

$$\bar{q}_i(t,z) = q_i(t,z) \tag{S22}$$

The *interstitial* gas velocity is related to the *superficial* gas velocity by

$$v = \frac{u}{\varepsilon} \tag{S23}$$

At time, $t = 0$, the inlet to the adsorber, $z = 0$, is subjected to a step input of the *n*-component gas mixture and this step input is maintained till the end of the adsorption cycle when steady-state conditions are reached.

$$t \geq 0; \quad p_i(0,t) = p_{i0}; \quad u(0,t) = u_0 \tag{S24}$$

where $u_0 = v_0\varepsilon$ is the superficial gas velocity at the inlet to the adsorber.

For simulations of the desorption cycle, we use a purge gas that is non-adsorbing (e.g. helium) that is fed to the fixed bed at the same superficial gas velocity $u_0 = v_0\varepsilon$ as in the adsorption cycle. The total pressure of the adsorbing components (1, 2, ..*n*) is maintained at 0.2 Pa. This choice ensures that the desorption cycle is operated under deep vacuum.

Methodology for transient breakthrough simulations

Typically, the adsorber length is divided into 100 slices, and each spherical crystallite was discretized into 20 equi-volume slices. The results thus obtained were confirmed to be of adequate accuracy. Combination of the discretized partial differential equations (PDEs) along with the algebraic equations describing mixture adsorption equilibrium (IAST, or mixed-gas Langmuir model, as appropriate), results in a set of differential-algebraic equations (DAEs), which are solved using BESIRK.[20] BESIRK is a sparse matrix solver, based on the semi-implicit Runge-Kutta method originally developed by Michelsen,[21] and extended with the Bulirsch-Stoer extrapolation method.[22] Use of BESIRK improves the numerical solution efficiency in solving the set of DAEs. The evaluation of the sparse Jacobian required in the numerical algorithm is largely based on analytic expressions.[11] Further details of the numerical procedures used in this work, are provided by Krishna and co-workers;[11, 12, 23, 24] interested readers are referred to our website that contains the numerical details.[12]

For comparing the separation performance of MOFs, two types of simulations may be carried out: (i) simulations in which the same volume of adsorbent is used, and (ii) simulations in which the same mass of adsorbent is used.

For the simulations which the same volume of adsorbent is held constant, we choose: adsorber length, L = 0.3 m; cross-sectional area, A = 1 m^2; superficial gas velocity in the bed, u_0 = 0.04 m s^{-1}; voidage of the packed bed, ε = 0.4. The volume of zeolite or MOF used in the simulations is $V_{ads} = LA(1-\varepsilon)$ = 0.18 m^3. Also, note that since the superficial gas velocity is specified, the specification of the cross-sectional area of the tube, A, is not relevant in the simulation results presented. The total volume of the bed is $V_{bed} = LA$. It is important to note that the volume of adsorbent, V_{ads}, includes the pore volume of the adsorbent material. If ρ is the framework density, the mass of the adsorbent in the bed is $m_{ads} = (1-\varepsilon)\times(L \text{ m})\times(A \text{ m}^2)\times(\rho \text{ kg m}^{-3})$kg. In these breakthrough simulations we use the same volume of adsorbent in the breakthrough apparatus, i.e. $(1-\varepsilon)\times A\times L$ = 0.18 m^3 = 180 L.

For the simulations which the same mass of adsorbent is held constant, we choose the mass of the adsorbent in the bed $m_{ads} = 180$ kg, cross-sectional area, A = 1 m^2; superficial gas velocity at the bed

inlet, u_0 = 0.04 m s^{-1}; voidage of the packed bed, ε = 0.4. The length L of the adsorber bed is chosen as $L = \frac{1000}{\rho} \times 0.3$ m. So, if the framework density is 1000 kg m^{-3}, the chosen bed length L = 0.3 m.

Also, the total pressures is assumed to be constant along the length of the fixed bed. Unless otherwise stated, most of the reported transient breakthrough simulations are performed at 298 K and $p_t = 10^5$ Pa total pressure.

For presenting the breakthrough simulation results, we use the dimensionless time, $\tau = \frac{tu}{L\varepsilon}$, obtained by dividing the actual time, t, by the characteristic time, $\frac{L}{v} = \frac{\varepsilon L}{u_0}$, where L is the length of adsorber, v is the interstitial gas velocity.[25]

As illustration, Figure S7 presents results of transient breakthrough simulations for 20/80 Xe/Kr mixtures at 298 K and 100 kPa in a fixed bed packed with SBMOF-2; the required input data on unary isotherms are available in published works.[7, 26, 27] The recovery of noble gases such as Xe and Kr from used nuclear fuels is an important industrial problem.[27] Figure S7a plots the dimensionless concentrations of Xe and Kr along the dimensionless length of the adsorber, $\frac{z}{L}$. Figure S7b plots the dimensionless concentrations of Xe and Kr at the exit of the fixed bed, $z = L$, as a function of the dimensionless time, $\tau = \frac{tu}{L\varepsilon}$.

The corresponding plots of the component molar loadings are shown in Figure S7c,d. The dotted lines in Figure S7 are the breakthroughs anticipated on the basis of a model that assumes that the spatio-temporal developments of the concentrations follows that of "shock waves", discussed in Chapter 5 The Shock-wave model for fixed bed adsorbers. We define the displacement time interval, $\Delta\tau = \tau_{Xe} - \tau_{Kr}$, as the difference between the breakthrough times of Xe (= τ_{Xe}) and Kr (= τ_{Kr}). During the displacement interval, $\Delta\tau$, that pure Kr with < 1000 ppm Xe can be recovered; see Figure S8a.

Methodology for transient breakthrough simulations

Pure Xe, with < 1000 ppm Kr, can be recovered during the desorption process achieved by applying vacuum; see Figure S8b.

For comparing the separation performance of different MOFs based on experimental data, the precise values of the bed voidage, ε, and the length of the bed L are not usually known. In such cases the use of the dimensionless time $\tau = \frac{tu}{L\varepsilon}$ is not feasible. It is appropriate to base the comparisons using the following parameter

$$\frac{\left(Q_0 = \text{flow rate m}^3\ \text{s}^{-1}\ \text{at STP}\right)\times\left(\text{time in s}\right)}{\left(\text{kg MOF packed in tube}\right)} = \frac{Q_0 t}{m_{ads}} = \text{m}^3\ \text{kg}^{-1} \tag{S25}$$

The volumetric flow rate of the feed mixture at the inlet to the adsorber $Q_0 = u_0 A \frac{273}{T}\frac{p_t}{10^5}$ m^3 s^{-1}, at STP conditions.

For comparison of breakthrough experiments with breakthrough simulations, it is most convenient to use $\frac{Q_0 t}{m_{ads}}$ as the x-axis.

4.1 List of Figures for Methodology for transient breakthrough simulations

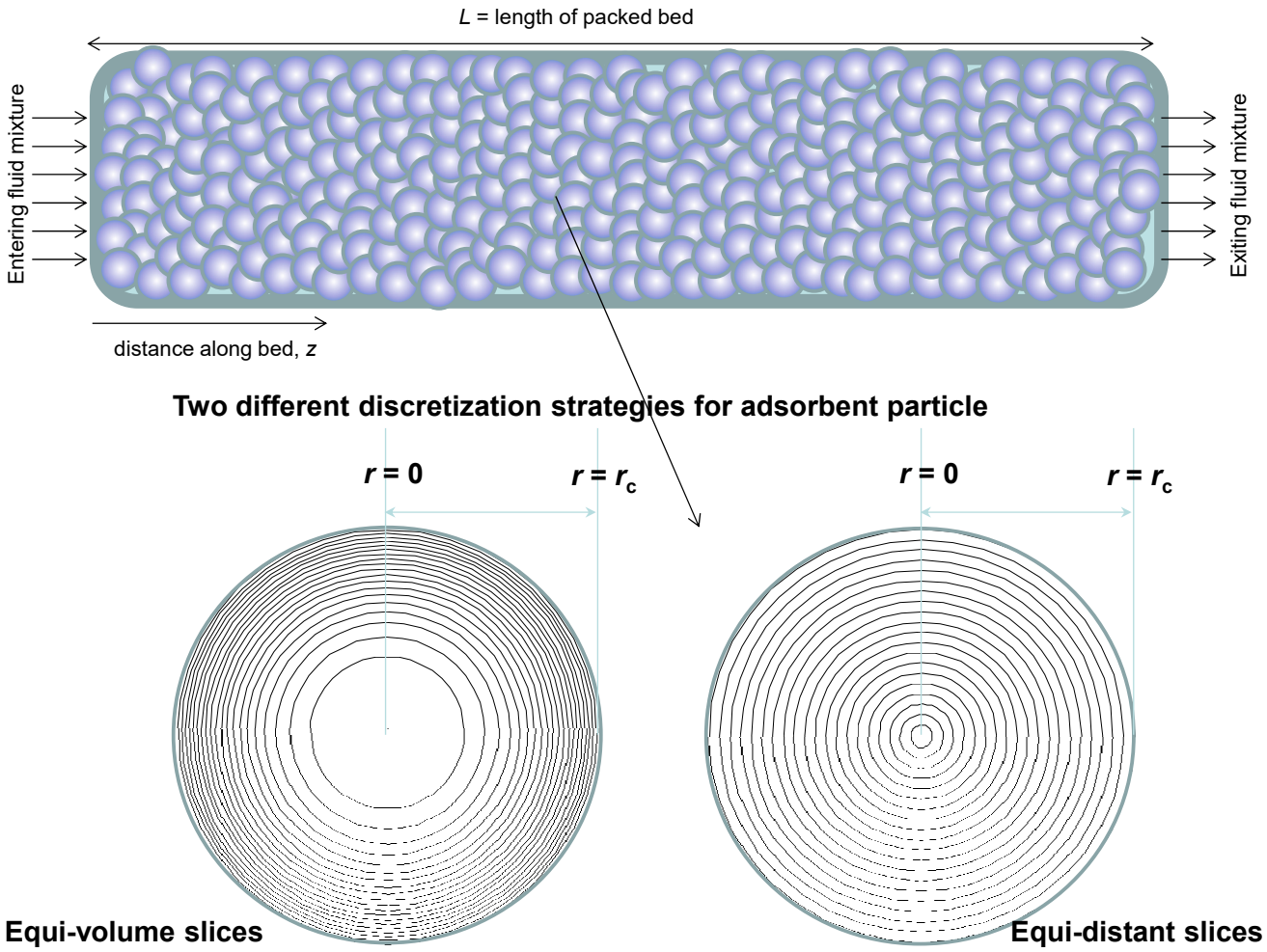

Figure S5. Two different discretization schemes for a single spherical crystallite.

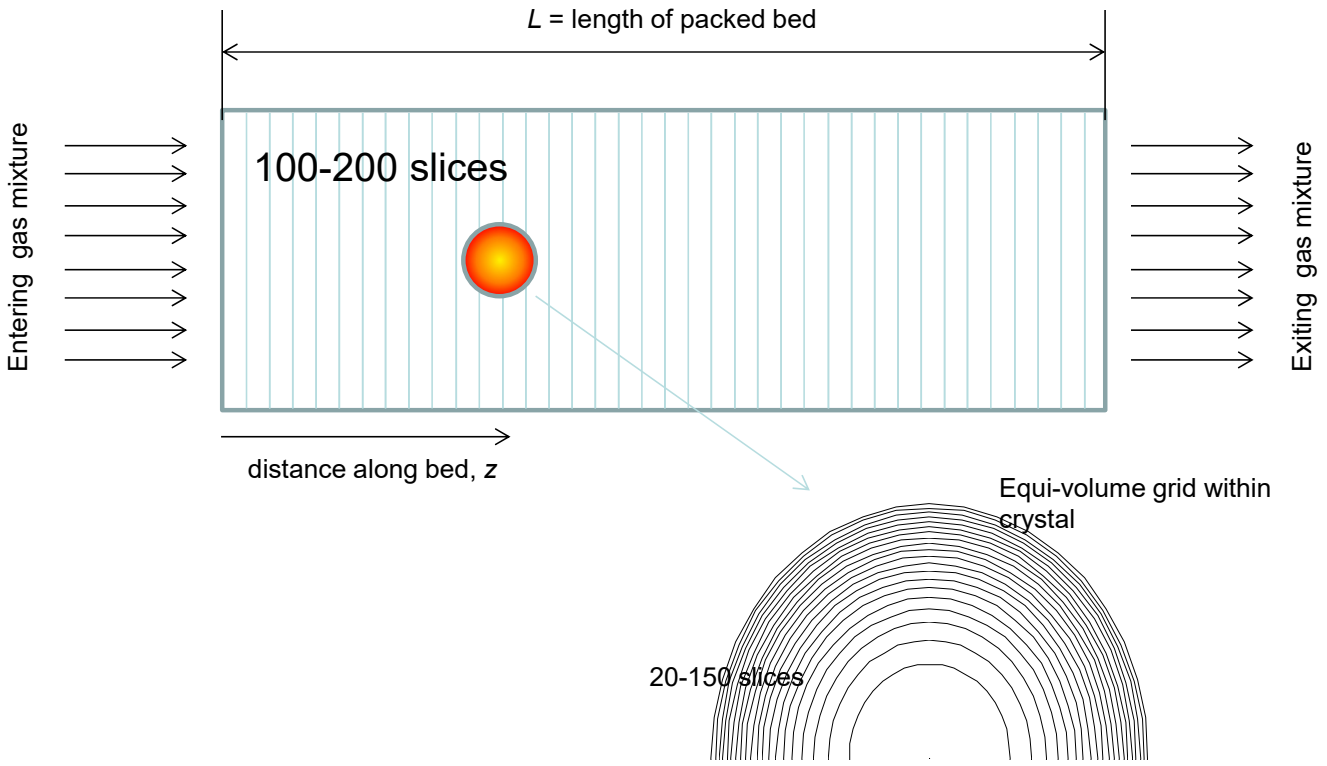

Figure S6. Discretization scheme for fixed bed adsorber.

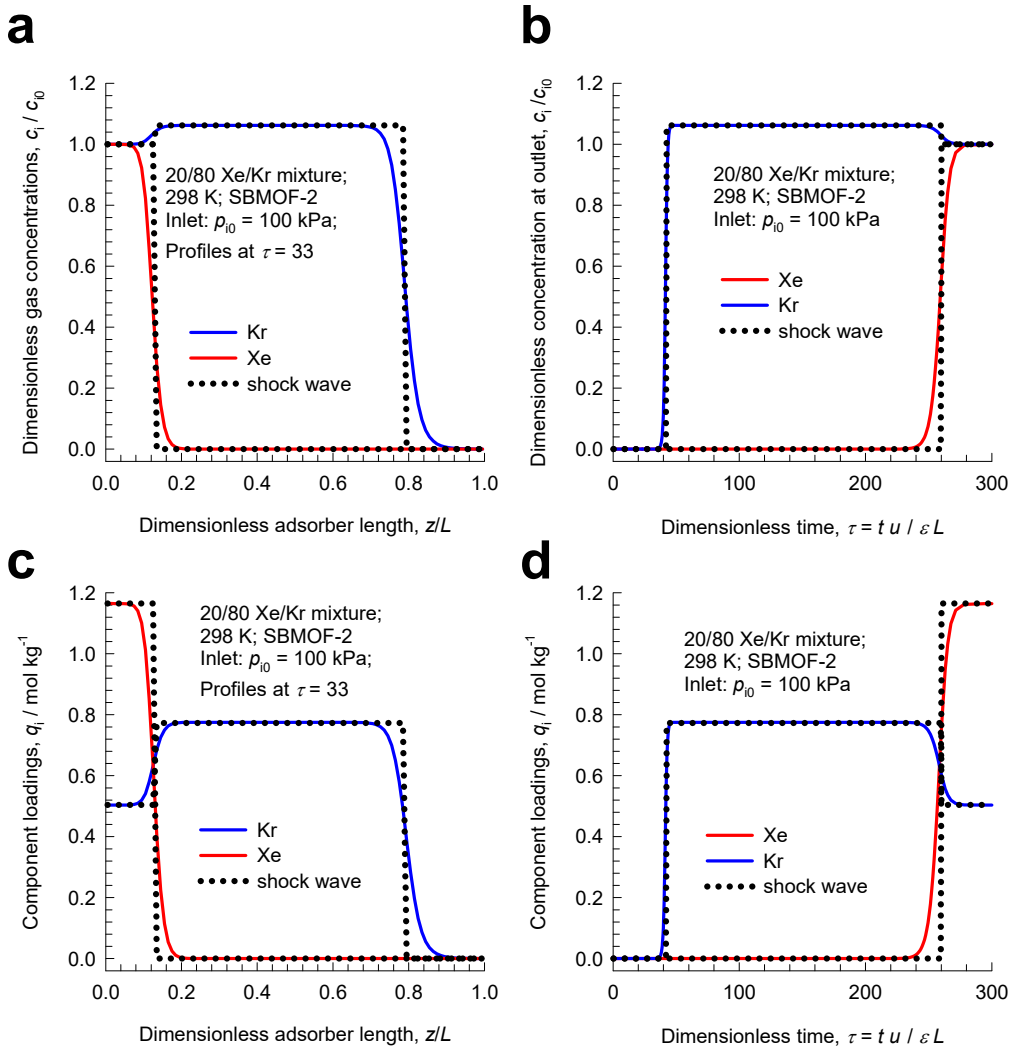

Figure S7. Transient breakthrough simulations for 20/80 Xe/Kr mixtures at 298 K and 100 kPa in a fixed bed packed with SBMOF-2. (a) Plot of dimensionless gas phase concentrations of Xe and Kr along the dimensionless length of the adsorber, $\frac{z}{L}$, monitored at $\tau = 33$. (b) Plot of dimensionless gas phase concentrations of Xe and Kr at the position $z = L$, as a function of the dimensionless time, $\tau = \frac{tu}{L\varepsilon}$. (c) Plot of component molar loadings along the dimensionless length of the adsorber, $\frac{z}{L}$, monitored at $\tau = 33$. (d) Plot of component molar loadings at $z = L$, as a function of the dimensionless time, $\tau = \frac{tu}{L\varepsilon}$.

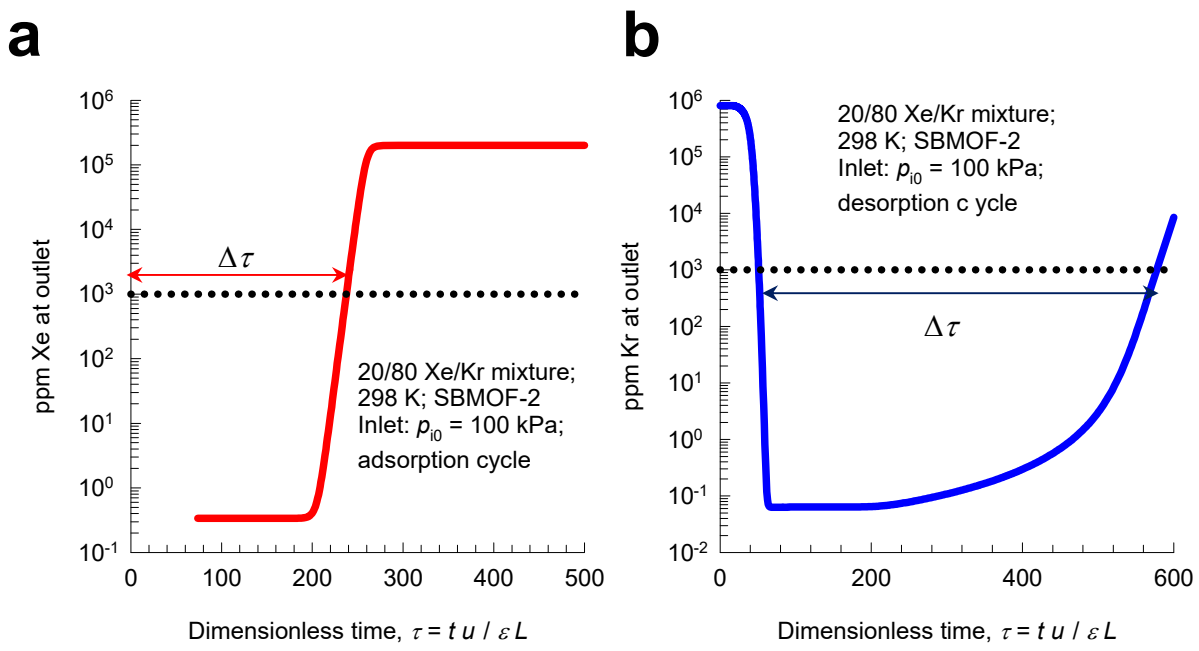

Figure S8. Transient breakthrough simulations for the (a) adsorption and (b) desorption cycles for separation of 20/80 Xe/Kr mixtures at 298 K and 100 kPa in a fixed bed packed with SBMOF-2. (a) Plot of ppm Xe vs $\tau = \frac{tu}{L\varepsilon}$ at the exit of fixed bed during the adsorption cycle. (b) Plot of ppm Kr vs $\tau = \frac{tu}{L\varepsilon}$ at the outlet during the desorption cycle.

5 The Shock-wave model for fixed bed adsorbers

5.1 Derivation of the shock-wave model relations

Kluge et al.[28] have published analytic solutions for transient breakthroughs of binary gas mixtures that are based on the assumption that the breakthroughs can be described in terms of "shock waves" that traverse the bed at two different velocities. For an A/B binary mixture, the more poorly adsorbed component B traverses the bed faster, and breaks through earlier; the more strongly adsorbed component A traverses the bed a lower velocity and breaks through at longer times. The analytic solutions are based on the following set of assumptions:

(1) Isothermal conditions prevail in the fixed bed

(2) The total pressure, p_t, is constant along the length L of the fixed bed, i.e. no pressure drop is taken into account

(3) Plug flow of gas through the bed

(4) No diffusional resistances, either intra-crystalline or external to the particles in the bed.

For the binary mixture of A, and B, eq (S17) is written by Kluge et al.[28] in the form

$$\left(\frac{\varepsilon}{(1-\varepsilon)}\right)\frac{\partial c_A}{\partial t}+\rho\frac{\partial q_A}{\partial t}+\frac{1}{(1-\varepsilon)}\frac{\partial (uc_A)}{\partial z}=0$$
$$\left(\frac{\varepsilon}{(1-\varepsilon)}\right)\frac{\partial c_B}{\partial t}+\rho\frac{\partial q_B}{\partial t}+\frac{1}{(1-\varepsilon)}\frac{\partial (uc_B)}{\partial z}=0 \qquad \text{(S26)}$$

In eq (S26) u is the superficial gas velocity, $u = v\varepsilon = \frac{Q}{A}$, where Q is the volumetric flow rate. At the entrance to the fixed bed we have $u_0 = v_0\varepsilon = \frac{Q_0}{A}$. It is customary in experimental studies to express Q_0 at the inlet to the breakthrough tube in units of $m^3\ s^{-1}$ or $mL\ min^{-1}$ at STP. The volumetric flow rate of the feed mixture at the inlet to the adsorber $Q_0 = u_0 A \frac{273}{T}\frac{p_t}{10^5}$ $m^3\ s^{-1}$, at STP conditions.

Equations (S26) are equivalent to equations (1) and (2) of Kluge et al.[28] It should be noted, that equations (1) and (2) of Kluge et al.[28] contain an additional term for the contribution of the pore volume; this term is absent in eq (S26) because in our formulation, the volume of adsorbent, $V_{ads} = (1-\varepsilon) AL = \frac{m_{ads}}{\rho}$, includes the pore volume of the adsorbent material; in other words, we use the appropriate density ρ, for the adsorbent material. Indeed, our formulation is also consistent with the work of Malek and Farooq.[29] Readers should also note that Kluge et al.[28] write the gas phase concentrations, and component loadings in mass units. Herein, we use molar units consistently. Furthermore, in the following set of equations, A is considered to be the more strongly adsorbed component, and B, the component that is more weakly adsorbed. In the set of equations presented by Kluge et al., component 1 is more weak adsorbed, and component 2 is more strongly adsorbed species.

The initial and boundary conditions are

$$\begin{aligned} &c_A = c_{A0}; c_B = c_{B0}; u = u_0; \quad t \geq 0; z = 0 \\ &c_A = 0; c_B = 0; q_A = 0; q_B = 0; \quad t = 0; \quad 0 < z < L \end{aligned} \tag{S27}$$

The ideal gas law dictates $c_A + c_B = c_t = \frac{p_t}{RT} = c_{A0} + c_{B0}$.

Kluge et al.[28] solve the set of eqs (S26), and (S27) assuming that the spatio-temporal variations of concentrations as a function of the dimensionless length, $\frac{z}{L}$, and dimensionless time, $\tau = \frac{tu}{L\varepsilon}$, are represented by shock wave fronts, shown as dotted lines in Figure S7, and Figure S8.

The solutions for the spatio-temporal development of concentration have the form given below

$$\begin{aligned} &c_A(z,t) = c_{A0} - c_{A0}\Phi\left(\frac{z}{L} - \frac{t}{t_A}\right); \quad c_B(z,t) = c_{B0} + (c_{dis} - c_{B0})\Phi\left(\frac{z}{L} - \frac{t}{t_A}\right) - c_{dis}\Phi\left(\frac{z}{L} - \frac{t}{t_B}\right) \\ &q_A(z,t) = q_{A0} - q_{A0}\Phi\left(\frac{z}{L} - \frac{t}{t_A}\right); \quad q_B(z,t) = q_{B0} + (q_{dis} - q_{B0})\Phi\left(\frac{z}{L} - \frac{t}{t_A}\right) - q_{dis}\Phi\left(\frac{z}{L} - \frac{t}{t_B}\right) \end{aligned} \tag{S28}$$

where $\Phi(\zeta)=\begin{Bmatrix}1,\zeta\geq 0\\0,\zeta<0\end{Bmatrix}$ is the Heaviside function. The subscript dis, refers to values during the displacement interval. For isobaric operations, the molar concentration $c_{dis}=c_{A0}+c_{B0}$. In dimensionless form, transient development of gas phase concentrations may be written as

$$\frac{c_A(z,\tau)}{c_{A0}}=1-\Phi\left(\frac{z}{L}-\frac{\tau}{\tau_A}\right);\quad \frac{c_B(z,\tau)}{c_{B0}}=1+\left(\frac{y_A}{y_B}\right)\Phi\left(\frac{z}{L}-\frac{\tau}{\tau_A}\right)-\frac{1}{y_B}\Phi\left(\frac{z}{L}-\frac{\tau}{\tau_B}\right) \tag{S29}$$

where c_{A0} and c_{B0} are the molar concentrations of the gaseous components entering the fixed bed, with mole fractions mole fractions y_A, and $y_B = 1 - y_A$; τ is the dimensionless time, $\tau=\frac{tu}{L\varepsilon}$; τ_A, and τ_B are the dimensionless breakthrough times of A, and B, respectively; since A is more strongly adsorbed, $\tau_A>\tau_B$.

Alternatively, eq (S28) may be expressed in terms of mole fractions in the gas phase

$$y_A(z,\tau)=y_{A0}-y_{A0}\Phi\left(\frac{z}{L}-\frac{\tau}{\tau_A}\right);\quad y_B(z,\tau)=y_{B0}+(1-y_{B0})\Phi\left(\frac{z}{L}-\frac{\tau}{\tau_A}\right)-\Phi\left(\frac{z}{L}-\frac{\tau}{\tau_B}\right) \tag{S30}$$

The "shock wave" solutions for separation of 20/60 Xe/Kr mixtures in SBMOF-2 are shown by the dotted lines in Figure S7, and Figure S8.

The equilibrated molar loading of the more strongly adsorbed component A in the bed is

$$q_A=\frac{c_{A0}}{m_{ads}}\left(u_0At_A-\varepsilon V_{bed}\right)=\frac{c_t y_{A0}}{\rho LA(1-\varepsilon)}\left(v_0\varepsilon At_A-\varepsilon LA\right)=\frac{\varepsilon}{(1-\varepsilon)}\frac{c_t y_{A0}}{\rho}(\tau_A-1)$$

$$Q_0=u_0A$$

$$q_A=\frac{c_{A0}}{m_{ads}}\left(Q_0t_A-\varepsilon AL\right)=\frac{y_{A0}c_t}{m_{ads}}\left(Q_0t_A-\varepsilon V_{bed}\right) \tag{S31}$$

$$q_A=\frac{\frac{\text{mol A}}{\text{m}^3\text{ gas}}\frac{\text{m}^3\text{ feed gas}}{\text{s}}}{\text{kg ads}}\text{s}-\frac{\frac{\text{mol A}}{\text{m}^3\text{ gas}}\text{m}^3\text{ void}}{\text{kg ads}}$$

where $\tau_A = \frac{v_0 t_A}{L}$ is the dimensionless time at which A breaks through. Eq (S30) is equivalent to equation (10) of Kluge et al.[28], but expressed consistently in molar units. In eq (S30) the mole fraction y_{A0} refers to the mole fraction of component A in the inlet feed mixture.

The equilibrated molar loading of the more poorly adsorbed component B in the bed, at the end of the adsorption cycle, is

$$\begin{aligned} q_B &= \frac{c_{B0}}{m_{ads}}\left(v_0 \varepsilon A t_A - \varepsilon v_0 A\left(t_A - t_B\right) - \varepsilon LA\right) - \frac{c_{A0}}{m_{ads}} v_0 \varepsilon A\left(t_A - t_B\right) \\ q_B &= \frac{c_{B0}}{m_{ads}}\left[Q_0 t_A - \left(t_A - t_B\right)Q_0 - \varepsilon LA\right] - \frac{c_{A0} Q_0}{m_{ads}}\left(t_A - t_B\right) \\ q_B &= \frac{c_t y_{B0}}{m_{ads}}\left[Q_0 t_A - \varepsilon AL\right] - \frac{c_t Q_0}{m_{ads}}\left(t_A - t_B\right) \end{aligned} \tag{S32}$$

$$q_B = \frac{\dfrac{\text{mol B}}{\text{m}^3\ \text{gas}}\dfrac{\text{m}^3\ \text{feed gas}}{\text{s}}}{\text{kg ads}}\text{s} - \frac{\dfrac{\text{mol B}}{\text{m}^3\ \text{gas}}\text{m}^3\ \text{void}}{\text{kg ads}} - \frac{\dfrac{\text{mol (A+B)}}{\text{m}^3\ \text{gas}}\dfrac{\text{m}^3\ \text{feed gas}}{\text{s}}}{\text{kg ads}}$$

Equation (S32) is equivalent to equation (12) of Kluge et al.[28], but expressed in molar units. We assume for the purposes of our development that the interstitial velocity remains constant during the entire breakthrough, and equals v_0 at the inlet. In terms of dimensionless time, eq (S32) simplifies to

$$q_B = \frac{\varepsilon}{\left(1-\varepsilon\right)}\frac{c_t y_{B0}}{\rho}\left(\tau_A - 1\right) - \frac{\varepsilon}{\left(1-\varepsilon\right)}\frac{c_t}{\rho}\left(\tau_A - \tau_B\right) \tag{S33}$$

The number of moles of gas that is purged during the time interval $t_B < t < t_A$ per kg of adsorbent in the bed is

$$\Delta q = \frac{c_t Q_0}{m_{ads}}\left(t_A - t_B\right) \tag{S34}$$

In terms of $q_A = \frac{y_{A0} c_t}{m_{ads}}\left(Q_0 t_A - \varepsilon V_{bed}\right)$ and $q_B = \frac{c_t y_{B0}}{m_{ads}}\left[Q_0 t_A - \varepsilon AL\right] - \frac{c_t Q_0}{m_{ads}}\left(t_A - t_B\right)$, eq (S34) may be re-written as

$$\Delta q = \frac{c_t Q_0}{m_{ads}}\left(t_A - t_B\right) = q_A \frac{y_{B0}}{y_{A0}} - q_B \tag{S35}$$

During the interval $t_B < t < t_A$ the purge gas contains only "pure" B and therefore $\Delta q = \frac{c_t Q_0}{m_{ads}}\left(t_A - t_B\right) = q_A \frac{y_{B0}}{y_{A0}} - q_B$ is the productivity of pure B, expressed per kg of adsorbent. Eq (S35) is an important new result that was not derived by Kluge et al.[28]

5.2 Simplified shock-wave equations

If we ignore the hold-up of components A, and B in the void volumes, $\frac{y_{A0}c_t}{m_{ads}}\left(\varepsilon AL\right)$, and $\frac{y_{B0}c_t}{m_{ads}}\left(\varepsilon AL\right)$, respectively, eqs (S31), (S33), and (S35) simplify to yield the key results of the shock-wave model:

$$
\begin{aligned}
q_A &= \frac{y_{A0}c_t Q_0}{m_{ads}} t_A \\
\Delta q &= \frac{c_t Q_0}{m_{ads}}\left(t_A - t_B\right) = q_A \frac{y_{B0}}{y_{A0}} - q_B \\
q_B &= \frac{y_{B0}c_t Q_0}{m_{ads}} t_A - \frac{c_t Q_0}{m_{ads}}\left(t_A - t_B\right)
\end{aligned}
\qquad \text{(S36)}
$$

Equation (S36) rationalizes the choice of $\frac{Q_0 t}{m_{ads}}$ as the appropriate *x*-axis for comparison of breakthrough experiments with different adsorbents.

The adsorption selectivity, S_{ads}, defined as

$$
S_{ads} = \frac{q_A / q_B}{y_{A0} / y_{B0}} = \frac{q_A / y_{A0}}{q_B / y_{B0}} \qquad \text{(S37)}
$$

Combining eqs (S36), and (S37) we obtain

$$
\begin{aligned}
\frac{\Delta t}{t_A} &= \frac{t_A - t_B}{t_A} = \frac{\Delta q}{q_A} y_{A0} = y_{B0} - \frac{q_B}{q_A} y_{A0} = y_{B0}\left(1 - \frac{1}{S_{ads}}\right) \\
S_{ads} &= \frac{1}{1 - \frac{\Delta t}{y_{B0} t_A}}
\end{aligned}
\qquad \text{(S38)}
$$

With increasing values of adsorption selectivities, there is an increase in the difference in the breakthrough times $\Delta t = t_A - t_B$. In the limiting case

$$S_{ads} \to \infty; \quad t_B \to 0; \quad \Delta t \to y_{B0} t_A \tag{S39}$$

To gain insights into the importance of selectivity, we investigated the separation of binary A/B mixtures using several "hypothetical" HypMOFs. The unary adsorption isotherms for each HypMOF is described by the 1-site Langmuir isotherm $q = q_{sat} \frac{bp}{1+bp}$. We take the saturation capacity of both A and B to be identical to each other $q_{sat} = 5$ mol kg^{-1}. This allows the use of the mixed-gas Langmuir model $\frac{q_A}{q_{sat}} = \frac{b_A p_A}{1 + b_A p_A + b_B p_B}$; $\frac{q_B}{q_{sat}} = \frac{b_B p_B}{1 + b_A p_A + b_B p_B}$ which is exact for this special case. Several different "hypothetical" HypMOFs are "constructed" by choice of the Langmir parameters b_A, b_B, yielding adsorption selectivities in the range $1.5 < S_{ads} < 100$. Transient breakthrough simulations were performed with the chosen parameters: adsorber length, L = 0.3 m; cross-sectional area, A = 1 m^2; superficial gas velocity in the bed, u = 0.04 m s^{-1}; voidage of the packed bed, ε = 0.4. The crystal densities are taken to be equal to 1000 kg m^{-3} for all MOFs.

Let us compare the separations of HypMOF_2 ($q_{sat} = 5; \quad b_A = 2 \times 10^{-4}; \quad b_A = 1 \times 10^{-4}; \quad S_{ads} = 2$) and HypMOF_50 ($q_{sat} = 5; \quad b_A = 2 \times 10^{-4}; \quad b_A = 4 \times 10^{-6}; \quad S_{ads} = 50$). The feed gas mixture composition, y_{A0} = y_{B0} = 0.5, and total pressure constant at the value $p_t = p_A + p_B = 100$ kPa. The transient breakthrough simulations, performed using the methodology described in Chapter 4 Methodology for transient breakthrough simulations are presented in Figure S9a. It is noteworthy that the breakthrough characteristics of HypMOF_2 are slightly distended, and that of HypMOF_50 yields much sharper breakthroughs. The breakthrough times t_A, t_B are determined to be to those corresponding to the times when the outlet gas contains 99.95% of B; in other words, product B with 99.95% purity can be recovered during the time interval $\Delta t = t_A - t_B$. For the entire set of simulations, Figure S9b plots of $\frac{\Delta t}{t_A} = \frac{t_A - t_B}{t_A}$ as function of the adsorption selectivity, S_{ads}. In conformity with eq (S39),

$S \to \infty$; $t_B \to 0$; $\Delta t/t_A \to y_{B0} = 0.5$. From a material balance on the adsorber, the productivity of 99.95% of B, expressed as mol per kg of adsorbent, can be determined. The productivity of 99.95% of B is plotted in Figure S9c as function of the separation potential, $\Delta q = q_A \frac{y_{B0}}{y_{A0}} - q_B$, determined from mixed-gas Langmuir model calculations. The deviation between the two sets is generally less than 20%; the accuracy increases with increasing values of S_{ads}.

Pure A can only be recovered in the desorption phase. Figure S10a,b show transient breakthrough simulations for (a) adsorption, and (b) desorption phases for HypMOF_10 ($q_{sat} = 5$; $b_A = 1\times10^{-3}$; $b_A = 1\times10^{-4}$; $S_{ads} = 10$) , with feed gas mixture composition, $y_A = 0.2$, and total pressure constant at the value $p_t = p_A + p_B = 100$ kPa. In the simulations of the desorption phase, the bed was purged with a non-adsorbing gas, such as helium, injected into the equilibrated bed, at time t = 0, at a total pressure of 100 kPa. Figure S10b shows that pure A that can be recovered from the exit product gas in the desorption cycle during a finite time interval. Transient breakthrough simulations were carried out for the desorption phase with varying feed gas mixture compositions, y_A = 0.1 (0.1)…0.9, keeping the total pressure constant at the value $p_t = p_A + p_B = 100$ kPa. The number of moles of 99.95% pure A recovered of MOF in the packed bed is plotted in Figure S10c as a function of the separation potential Δq, defined as

$$\Delta q = q_A - q_B \frac{y_{A0}}{y_{B0}}; \quad \text{desorption cycle} \tag{S40}$$

We again note a linear dependence of the productivity of pure A with the separation potential.

5.3 List of Figures for The Shock-wave model for fixed bed adsorbers

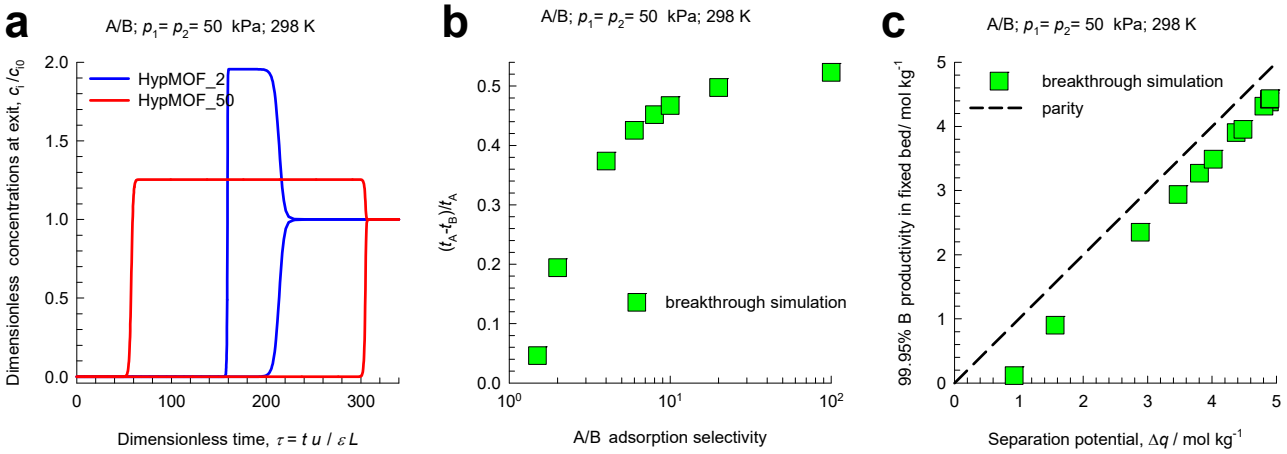

Figure S9. (a) Transient breakthrough simulations for equimolar A/B mixtures in a fixed bed packed with HypMOF_2 and HypMOF_50, operating at 298 K, and a total pressure of 100 kPa. The plot shows the normalized gas phase molar concentrations of A and B in the exit of the fixed bed adsorber, as a function of the dimensionless time, $\tau = \frac{tu}{L\varepsilon}$. (b) Plot of $\frac{\Delta t}{t_A} = \frac{t_A - t_B}{t_A}$ as function of the adsorption selectivity, S_{ads}. (c) Plot of the number of moles of 99.95% pure B produced per kg of HypMOF in the packed bed, plotted as a function of separation potential, Δq.

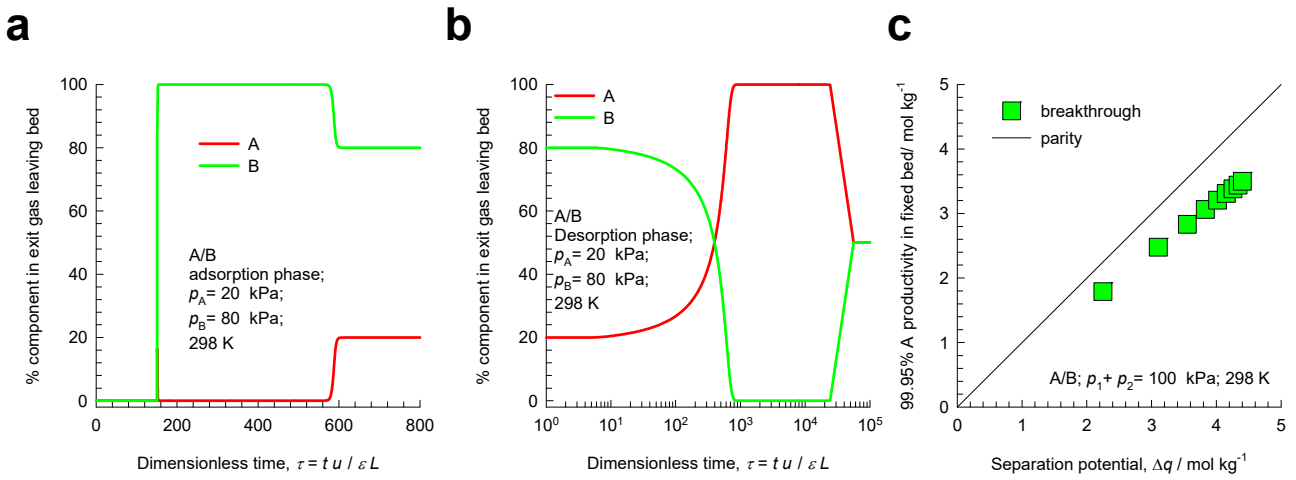

Figure S10. (a, b) Transient breakthrough simulations for (a) adsorption, and (b) desorption phases for HypMOF_10 with, $q_{sat} = 5$ mol kg^{-1}, and $S_{ads} = b_A/b_B = 10$ with feed gas mixture composition, y_A = 0.2, and total pressure constant at the value $p_t = p_A + p_B = 100$ kPa. The plots show the % gas phase compositions of A and B in the exit of the fixed bed adsorber, as a function of the dimensionless time. For the desorption phase, the % compositions are on helium-free basis. (c) The plot shows the number of moles of 99.95% pure A that can be recovered from the exit product gas in the desorption cycle, per kg of MOF in the packed bed, as a function of the separation potential Δq, calculated using $\Delta q = q_A - q_B \dfrac{y_A}{1-y_A}$.

6 H_2 production from steam-methane reforming

Most commonly, hydrogen is produced by the catalytic reforming of natural gas combined with a water gas shift reaction step, from which a hydrogen stream containing a number of impurities such as H_2O vapor, CO_2, CH_4, CO, and N_2 is obtained.[30-32] These impurities must be removed in order to attain the 99.95%+ H_2 purity that is normally demanded.[30] In fuel cell applications, the purity demands are as high as 99.99+%.[31, 33] The separation is usually carried out a large scale in PSA units, operating at pressures reaching about 7 MPa, using the Skarstrom, or modified Skarstrom PSA cycle. There are multiple steps, or stages, involved in the operation of each of the beds in the Skarstrom cycle; see schematic in Figure S11.[2, 3, 13]

In the simplest case, the four steps in the sequence are as follows. [2, 3, 13]

(a) Pressurization (with feed or raffinate product)

(b) High pressure adsorption separation with feed, with withdrawal of purified raffinate

(c) Depressurization, or "blowdown", counter-current to the feed

(d) Desorption at the lower operating pressure. This is accomplished by evacuation or purging the bed with (a portion) of the purified raffinate product

The use of 3-layer adsorbent beds is another important characteristic of the currently employed PSA technology for hydrogen purification;[31] see Figure S11. Commonly, the first layer is either alumina or silica that retains the water vapor. Then an activated carbon (AC) layer is used to selectively adsorb CO_2. The last layer is a cation-exchanged zeolite (such LTA-5A,[34, 35] with Na^+ and Ca^{++} extra-framework cations, and NaX,[36] also commonly denoted by its trade name 13X, with Na^+ extra-framework cations) with enhanced capacity for CO, and N_2. CO_2 and water vapor are strongly adsorbed in the zeolite and cannot be readily desorbed by decreasing the pressure and start to accumulate in this adsorbent as the cycles proceed. The main task of the alumina and AC layers is to prevent the H_2O

vapor and CO_2 from reaching the zeolite layer.[31] Banu et al.[32] have investigated the possibility of use of MOFs as replacement for cation-exchanged zeolites.

6.1 Comparison of Activated Carbon, LTA-5A, and CuBTC as adsorbents

As illustration, let us consider the production of purified H_2 from a feed containing 73/4/3/4/16 $H_2/N_2/CO/CH_4/CO_2$ mixtures.

In the following, we consider step (b) of the above scheme using three different adsorbent materials, Activated Carbon, LTA-5A zeolite, and CuBTC.

Figure S12(a) presents data on the polarizabilities of variety of gaseous molecules, such as H_2, N_2, CO, CH_4, and CO_2, encountered in hydrogen purification processes. The unary isotherm data of these guest molecules in activated carbon (AC) are shown in Figure S12(b). The binding strengths of these guest molecules follow the hierarchy $H_2 < N_2 < CO < CH_4 < CO_2$. Since the activated carbon has no surface functionalities or surface charges, the hierarchy of binding strengths should be dictated by the corresponding polarizabilities. This is indeed the case, as evidenced by the comparison of Figure S12(a,b).

Figure S13 shows the transient breakthrough of 73/4/3/4/16 $H_2/N_2/CO/CH_4/CO_2$ mixture, typical of steam methane reformer off-gas, in fixed bed adsorber packed with activated carbon, operating at 2 MPa total pressure and T = 313 K. The breakthrough simulation methodology is described in Chapter 4 Methodology for transient breakthrough simulations. In the simulations, we choose the mass of the adsorbent in the bed $m_{ads} = 180$ kg, cross-sectional area, A = 1 m^2; superficial gas velocity at the bed inlet, u_0 = 0.04 m s^{-1}; voidage of the packed bed, ε = 0.4. The framework density of AC is $\rho = 842$ kg m^{-3}. The length L of the adsorber bed is chosen as $L = \frac{1000}{\rho} \times 0.3 = 0.356295$ m. For presenting the breakthrough simulation results, we use as x-axis the dimensionless time, $\tau = \frac{tv}{L} = \frac{tu_0}{\varepsilon L}$, obtained by

dividing the actual time, *t*, by the characteristic time, $\frac{L}{v}=\frac{\varepsilon L}{u_0}$, where *L* is the length of adsorber, *v* is the interstitial gas velocity;[25] see Figure S13a. The same data is plotted in Figure S13b using $Q_0 t/m_{ads}$ as *x*-axis where Q_0 is the volumetric flow rate of the gas mixture at the inlet to the fixed bed, expressed in L s^{-1}, at STP conditions.

The hierarchy of breakthrough times $H_2 < N_2 < CO < CH_4 < CO_2$ follows the hierarchy of binding strengths. If the production of say 99.95% pure H_2 is desired, then the productivity of 99.95%+ pure H_2 will be dictated by the difference of the breakthrough times of H_2 and N_2. Choosing an adsorbent with stronger binding of N_2 would result in a higher productivity of 99.95%+ pure H_2.

One strategy to increase the binding strength of N_2 with respect to that of H_2 is to use say LTA-5A zeolite (also called 5A or NaCaA zeolite; contains 96Si, 96 Al, 32 Na^+, 32 Ca^{++} per unit cell; Si/Al=1) as adsorbent; the structural details are provided in Figure S14. The extra-framework cations Na^+, and Ca^{++} cause electrostatic interactions with the guest molecules, enhancing the binding strengths significantly over that dictated by London – van der Waals interactions. The strength of these electrostatic interactions depend on the dipole moments and quadrupole moments of the guest molecules.

Figure S15a shows the unary adsorption isotherms of H_2, N_2, CO, CH_4, and CO_2 in LTA-5A at 313 K. The binding strengths of these guest molecules follow the hierarchy $H_2 < N_2 < CH_4 < CO < CO_2$. In comparison with activated carbon (cf. Figure S12b) it is noteworthy that CO has a stronger binding strength than CH_4 in LTA-5A. The polarizability of CH_4 is higher than that of CO, but does not possess either dipole or significant quadrupole moments. Therefore, in a non-charged adsorbent such as activated carbon, the adsorption strength of CH_4 is higher than that of CO. However, in LTA-5A, CO has a higher adsorption strength than CH_4 due to the significant contribution of $\phi_{F\mu} \propto \mu\frac{q}{r^2}$.

Figure S15b shows the transient breakthrough of 73/4/3/4/16 $H_2/N_2/CO/CH_4/CO_2$ mixture in fixed bed adsorber packed with LTA-5A, operating at 2 MPa total pressure and T = 313 K. In the simulations, we choose the mass of the adsorbent in the bed $m_{ads} = 180$ kg, cross-sectional area, A = 1 m^2; superficial

gas velocity at the bed inlet, u_0 = 0.04 m s^{-1}; voidage of the packed bed, ε = 0.4. The framework density of LTA-5A is $\rho = 1508$ kg m^{-3}. The length L of the adsorber bed is chosen as $L = \frac{1000}{\rho} \times 0.3 = 0.2$ m. For presenting the breakthrough simulation results, we use as x-axis the dimensionless time, $\tau = \frac{tv}{L} = \frac{tu_0}{\varepsilon L}$, obtained by dividing the actual time, t, by the characteristic time, $\frac{L}{v} = \frac{\varepsilon L}{u_0}$, where L is the length of adsorber, v is the interstitial gas velocity;[7, 25] see Figure S15b. The same data is plotted in Figure S15c using $Q_0 t / m_{ads}$ as x-axis where Q_0 is the volumetric flow rate of the gas mixture at the inlet to the fixed bed, expressed in L s^{-1}, at STP conditions. The hierarchy of breakthrough times $H_2 < N_2 < CH_4 < CO < CO_2$ follows the hierarchy of binding strengths.

Figure S16a shows the transient breakthrough of 73/4/3/4/16 $H_2/N_2/CO/CH_4/CO_2$ mixture in fixed bed adsorber packed with UiO-66(Zr)-Br, operating at 2 MPa total pressure and T = 313 K. In the simulations, we choose the mass of the adsorbent in the bed $m_{ads} = 180$ kg, cross-sectional area, A = 1 m^2; superficial gas velocity at the bed inlet, u_0 = 0.04 m s^{-1}; voidage of the packed bed, ε = 0.4. The length L of the adsorber bed is chosen as $L = 0.3$ m. For presenting the breakthrough simulation results, we use as x-axis the dimensionless time, $\tau = \frac{tv}{L} = \frac{tu_0}{\varepsilon L}$, obtained by dividing the actual time, t, by the characteristic time, $\frac{L}{v} = \frac{\varepsilon L}{u_0}$, where L is the length of adsorber, v is the interstitial gas velocity;[25] see Figure S16a. The same data is plotted in Figure S16b using $Q_0 t / m_{ads}$ as x-axis where Q_0 is the volumetric flow rate of the gas mixture at the inlet to the fixed bed, expressed in L s^{-1}, at STP conditions. The hierarchy of breakthrough times is $H_2 < N_2 < CO < CH_4 < CO_2$.

The stronger binding of N_2 in LTA-5A as compared to AC is due to the contribution of the quadrupole moment of N_2: $\phi_{FQ} \propto Q\frac{q}{r^3}$. Consequently, the breakthrough of N_2 occurs significantly later with LTA-5A, as compared to activated carbon; compare Figure S13 and Figure S15. Due to the later breakthrough of N_2 in LTA-5A, the productivity of pure H_2 in a fixed bed adsorber is higher with LTA-

5A; see the comparison of H_2 breakthroughs in Figure S17a. From a material balance on the adsorber, the productivity of H_2 with a purity of 99.95%+ is:

4 L kg^{-1} of AC at STP,

49.5 L kg^{-1} of LTA-5A at STP,

and 58.9 mol kg^{-1} of UiO-66(Zr)-Br.

UiO-66(Zr)-Br has a higher productivity than LTA-5A. Figure S17b presents a plot of the productivity of H_2 with a purity of 99.95%+ as a function of the separation potential, calculated from IAST

$$\Delta q = \left(q_{CO2} + q_{CO} + q_{CH4} + q_{N2}\right)\frac{y_{H2}}{\left(1-y_{H2}\right)} - q_{H2} \tag{S41}$$

We note that the productivities are approximately linearly related to Δq and therefore Δq can be used for screening MOFs.

We now consider the regenerabilities.

Due to the large quadrupole moment of CO_2, the significantly large contribution of $\phi_{FQ} \propto Q\frac{q}{r^3}$ causes the loading of CO_2 in LTA-5A to be significantly higher than that of activated carbon; see Figure S18.

The strong binding of CO_2 in LTA-5A is disadvantageous because deep vacuum will be required to reduce the CO_2 loading to the desired level during the purge step (d) in Figure S11. Consequently, despite the superior separation performance of LTA-5A, resulting in higher productivity of pure H_2 per kg of adsorbent, LTA-5A is not used on its own in the PSA schemes. Industrial practice is to use multi-layered beds (see Figure S18), consisting of:

(a) activated alumina, or silica gel, to remove water from the feed mixtures

(b) activated carbon layer, that has the function of adsorbing most of the CO_2 present in the feed mixture

(c) LTA-5A layer, whose function is to remove the remainder of the impurities N_2, CO, CH_4 in order to meet with the desired H_2 product purity, typically 99.95%+.

6.2 List of Tables for H2 production from steam-methane reforming

Table S1. Dual-site Langmuir parameter fits for CO_2 in LTA-5A zeolite. These parameters are based on the unary isotherm data reported in Table A1 of Mofarahi and Gholipour[37] at temperatures of 273 K, 283 K, 303 K, 323 K, and 343 K.

	Site A			Site B		
	$q_{A,sat}$ mol kg^{-1}	b_{A0} Pa^{-1}	E_A kJ mol^{-1}	$q_{B,sat}$ mol kg^{-1}	b_{B0} Pa^{-1}	E_B kJ mol^{-1}
CO_2	1.5	4.5E-10	23.5	2.5	2.99E-12	49

Table S2. Single-site Langmuir parameter fits for CH_4 and N_2 in LTA-5A zeolite. These parameters are based on the unary isotherm data reported in Table 3 and Table 4 of Bakhtyari and Mofarahi[38] at temperatures of 273 K, 283 K, 303 K, 323 K, and 343 K.

	q_{sat} mol kg^{-1}	b_0 Pa^{-1}	E kJ mol^{-1}
CH_4	3.1	9.43E-10	19
N_2	2.5	1.68E-09	16.6

Table S3. Dual-site Langmuir parameter fits for H_2 and CO in LTA-5A zeolite. These parameters are those reported in Table 3 of Jamali et al.[39]

	Site A			Site B		
	$q_{A,sat}$ mol kg^{-1}	b_{A0} Pa^{-1}	E_A kJ mol^{-1}	$q_{B,sat}$ mol kg^{-1}	b_{B0} Pa^{-1}	E_B kJ mol^{-1}
H_2	0.4965	1.65E-08	7.62	0.03725	5.59E-09	14.1
CO	2.502	6.56E-11	24.13	1.182	1.88E-11	34.48

6.3 List of Figures for H2 production from steam-methane reforming

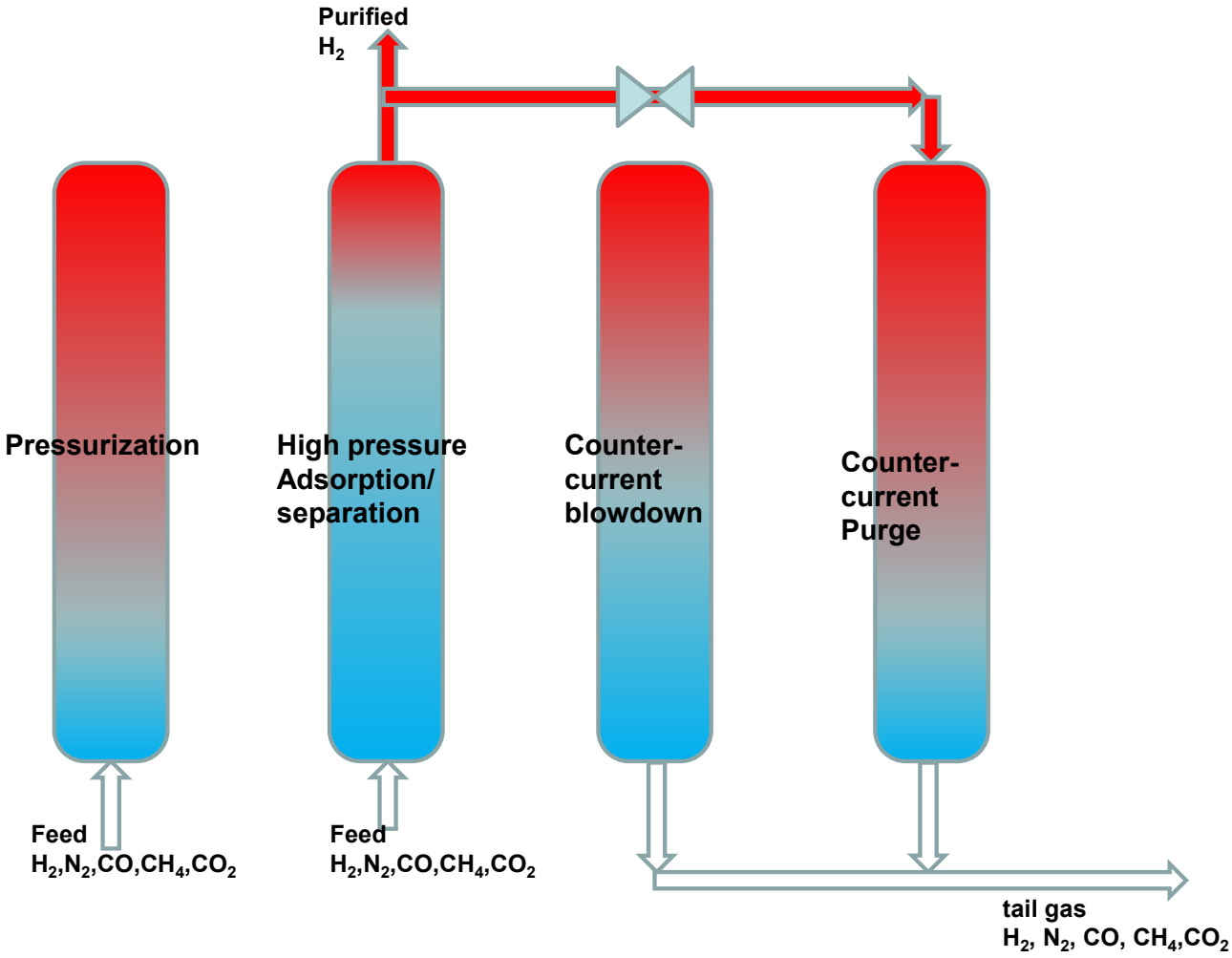

Figure S11. Sequential steps in the operation of a single bed in the Skarstrom cycle for H_2 purification.[2, 3, 13, 31]

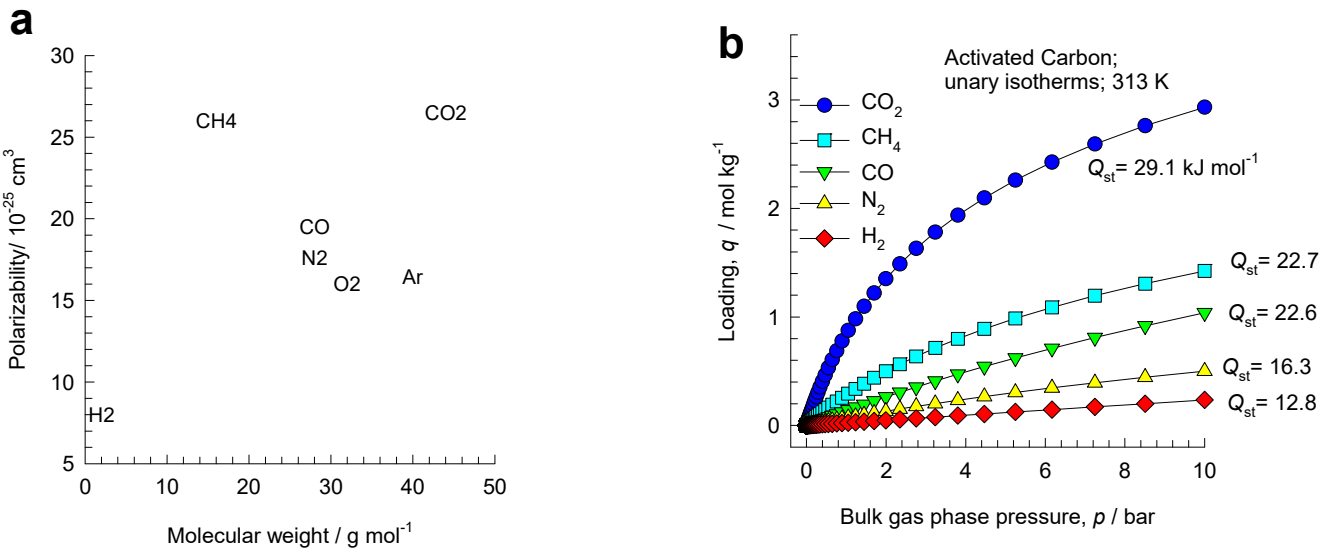

The binding strengths are primarily dictated by the polarizabilities. The larger the molecule, the higher the polarizability

Figure S12. (a) Polarizabilities of variety of gaseous molecules encountered in hydrogen purification processes. The data on polarizabilities are taken from Sircar and Myers.[4] (b) Unary isotherms at 313 K in activated carbon. The multi-site Langmuir parameters are listed in Table 4 of Ribeiro et al;[31] These parameters were used to refit the isotherms using dual-site Langmuir model; these unary isotherms at 313 K are plotted in (b). Also indicated in (b) are the isosteric heats of adsorption, Q_{st}, as listed in Table 4 of Ribeiro et al.[31]

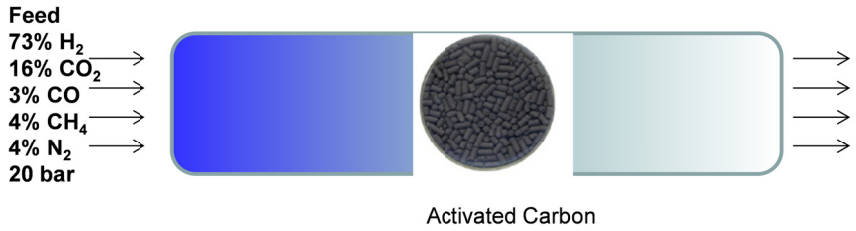

Purity of H_2 is dictated by N_2 breakthrough; the hierarchy of breakthroughs dictated by London – van der Waal dispersion interactions

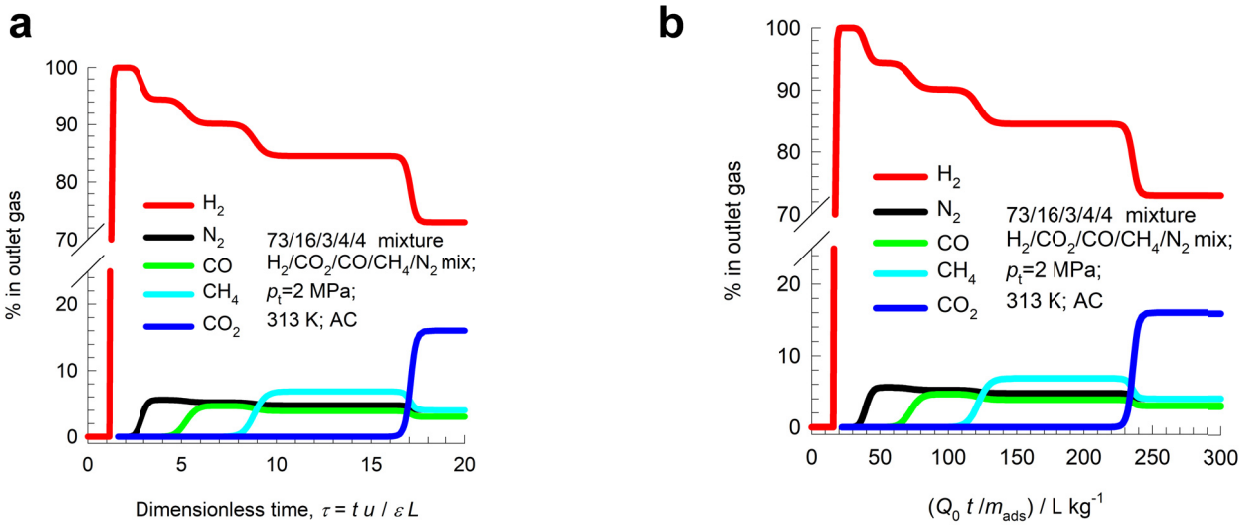

Figure S13. (a, b) Transient breakthrough of 73/4/3/4/16 $H_2/N_2/CO/CH_4/CO_2$ mixture in fixed bed adsorber packed with activated carbon operating at a total pressure of 2 MPa, and T = 313 K. The transient breakthrough simulation methodology is described in Chapter 4 Methodology for transient breakthrough simulations. These breakthroughs are performed assuming negligible axial dispersion, and negligible diffusional influences. In (b) we use $Q_0 t/m_{ads}$ as x-axis where Q_0 is the volumetric flow rate of the gas mixture at the inlet to the fixed bed, expressed in L s^{-1}, at STP conditions. The unary isotherm data are from Ribeiro et al.,[31] after re-fitting using the dual-site Langmuir model. In the breakthrough simulations, the mixture adsorption equilibrium was determined using the IAST.

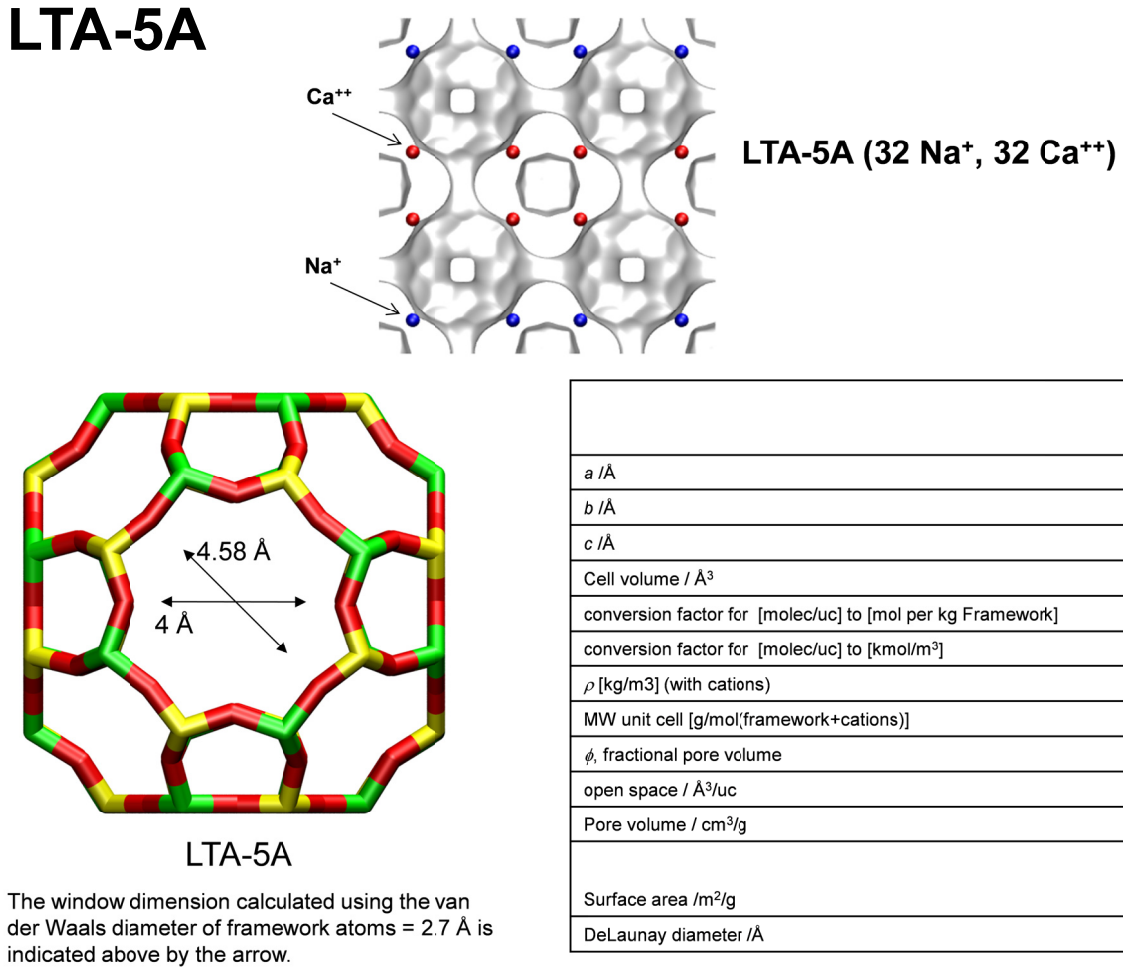

	LTA-5A
a /Å	24.555
b /Å	24.555
c /Å	24.555
Cell volume / Å^3	14805.39
conversion factor for [molec/uc] to [mol per kg Framework]	0.0744
conversion factor for [molec/uc] to [kmol/m^3]	0.2955
ρ [kg/m3] (with cations)	1508.376
MW unit cell [g/mol framework+cations)]	13448.48
ϕ, fractional pore volume	0.380
open space / Å^3/uc	5620.4
Pore volume / cm^3/g	0.252
Surface area /m^2/g	
DeLaunay diameter /Å	4.00

Figure S14. Structural details of LTA-5A zeolite.

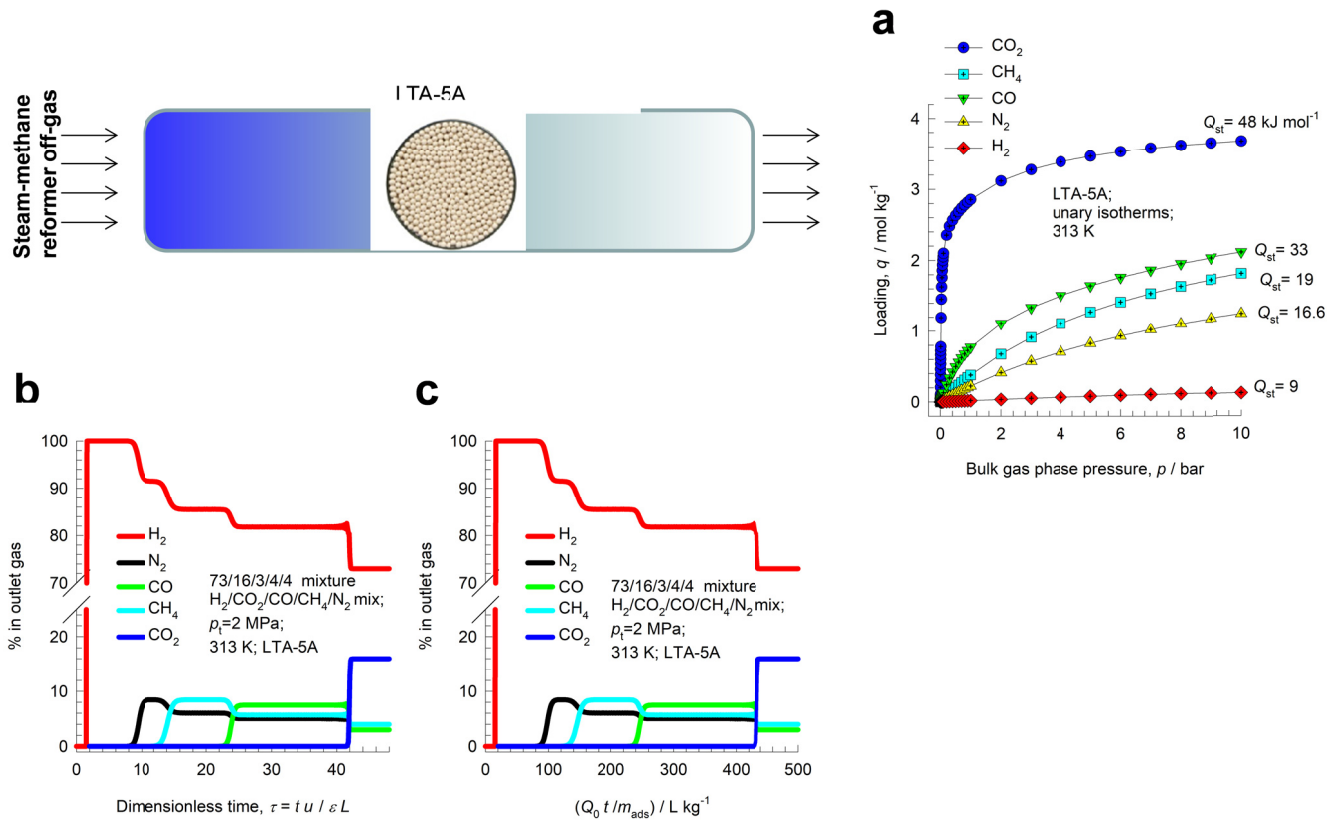

Figure S15. (a) Unary isotherms of H_2, N_2, CO, CH_4, and CO_2 at 313 K in LTA-5A. The unary isotherm data are culled from the literature, and provided in Table S1, Table S2, and Table S3 Also indicated in (a) are the isosteric heats of adsorption, Q_{st}. (b, c) Transient breakthrough of 73/4/3/4/16 $H_2/N_2/CO/CH_4/CO_2$ mixture in fixed bed adsorber packed with LTA-5A operating at a total pressure of 2 MPa, and T = 313 K. The transient breakthrough simulation methodology is described in Chapter 4 Methodology for transient breakthrough simulations. These breakthroughs are performed assuming negligible axial dispersion, and negligible diffusional influences.

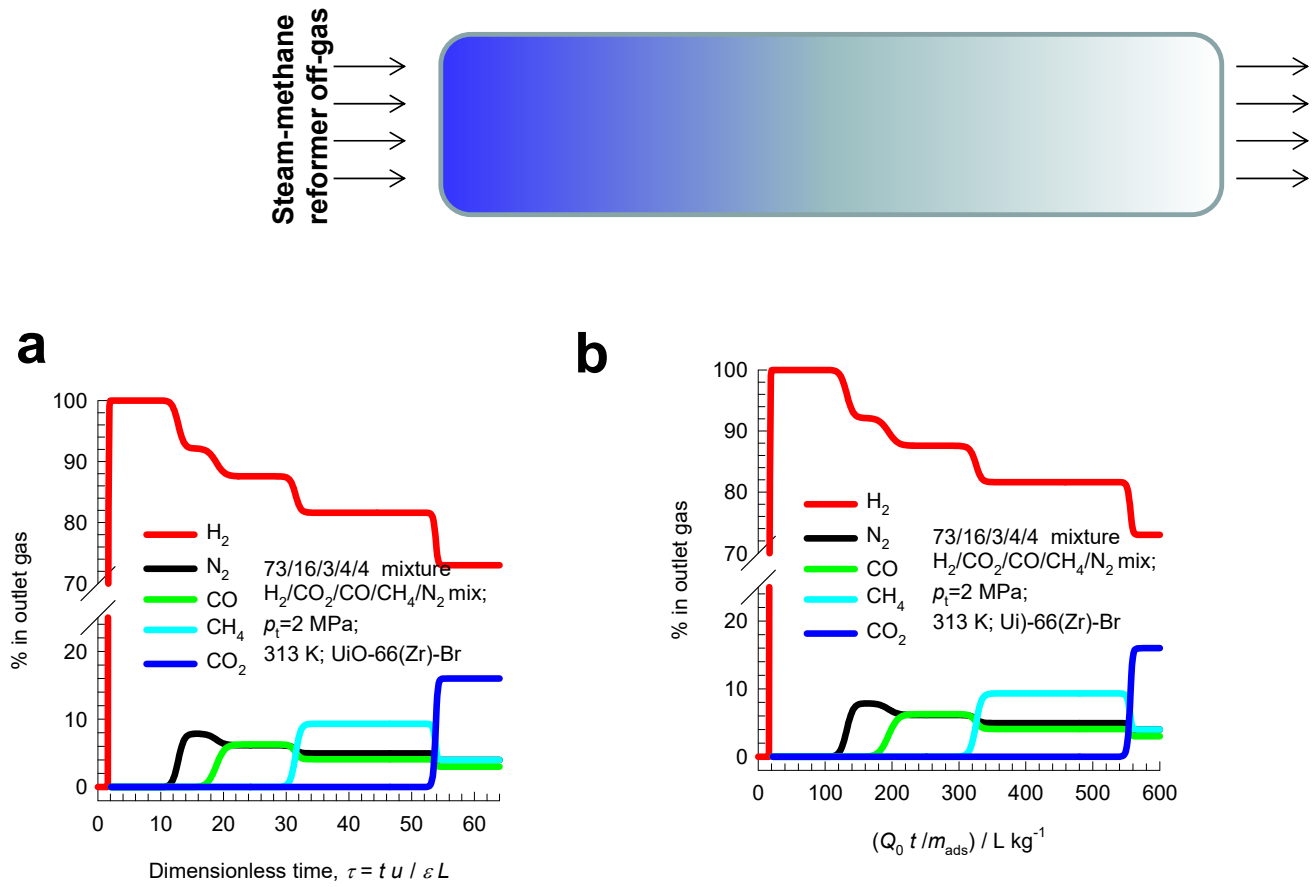

Figure S16. (a , b) Transient breakthrough of 73/4/3/4/16 $H_2/N_2/CO/CH_4/CO_2$ mixture in fixed bed adsorber packed with UiO-66(Zr)-Br operating at a total pressure of 2 MPa, and T = 313 K. The unary isotherm data are taken from Table S3 of Banu et al. The transient breakthrough simulation methodology is described in Chapter 4 Methodology for transient breakthrough simulations. These breakthroughs are performed assuming negligible axial dispersion, and negligible diffusional influences

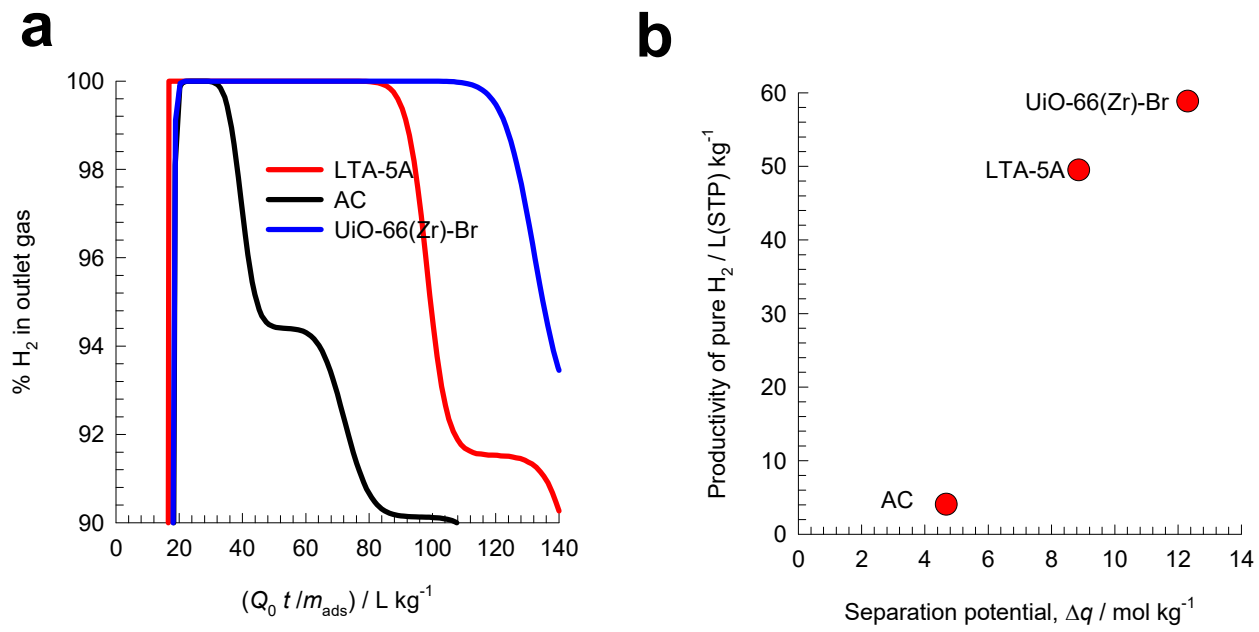

Figure S17. (a) Comparison of the breakthroughs of H_2 in fixed beds packed with activated carbon, LTA-5A, and UiO-66(Zr)-Br, operating at 2 MPa at 313 K. (b) Productivity of 99.95%+ pure H_2 plotted as function of the separation potential.

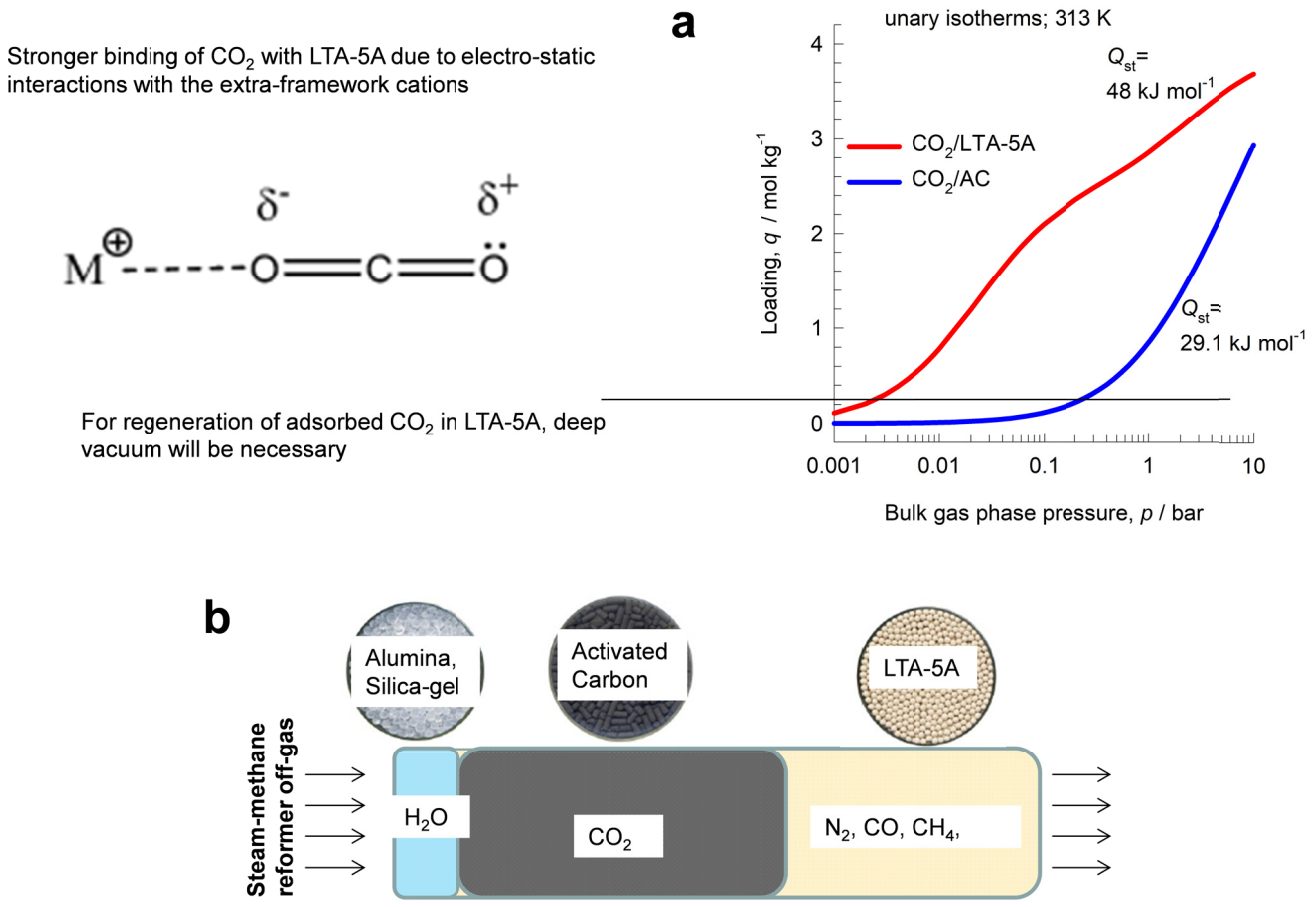

Figure S18. (a) Comparison of the unary isotherms of CO_2 in activated carbon and LTA-5A at 313 K. (b) Schematic of multi-layered bed for H_2 purification. [2, 3, 13, 31]

7 Separation of C_2H_2/CO_2 mixtures

Ethyne (C_2H_2), widely used as a fuel in welding equipment and also a very important building block in industrial chemical synthesis, is commonly manufactured by the partial combustion of CH_4 or comes from cracking of hydrocarbons. In the reactor product, C_2H_2 co-exists with CO_2 and unreacted CH_4. The separation of C_2H_2/CO_2 mixtures is particularly challenging in view of the similarity in the molecular sizes, shapes (3.32 × 3.34 × 5.7 $Å^3$ for C_2H_2; 3.18 × 3.33 × 5.36 Å3 for CO_2);[40, 41] both molecules possess zero dipole moments and approximately the same quadrupole moment. Since the boiling points of C_2H_2, and CO_2 are close, 189.3 K and 194.7 K, respectively, distillation separations need to operate at cryogenic temperatures and high pressures. A number of recently developed MOFs offer the potential of use in adsorptive separations of C_2H_2/CO_2 mixtures.[42-54]

For separation of C_2H_2(1)/CO_2(2) mixtures, we have also compared the performance of nine MOFs that have been suggested in the literature: PCP-33,[49] HOF-3,[50] TIFSIX-2-Cu-i,[51] JCM-1,[52] DICRO-4-Cu-i,[53] MUF-17,[54] UTSA-74,[48] FJU-90,[45] and FeNi-M'MOF.[43] The unary isotherm data for C_2H_2, and CO_2 for these 9 MOFs are culled from the literature sources.

For analysis of the separations of C_2H_2/CO_2 mixtures using TIFSIX-2-Cu-i, JCM-1, DICRO-4-Cu-i, and MUF-17 the unary isotherm data fits for C_2H_2, and CO_2 reported in the Supporting Material accompanying the original publications were used; the sources are specified below.

TIFSIX-2-Cu-i: Dual-site Langmuir-Freundlich parameters in Figure S15, and S16 of Chen et al. [51],

JCM-1: Dual-site Langmuir parameters in Table S3 of Lee et al.,[52]

DICRO-4-Cu-i: Dual-site Langmuir-Freundlich parameters in Figure S13, and S14 of Scott et al. [53],

MUF-17: Dual-site Langmuir parameters in Figure S13 of Qazvini et al. [54]

Separation of C2H2/CO2 mixtures

All the nine selected MOFs are selective to C_2H_2. Consequently, the desired ethyne product is available in the blowdown phase of the Skarstrom cycle of fixed bed operations, as shown in the schematic in Figure S19.

Figure S20a compares the IAST calculations of the component loadings q_1, q_2 for adsorption of equimolar $C_2H_2(1)/CO_2(2)$ mixtures in nine different MOFs operating at 298 K and 100 kPa. It is noteworthy that FJU-90 has the highest uptake capacity for ethyne.

Figure S20b plots the IAST calculations of the separation potential $\Delta q = q_1 - q_2 \frac{y_{10}}{y_{20}}$ vs the adsorption selectivity S_{ads}. The MOF with the highest selectivity is FeNi-M'MOF, but the MOF with the highest value of the separation potential is FJU-90. We attempt to obtain confirmation of this by performing transient breakthrough simulations of the adsorption/desorption cyles.

As illustration, Figure S21a presents the transient breakthrough simulations for the adsorption phase of $C_2H_2(1)/CO_2(2)$ mixture in a fixed bed adsorber packed with FJU-90, operating at 100 kPa and 298 K. Figure S21b presents simulations of the corresponding blowdown cycle in which the equilibrated bed is subject to deep vacuum (0.2 Pa). For convenience of the calculations, the desorption simulations are performed for co-current vacuum blowdown. During the time interval indicated by the arrow, C_2H_2 of the desired purity can be recovered. For a desired purity of 99%, the amount of 99%+ pure C_2H_2 can be determined from a material balance on the adsorber in the desorption cycle. These productivity values, expressed as L of desired product (at STP), per kg of adsorbent in packed bed, for the nine different MOFs are plotted in Figure S21c. The *x*-axis in Figure S21c is the separation potential, Δq, calculated using eq (S40) with $y_{10} = y_{20} = 0.5$, that represents the maximum C_2H_2 productivity that is achievable if the concentration "fronts" traversed the column in the form of shock waves during the desorption cycle. We note that the productivities determined from the transient breakthrough simulations (denoted as symbols) are linearly related to Δq. Also shown by the continuous solid line in Figure S21c is the parity line $22.4 \times \Delta q$ for the productivities. The actual productivities are lower than the maximum

values because of the distended nature of the breakthroughs. The important conclusion to emerge is that separation potential, Δq, is the appropriate metric to use in the screening of MOFs for $C_2H_2(1)/CO_2(2)$ mixture separations. The MOF with the highest value of C_2H_2 productivity is FJU-90 despite the fact that its selectivity is lower than that of FeNi-M'MOF.

7.1 List of Figures for Separation of C2H2/CO2 mixtures

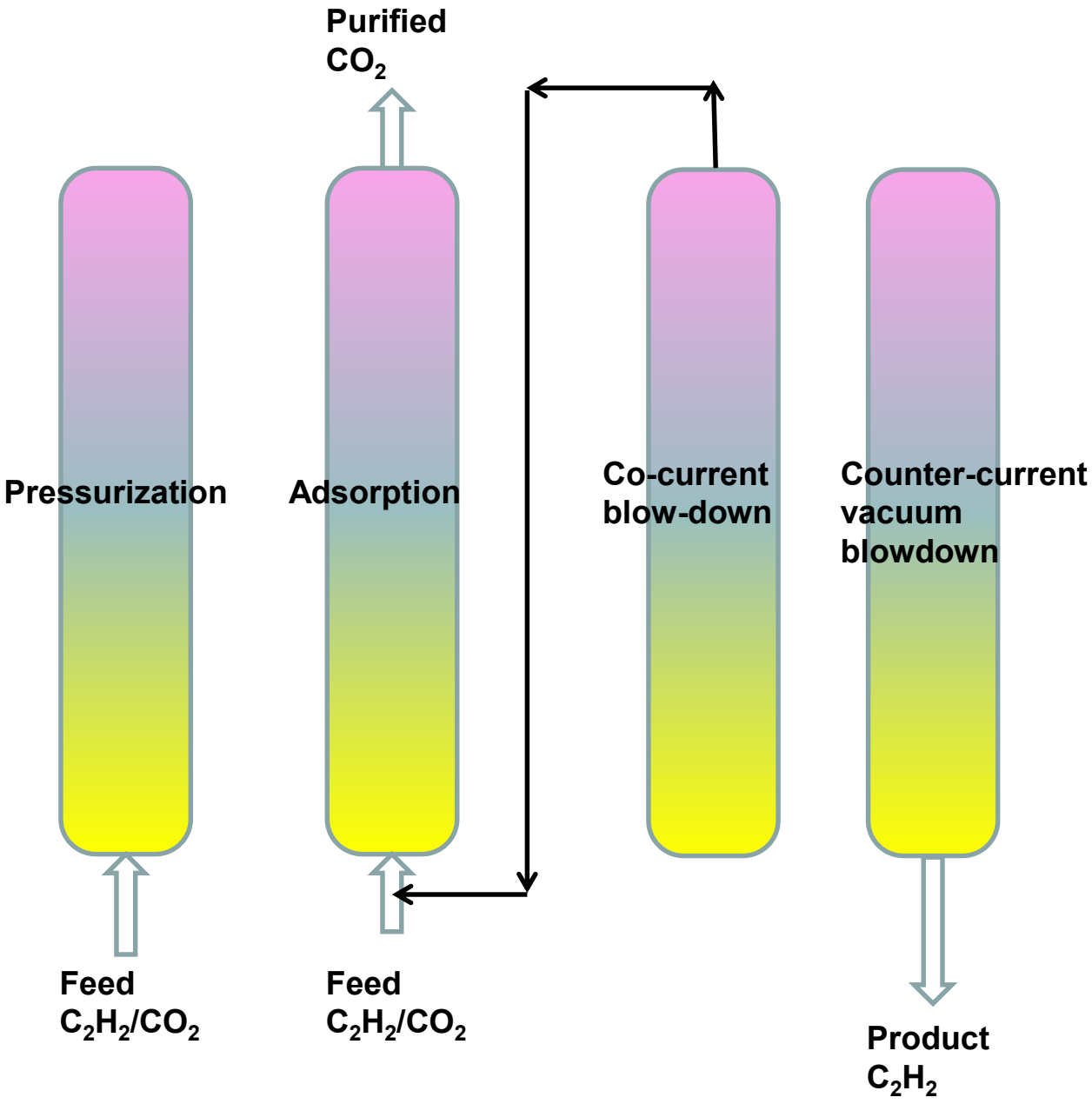

Figure S19. Sequential steps in the operation of a fixed-bed adsorber in the Skarstrom cycle for $C_2H_2(1)/CO_2(2)$ separation.

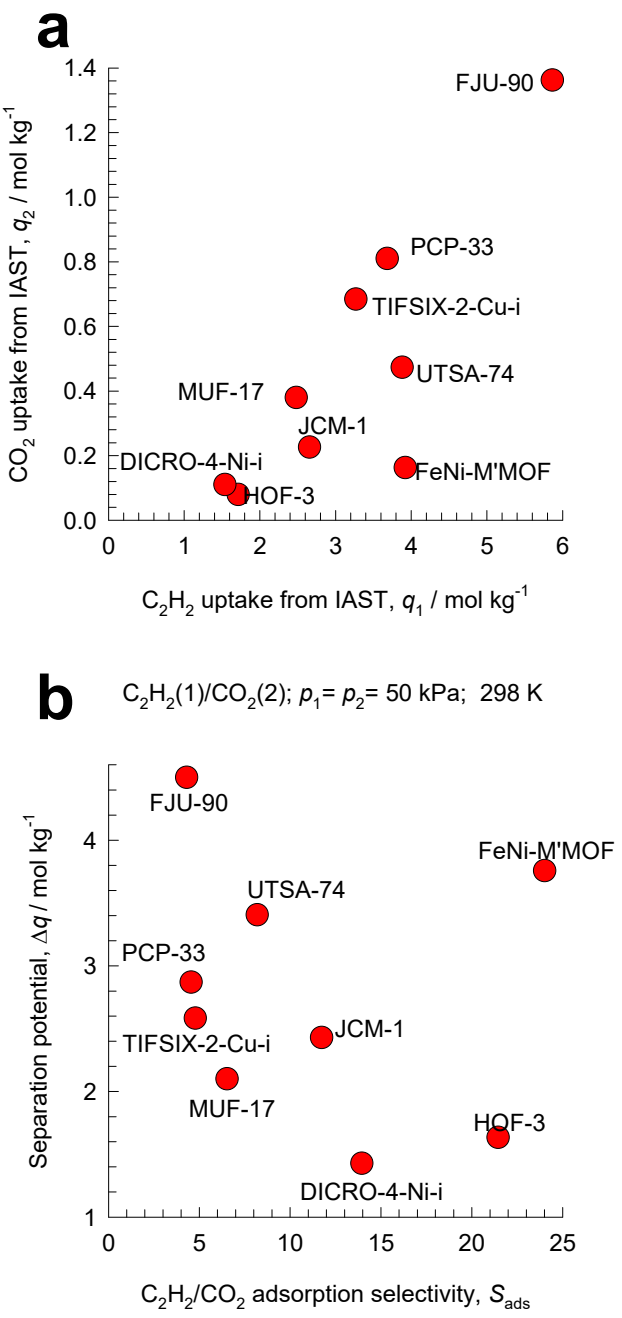

Figure S20. (a) IAST calculations of the component loadings q_1, q_2 for adsorption of equimolar $C_2H_2(1)/CO_2(2)$ mixtures in nine different MOFs operating at 298 K and 100 kPa. (b) IAST calculations of the component loadings S_{ads} and separation potential $\Delta q = q_1 - q_2 \frac{y_{10}}{y_{20}}$ for adsorption of $C_2H_2(1)/CO_2(2)$ mixtures in nine different MOFs operating at 298 K and 100 kPa,with $y_{10} = y_{20} = 0.5$.

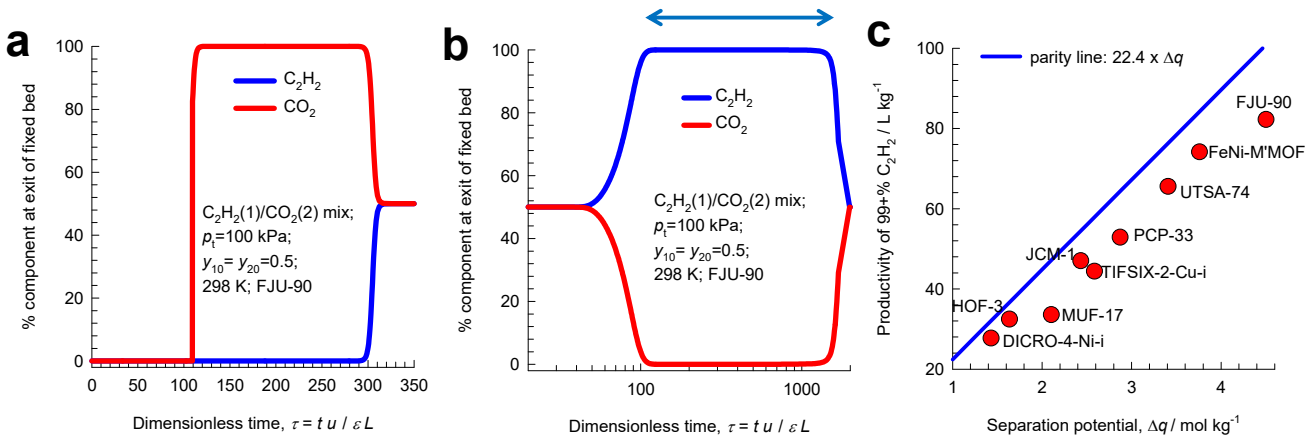

Figure S21. (a) Simulations of transient breakthroughs of $C_2H_2(1)/CO_2(2)$ mixtures in fixed bed packed with FJU-90 operating at 298 K and 100 kPa with feed compositions $y_{10} = y_{20} = 0.5$. (b) Simulations of transient desorption (blowdown) under deep vacuum (0.2 Pa total pressure) and 298 K. During the time interval indicated by the arrow, C_2H_2 product containing < 1% CO_2 can be recovered. (c) Productivity of 99%+ pure C_2H_2 product, determined by transient desorption simulations for PCP-33,[49] HOF-3,[50] TIFSIX-2-Cu-i,[51] JCM-1,[52] DICRO-4-Cu-i,[53] MUF-17,[54] UTSA-74,[48] FJU-90,[45] and FeNi-M'MOF[43] at 298 K and 100 kPa, plotted as a function of the separation potential $\Delta q = q_1 - q_2 \frac{y_{10}}{y_{20}}$, with $y_{10} = y_{20} = 0.5$.

8 Separation of N_2/CH_4 mixtures

Many natural gas reserves contain nitrogen in concentrations ranging to about 20%.[55] To meet pipeline specifications, the nitrogen level must be reduced to below 4%.[56] A large majority of nitrogen removal facilities use cryogenic distillation, but such units are economical only for large capacity wells. For smaller reserves pressure swing adsorption technology has economic benefits, especially because the feed mixtures are available at high pressures.[55, 56] It is desirable to use adsorbents in pressure swing adsorption (PSA) units that are selective to N_2. For most known adsorbents, the adsorption selectivity for separation of N_2/CH_4 mixtures is in favor of CH_4 due to its higher polarizability; see Figure S3a,b. The notable exception is MIL-100(Cr), activated at 523 K, that shows adsorption selectivity in favor of N_2.[57]

One practical solution is to rely on diffusion selectivities by using microporous materials, such as LTA-4A zeolite, ETS-4 (ETS = Engelhard Titano-silicate; ETS-4 is also named as CTS-1 = Contracted Titano Silicate -1), and clinoptilolites, that have significantly higher diffusivities of N_2, compared to that of CH_4.[2, 56, 58-60]

The earliest study demonstrating the possibility of using LTA-4A zeolite, utilizing diffusion selectivities for separating $N_2(1)/CH_4(2)$ mixtures is contained in the classic paper of Habgood.[60] LTA-4A zeolite (also called 4A or NaA zeolite) contains extra-framework cations (containing 96Si, 96 Al, 96 Na^+ per unit cell; Si/Al=1). LTA-4A zeolite consists of cages of 743 $Å^3$ volume, separated by 4.11 Å × 4.47 Å 8-ring windows. The pore landscape and structural details of LTA-4A zeolite are provided in Figure S22. The Na^+ cations partially block the window sites, leading to low magnitudes of guest diffusivities. The partial blocking of the windows enhances efficacy of kinetic separations, because it significantly enhances the ratio of the diffusivities of mobile and tardier species. Molecules jump one-at-a-time across the windows of LTA-4A. Nitrogen is a "pencil-like" molecule (4.4 Å × 3.3 Å) that can

hop length-wise across the narrow windows; the "spherical" CH_4 (3.7 Å) is much more severely constrained and has a diffusivity that is about 22 times lower than that of N_2.

By tuning the size of the microporous channels and using ETS-4 as adsorbent, CH_4 can be practically excluded from the pores favor the selective uptake of N_2 from $N_2(1)/CH_4(2)$ mixtures.[56, 58, 61] Nitrogen is a "pencil-like" molecule, of 4.4 Å × 3.3 Å size; CH_4 is a spherical molecule of 3.7 Å size. The pores of Ba-ETS-4 virtually exclude methane molecules; see Figure S23a.

Figure S23b shows the transient breakthrough of 20/80 $N_2(1)/CH_4(2)$ mixture in fixed bed adsorber packed with Ba-ETS-4, operating at 1 MPa total pressure and T = 283 K. These simulation also include intra-crystalline diffusional limitations. The Maxwell-Stefan diffusivities used in the simulations are: $Đ_1/r_c^2 = 2.8\times10^{-2}$ s^{-1}; $Đ_2/r_c^2 = 6.7\times10^{-6}$ s^{-1}. The breakthrough simulation methodology is described in Chapter 4 Methodology for transient breakthrough simulations. In the simulations, we choose the mass of the adsorbent in the bed $m_{ads} = 180$ kg, cross-sectional area, A = 1 m^2; superficial gas velocity at the bed inlet, u_0 = 0.04 m s^{-1}; voidage of the packed bed, ε = 0.4. The framework density of Ba-ETS-4 is $\rho = 1720$ kg m^{-3}. The length L of the adsorber bed is chosen as $L = \frac{1000}{\rho}\times 0.3 = 0.174419$ m. For presenting the breakthrough simulation results, we use the dimensionless time, $\tau = \frac{tv}{L} = \frac{tu_0}{\varepsilon L}$, obtained by dividing the actual time, t, by the characteristic time, $\frac{L}{v} = \frac{\varepsilon L}{u_0}$, where L is the length of adsorber, v is the interstitial gas velocity.[25] We note that the breakthrough of $CH_4(2)$ occurs practically at time $t \approx 0$, implying that hardly any CH_4 enters the pores of Ba-ETS-4. In Figure S23c we use $Q_0 t/m_{ads}$ as x-axis where Q_0 is the volumetric flow rate of the gas mixture at the inlet to the fixed bed, expressed in L s^{-1}, at STP conditions.

Bhadra[56, 62] have developed a detailed mathematical model for a PSA scheme for purification of natural gas using Ba-ETS-4, using the steps shown in Figure S24. In this scheme the inclusion of the co-current blowdown step (suggested by Jayaraman et al.[59] for N_2/CH_4 mixture separations with

clinoptilolites) increases the CH_4 recovery. At the end of the counter-current blowdown step, the bed contains both nitrogen (fast diffusing) and methane (slow diffusing). Thus if the bed is simply closed at one end and left for a period of time the nitrogen will diffuse out first followed by the methane so the system is, in effect, self-purging (fifth step in the sequence).

Figure S25b presents transient breakthrough of 20/80 $N_2(1)/CH_4(2)$ mixture in fixed bed adsorber packed with MIL-100(Cr) operating at 283 K, and total pressure p_t = 1 MPa. These simulations ignore intra-crystalline diffusional limitations. The breakthrough simulation methodology is described in Chapter 4 Methodology for transient breakthrough simulations. In the simulations, we choose the mass of the adsorbent in the bed $m_{ads} = 180$ kg, cross-sectional area, A = 1 m^2; superficial gas velocity at the bed inlet, u_0 = 0.04 m s^{-1}; voidage of the packed bed, $\varepsilon = 0.4$. The framework density of MIL-100(Cr) is $\rho = 705$ kg m^{-3}. The length L of the adsorber bed is chosen as $L = \frac{1000}{\rho} \times 0.3 = 0.425532$ m. For presenting the breakthrough simulation results, we use $Q_0 t / m_{ads}$ as x-axis where Q_0 is the volumetric flow rate of the gas mixture at the inlet to the fixed bed, expressed in L s^{-1}, at STP conditions. We note that the breakthrough of CH_4 occurs significantly later than that with BaETS-4, implying that a significant amount of CH_4 gets adsorbed; Figure S25c. This implies that recovery of 96%+ pure CH_4 is likely to be unacceptably low.

8.1 List of Figures for Separation of N2/CH4 mixtures

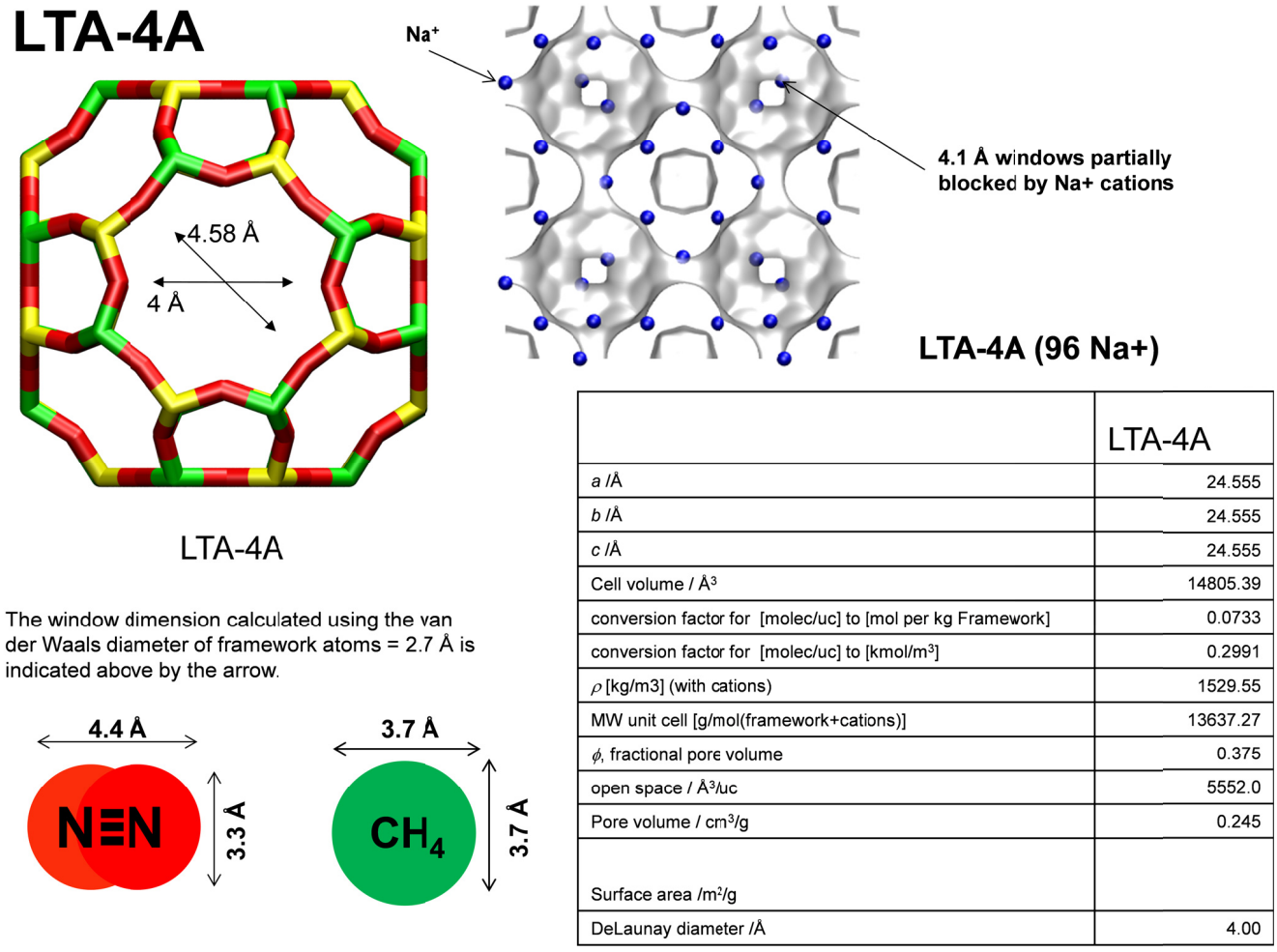

	LTA-4A
a /Å	24.555
b /Å	24.555
c /Å	24.555
Cell volume / Å^3	14805.39
conversion factor for [molec/uc] to [mol per kg Framework]	0.0733
conversion factor for [molec/uc] to [kmol/m^3]	0.2991
ρ [kg/m3] (with cations)	1529.55
MW unit cell [g/mol(framework+cations)]	13637.27
ϕ, fractional pore volume	0.375
open space / Å^3/uc	5552.0
Pore volume / cm^3/g	0.245
Surface area /m^2/g	
DeLaunay diameter /Å	4.00

Figure S22. Structural details of LTA-4A zeolite.

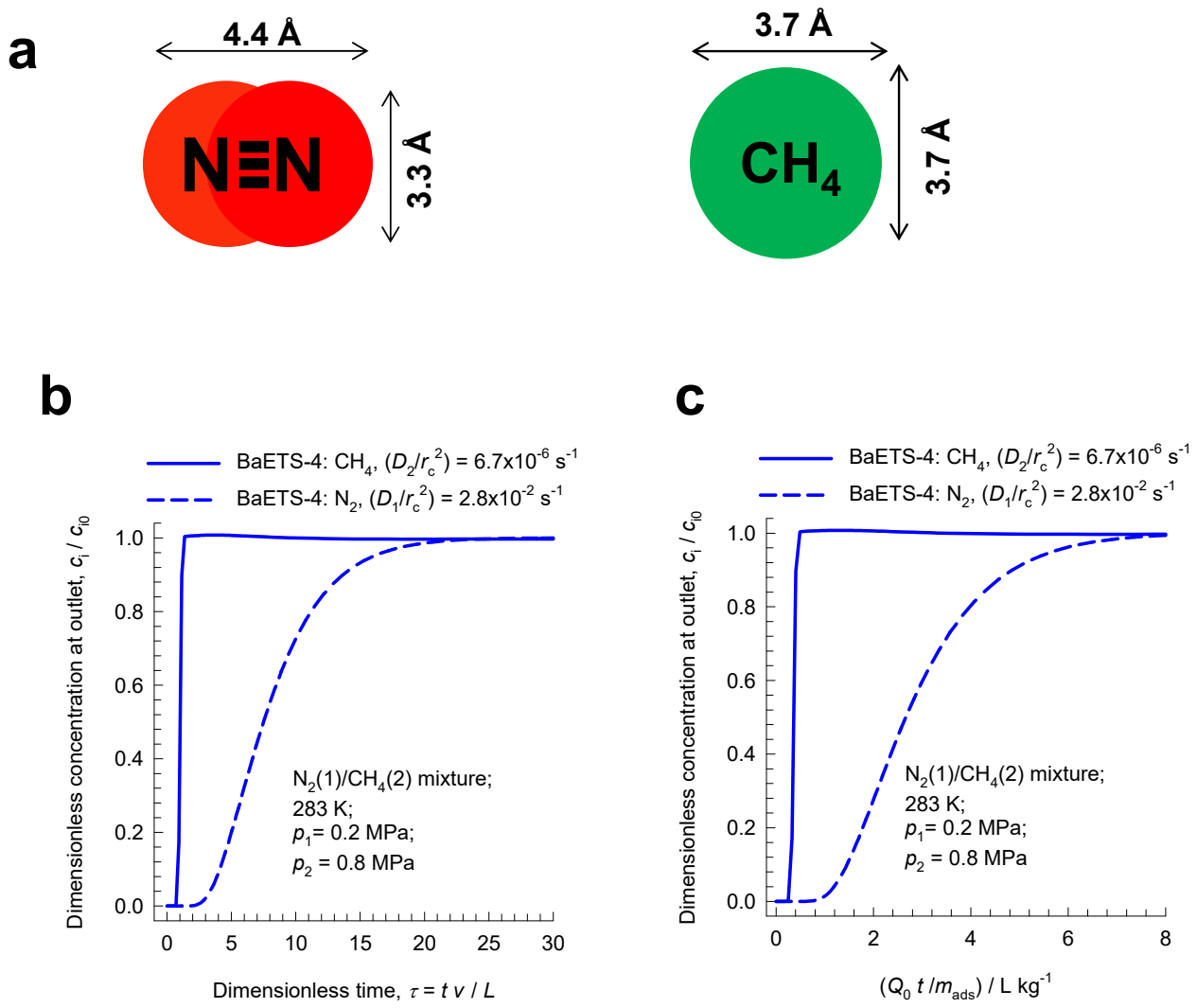

Figure S23. (a) Schematic showing the molecular dimensions. (b, c) Transient breakthrough of 20/80 $N_2(1)/CH_4(2)$ mixture in fixed bed adsorber packed with Ba-ETS-4 operating at 283 K, and total pressure p_t = 1 MPa. In (c) the parameter $Q_0 t/m_{ads}$ is used as *x*-axis where Q_0 is the volumetric flow rate of the gas mixture at the inlet to the fixed bed, expressed in L s^{-1}, at STP conditions.

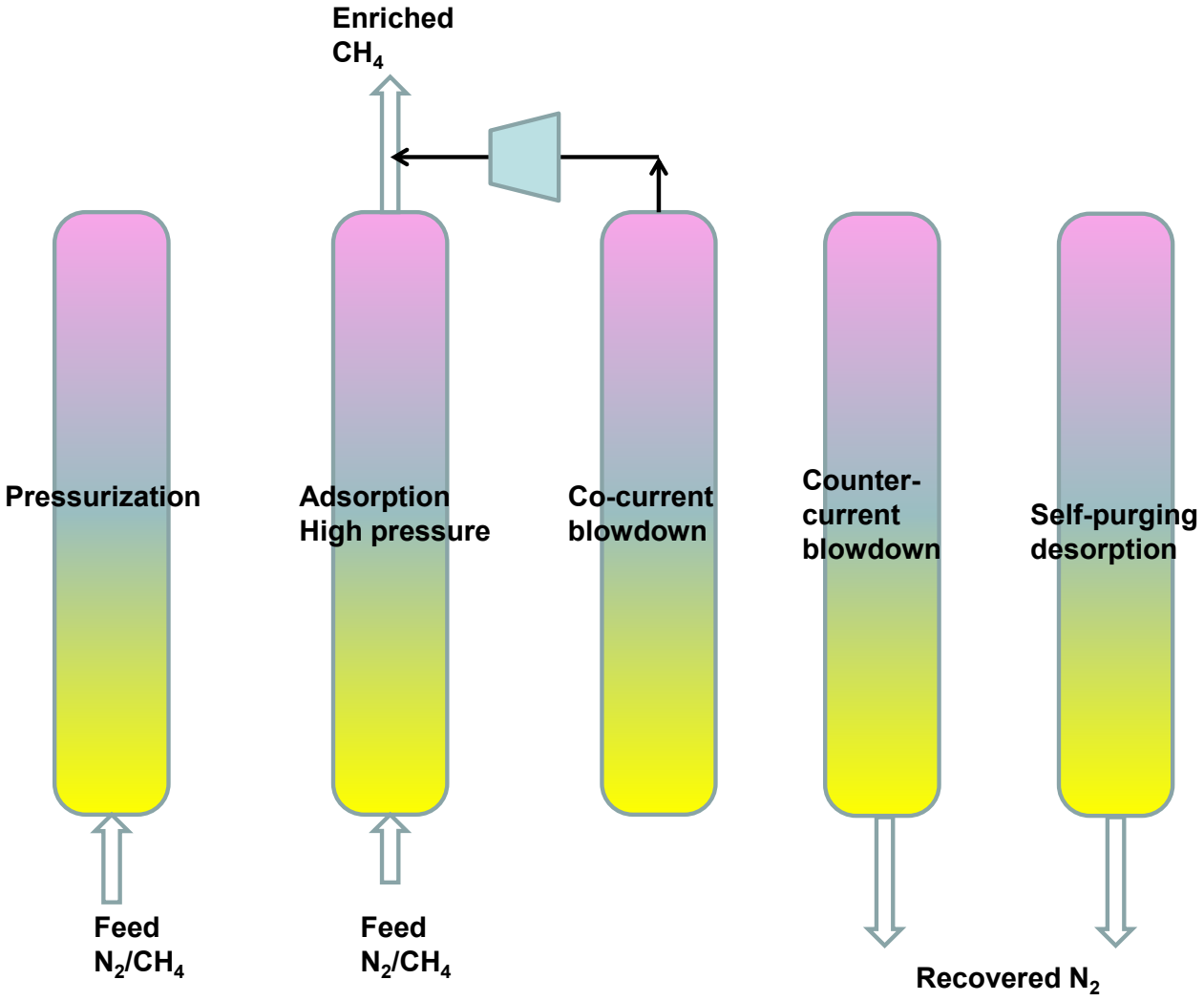

Figure S24. Different steps in the production of purified CH_4 using an adsorbent such as LTA-4A zeolite, Ba-ETS-4, and clinoptilolite, that rely on kinetic selectivity. The scheme shows the sequence of processing of a single bed in a multi-bed PSA scheme. Adapted from Jayaraman et al.[59]

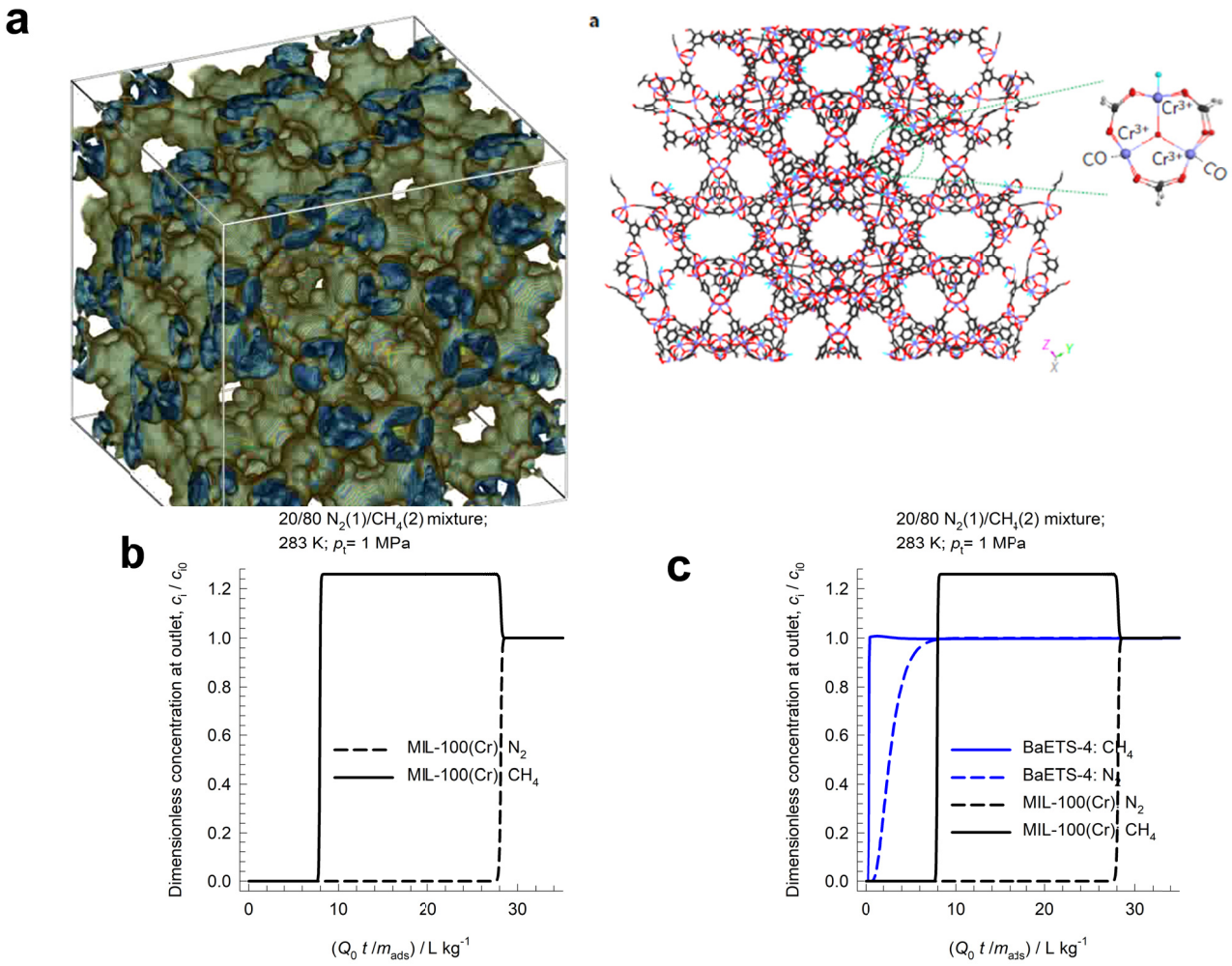

Figure S25. (a) Structure of MIL-100 (Cr). (b) Transient breakthrough of 20/80 $N_2(1)/CH_4(2)$ mixture in fixed bed adsorber packed with MIL-100(Cr) operating at 283 K, and total pressure p_t = 1 MPa. The unary isotherms are those reported by Yoon et al.[57] (c) Comparison of the transient breakthroughs of 20/80 $N_2(1)/CH_4(2)$ mixture in fixed bed adsorber packed with MIL-100(Cr) and Ba-ETS-4.

9 Separation of O_2/N_2 mixtures

The separation of air to produce N_2 and O_2 of high purities is one of the most important industrial processes that uses pressure swing adsorption technology.[13, 63] The process technologies are geared to either production of purified O_2 or purified N_2. Cryogenic distillation has been the common technologies for this separation, but adsorptive separations offer energy efficient alternatives. Purified O_2 is required for a wide variety of applications that include portable adsorption units for medical applications and in space vehicles. Nitrogen is required in applications where it is desired or necessary to exclude oxygen. Typical industrial applications include preservation of fruit and produce during trucking, the blanketing of fuel tanks of fighter aircraft, the inerting of reactors in a number of pharmaceutical processes, laser cutting. N_2 is required for use in laboratory analytical equipment such as GC, LC, LCMS, FTIR, ICP, and in glove boxes.

For production of purified O_2, cation-exchanged zeolites LTA-5A (also called 5A or NaCaA zeolite containing 96 Si, 96 Al, 32 Na^+, 32 Ca^{++} per unit cell; Si/Al=1), NaX (also called 13 X zeolite, containing 106 Si, 86 Al, 86 Na^+ per unit cell; Si/Al=1.23), CaX, LiX, and LiLSX (= low silica LiX zeolite) and can be used as selective adsorbents.[4, 63-66] The larger permanent quadrupole of N_2 compared to that of O_2 is responsible for the stronger adsorption strength of N_2 on these zeolites.[4] Both O_2, and N_2 have similar polarizabilities and magnetic susceptibilies. However, the quadrupole moment of N_2 is about 4 times that of O_2. The Skarstrom cycle can be used, with modifications such as the introduction of a pressure equalization step, for production of enriched O_2 using say LiLSX zeolite. The different steps (stages) in the operation of a single bed for producing oxygen in small-scale units are shown in Figure S26, that has been adapted from Ruthven and Farooq.[67] Desorption of the preferentially adsorbed nitrogen is achieved by pressure reduction followed by purging with a fraction of the oxygen product to remove the nitrogen from the interstices of the bed. Further details are available in the excellent texts of Ruthven et al.[13], and Yang.[2, 68]

Separation of O2/N2 mixtures

For production of purified N_2 from air, a different strategy is often employed that rely on diffusion selectivity.[69, 70] Diffusion-selective separation are achieved with Carbon Molecular Sieve (CMS), and LTA-4A zeolite. Diffusion limitations manifest in LTA-4A because the window regions are partially blocked by the cations; see pore landscape in Figure S27. The same basic Skarstrom cycle can be used, with the kinetically selective 4A zeolite or carbon molecular sieve adsorbent, in a nitrogen production process. However, in such a system purging with nitrogen to remove the faster diffusing oxygen from the bed is undesirable since, as well as wasting product, a certain fraction of the slowly diffusing nitrogen will be adsorbed, thus reducing the capacity for oxygen during the next adsorption step. At the end of the counter-current blowdown step (see Figure S28), the adsorbent contains both oxygen (fast diffusing) and nitrogen (slow diffusing). Thus if the bed is simply closed at one end and left for a period of time, oxygen will diffuse out first followed by nitrogen so the system is, in effect, self purging. [13, 67]

9.1 List of Figures for Separation of O2/N2 mixtures

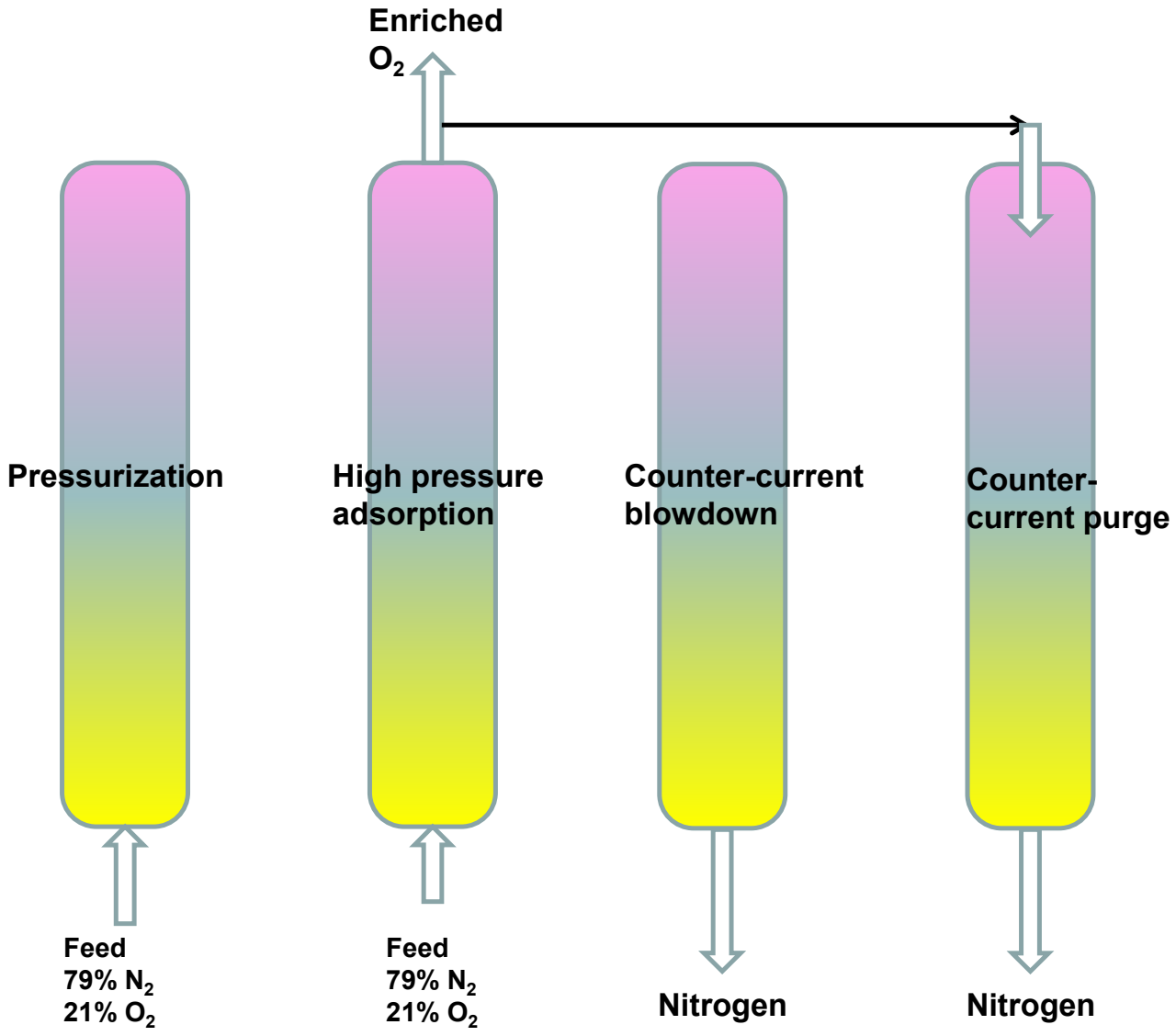

Figure S26. Different steps in the production of purified O_2 using an adsorbent such as LiLSX. The scheme shows the sequence of processing of a single bed in a multi-bed PSA scheme. Adapted from Ruthven and Farooq.[67]

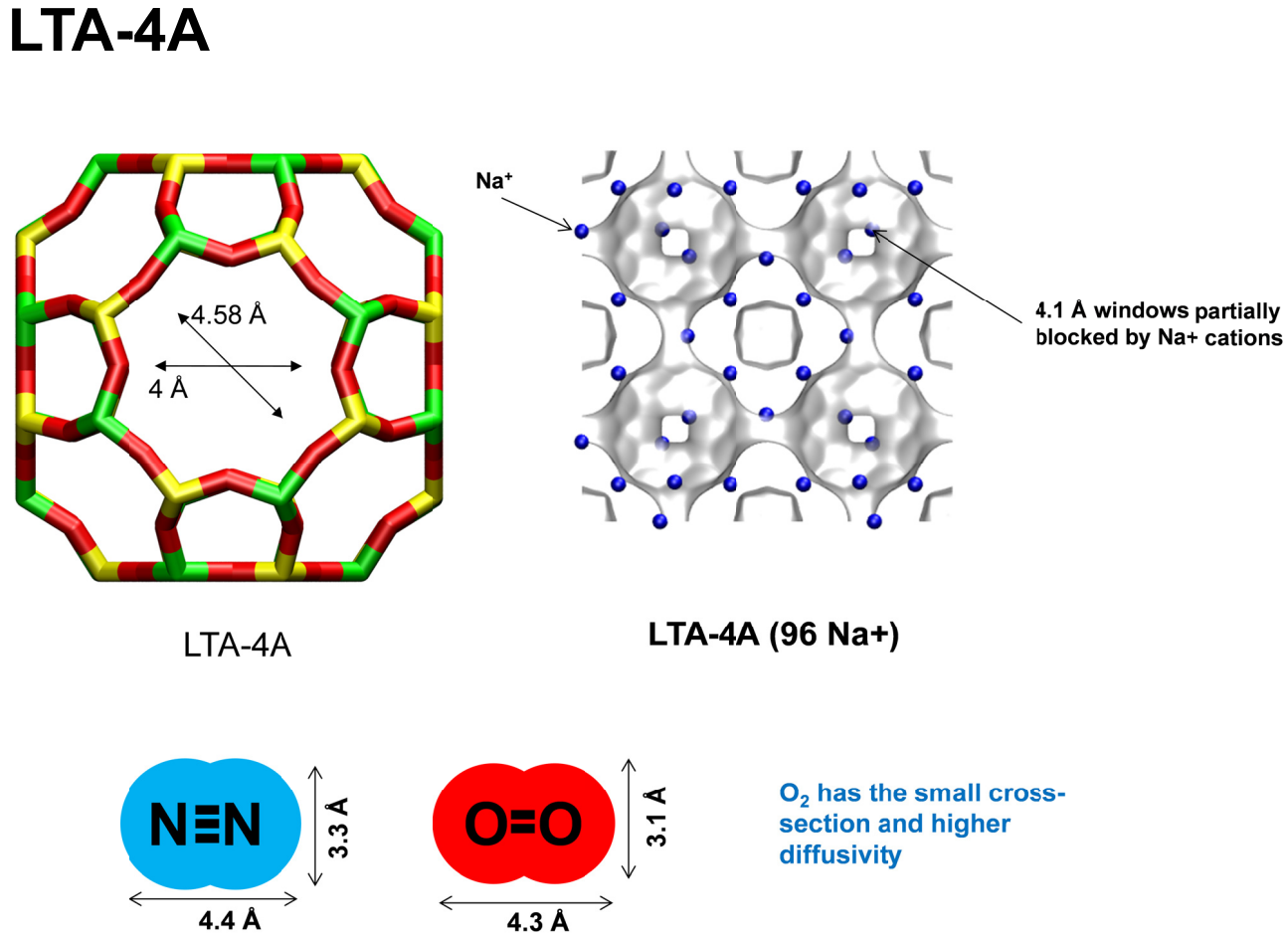

Figure S27. Partial blocking of the windows of LTA-4A zeolite.

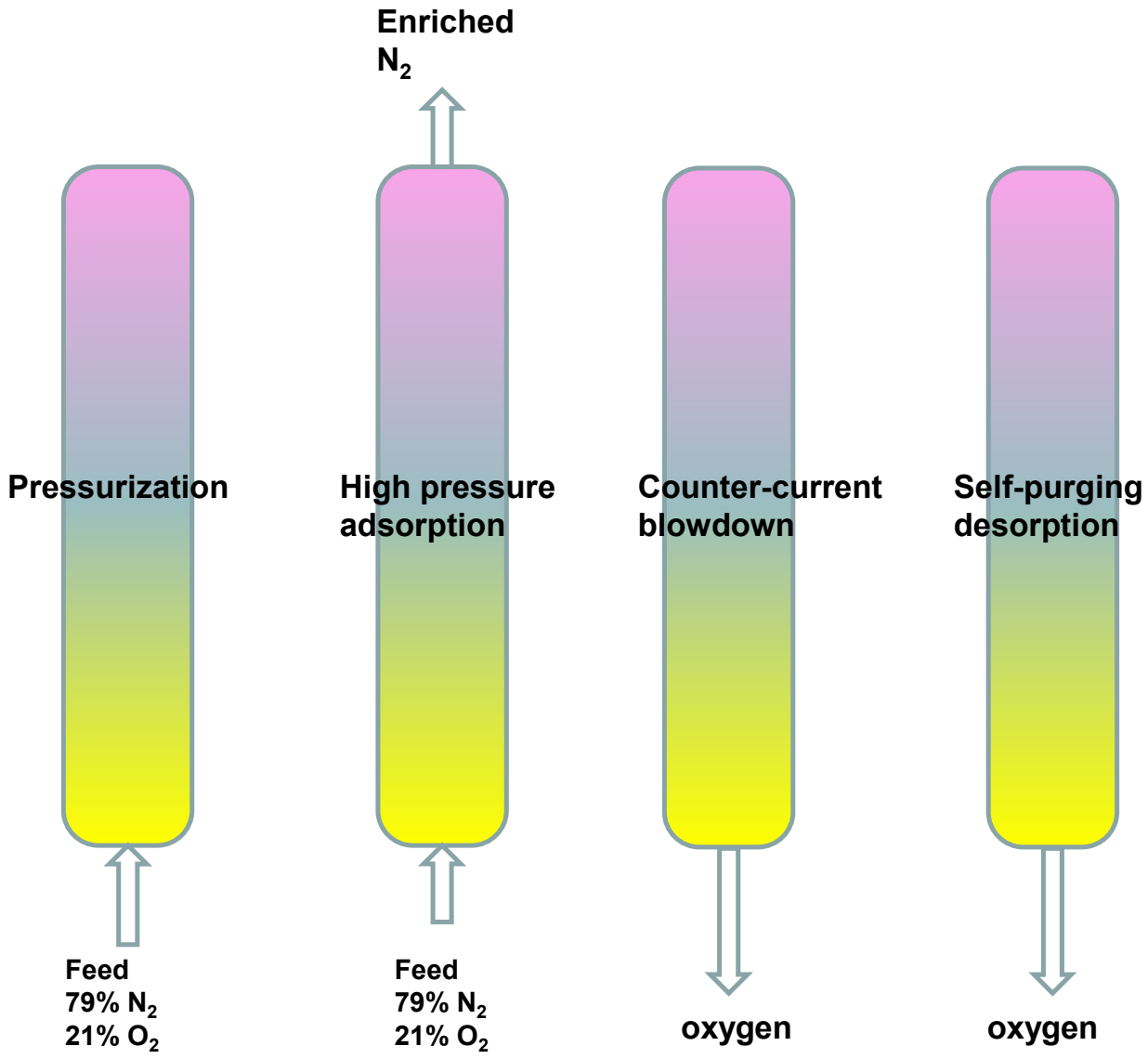

Figure S28. Different steps in the production of purified N_2 using an adsorbent such as LTA-4A, that relies on kinetic selectivity. The scheme shows the sequence of processing of a single bed in a multi-bed PSA scheme. Adapted from Ruthven and Farooq.[67]

10 Separation of C_2H_4/C_2H_6 and C_3H_6/C_3H_8 mixtures

Ethene is an important chemical used as feedstock in manufacture of polymers such as polyethene, polyvinyl chloride, polyester, polystyrene as well as other organic chemicals. Propene is mostly used to make polypropylene, which accounts for nearly two-thirds of global propylene consumption. Other outlets include acrylonitrile, propylene oxide, a number of alcohols, cumene and acrylic acid. Propene is a by-product from the steam cracking of liquid feedstocks such as naphtha and liquefied petroleum gas (LPG), as well as off-gases produced in fluid catalytic cracking (FCC) units in refineries.

Key processing steps in preparing feedstocks for polymer production are the separations of ethene/ethane, and propene/propane mixtures.

The boiling points are below ambient temperatures: ethane (184.5 K), ethene (169.4 K), propane (231.3 K), propene (226 K). Due to the small differences in the boiling points, the separations of ethene/ethane, and propene/propane mixtures have low relative volatilities, in the range of 1.1 – 1.2. These separations are traditionally carried out by distillation columns that operate at high pressures and low temperatures. The purity requirement of the alkenes as feedstocks to polymerization reactors is 99.95%, and consequently the distillation columns are some of the largest and tallest distillation columns used in the petrochemical industries with about 150 - 200 trays, and operating at reflux ratios of about 15. Distillation is energy intensive, and adsorptive separations offer an attractive, energy-efficient, alternative.

Figure S29(a,b,c) presents data on the polarizabilities, dipole moments, and quadrupole moments of C_2H_4, C_2H_6, C_3H_6, and C_3H_8. C_3H_8 has a significantly large dipole moment. Figure S30 and Figure S31 provide the molecular dimensions. Each of the unsaturated alkenes C_2H_4, and C_3H_6 possesses a pi-bond, and the preferential adsorption of the alkene from the corresponding alkane with the same number of C atoms can be achieved by choosing zeolitic adsorbents with extra-framework cations, or MOFs with

unsaturated "open" metal sites.[71] All of the atoms of C_2H_4 lie on the same plane (see Figure S30), and its dipole moment is zero; however it does possess a quadrupole moment.

It is to be noted that the polarizability of the alkane (C_2H_6, C_3H_8) is slightly higher than that of the corresponding alkene (C_2H_4, C_3H_6). The unary adsorption isotherms in ZIF-8, that does not contain extra-framework cations or unsaturated metal atoms show that the alkane is slightly more strongly adsorbed than the corresponding alkene.

Several microporous crystalline materials have potential for separation of ethene/ethane and propene/propane mixtures.[24, 71-75] With great potential for alkene/alkane separations are MOFs with coordinatively unsaturated metal centers that may be created by evacuation of frameworks that have metal-bound solvent molecules. This strategy has been employed to expose M^{2+} cation sites in M_2(dobdc) [M = Mg, Mn, Co, Ni, Zn, Fe; $dobdc^{4-}$ = 2,5- dioxido-1,4-benzenedicarboxylate]; these MOFs are also referred to as M-MOF-74 and CPO-27-M. Unsaturated alkynes, and alkenes such as C_2H_2, C_2H_4, and C_3H_6 can bind with Fe^{2+} of Fe_2(dobdc), with side-on attachment and π-coordination; [71, 76] see Figure S32. The capability of M_2(dobdc) for the technologically important separations of C_2H_2/C_2H_4, C_2H_4/C_2H_6, and C_3H_6/C_3H_8 mixtures has been established in laboratory studies.[71, 76] Other adsorbents that are also based on adsorption selectivity in favor of the unsaturated propene include: CuBTC,[77] LTA-4A zeolite,[73, 74] and NaX (= 13X) zeolite.[73, 75]

10.1 Separation of C_3H_6/C_3H_8 mixtures

An important disadvantage of the alkene/alkane separations with the adsorbents listed above is that the desired alkene product, required for production of polymer grade feedstock, can only be recovered in the desorption phase. As illustration, Figure S33 shows the experimental adsorption/desorption data of Bloch et al.[71] for separation of C_3H_6/C_3H_8 mixture using Fe_2(dobdc). In practice, it becomes necessary to operate with multiple beds involving five different steps; the C_3H_6 product of the desired purity is recovered in the final step by counter-current vacuum blowdown;[74, 75, 78] see Figure S34.

Separation of C2H4/C2H6 and C3H6/C3H8 mixtures

The recovery of high purity C_3H_6 product in the final vacuum blowdown step is expected to be enhanced if C_3H_8 is (almost) excluded during the high pressure adsorption cycle. Near-total exclusion of C_3H_8 is achievable by kinetically based separations using cage-type zeolites with 8-ring windows. Due to the small cross-section of the propene molecule (see Figure S31), kinetic separations, selective to propene, are possible using all-silica CHA zeolite. CHA zeolite (also named SiCHA), consists of cages of volume 316 Å^3, separated by 3.8 Å × 4.2 Å 8-ring windows; the pore landscape and structural details are provided in Figure S35, and Figure S36).[72, 79-81]

Ruthven and Reyes[81] compare the ratio of diffusivities of propene to that of propene in CHA with the corresponding values in DDR; see Figure S37. Their data show that CHA is the more effective sieve.

It is to be noted for LTA-4A zeolite,[73, 74] both mixture adsorption and diffusion favor propene, whereas with all-silica CHA zeolite, the adsorption equilibrium is in favor of propane, whereas diffusion favors propene.

Customized for C_3H_6/C_3H_8 separations, Cadiau et al.[82] report the synthesis of NbOFFIVE-1-Ni (= KAUST-7), that belongs to the same class of SIFSIX materials,[83] using pyrazine as the organic linker; see Figure S38a. The $(SiF_6)^{2-}$ pillars in the cage are replaced with somewhat bulkier $(NbOF_5)^{2-}$ pillars. This causes tilting of the pyrazine molecule on the linker, effectively reducing the aperture opening from 0.50 nm [with $(SiF_6)^{2-}$ pillars] to 0.30 nm. The small aperture permits ingress of the smaller C_3H_6 molecules, but practically excludes C_3H_8 on the basis of subtle differences in bond lengths, bond angles, molecular sizes and conformations (see Figure S31).

Figure S38b shows transient breakthrough simulations for the adsorption cycle for separation of 50/50 C_3H_6/C_3H_8 mixtures in fixed bed adsorbers packed with KAUST-7. The unary isotherms data are provided in Table S4. In the transient breakthrough simulations, the IAST was used to describe mixture adsorption equilibrium. These simulations also include intra-crystalline diffusional limitations; the Maxwell-Stefan diffusivities are chosen as: $Đ_1/r_c^2 = 1\times10^{-3}$ s^{-1}; $Đ_2/r_c^2 = 1\times10^{-5}$ s^{-1}; $Đ_1/Đ_2 = 100$.

Separation of C2H4/C2H6 and C3H6/C3H8 mixtures

The breakthrough simulation methodology is described in Chapter 4 Methodology for transient breakthrough simulations. In the simulations, we choose the mass of the adsorbent in the bed $m_{ads} = 180$ kg, cross-sectional area, A = 1 m^2; superficial gas velocity at the bed inlet, u_0 = 0.04 m s^{-1}; voidage of the packed bed, ε = 0.4. The framework density of KAUST-7 is $\rho = 1734$ kg m^{-3}. The length L of the adsorber bed is chosen as $L = \frac{1000}{\rho} \times 0.3 = 0.17301$ m.

Figure S38c compares the breakthrough performance of KAUST-7 with that of Ni_2(dobdc), Zn_2(dobdc), NaX, and LTA-5A using $\frac{\left(Q_0 = \text{flow rate L s}^{-1} \text{ at STP}\right) \times \left(\text{time in s}\right)}{\left(\text{kg MOF packed in tube}\right)} = \frac{Q_0 t}{m_{ads}} = \text{L kg}^{-1}$ as the x-axis. Due to the near total exclusion of C_3H_8 from the pores of KAUST-7, the achievement of the 99.95% C_3H_6 purity target during the final evacuation phase of the PSA cycle in Figure S34 is expected to be facilitated.

Due to the significantly lower diffusivity of C_3H_8, the desorption process is self-purging;[13, 67] Thus if the bed is simply closed at one end and left for a period of time, C_3H_6 will diffuse out first followed by C_3H_8. To underscore this point, Figure S39a presents transient breakthrough simulations for the desorption cycle for separation of 50/50 C_3H_6/C_3H_8 mixtures in fixed bed adsorbers packed with KAUST-7, operating at 298 K and 100 kPa total pressure. These simulations also include intra-crystalline diffusional limitations; the Maxwell-Stefan diffusivities are chosen as: $Đ_1/r_c^2 = 1\times10^{-3}$ s^{-1}; $Đ_2/r_c^2 = 1\times10^{-5}$ s^{-1}; $Đ_1/Đ_2 = 100$. The y-axis is the dimensionless concentrations at the exit of the fixed bed. We note that the desorption of the unsaturated alkene occurs much quicker than that of the saturated alkane. Figure S39b presents a comparison of the transient breakthrough simulations for desorption of 50/50 C_3H_6/C_3H_8 mixtures in fixed bed adsorbers packed with KAUST-7 using three different ratios of diffusivities are used $Đ_1/Đ_2$ = 1, 10, 100, while maintaining $Đ_1/r_c^2 = 1\times10^{-3}$ s^{-1}. The desorption of C_3H_8 is much slower for the scenario in which $Đ_1/Đ_2$ = 100; this implies that the amount of C_3H_6 of required purity will be higher.

From a material balance on the adsorber, the productivity of 99%+ pure C_3H_6 can be determined; the values are:

$Đ_1/Đ_2$ = 1; 99%+ pure C_3H_6 productivity = 15.7 L kg^{-1} at STP,

$Đ_1/Đ_2$ = 10; 99%+ pure C_3H_6 productivity = 18.9 L kg^{-1} at STP,

$Đ_1/Đ_2$ = 100; 99%+ pure C_3H_6 productivity = 24.3 L kg^{-1} at STP.

A detailed process design exercise, such as that reported by Khalighi et al.,[72, 78] will be required in order to compare the productivities of 99%+ pure C_3H_6 using KAUST-7 and other MOFs.

The productivities of 99%+ pure C_3H_6 of Ni_2(dobdc), Zn_2(dobdc), NaX, and LTA-5A are compared with that of KAUST-7 ($Đ_1/Đ_2$ = 100) with that of

10.2 Separation of C_2H_4/C_2H_6 mixtures

The recovery of purified alkene is much easier if the microporous adsorbent selectively adsorbs the saturated alkane. It is to be noted that the polarizability of the C_2H_6 is slightly higher than that of C_2H_4 due to the larger molar mass; see Figure S29. A number of microporous adsorbents such as $Fe_2(O_2)$(dobdc),[84] $Cu(Qc)_2$,[85] MUF-15,[86] PCN-250,[87] ZIF-7,[88, 89] ZIF-8,[9, 90] IRMOF-8,[91] Ni(bdc)$(ted)_{0.5}$,[92] MAF-49,[91] CPM-233,[93] and CPM-733[93] adsorb the saturated alkane selectively exploiting the differences in van der Waals interactions resulting from the higher polarizability of C_2H_6.

Figure S41a presents IAST calculations of the C_2H_6 uptake q_2 vs the separation selectivity S_{ads} of 90/10 C_2H_4/C_2H_6 mixture adsorption at 298 K and 100 kPa in four different MOFs. The hierarchy of separation selectivities is $Cu(Qc)_2$ > CPM-733 ≈ MUF-15 > CPM-233. However, due to the higher C_2H_6 uptake capacity of CPM-733, the separation potential, Δq, follows the hierarchy CPM-733 > CPM-233 > MUF-15 > $Cu(Qc)_2$. The separation potential of $Cu(Qc)_2$ is the lowest because it has the smallest C_2H_6 uptake. In order to verify the hierarchy of Δq determined from IAST, transient breakthrough simulations were carried out for CPM-733, CPM-233, MUF-15, and $Cu(Qc)_2$; see Figure S41b. The dimensionless concentrations at the exit of the packed bed is plotted as function of $Q_0 t/m_{ads}$.

Separation of C2H4/C2H6 and C3H6/C3H8 mixtures

During the interval indicated by the arrows, purified C_2H_4 can be recovered. The productivities follow the hierarchy CPM-733 > CPM-233 > MUF-15 > $Cu(Qc)_2$, that is in line with the hierarchy of Δq values. From the transient breakthrough simulations the amount of 99.95%+ pure C_2H_4 product recovered during the displacement intervals can be determined. The productivity values show a near-linear dependence on Δq; see Figure S41c.

10.3 List of Tables for Separation of C2H4/C2H6 and C3H6/C3H8 mixtures

Table S4. Dual-site Langmuir-Freundlich parameters for C_3H_6, and C_3H_8 in KAUST. These isotherm isotherm fit parameters were determined by scanning the experimental data at 298 K as reported in Figures 3b of Cadiau et al.[82] The unary isotherm data for C_3H_6, and C_3H_8 were fitted with the dual-site Langmuir-Freundlich isotherm model

$$q = q_{A,sat}\frac{b_A p^{\nu A}}{1+b_A p^{\nu A}} + q_{B,sat}\frac{b_B p^{\nu B}}{1+b_B p^{\nu B}}$$

The dual-site Langmuir-Freundlich parameters are

	Site A			Site B		
	$q_{A,sat}$ mol kg^{-1}	b_{A0} Pa$^{-\nu_A}$	ν_A dimensionless	$q_{B,sat}$ mol kg^{-1}	b_{B0} Pa$^{-\nu_B}$	ν_B dimensionless
C_3H_6	2	3.58-07	1.4	1	1E-07	1
C_3H_8	2.1	2.6E-05	1			

Table S5. Dual-site Langmuir-Freundlich parameters for C_3H_6/C_3H_8 in ZIF-67. These isotherm isotherm fit parameters were determined by scanning the experimental data at 273 K and 298 K as reported in Figures 2c of Andres-Garcia et al.[94]

The pure component isotherm data for C_3H_6, and C_3H_8 in ZIF-67, measured at 273 K, and 298 K by Andres-Garcia et al.[94] were fitted with the dual-site Langmuir-Freundlich isotherm model

$$q = q_{A,sat}\frac{b_A p^{\nu A}}{1+b_A p^{\nu A}} + q_{B,sat}\frac{b_B p^{\nu B}}{1+b_B p^{\nu B}}$$

with T-dependent parameters b_A, and b_B

$$b_A = b_{A0}\exp\left(\frac{E_A}{RT}\right); \quad b_B = b_{B0}\exp\left(\frac{E_B}{RT}\right)$$

The dual-site Langmuir-Freundlich parameters are

	Site A				Site B			
	$q_{A,sat}$ mol kg^{-1}	b_{A0} Pa$^{-\nu_A}$	E_A kJ mol^{-1}	ν_A dimensionless	$q_{B,sat}$ mol kg^{-1}	b_{B0} Pa$^{-\nu_B}$	E_B kJ mol^{-1}	ν_B dimensionless
C_3H_6	2.4	1.59E-09	20	1	3	1.17E-24	46	3.4
C_3H_8	2.6	7.64E-11	36	0.83	1.7	4.23E-20	52	2.5

10.4 List of Figures for Separation of C2H4/C2H6 and C3H6/C3H8 mixtures

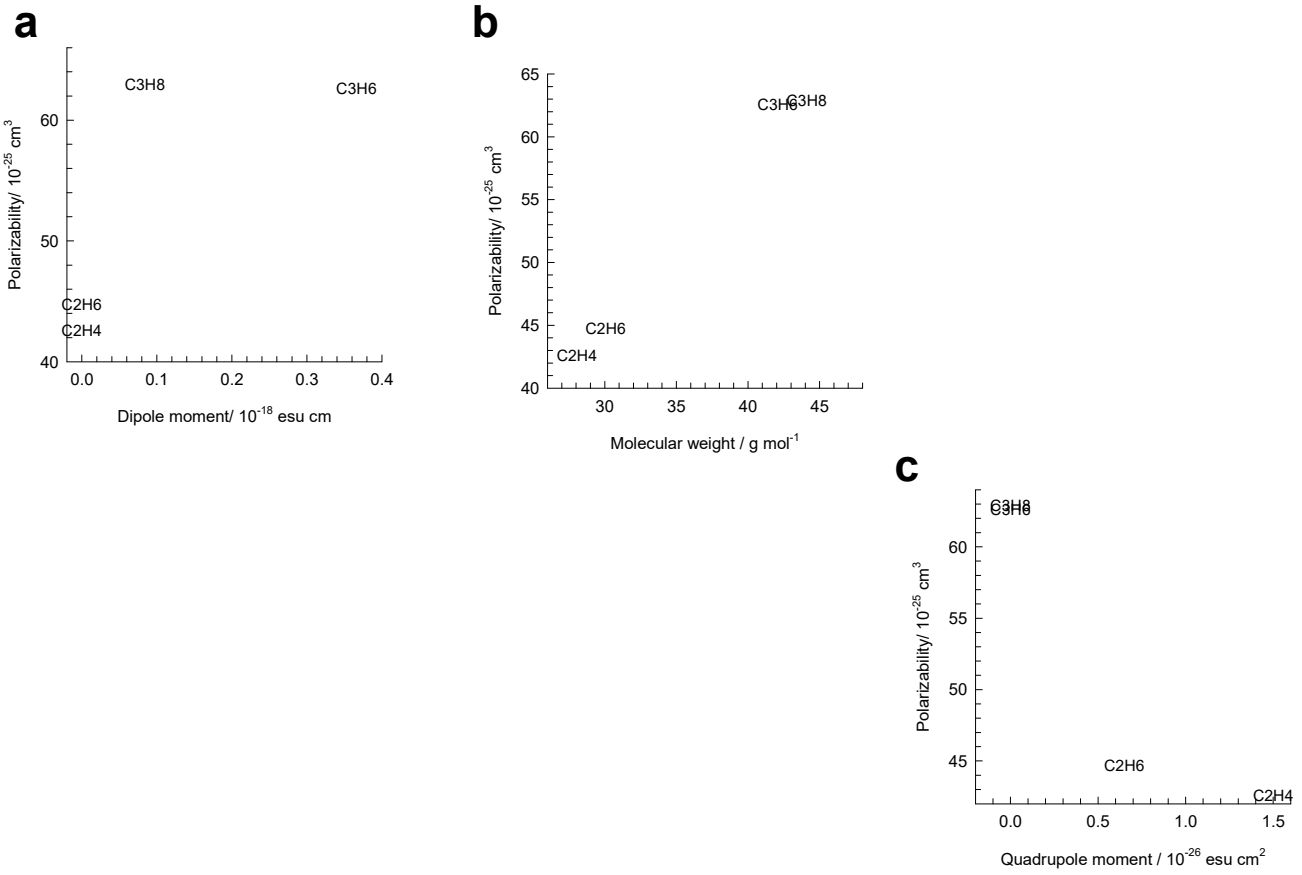

Figure S29. (a, b, c) Polarizabilities, dipole moments, and quadrupole moments of C_2H_4, C_2H_6, C_3H_6, and C_3H_8. The data are taken from Sircar and Myers.[4]

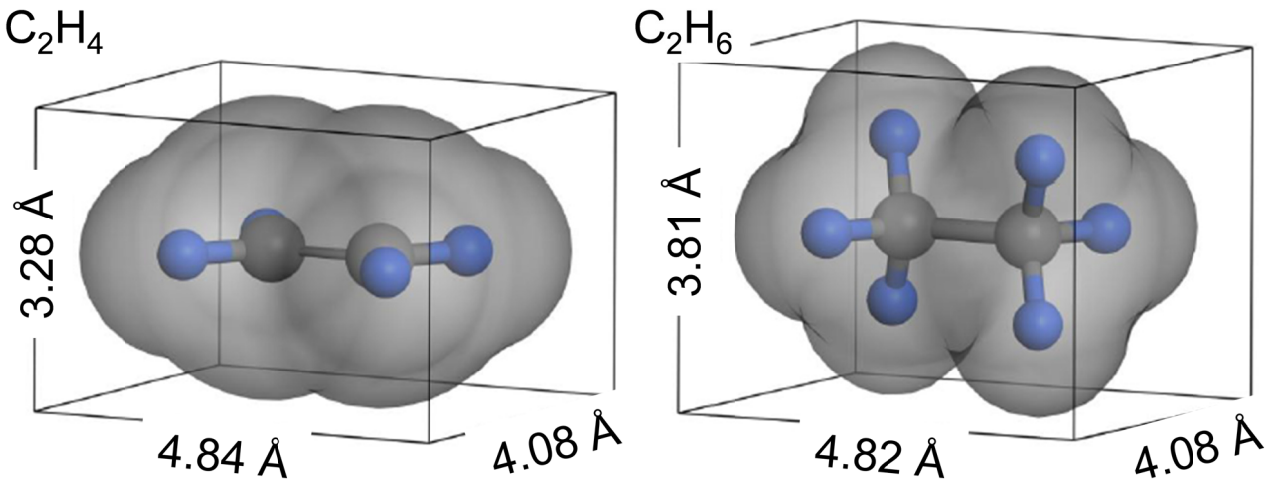

Figure S30. Bond lengths and molecular dimnesions for C_2H_4, and C_2H_6.

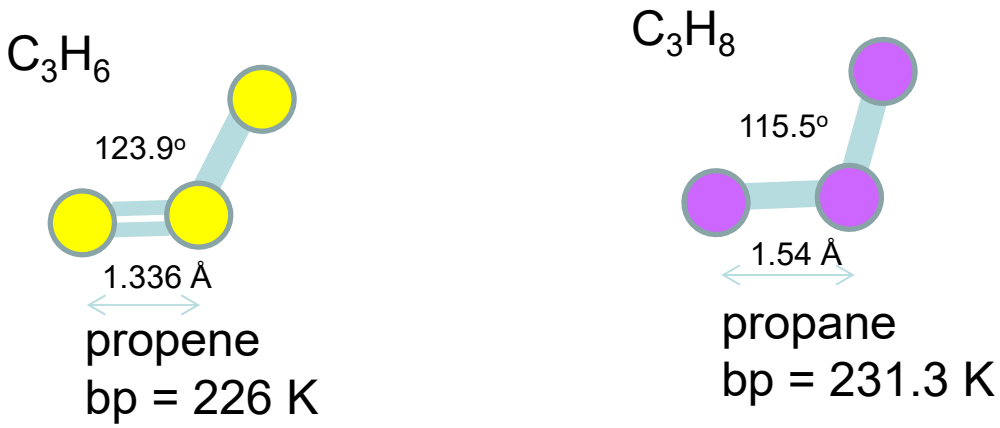

Figure S31. Bond lengths and molecular dimensions for C_3H_6, and C_3H_8.

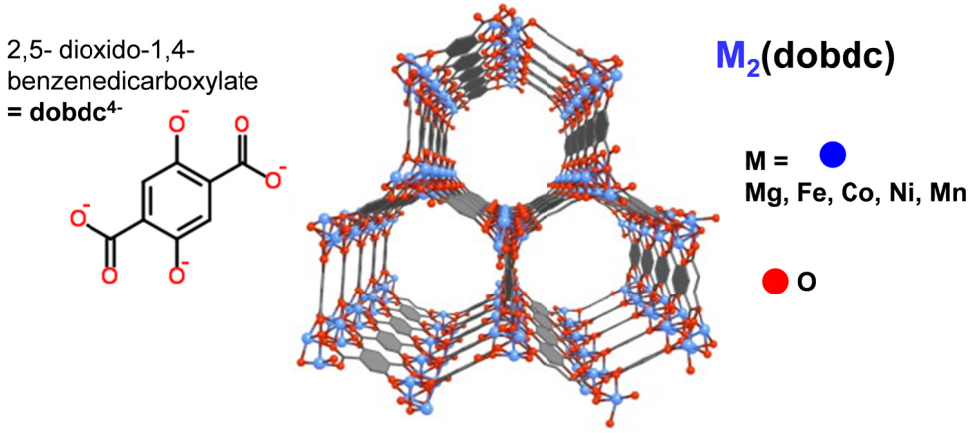

Interaction between the π orbital of the alkyne or alkene with the unsaturated M atoms

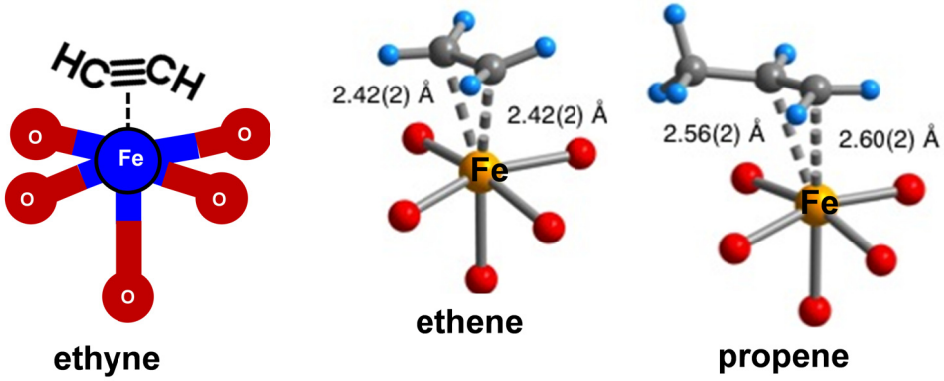

Figure S32. Unsaturated alkynes, and alkenes such as C_2H_2, C_2H_4, and C_3H_6 can bind with M^{2+} of M-MOF-74, with side-on attachment and π-coordination; [71] Adapted from Bloch et al.[71]

Separation of C2H4/C2H6 and C3H6/C3H8 mixtures

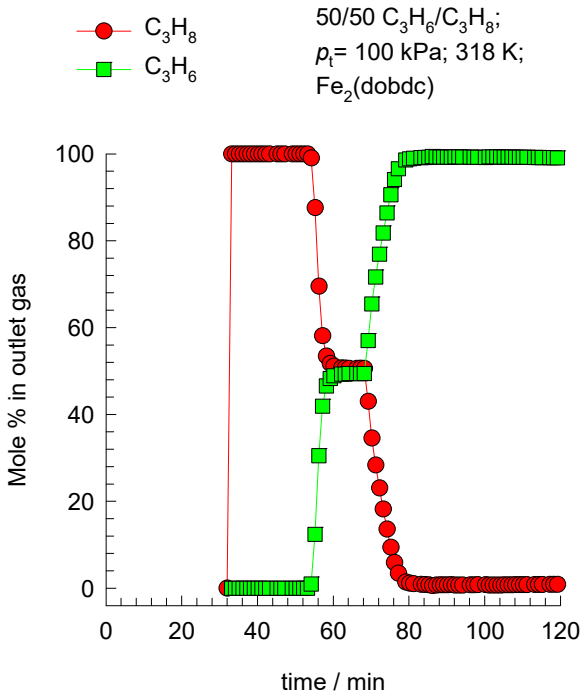

Figure S33. Experimental adsorption/desorption data of Bloch et al.[71] for separation of C_3H_6/C_3H_8 mixture using Fe_2(dobdc) at 318 K. The desorption is achieved by nitrogen purge.

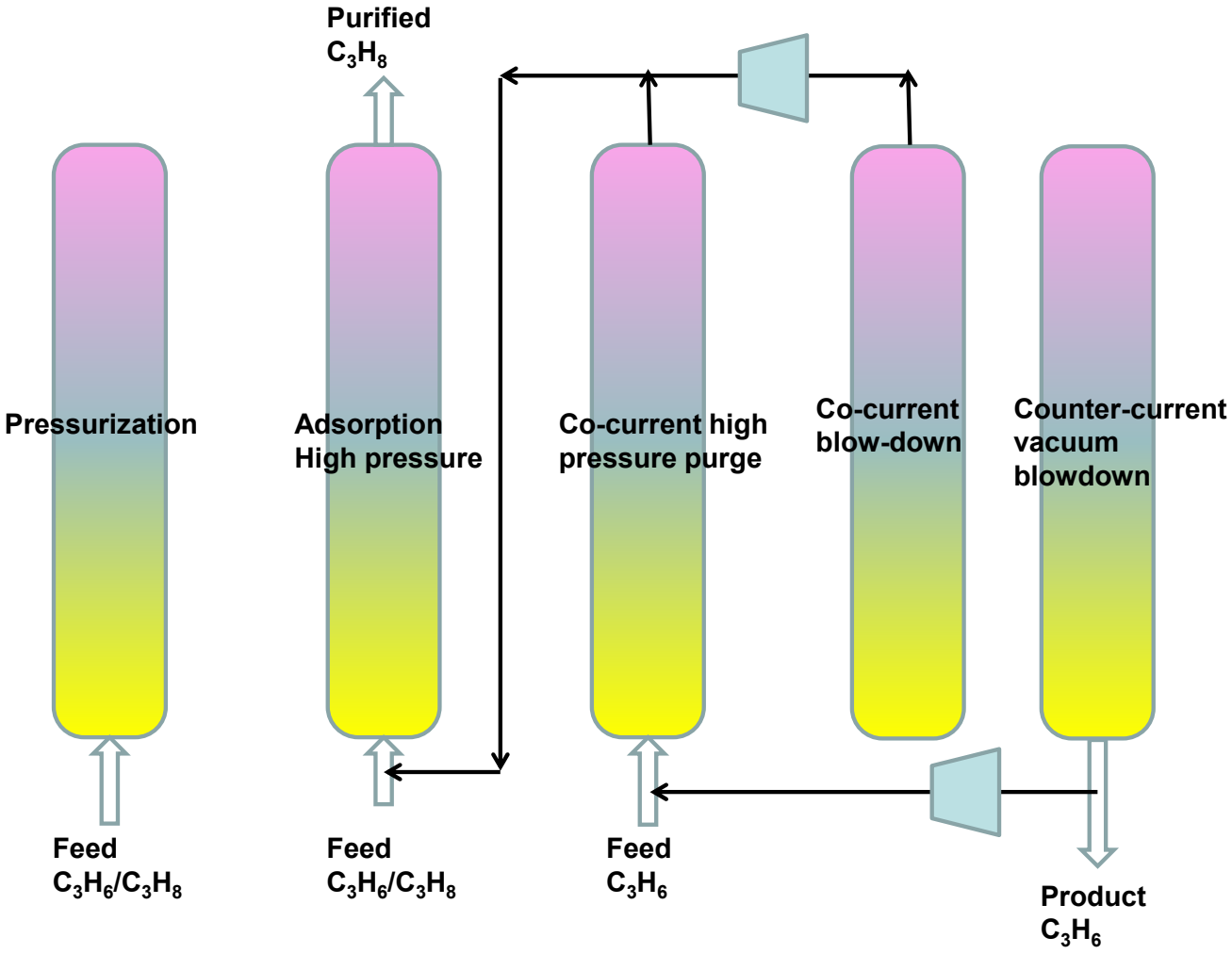

Figure S34. Five-step P(V)SA process for separating C_3H_6/C_3H_8 mixtures.[74, 75, 78]

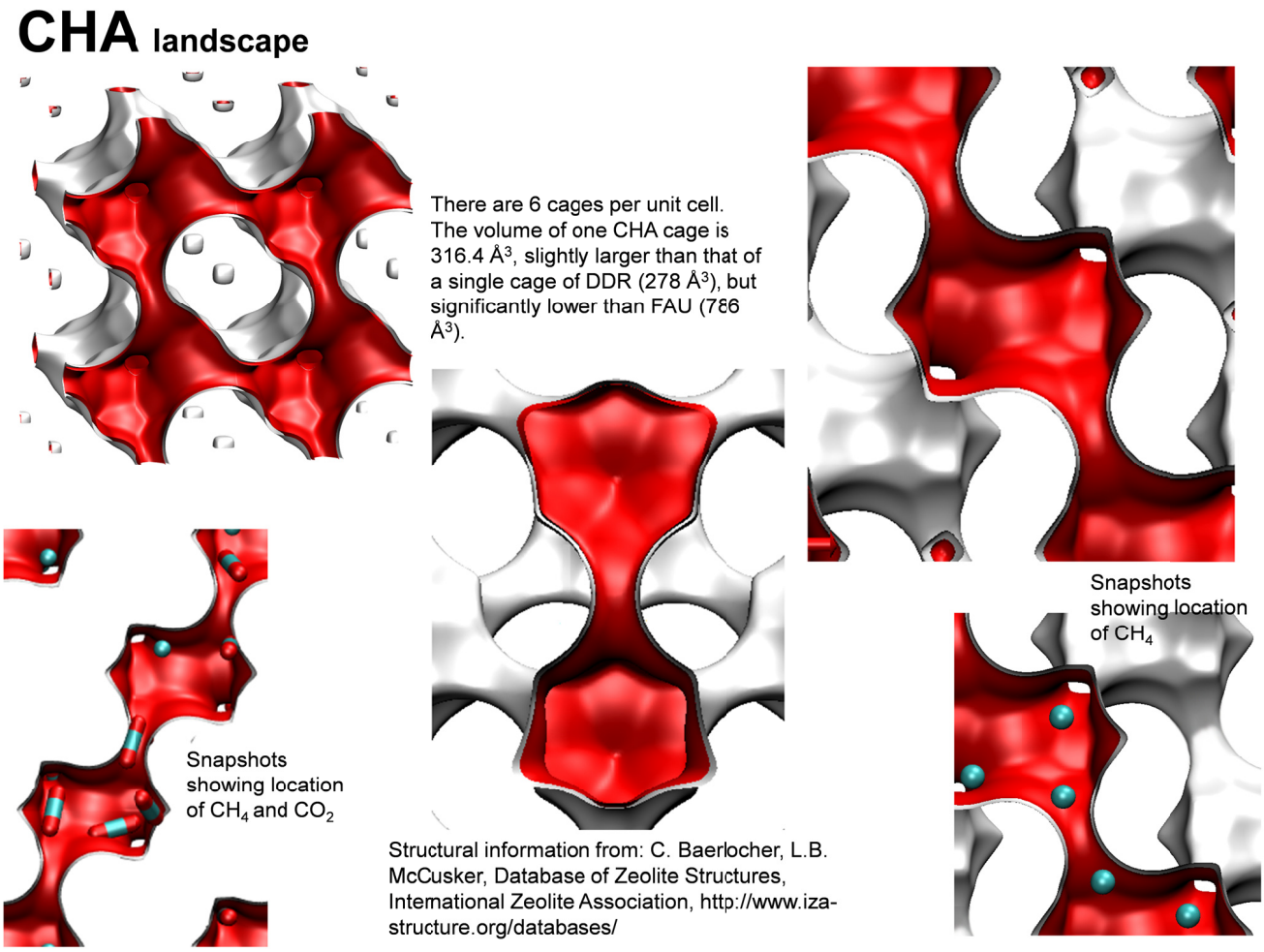

Figure S35. Pore landscape and structural details of all-silica CHA zeolite, also called SiCHA.

CHA window and pore dimensions

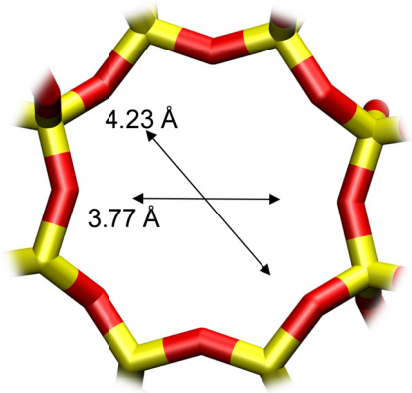

CHA

The window dimensions calculated using the van der Waals diameter of framework atoms = 2.7 Å are indicated above by the arrows.

	CHA
a /Å	15.075
b /Å	23.907
c /Å	13.803
Cell volume / Å^3	4974.574
conversion factor for [molec/uc] to [mol per kg Framework]	0.2312
conversion factor for [molec/uc] to [kmol/m^3]	0.8747
ρ [kg/m3]	1444.1
MW unit cell [g/mol(framework)]	4326.106
ψ, fractional pore volume	0.382
open space / Å^3/uc	1898.4
Pore volume / cm^3/g	0.264
Surface area /m^2/g	758.0
DeLaunay diameter /Å	3.77

Figure S36. Pore landscape and structural details of all-silica CHA zeolite, also called SiCHA.

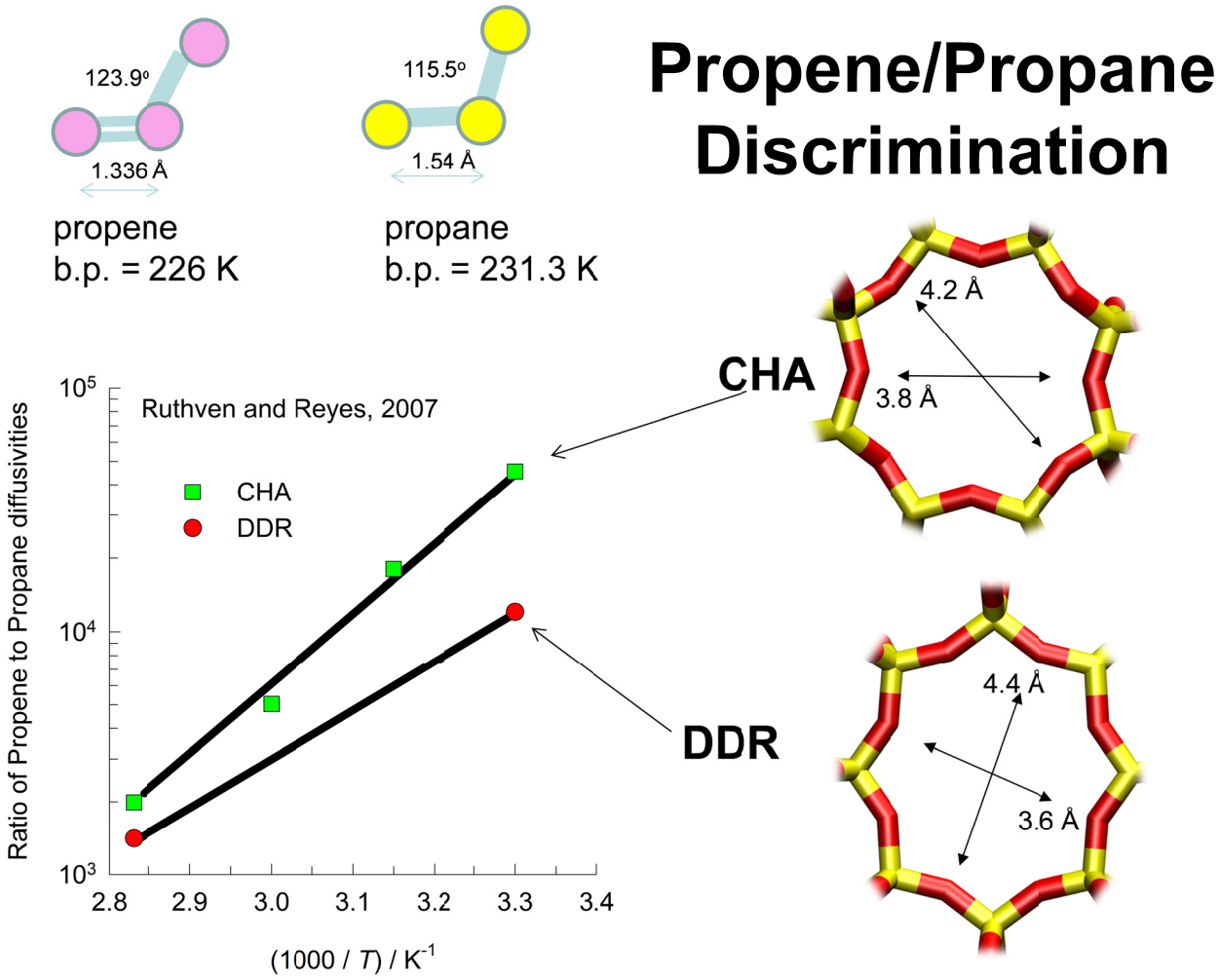

Figure S37. Data of Ruthven and Reyes[81] for the ratio of diffusivities of propene to that of propane in all-silica CHA and DDR zeolites.

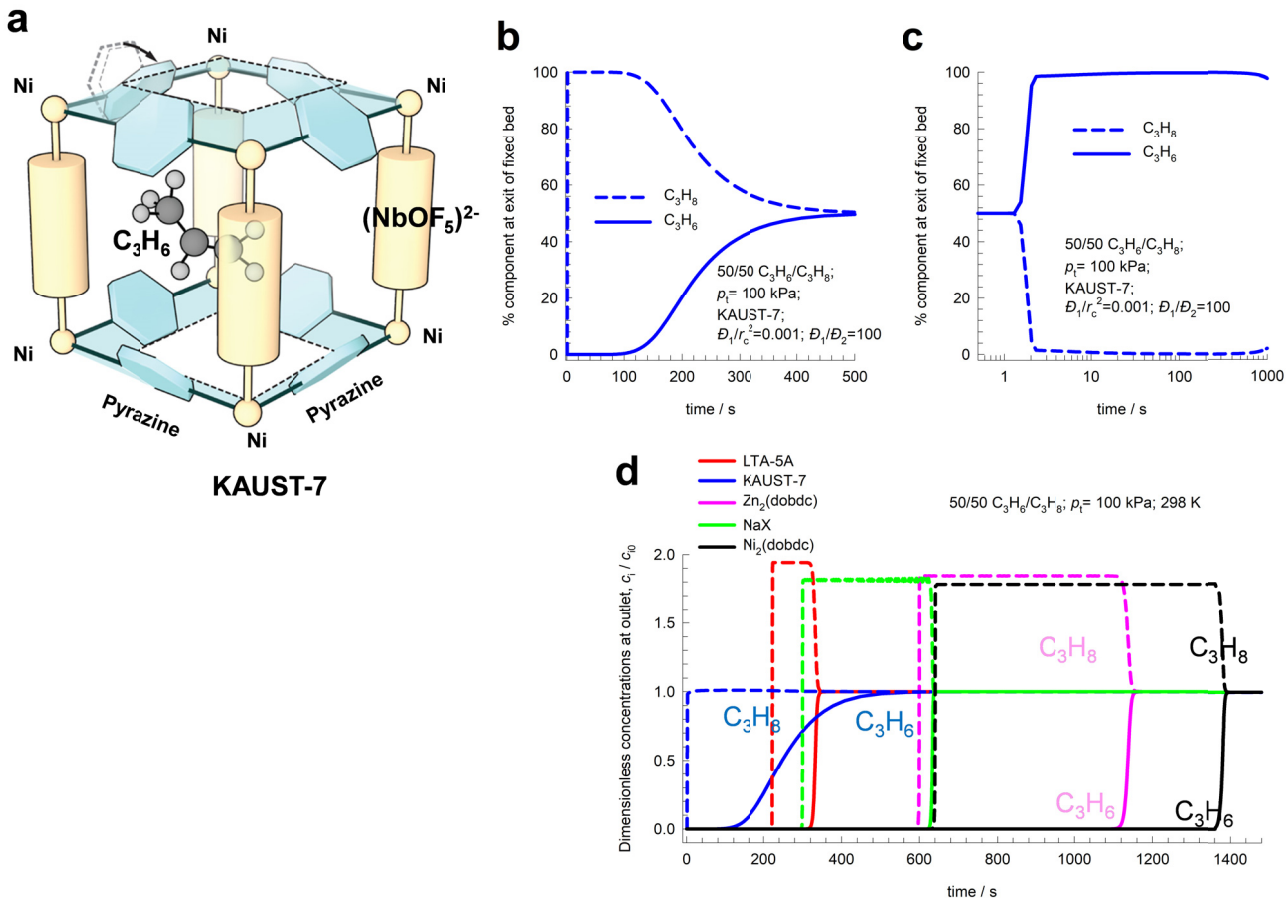

Figure S38. (a) Structure of NbOFFIVE-1-Ni (= KAUST-7), highlighting the C_3H_6 binding with $(NbOF_5)^{2-}$ anions. Adapted from Lin.[95] (b, c) Transient breakthrough simulations for the (b) adsorption, and (c) desorption cycles for separation of 50/50 C_3H_6/C_3H_8 mixtures in fixed bed adsorbers packed with KAUST-7, operating at 298 K and 100 kPa total pressure. The unary isotherms data used in the simulations are provided in Table S4. In the transient breakthrough simulations, the IAST was used to describe mixture adsorption equilibrium. (d) Comparison of the transient breakthrough simulations for separation of 50/50 C_3H_6/C_3H_8 mixtures in fixed bed adsorbers packed with KAUST-7, LTA-5A, NaX, Ni_2(dobdc) and Zn_2(dobdc) operating at 298 K and 100 kPa. The isotherm data for Ni_2(dobdc), and Zn_2(dobdc) are taken from Geier et al.[76] The isotherm data for LTA-5A, and NaX zeolites are taken from Divekar et al.[96]

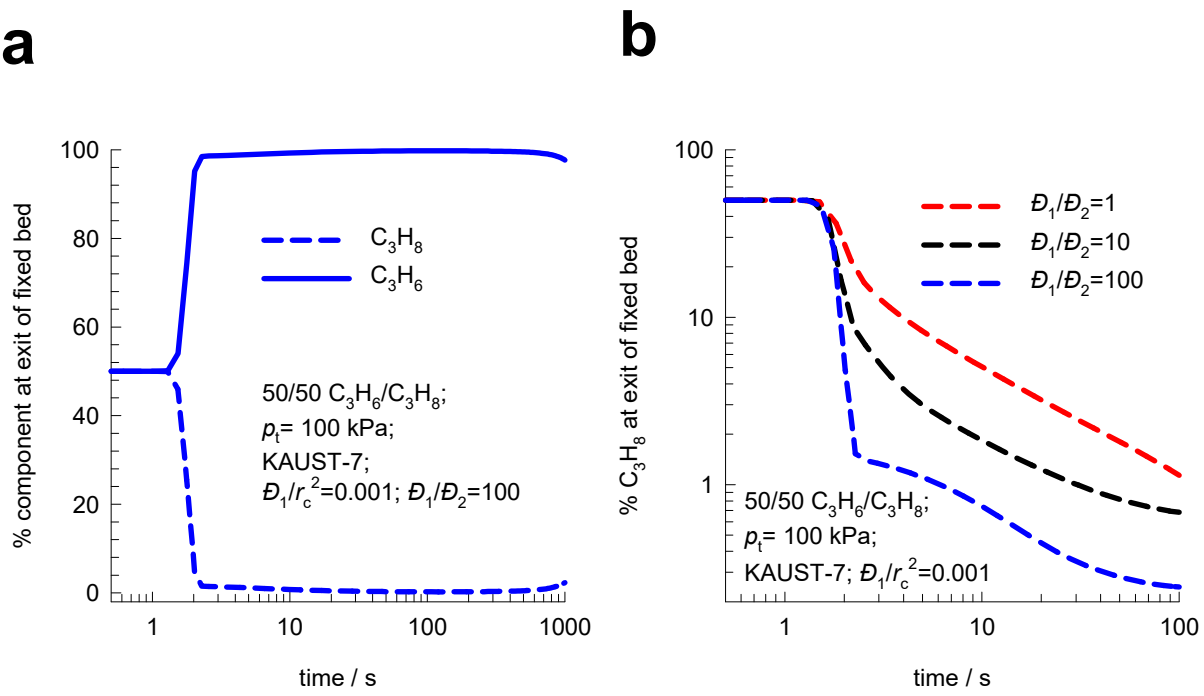

Figure S39. (a) Transient breakthrough simulations for the desorption cycle for separation of 50/50 C_3H_6/C_3H_8 mixtures in fixed bed adsorbers packed with KAUST-7, operating at 298 K and 100 kPa total pressure. The unary isotherms data used in the simulations are provided in Table S4. These simulations also include intra-crystalline diffusional limitations; the Maxwell-Stefan diffusivities are chosen as: $Đ_1/r_c^2 = 1\times10^{-3}$ s^{-1}; $Đ_2/r_c^2 = 1\times10^{-5}$ s^{-1}; $Đ_1/Đ_2 = 100$. The *y*-axis is the % component at the exit of the fixed bed. (b) Comparison of the transient breakthrough simulations for desorption of 50/50 C_3H_6/C_3H_8 mixtures in fixed bed adsorbers packed with KAUST-7; three different ratios of diffusivities are used $Đ_1/Đ_2 = 1$, 10, 100, while maintaining $Đ_1/r_c^2 = 1\times10^{-3}$ s^{-1}.

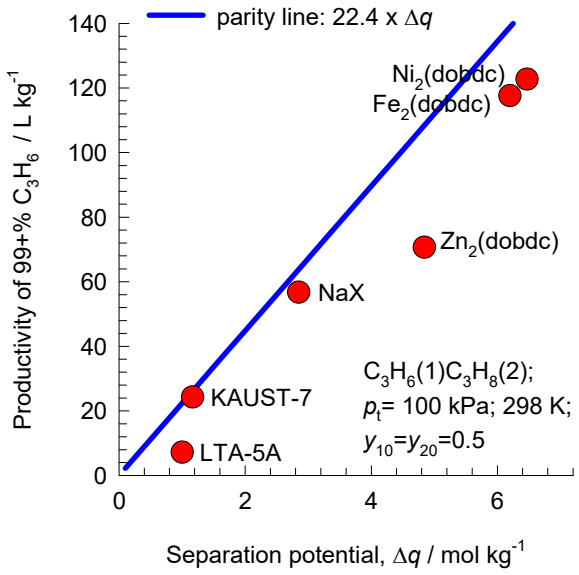

Figure S40. Productivities of 99%+ pure C_3H_6 obtained with Ni_2(dobdc), Zn_2(dobdc), NaX, and LTA-5A are compared with that of KAUST-7 ($Đ_1/Đ_2$ = 100) determined from transient breakthrough simulations, plotted as a function of the separation potential $\Delta q = q_1 - q_2 \frac{y_{10}}{y_{20}}$, where y_{10}, y_{20} are the mole fractions of the feed mixture during the adsorption cycle.

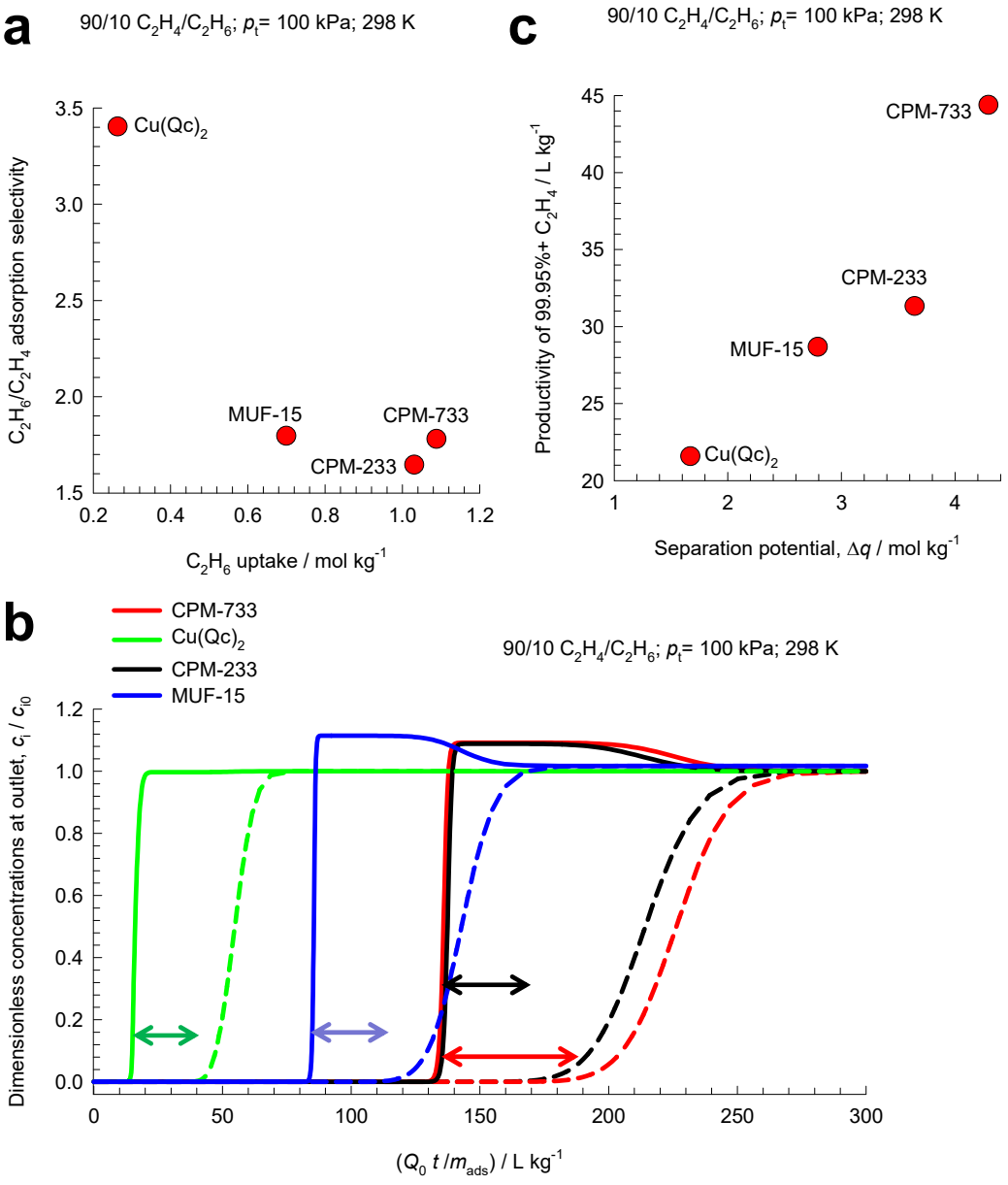

Figure S41. (a) IAST calculations of the C_2H_6 uptake q_2 vs the separation selectivity S_{ads} of 90/10 C_2H_4/C_2H_6 mixture adsorption at 298 K and 100 kPa in four different MOFs. (b) Transient breakthrough simulations for separation of 90/10 C_2H_4/C_2H_6 mixture adsorption at 298 K and 100 kPa in fixed beds packed with CPM-733, CPM-233, MUF-15, and $Cu(Qc)_2$. (c) Productivity of 99.95%+ pure C_2H_4 product recovered during the displacement intervals, plotted as function of the separation potential Δq. The unary isotherm data are taken from Yang et al.[93]

11 Separation of C_2H_2/C_2H_4 mixtures

In steam cracking of ethane to produce ethene, one of the by-products is ethyne, more commonly referred to as acetylene. Typically, the C_2H_2 content of C_2H_2/C_2H_4 feed mixtures is 1%. Ethyne has a deleterious effect on end-products of ethene, such as polyethene. Removal of ethyne from ethene streams is essential because the presence of ethyne at levels higher than 40 ppm will poison the catalyst used for polymerization of ethene. The selective removal of ethyne is conventionally carried out by absorption in dimethyl formamide (DMF). A typical processing scheme involves three steps: (1) acetylene absorption in a tray column, (2) stripping of ethene from the solvent DMF, and (3) DMF regeneration with recovery of ethyne. Selective C_2H_2 adsorption using microporous materials affords an energy-efficient alternative. For example, ethyne binds more strongly than C_2H_4, with side-on attachment and π-coordination, with Fe^{2+} of Fe_2(dobdc), with side-on attachment and π-coordination; [71, 76] see Figure S32.

Cui et al.[83] report a series of coordination networks composed of inorganic anions of $(SiF_6)^{2-}$ (hexafluorosilicate, SIFSIX), that offer potential for separation of C_2H_2/C_2H_4 mixtures. In these SIFSIX materials, two-dimensional (2D) nets of organic ligand (= pyridine) and metal (Cu, Ni, or Zn) node are pillared with $(SiF_6)^{2-}$ anions in the third dimension to form 3D coordination networks that have primitive cubic topology; see Figure S42.

Figure S42a shows the structure of SIFSIX-1-Cu (1 = 4,4'-bipyridene). The pore sizes within this family of materials can be systematically tuned by changing the length of the organic linkers, the metal node, and/or the framework interpenetration. Figure S42b shows the structure SIFSIX-2-Cu-i (2 = 4,4'-dipyridylacetylene, i = interpenetrated); in this case, each C_2H_2 molecule is bound by two F atoms from different nets. The binding of C_2H_4 with the F atoms is weaker because it is far less acidic than C_2H_2.

Figure S43a presents IAST calculations of the component loadings q_1, q_2, for 1/99 C_2H_2(1)/C_2H_4(2) mixture adsorption in SIFSIX-1-Cu, SIFSIX-2-Cu-i, SIFSIX-3-Zn, Mg_2(dobdc), and NOTT-300 at 298

K and 100 kPa. Figure S43b plots the separation potential $\Delta q = q_1 \frac{y_2}{y_1} - q_2$ vs adsorpton selectivity $S_{ads} = \frac{q_1/q_2}{y_1/y_2}$. SIFSIX-2-Cu-i has the combination of the highest C_2H_2 uptake capacity, q_1, along with the highest adsorption selectivity S_{ads}; consequently it has the highest separation potential Δq.

In order to confirm the highest separation potential of SIFSIX-2-Cu-i, transient breakthrough simulations were performed; in Figure S43c the dimensionless concentrations the exit of the fixed bed are plotted as function of $Q_0 t/m_{ads}$, where Q_0 is the volumetric flow rate of the gas mixture at the inlet to the fixed bed, expressed in $m^3\ s^{-1}$, at STP conditions. During the interval indicated by the arrows in Figure S43c, purified C_2H_4 can be recovered. Figure S44a plots the ppm C_2H_2 in the gas mixture at the outlet of the fixed bed, as a function of $Q_0 t/m_{ads}$. From a material balance on the adsorber, we can determine the productivity of purified C_2H_4, containing less than 40 ppm that can be expressed as m^3 C_2H_4 (at STP) per kg of adsorbent in the packed bed. This productivity is found to be a linear function of separation potential Δq; see Figure S44b. This confirms that the separation potential Δq is the appropriate metric for screening MOFs for C_2H_2/C_2H_4 mixture separations.

11.1 List of Figures for Separation of C2H2/C2H4 mixtures

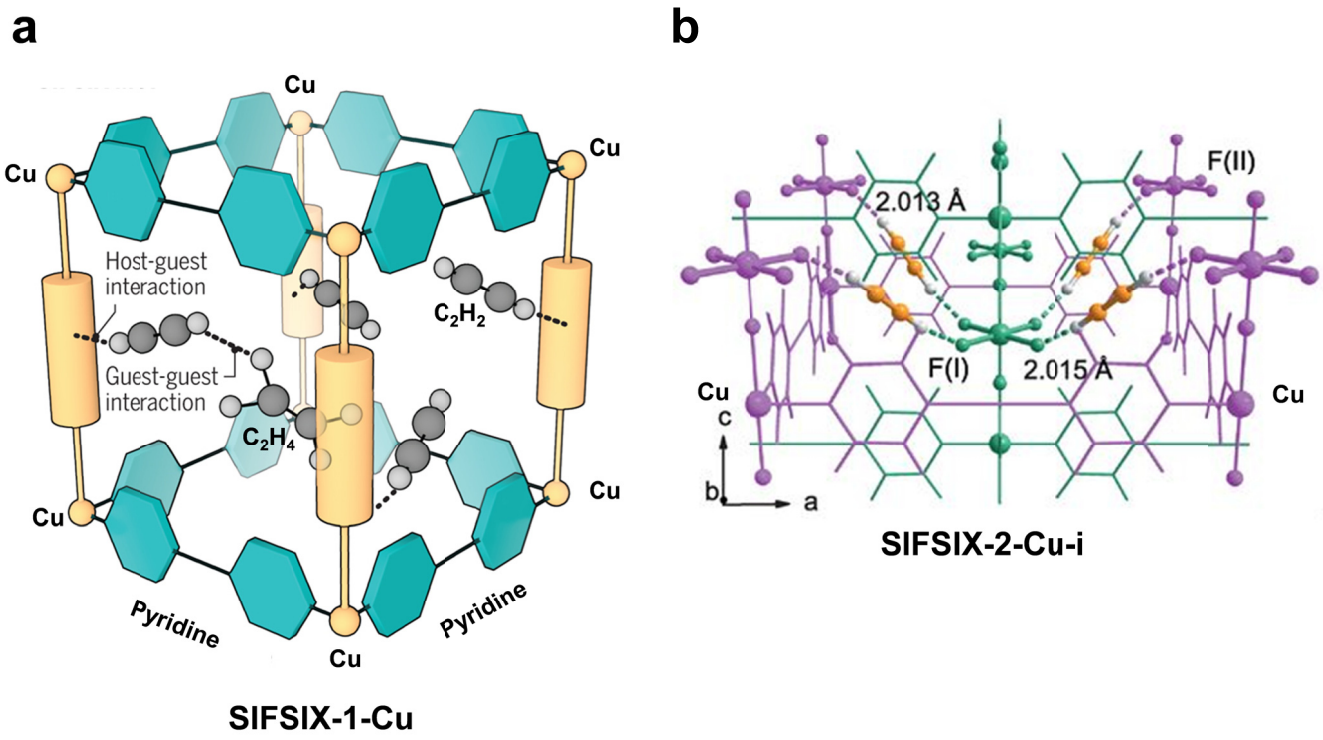

Figure S42. (a) Structures of (a) SIFSIX-1-Cu, and (b) SIFSIX-2-Cu-i, highlighting the C_2H_2 binding with $(SiF_6)^{2-}$ anions. Adapted from Lin [95] and Cui et al. [83]

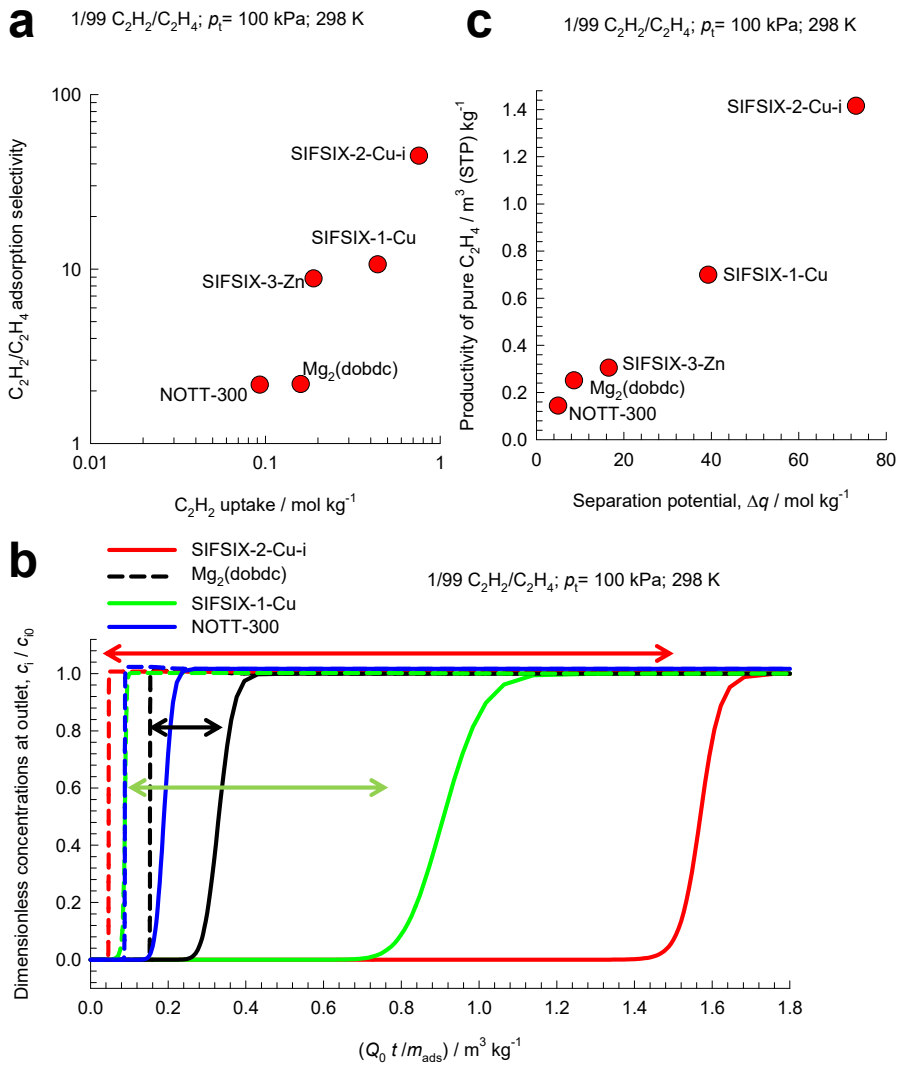

Figure S43. (a, b) IAST calculations of the (a) component loadings q_i, (b) separation potential Δq vs separation selectivity S_{ads} for 1/99 C_2H_2/C_2H_4 mixture adsorption at 298 K and 100 kPa in SIFSIX-1-Cu, SIFSIX-2-Cu-I, SIFSIX-3-Zn, Mg_2(dobdc), and NOTT-300. (a) Plot of the adsorption selectivity vs C_2H_2 uptake capacity. (b) Transient breakthrough simulations for 1/99 C_2H_2/C_2H_4 mixture adsorption at 298 K and 100 kPa in fixed bed packed with four different MOFs. The dimensionless concentrations the exit of the fixed bed are plotted as function of $Q_0 t / m_{ads}$, where Q_0 is the volumetric flow rate of the gas mixture at the inlet to the fixed bed, expressed in m^3 s^{-1}, at STP conditions.

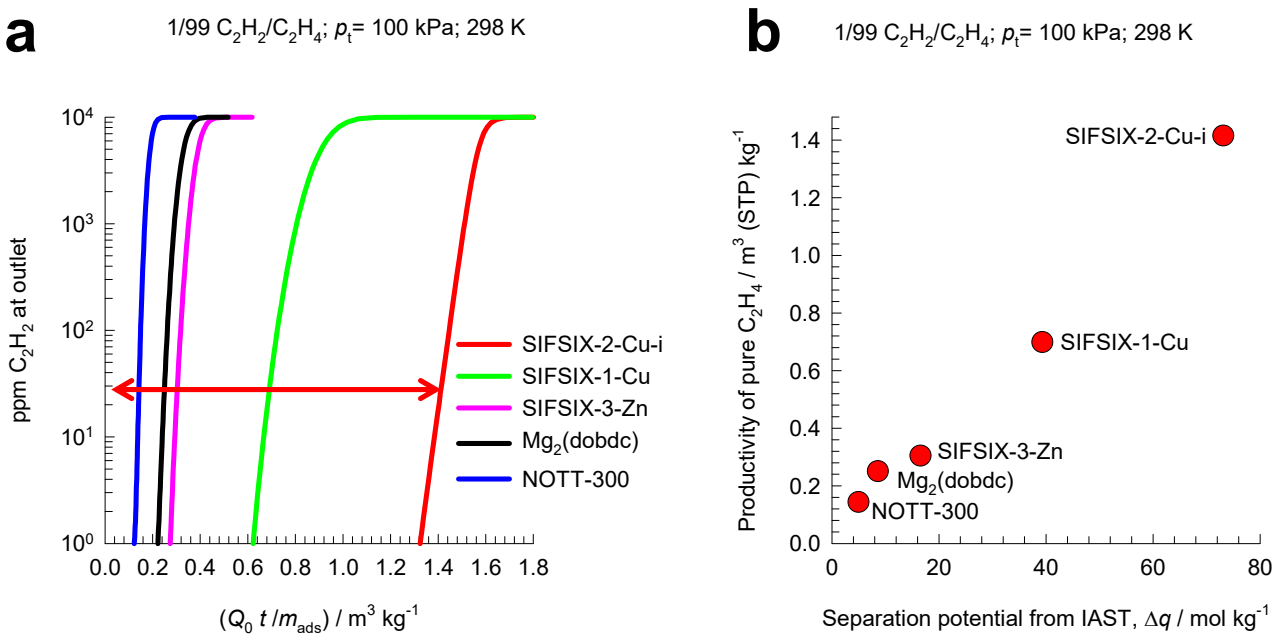

Figure S44. (a) Transient breakthrough simulations for 1/99 C_2H_2/C_2H_4 mixture adsorption at 298 K and 100 kPa in fixed bed packed with five different MOFs. The ppm C_2H_2 in the gas mixture at the outlet of the fixed bed, is plotted as a function of $Q_0 t/m_{ads}$, where Q_0 is the volumetric flow rate of the gas mixture at the inlet to the fixed bed, expressed in m^3 s^{-1}, at STP conditions. (b) Productivity of pure C_2H_4, containing less than 40 ppm C_2H_2, plotted as a function of the separation potential, Δq.

12 Separation of CO_2/CH_4 and CO_2/N_2 mixtures

We analyze a set of experimental breakthroughs for 50/50 CO_2/CH_4 mixtures in bed packed with Ni_2(dobdc) and Kureha carbon measured in the same set-up and reported by Chen et al.[97] and Yu et al.[98] The tube length, L =100 mm and the internal diameter, d = 4.65 mm; see schematic in Figure S45. The cross-sectional area of the tube, is $A = \frac{\pi}{4} d^2$. The volume of the empty tube, V, is $V = AL$. Let m_{ads} represent the mass of adsorbent packed into the tube. The volume occupied by the adsorbent crystalline material, V_{ads}, is $V_{ads} = \frac{m_{ads}}{\rho}$. A precisely determined mass of each adsorbent (Ni-MOF-74 pellet sample = 576.1 mg, and Kureha carbon = 760 mg) was filled into the column and then heated in flowing He with a rate of 20 ml (STP) min^{-1} at 423 K for 8 h prior to the breakthrough measurements. The breakthrough curves were then measured by switching the He flow to a flow containing CO_2 and CH_4 in He (used as a balance) with a CO_2:CH_4:He mole composition of 1:1:2 at a total flow rate of 8 mL (STP) min^{-1}. The partial pressures at the inlet are $p_1 = p_2$ = 100 kPa; p_3 = 200 kPa. As illustration, Figure S46 compares the experimental breakthroughs for CO_2(1)/CH_4(2)/He(3) in packed bed with Ni_2(dobdc), and Kureha carbon at 298 K. For comparing the breakthrough performance Ni_2(dobdc) and Kureha carbon, with different masses of adsorbent in the packed tube, it is appropriate to base the comparisons using the following parameter

$$\frac{\left(Q_0 = \text{flow rate L s}^{-1} \text{ at STP}\right) \times \left(\text{time in s}\right)}{\left(\text{kg MOF packed in tube}\right)} = \frac{Q_0 t}{m_{ads}} = \text{L kg}^{-1} \tag{S42}$$

as the x-axis.

For both materials, there is a finite time interval within which 99%+ pure CH_4 can be produced. For Ni_2(dobdc) it is possible to produce CH_4 with 99%+ purity during the time interval indicated by the arrow. A material balance for the time interval $t = t_1 - t_2$ allows us to determine the productivity of CH_4 with the specified 99%+ purity

Separation of CO2/CH4 and CO2/N2 mixtures

$$\text{CH}_4 \text{ productivity} = \frac{c_t Q_{He}}{m_{ads}} \int_{t_1}^{t_2} \left(\frac{y_{CH4,exit}}{y_{He,exit}} \right) dt \tag{S43}$$

The productivities of 99% pure CH_4 can be determined using an appropriate quadrature formula; the values are 5 mol kg^{-1} for Ni_2(dobdc) and 0.58 mol kg^{-1} for Kureha carbon.

Figure S47 compares the breakthroughs of 1:1:2 CO_2/CH_4/He and 1:1:2 CO_2/N_2/He mixtures at a total flow rate of 8 mL (STP) min^{-1} in a tube packed with Kureha carbon. Due to the higher CO_2/N_2 selectivities, the displacement interval during which purified N_2 can be recovered is larger than the interval during which 99% pure CH_4 is recovered. The productivities of 99% pure N_2 can be determined using an appropriate quadrature formula; the value are 1.9 mol kg^{-1}.

The gravimetric CO_2 uptake can be calculated from

$$\text{CO}_2 \text{ uptake} = \frac{c_t Q_{He}}{m_{ads}} \int_0^{t_{ss}} \left(\frac{y_{CO2,inlet}}{y_{He,inlet}} - \frac{y_{CO2,exit}}{y_{He,exit}} \right) dt - \frac{\left(c_t y_{CO2,exit}\right)}{m_{ads}} \left(AL - V_{ads} \right) \tag{S44}$$

Figure S48 presents the experimental breakthrough data of Li et al.[99] for CO_2/CH_4 mixtures in packed bed with Mg_2(dobdc) (= MgMOF-74), Co_2(dobdc) (= CoMOF-74), MIL-100(Cr), and Activated Carbon (AC) at 298 K. The *y*-axis represents the % CO_2, and CH_4 of in the exit gas phase. The partial pressures at the inlet are p_1 = 40 kPa; p_2 = 60 kPa; p_t = 100 kPa. The total flow rate of the gas mixture at the inlet is 30 mL min^{-1} (at STP). The continuous solid lines are the shock wave model, adjusting the breakthrough times to match the experiments. The masses of the adsorbents in the packed tube are not same, and therefore the *x*-axis is $\frac{\left(Q_0 = \text{flow rate L s}^{-1} \text{ at STP}\right) \times \left(\text{time in s}\right)}{\left(\text{kg MOF packed in tube}\right)} = \frac{Q_0 t}{m_{ads}} = \text{L kg}^{-1}$ in Figure S49a. For each of the four materials, there is a displacement interval during which purified CH_4 can be recovered. The productivities follow the hierarchy Mg_2(dobdc) > Co_2(dobdc) > MIL-100(Cr) > AC. Figure S49b presents a plot of the productivity of 95%+ pure CH_4 as function of the separation potential Δq. The 95%+ pure CH_4 productivities follow the same hierarchy as the Δq values, indicating that the separation potential can be used for screening purposes.

Separation of CO2/CH4 and CO2/N2 mixtures

12.1 List of Figures for Separation of CO2/CH4 and CO2/N2 mixtures

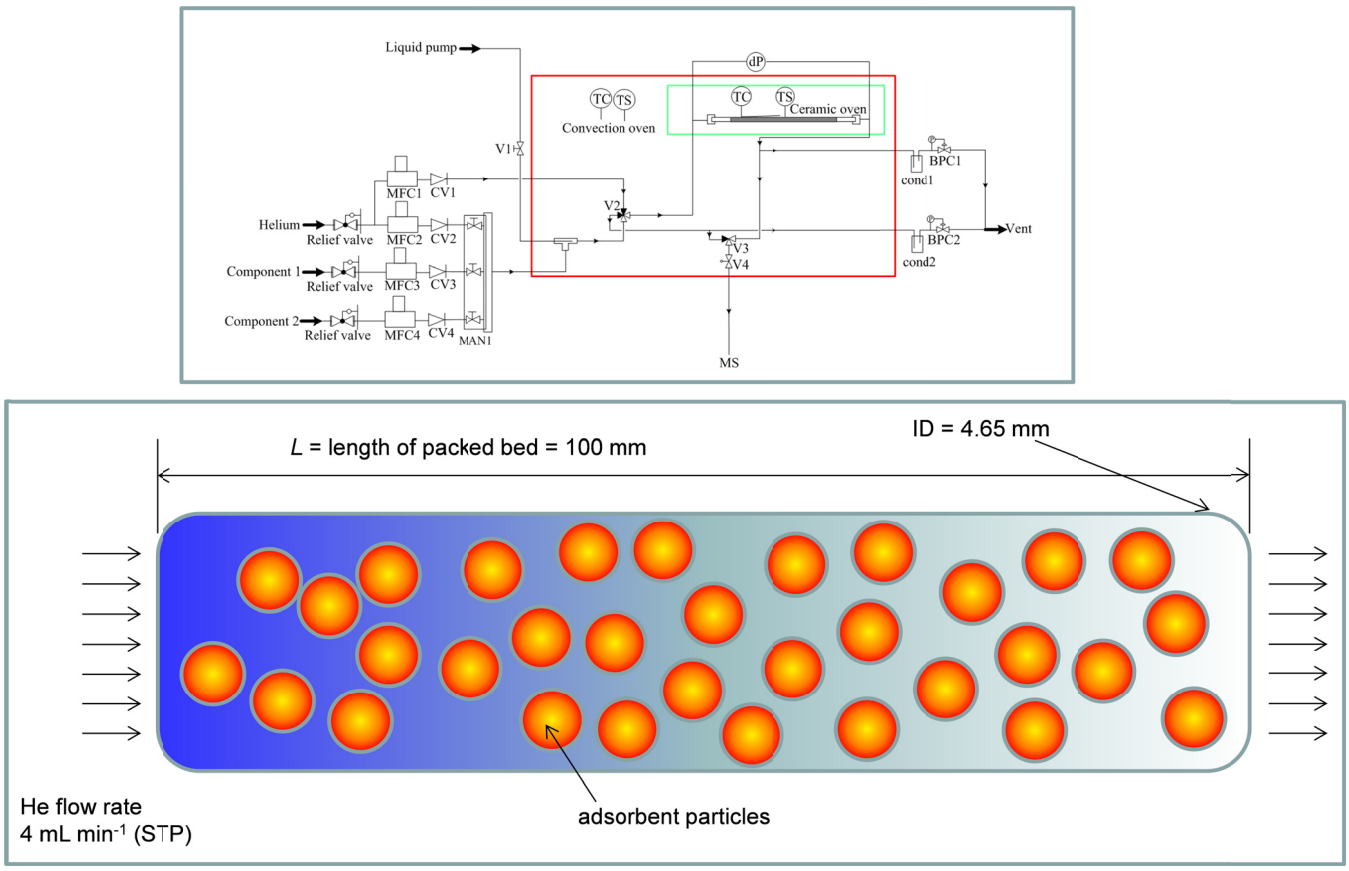

Figure S45. Schematic of the breakthrough tube. The tube diameter is 4.65 mm, and tube length L = 100 mm. The mass of adsorbent used in the bed is: Ni_2(dobdc) = 576.1 mg, and Kureha carbon = 760 mg. The gas phase used in the experiments consisted of CO_2/CH_4/He mixtures. The gas phase compositions at the inlet were maintained at 25/25/50.The flow rate of He was maintained constant at 4 mL min^{-1} at STP conditions.

Separation of CO2/CH4 and CO2/N2 mixtures

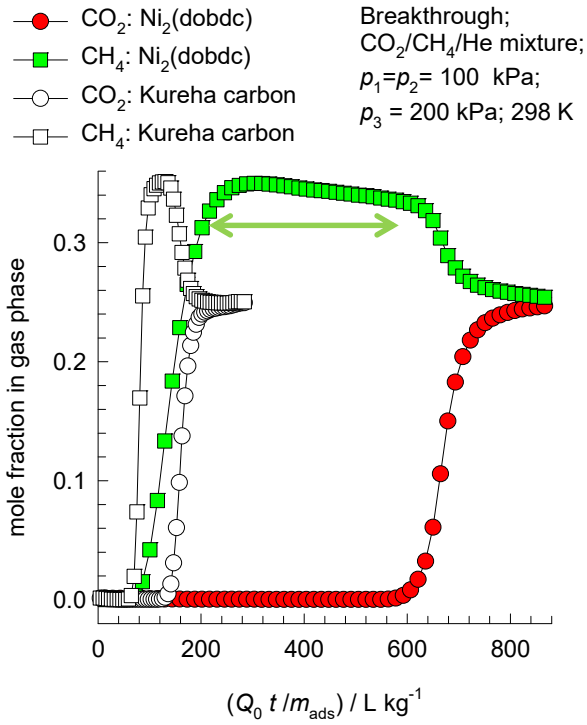

Figure S46. Experimental breakthroughs of Chen et al.[97] and Yu et al.[98] for CO_2(1)/CH_4(2)/He(3) mixtures in packed bed with Ni_2(dobdc), and Kureha carbon at 298 K, plotted as a function of $Q_0 t/m_{ads} = \text{L kg}^{-1}$. The partial pressures at the inlet are $p_1 = p_2 = 100$ kPa; $p_3 = 200$ kPa. The *y*-axis represents the mole fractions of CO_2 and CH_4 in the exit gas phase; the mole fraction of He is not plotted.

Separation of CO2/CH4 and CO2/N2 mixtures

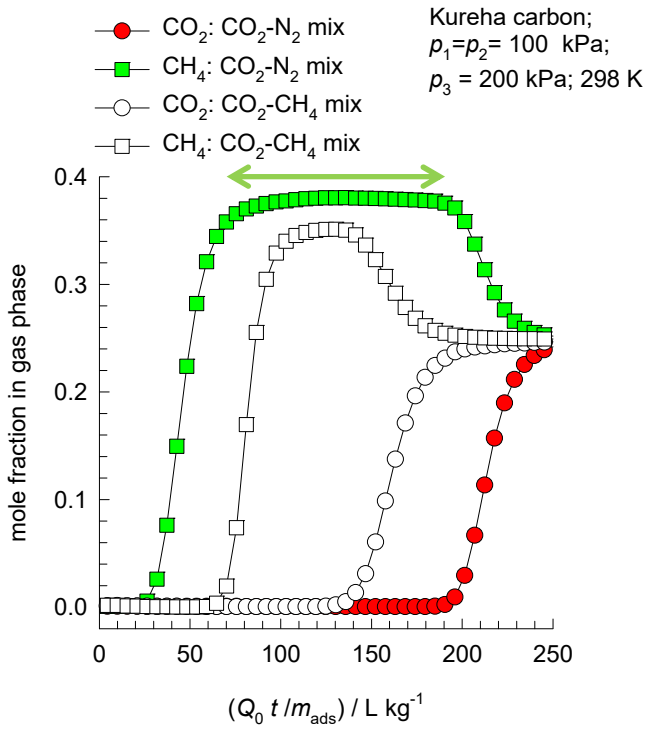

Figure S47. Experimental breakthroughs of Yu et al.[98] for $CO_2(1)/CH_4(2)/He(3)$ and $CO_2(1)/N_2(2)/He(3)$ mixtures in packed bed with Kureha carbon at 298 K, plotted as a function of $Q_0 t/m_{ads} = \text{L kg}^{-1}$. The partial pressures at the inlet are $p_1 = p_2 = 100$ kPa; $p_3 = 200$ kPa. The y-axis represents the mole fractions of CO_2 and CH_4 (or N_2) in the exit gas phase; the mole fraction of He is not plotted.

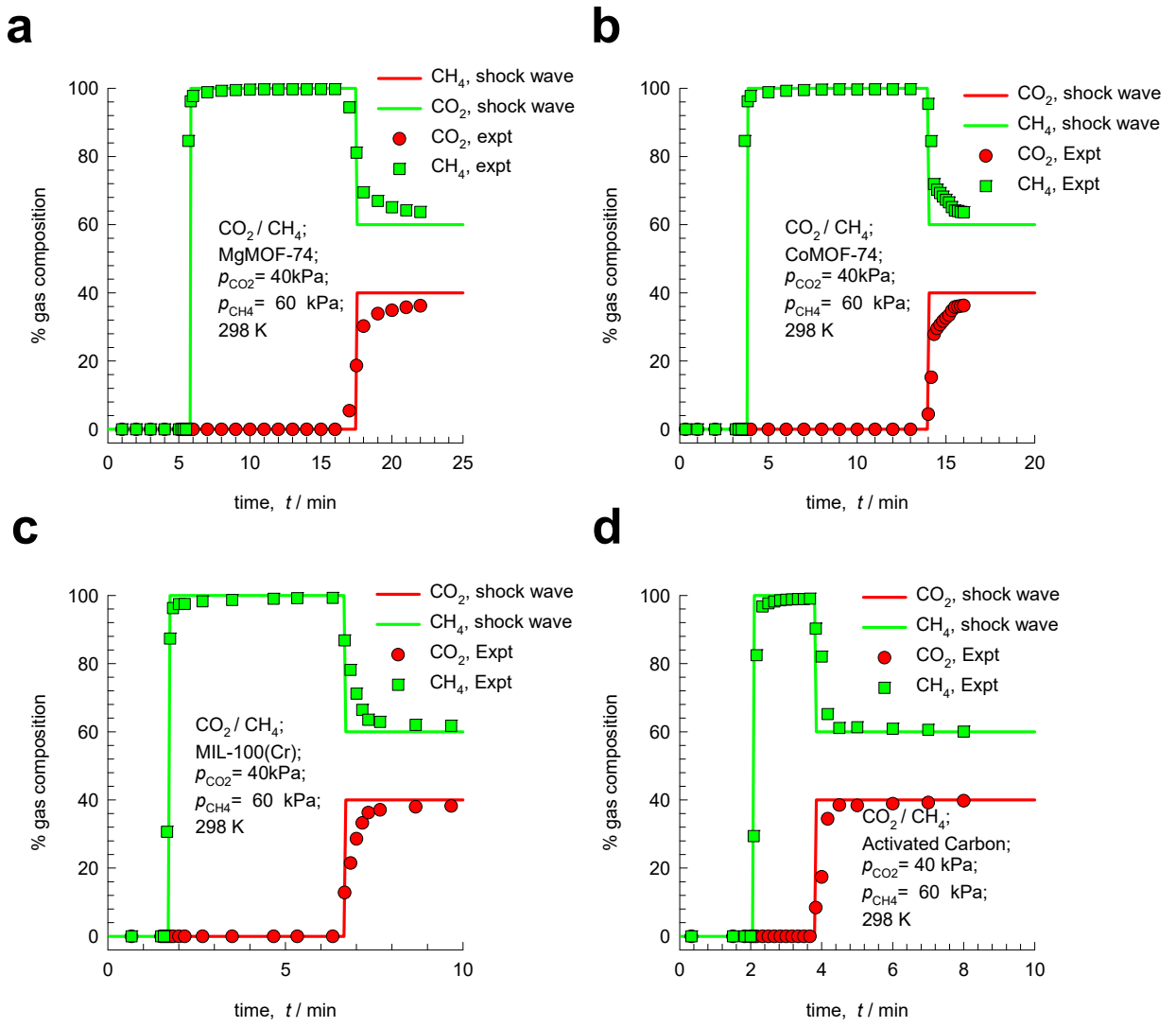

Figure S48. (a, b, c, d) Experimental breakthroughs for CO_2/CH_4 mixtures in packed bed with (a) Mg_2(dobdc) (= MgMOF-74), (b) Co_2(dobdc) (= CoMOF-74), (c) MIL-100(Cr), and (d) Activated Carbon (AC) at 298 K. The *y*-axis represents the % CO_2 and CH_4 in the exit gas phase. The continuous solid lines are the calculations using the shock wave model. The partial pressures at the inlet are $p_1 = 40$ kPa; $p_2 = 60$ kPa; $p_t = 100$ kPa. The flow rate of the gas mixture at the inlet is Q_0 =30 mL min^{-1} at STP.

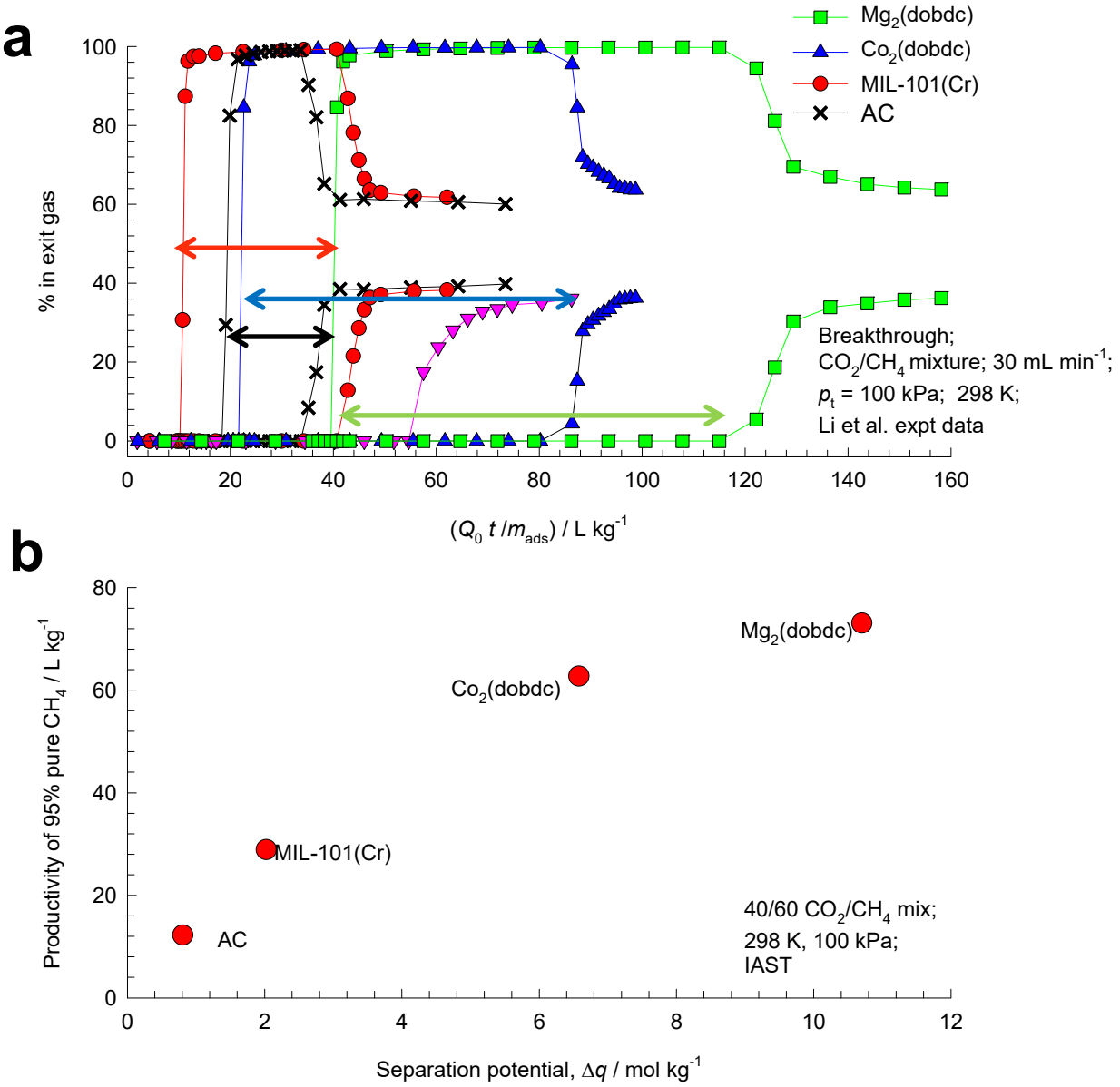

Figure S49. (a) Experimental breakthroughs for CO_2/CH_4 mixtures in packed bed with Mg_2(dobdc), Co_2(dobdc), MIL-100(Cr), and Activated Carbon (AC) at 298 K. The partial pressures at the inlet are p_1 = 40 kPa; p_2 = 60 kPa; p_t = 100 kPa. The experimental data, indicated by the symbols are from Li et al.[99] The % CO_2 and CH_4 in the exit gas phase are plotted as a function of $Q_0 t/m_{ads}$ = L kg^{-1}. (b) Productivity of 95% pure CH_4 plotted as function of the separation potential.

13 Separation of hexane isomers

13.1 Background on hexane isomers separation

The separation of hexane isomers, n-hexane (nC6), 2-methylpentane (2MP), 3-methylpentane (3MP), 2,2 dimethylbutane (22DMB), and 2,3 dimethylbutane (23DMB) is required for production of high-octane gasoline. The values of the Research Octane Number (RON) increases with the degree of branching; Table S6 lists the Research Octane Numbers (RON) of C6 alkanes.[100] The di-branched isomers (22DMB, 23DMB) have significantly higher RON values than that of the linear isomer (nC6), and mono-branched isomers (2MP, 3MP). The RON values are: nC6 = 30, 2MP = 74.5, 3MP = 75.5, 22DMB = 94, 23DMB = 105. Therefore, di-branched isomers are preferred products for incorporation into the high-octane gasoline pool.[9, 101, 102] Table S6 also lists the boiling points of alkane isomers. Due to the small differences in boiling points, distillation is energy intensive.

Currently, the separation of hexane isomers is performed using LTA-5A zeolite that operates on the principle of molecular sieving; see Figure S50. Linear nC6 can hop from one cage to the adjacent cage through the 4 Å windows of LTA-5A, but branched alkanes are largely excluded. An improved separation scheme, pictured in Figure S51, would require an adsorbent that would separate the di-branched isomers 22DMB and 23DMB from the nC6, 2MP, and 3MP; this would allow the low-RON components to be recycled back to the isomerization reactor. The separation of 22DMB and 23DMB from the remaining isomers is a difficult task because it requires distinguishing molecules on the *degree* of branching; such a separation is not feasible with the currently used LTA-5A. Typically, in such a processing scheme the aim would be to produce a product stream from the separation step with RON value > 92. This requirement of 92+ RON implies that the product stream will contain predominantly the di-branched isomers 22DMB and 23DMB, while allowing a small proportion of 2MP and 3MP to be incorporated into the product stream. Sharp separations between mono- and di- branched isomers is not a strict requirement.

Separation of hexane isomers

Since the RON values of both 22DMB and 23DMB are higher than 92, the desired separation is between the di-branched isomers and the mono-branched isomers. The appropriate expression for the separation potential is given by

$$\Delta q_{(22DMB+23DMB)/(nC6+2MP+3MP)} = \left(q_{nC6} + q_{2MP} + q_{3MP}\right)\frac{y_{22MB} + y_{23DMB}}{1 - y_{22MB} - y_{23DMB}} - \left(q_{22DMB} + q_{23DMB}\right) \quad \text{(S45)}$$

According to a patent granted to Universal Oil Products (UOP) for separation of hexane isomers,[103-105] the desired separation of hexane isomers as portrayed in Figure S51 is achievable with a variety of materials; see the pulse chromatographic separation data as presented in the UOP patents, and reproduced in Figure S52. The UOP patent states:

"The adsorbent may be silicalite, ferrierite, zeolite Beta, MAPO-31, SAPO-31, SAPO-11, zeolite X ion exchanged with alkaline cations, alkaline earth cations, or a mixture thereof, and zeolite Y ion exchanged with alkaline cations…."

Even though a vast number of zeolites are named in the patent, a careful examination of the separation performance of all zeolites[8, 9, 106] reveals the pulse chromatographic separation data in Figure S52 is obtained with MFI (silicalite) zeolite. MFI zeolite (also called silicalite-1) has a topology consisting of a set of intersecting straight channels, and zig-zag (or sinusoidal) channels of approximately 5.5 Å size. The pore landscapes and structural details are provided in Figure S53, and Figure S54. This chromatographic pulse data clearly shows the potential of MFI zeolite to separate a mixture of hexane isomers into three different fractions consisting of linear, mono-branched, and di-branched isomers. The separation relies essentially on configurational entropy effects. Linear alkanes can locate anywhere along the straight and zig-zag channels; see snapshots in Figure S55. The linear isomers are not "configurationally challenged". Mono-branched and di-branched isomers prefer to locate at the intersections of MFI, because these are too bulky to locate within the channels; see computational snapshots in Figure S56 and Figure S57.[107] The branched isomers are subject to a configurational "penalty".

Separation of hexane isomers

Figure S58 shows the transient breakthrough for 5-component nC6/2MP/3MP/22DMB/23DMB mixture in a fixed bed adsorber packed with MFI (framework density ρ = 1.796 kg L^{-1}) operating at a total pressure of 100 kPa and 433 K. The partial pressures of the components in the bulk gas phase at the inlet are $p_1 = p_2 = p_3 = p_4 = p_5$ = 20 kPa. The breakthrough simulation methodology is described in Chapter 4 Methodology for transient breakthrough simulations, in which intra-crystalline diffusion effects are taken into account using the input values as in previous works.[9, 108] In the simulations, we choose the mass of the adsorbent in the bed $m_{ads} = 180$ kg, cross-sectional area, A = 1 m^2; superficial gas velocity at the bed inlet, u_0 = 0.04 m s^{-1}; voidage of the packed bed, ε = 0.4. The framework density of MFI is $\rho = 1796$ kg m^{-3}. The length L of the adsorber bed is chosen as $L = \frac{1000}{\rho} \times 0.3 = 0.167002$ m. The CBMC simulated unary isotherms are fitted with the parameters specified in Table S7. For comparing the breakthrough performance of MFI with other adsorbents, it is appropriate to base the comparisons using $\frac{\left(Q_0 = \text{flow rate L s}^{-1} \text{ at STP}\right) \times \left(\text{time in s}\right)}{\left(\text{kg MOF packed in tube}\right)} = \frac{Q_0 t}{m_{ads}} = \text{L kg}^{-1}$ as the x-axis. The y-axis are the dimensionless concentrations of the component hexanes in the outlet of the fixed bed.

Herm et al.[100] report the synthesis of $Fe_2(BDP)_3$ [BDP^{2-} = benzenedipyrazolate] that has 1D channels which are triangular in shape and a pore size of 4.9 Å; see Figure S59). Molecular simulations provide insights into the workings of $Fe_2(BDP)_3$. The linear nC6 can align optimally along the V-shaped gutters, and exert the best van der Waals interaction with the framework. The interactions of the mono- and di-branched isomers are less effective, resulting in considerably lower adsorption strengths. The hierarchy of breakthroughs reported in the transient experiments of Herm [100] is 22DMB, 23DMB, 3MP, 2MP, and nC6 (cf. Figure S60); this hierarchy is dictated by a combination of adsorption strengths (nC6 >> 2MP ≈ 3MP >> 22DMB ≈ 23DMB) and diffusivities (nC6 > 2MP ≈ 3MP > 22DMB ≈ 23DMB). The di-branched isomers 22DMB and 23DMB can be recovered in the early stages of the transient breakthrough in fixed bed adsorbers. The experimentally determined breakthroughs in fixed bed

adsorbers displays distended characteristics that is indicative of strong intra-crystalline diffusional limitations within the 4.9 Å channels.

For comparison of the 92+ RON productivities of $Fe_2(BDP)_3$ with that of MFI, we carried out transient breakthrough simulations using experimental data of the unary isotherms of hexane isomers; the isotherm data fits are presented in Table S8. The simulation results are shown in Figure S61 in which the dimensionless concentrations of the hexane isomers exiting the fixed bed are plotted as a function of $\frac{\left(Q_0 = \text{flow rate L s}^{-1} \text{ at STP}\right)\times\left(\text{time in s}\right)}{\left(\text{kg MOF packed in tube}\right)} = \frac{Q_0 t}{m_{ads}} = \text{L kg}^{-1}$ as the *x*-axis. The breakthrough simulation methodology is described in Chapter 4 Methodology for transient breakthrough simulations, in which intra-crystalline diffusion effects are taken into account using the input values as in previous works.[9, 108]. In the simulations, we choose the mass of the adsorbent in the bed $m_{ads} = 180$ kg, cross-sectional area, A = 1 m^2; superficial gas velocity at the bed inlet, u_0 = 0.04 m s^{-1}; voidage of the packed bed, ε = 0.4.The framework density of $Fe_2(BDP)_3$ is $\rho = 1145.461$ kg m^{-3}. The length L of the adsorber bed is chosen as $L = \frac{1000}{\rho}\times 0.3 = 0.261903$ m.

By comparison of the adsorption selectivities, S_{ads}, defined in a specific manner in their paper, Dubbeldam et al.[102] concluded that ZIF-77 is the best choice as adsorbent for separation of hexane isomers. ZIF-77 has a characteristic pore dimension of 4.5 Å significantly smaller than the 5.5 Å channel dimensions of MFI.

For comparison of the 92+ RON productivities of ZIF-77 with that of $Fe_2(BDP)_3$ and MFI, we carried out transient breakthrough simulations using CBMC simulated data of the unary isotherms of hexane isomers; the isotherm data fits are presented in Table S9. The simulation results are shown in Figure S62 in which the component mole fractions of the hexane isomers exiting the fixed bed are plotted as a function of $\frac{\left(Q_0 = \text{flow rate L s}^{-1} \text{ at STP}\right)\times\left(\text{time in s}\right)}{\left(\text{kg MOF packed in tube}\right)} = \frac{Q_0 t}{m_{ads}} = \text{L kg}^{-1}$ as the *x*-axis. The breakthrough simulation methodology is described in Chapter 4 Methodology for transient breakthrough simulations,

in which intra-crystalline diffusion effects are taken into account using the input values as in previous works.[9, 108] In the simulations, we choose the mass of the adsorbent in the bed $m_{ads} = 180$ kg, cross-sectional area, A = 1 m^2; superficial gas velocity at the bed inlet, u_0 = 0.04 m s^{-1}; voidage of the packed bed, ε = 0.4.The framework density of ZIF-77 is $\rho = 1552.86$ kg m^{-3}. The length L of the adsorber bed is chosen as $L = \frac{1000}{\rho} \times 0.3 = 0.193192$ m.

Figure S63a compares the RON of product gas mixture exiting fixed bed adsorber packed with ZIF-77, and $Fe_2(BDP)_3$, plotted as a function of $\frac{Q_0 t}{m_{ads}}$. For the time interval during with the product RON > 92, the amount of product mixture purged during the time interval can be determined from a material balance. Expressed in terms of moles of product gas mixture, per kg of adsorbent in the packed bed, the productivities of ZIF-77, and $Fe_2(BDP)_3$ are, respectively, 1.95, and 3.4 L kg^{-1} at STP conditions.

13.2 List of Tables for Separation of hexane isomers

Table S6. Research Octane Numbers (RON) and boiling points of C6 alkanes. Information collected from a variety of web sources.

Hexane isomer	Research Octane Number (RON)	Boiling point K
n-hexane (nC6)	30	341.5
2-methyl pentane (2MP)	74.5	333.1
3-methyl pentane (3MP)	75.5	336.5
2,2 dimethyl butane (22DMB)	94	323.15
2,3 dimethyl butane (23DMB)	105	331.2

Separation of hexane isomers

Table S7. Dual-site Langmuir-Freundlich parameters for unary hexane isomers at 433 K in MFI zeolite. $\Theta_i = \Theta_{i,A,sat} \frac{b_{i,A} p_i^{\nu_A}}{1 + b_{i,A_i}{}^{\nu_A}} + \Theta_{i,B,sat} \frac{b_{i,B} p_i^{\nu_B}}{1 + b_{i,B} p_i^{\nu_B}}$

The fits are based on CBMC simulation data of Krishna and van Baten.[107]

	Site A			Site B		
	$\Theta_{A,sat}$ molecules uc^{-1}	b_A $Pa^{-\nu_A}$	ν_A dimensionless	$\Theta_{B,sat}$ molecules uc^{-1}	b_B $Pa^{-\nu_B}$	ν_B dimensionless
nC6	3.2	2.21×10^{-8}	1.6	4.3	7.42×10^{-4}	1
2MP	4	7.85×10^{-4}	1.03			
3MP	4	4.22×10^{-4}	1.02	1	9.88×10^{-7}	1
22DMB	4	2.55×10^{-4}	1.02			
23DMB	4	4.59×10^{-4}	1.02			

Separation of hexane isomers

Table S8. Dual-Langmuir-Freundlich parameter fits for $Fe_2(BDP)_3$ based on the experimental data of Herm et al.[100] for isotherms at 403 K, 433 K, and 473 K. These isotherms were fitted with with *T*-dependent parameters

$$q = q_{A,sat}\frac{b_A p^{\nu_A}}{1+b_A p^{\nu_A}} + q_{B,sat}\frac{b_B p^{\nu_B}}{1+b_B p^{\nu_B}}$$

$$b_A = b_{A0}\exp\left(\frac{E_A}{RT}\right); \quad b_B = b_{B0}\exp\left(\frac{E_B}{RT}\right)$$

	Site A				Site B			
	$q_{A,sat}$ mol kg^{-1}	b_{A0} Pa$^{-\nu_i}$	E_A kJ mol^{-1}	ν_A dimensionless	$q_{B,sat}$ mol kg^{-1}	b_{B0} Pa$^{-\nu_i}$	E_B kJ mol^{-1}	ν_B dimensionless
nC6	0.28	2.74×10^{-26}	111	3	1.17	8.86×10^{-13}	73	1.02
2MP	0.78	2.13×10^{-13}	76	1.1	0.63	5.61×10^{-17}	89	1.36
3MP	0.36	4.62×10^{-13}	76	1.1	1.07	1.34×10^{-16}	89	1.36
22DMB	0.53	1.33×10^{-32}	167	2.9	0.94	1.42×10^{-12}	67	1
23DMB	0.61	9.74×10^{-33}	167	2.9	0.92	1.49×10^{-12}	67	1

Separation of hexane isomers

Table S9. Dual-site Langmuir parameters for pure component hexane isomers at 433 K in ZIF-77. The fits are based on the CBMC simulations of Dubbeldam et al.[102] $q_i = q_{A,sat}\frac{b_A f}{1+b_A f} + q_{B,sat}\frac{b_B f}{1+b_B f}$

	Site A		Site B	
	$q_{A,sat}$ mol/kg	b_A Pa^{-1}	$q_{B,sat}$ mol/kg	b_B Pa^{-1}
nC6	0.81	5.25×10^{-4}	0.59	2.24×10^{-6}
2MP	0.92	4.95×10^{-5}	0.43	1.66×10^{-8}
3MP	0.8	2.15×10^{-5}	0.4	5.15×10^{-8}
22DMB	0.7	2.1×10^{-8}		
23DMB	0.96	6.31×10^{-7}	0.2	3.65×10^{-9}

13.3 List of Figures for Separation of hexane isomers

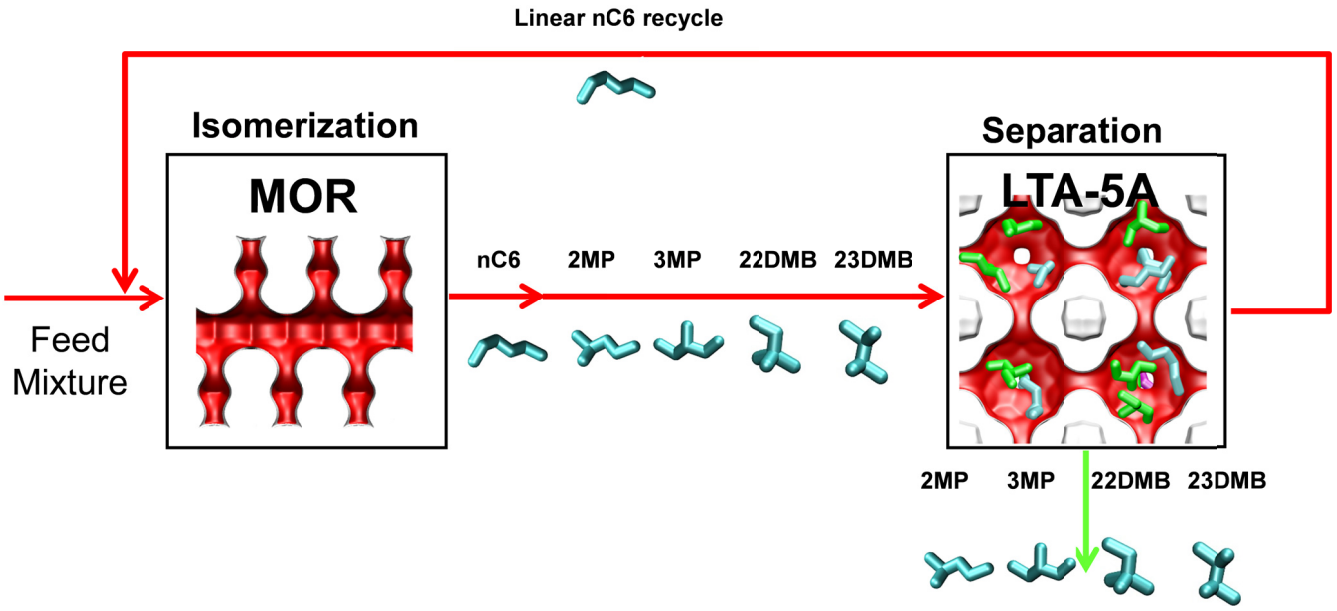

Figure S50. Currently employed processing scheme for nC6 isomerization and subsequent separation step using LTA-5A zeolite.

Separation of hexane isomers

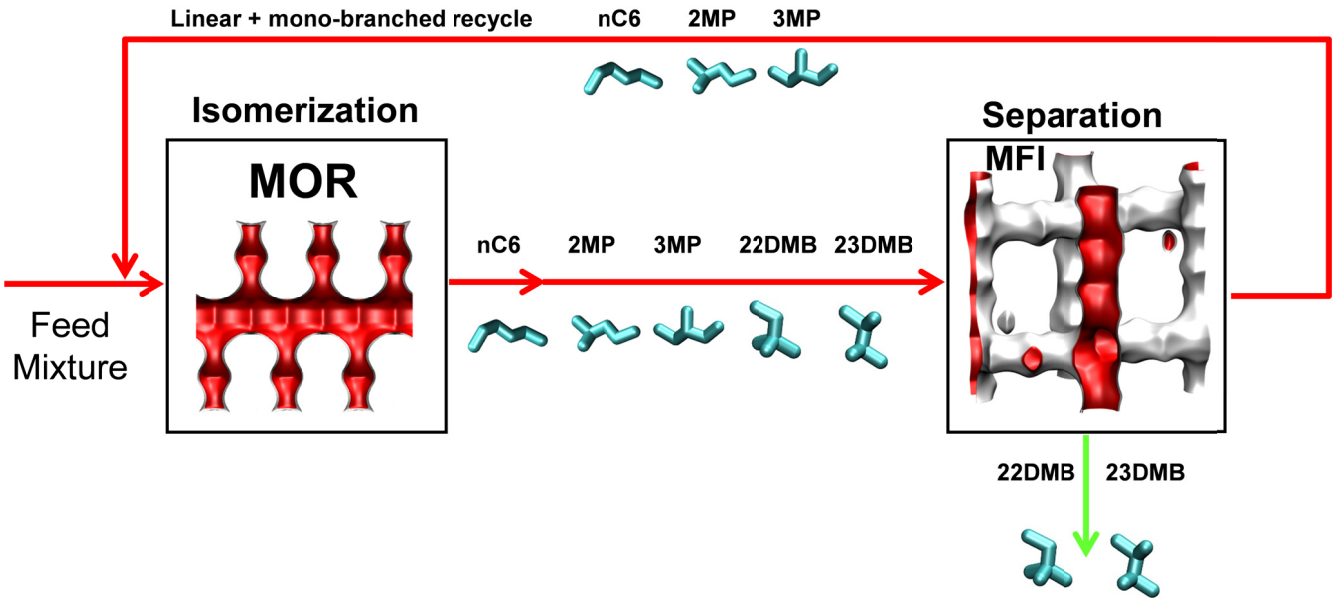

Figure S51. Improved processing scheme for the nC6 isomerization process using MFI zeolite in the separation step.

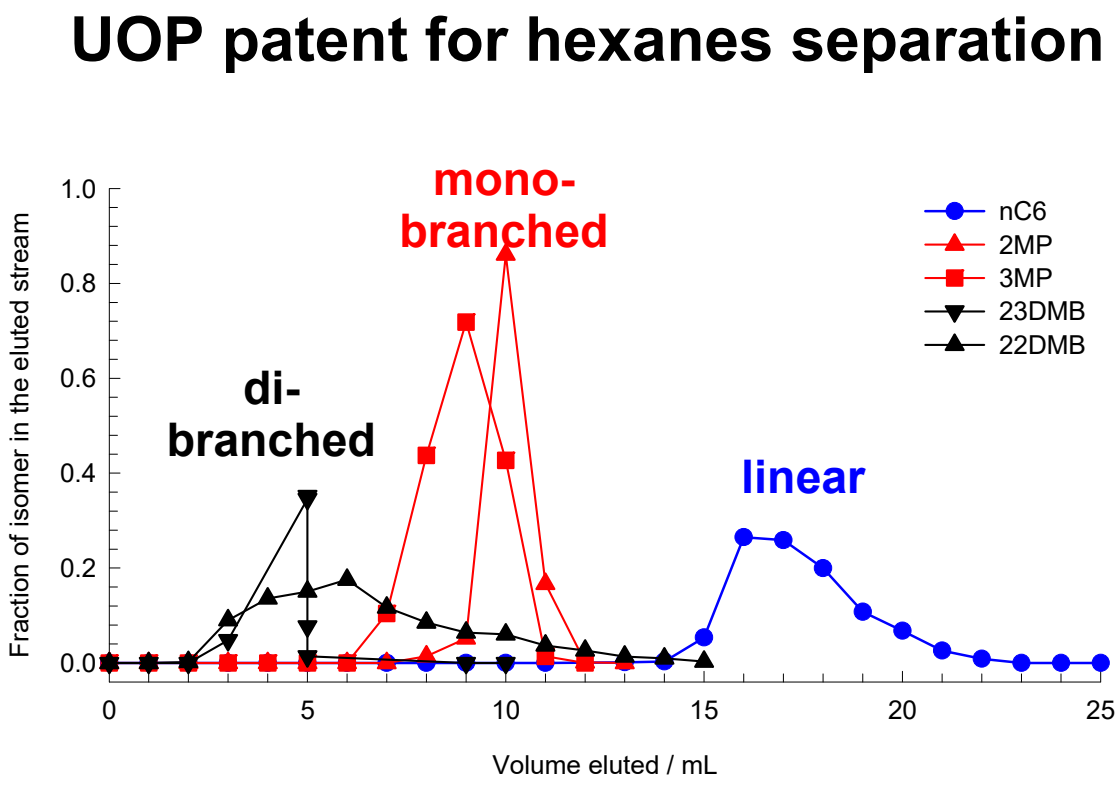

The adsorbent may be silicalite, ferrierite, zeolite Beta, MAPO-31, SAPO-31, SAPO-11, zeolite X ion exchanged with alkaline cations, alkaline earth cations, or a mixture thereof, and zeolite Y ion exchanged with alkaline cations..

Figure S52 Pulsed chromatographic separation of hexane isomers as reported in the patents assigned to Universal Oil Products (UOP).[103-105]

MFI pore landscape

	MFI
a /Å	20.022
b /Å	19.899
c /Å	13.383
Cell volume / Å^3	5332.025
conversion factor for [molec/uc] to [mol per kg Framework]	0.1734
conversion factor for [molec/uc] to [kmol/m^3]	1.0477
ρ [kg/m3]	1796.386
MW unit cell [g/mol(framework)]	5768.141
ϕ, fractional pore volume	0.297
open space / Å^3/uc	1584.9
Pore volume / cm^3/g	0.165
Surface area /m^2/g	487.0
DeLaunay diameter /Å	5.16

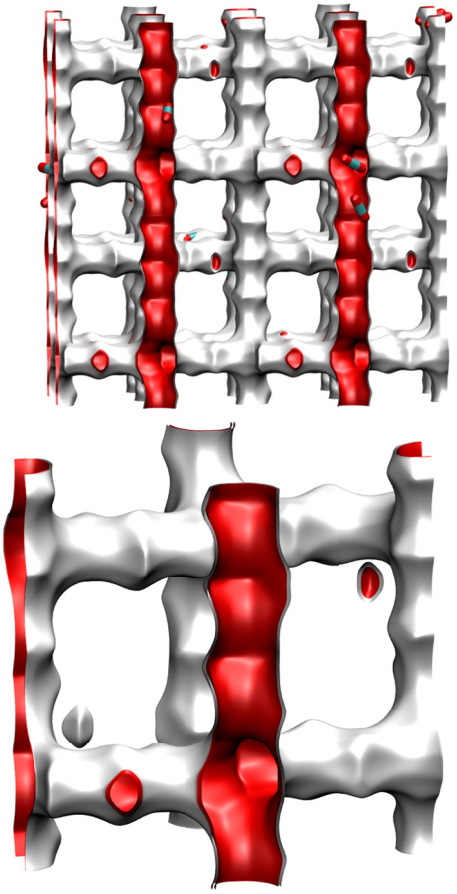

Figure S53. Structural details and pore landscape for MFI zeolite.

10 ring channel of MFI viewed along [100]

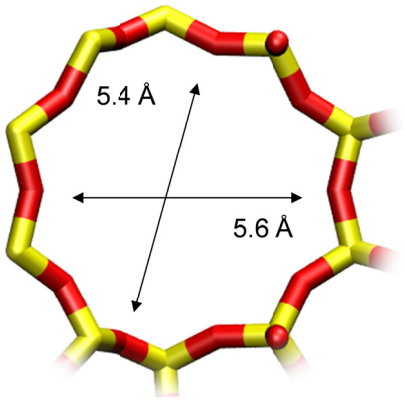

10 ring channel of MFI viewed along [010]

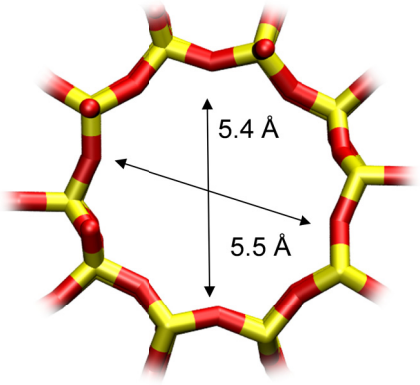

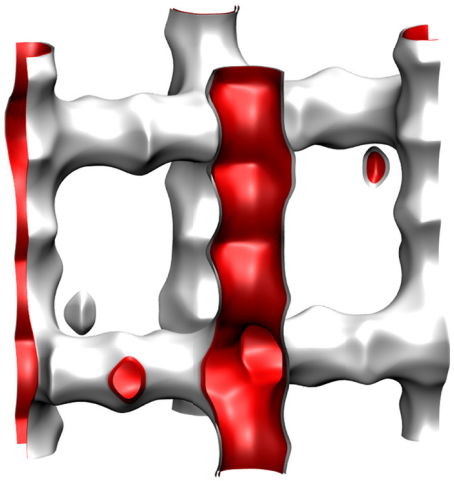

Figure S54. Structural details and pore landscape for MFI zeolite.

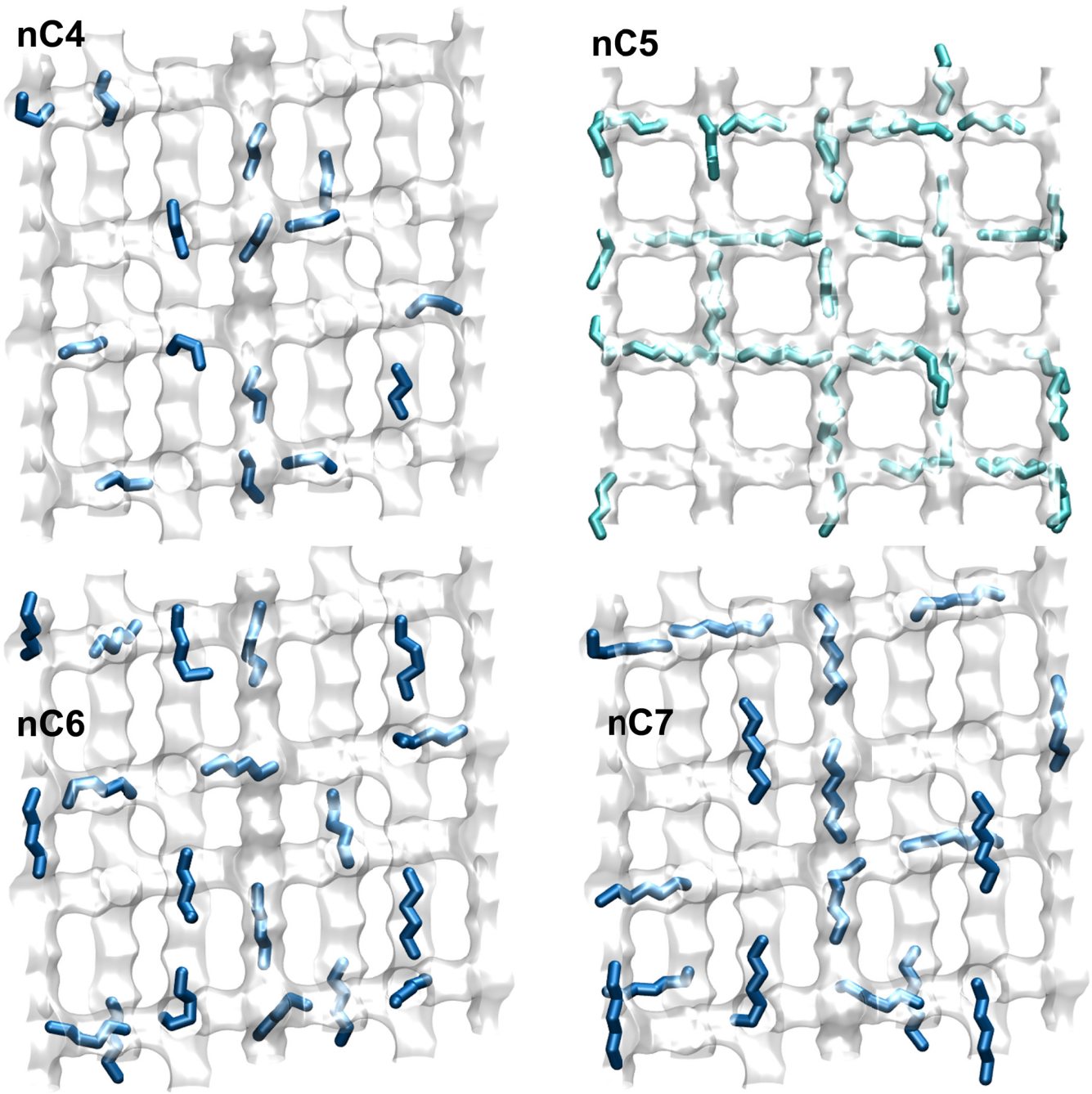

Figure S55. Computational snapshots showing the location of linear alkanes (nC4, nC5, nC6, nC7) within the intersecting channel topology of MFI zeolite.

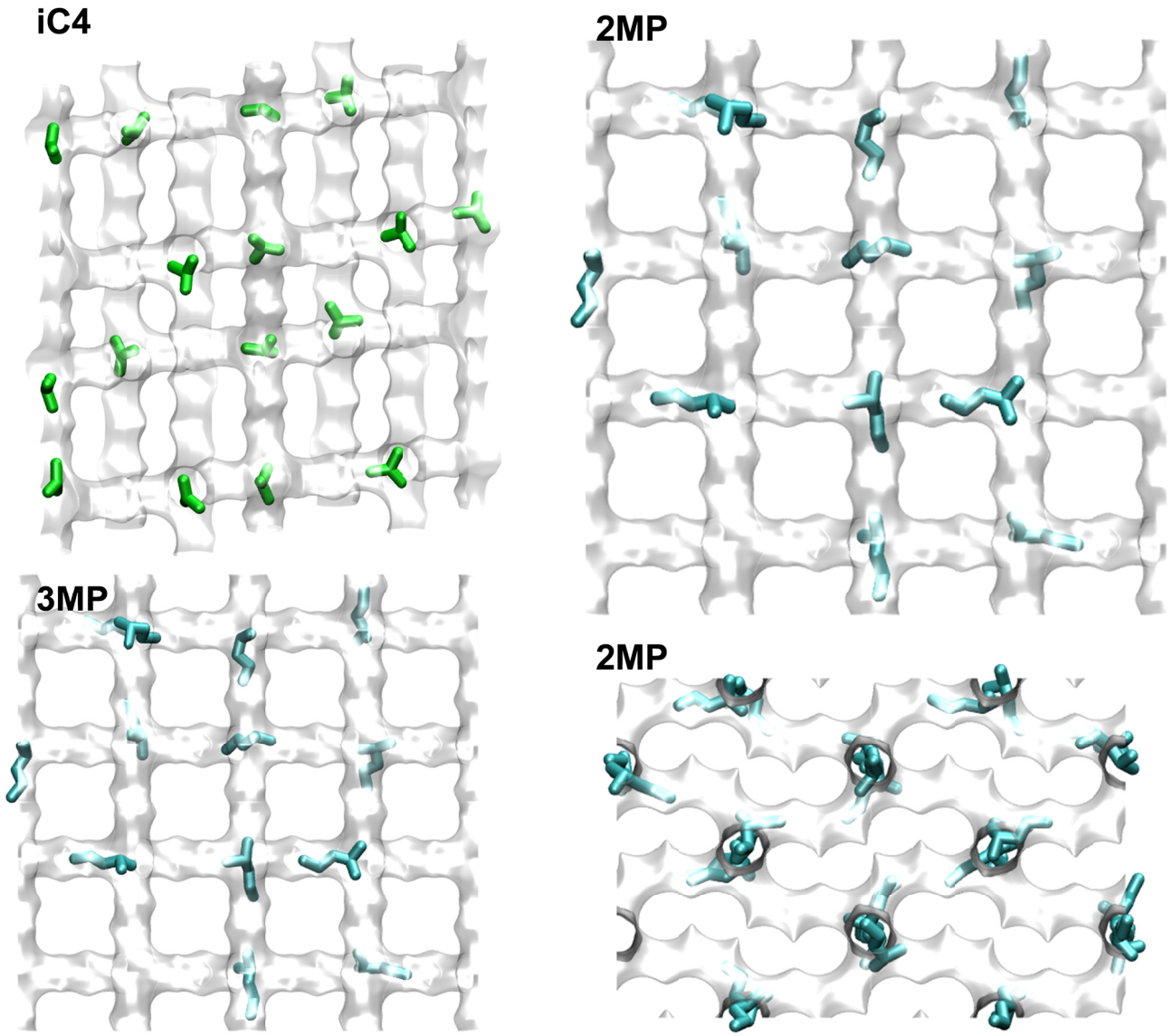

Figure S56. Computational snapshots showing the location of mono-branched alkanes at the channel intersections of MFI zeolite.

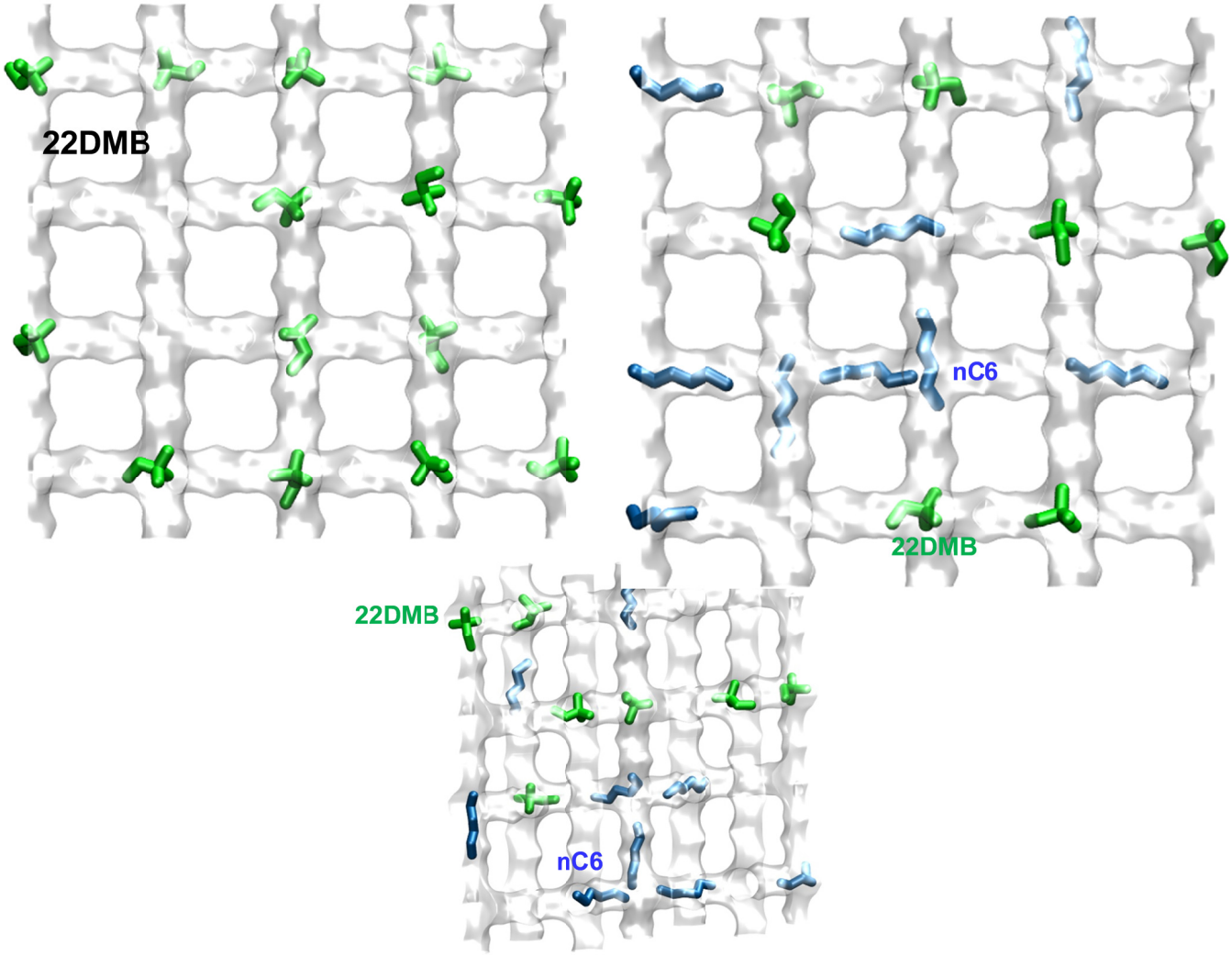

Figure S57. Computational snapshots showing the location of di-branched 22DMB at the channel intersections of MFI zeolite.

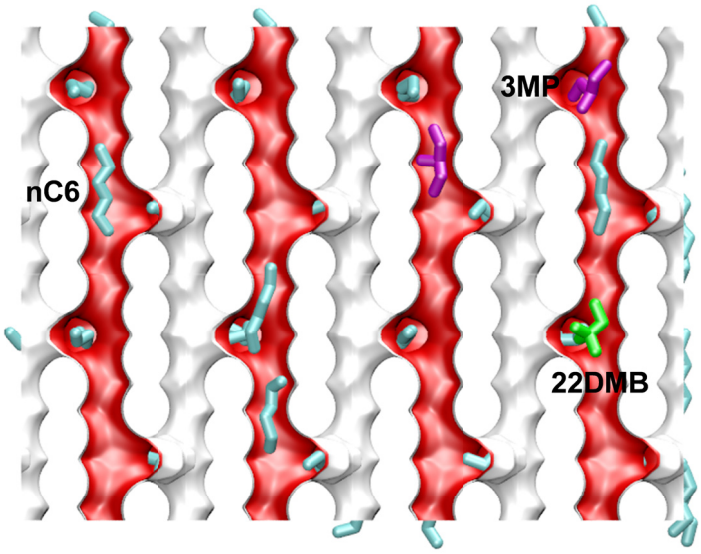

Snapshots showing the location of nC6, 3MP, and 22DMB within the intersecting channels of MFI.

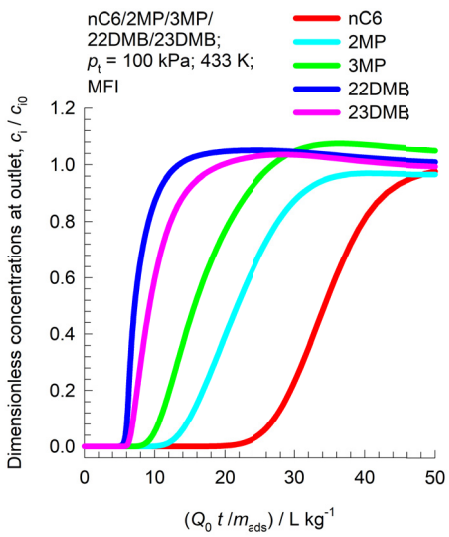

Figure S58. Simulations of breakthrough characteristics for 5-component nC6/2MP/3MP/22DMB/23DMB mixture in a fixed bed adsorber packed with MFI (framework density ρ = 1.796 kg L^{-1}) operating at a total pressure of 100 kPa and 433 K. The partial pressures of the components in the bulk gas phase at the inlet are $p_1 = p_2 = p_3 = p_4 = p_5$ = 20 kPa. The CBMC simulated unary isotherms are fitted with the parameters specified in Table S7.

Separation of hexane isomers

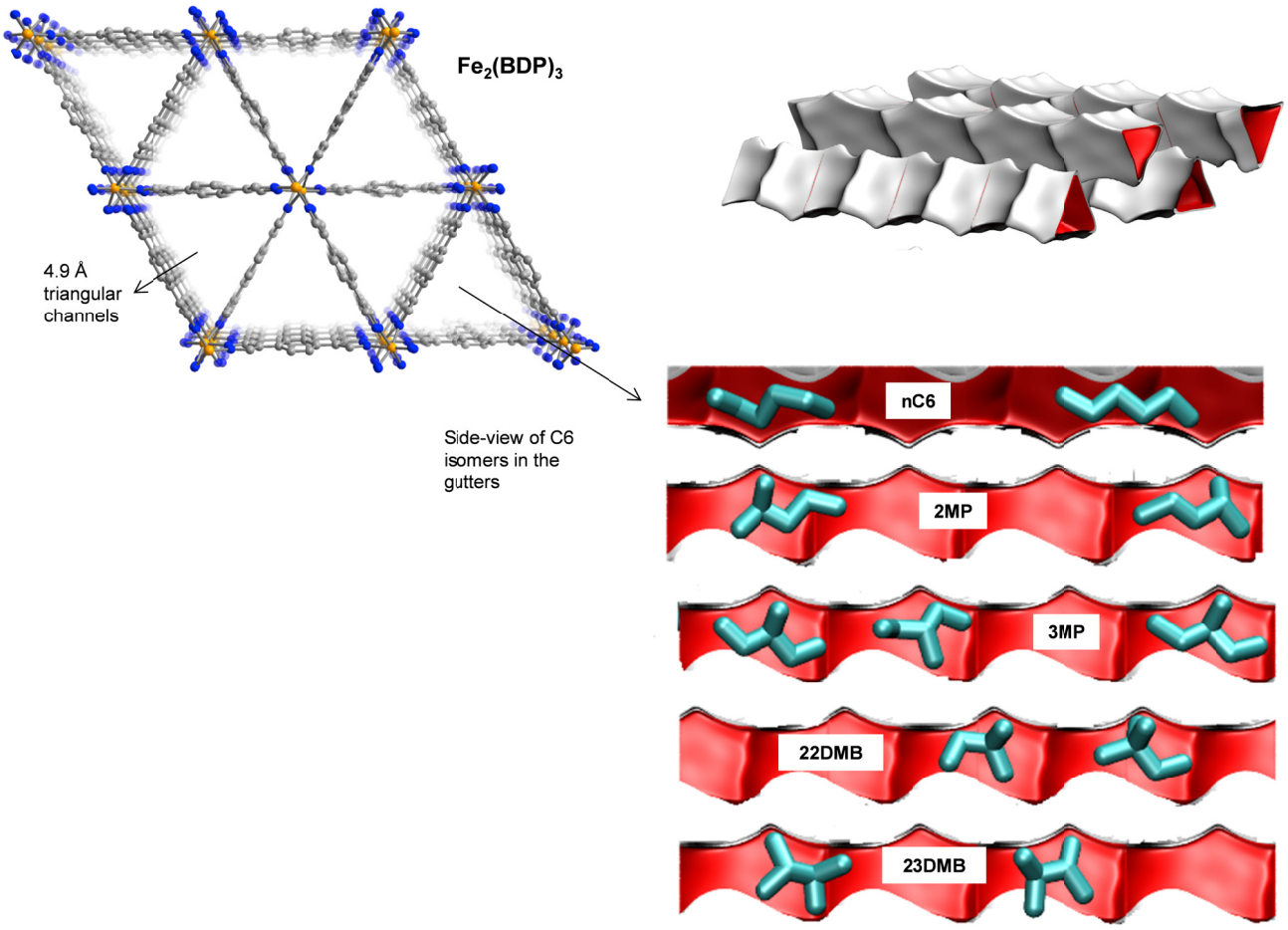

Figure S59. The triangular channel topology of $Fe_2(BDP)_3$.[100] Also shown are computational snapshots (side-on view) of the conformations of nC6, 2MP, 3MP, 22DMB, and 23DMB within the triangular channels.

Separation of hexane isomers

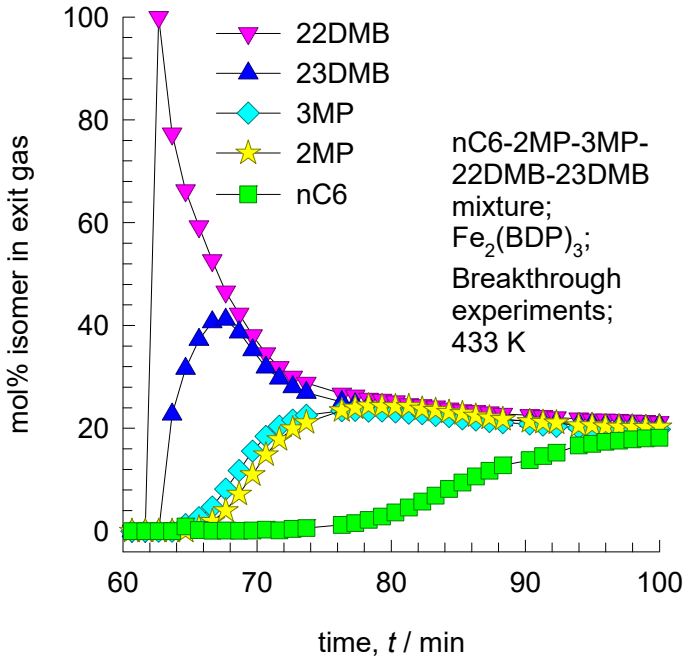

Figure S60. Experimental data on transient breakthrough of hexane isomers in a fixed bed packed with $Fe_2(BDP)_3$.[100]

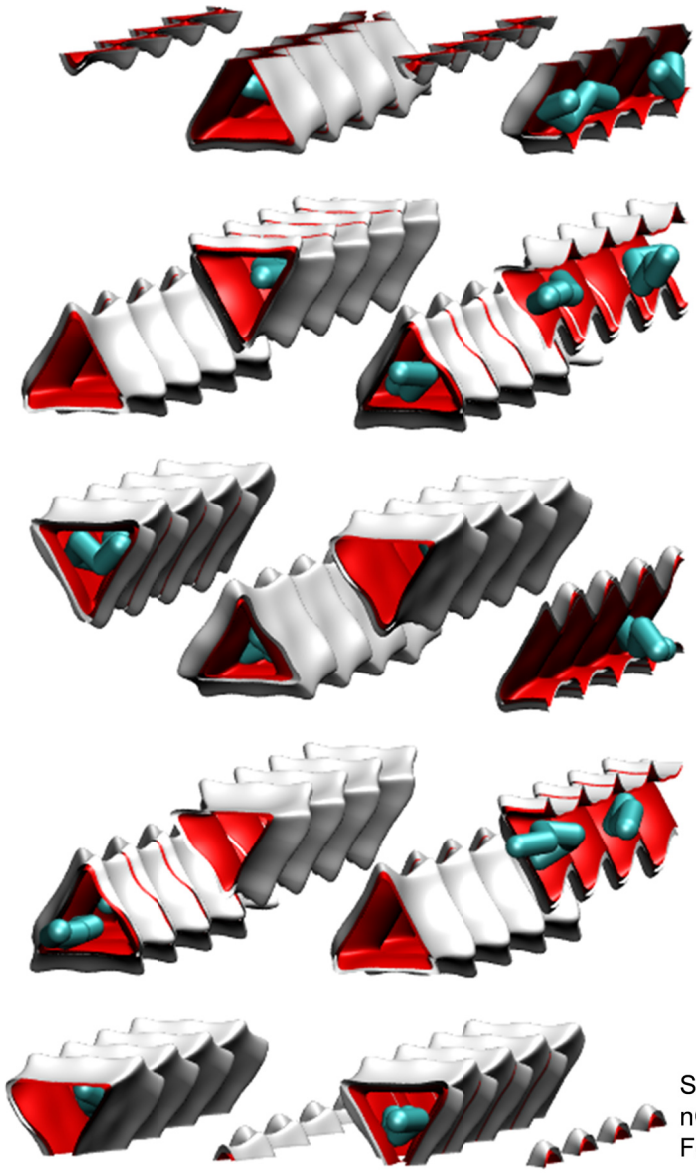

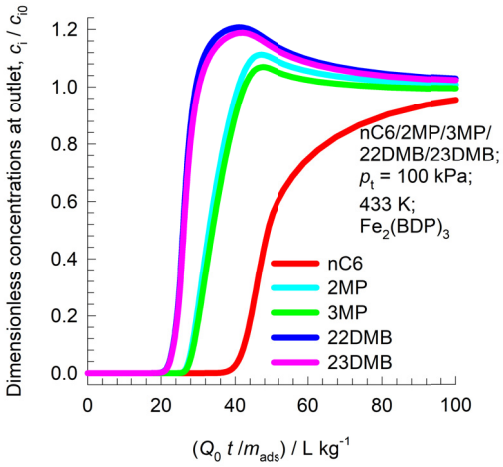

Snapshots showing the location of nC6 within the triangular channels of $Fe_2(BDP)_3$.

Figure S61. Simulations of breakthrough characteristics for 5-component nC6/2MP/3MP/22DMB/23DMB mixture in a fixed bed adsorber packed with $Fe_2(BDP)_3$, (framework density ρ = 1.145 kg L^{-1}), operating at a total pressure of 100 kPa and 433 K. The partial pressures of the components in the bulk gas phase at the inlet are $p_1 = p_2 = p_3 = p_4 = p_5$ = 20 kPa. The CBMC simulated pure component isotherms are fitted with the parameters specified in Table S8.

Separation of hexane isomers

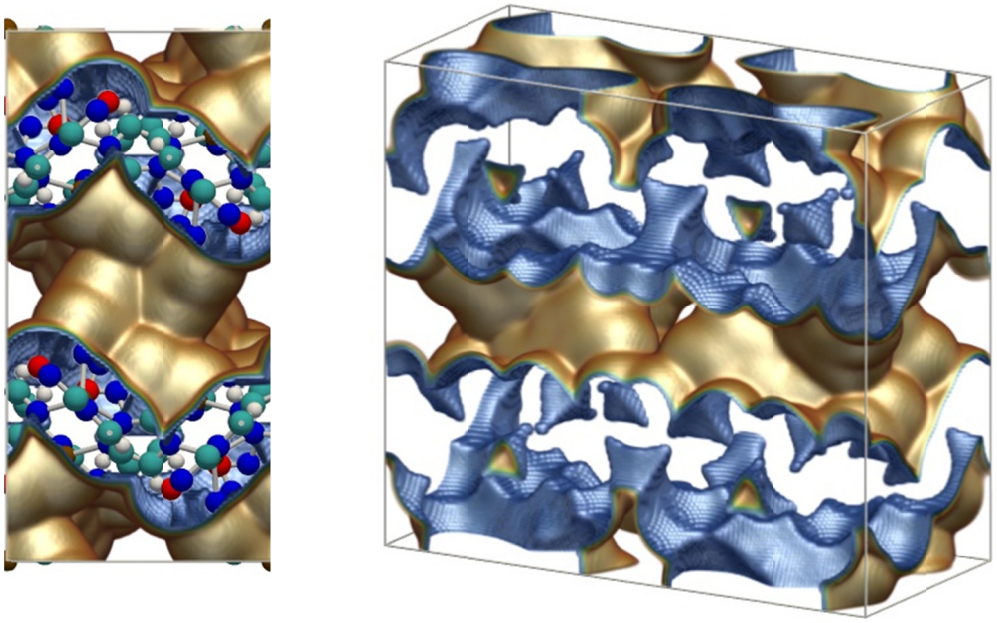

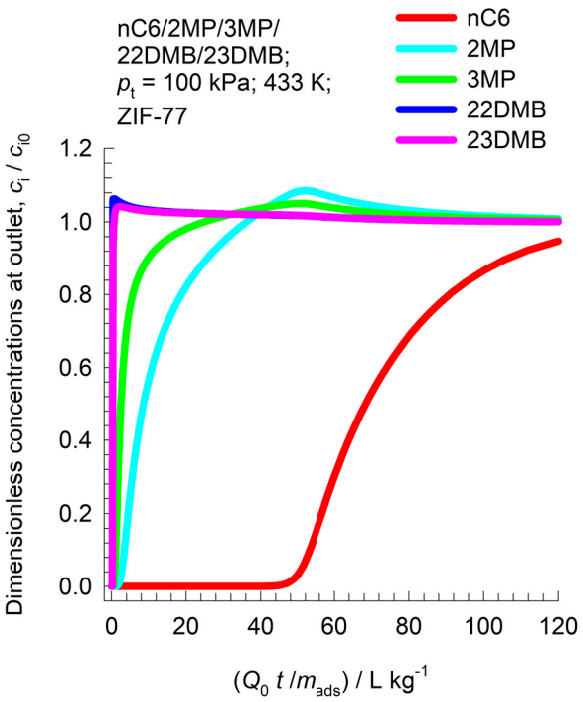

Figure S62. Simulations of breakthrough characteristics for 5-component nC6/2MP/3MP/22DMB/23DMB mixture in a fixed bed adsorber packed with ZIF-77 (framework density ρ = 1.552 kg L^{-1}) operating at a total pressure of 100 kPa and 433 K. The partial pressures of the components in the bulk gas phase at the inlet are $p_1 = p_2 = p_3 = p_4 = p_5$ = 20 kPa. The CBMC simulated pure component isotherms are fitted with the parameters specified in Table S9.

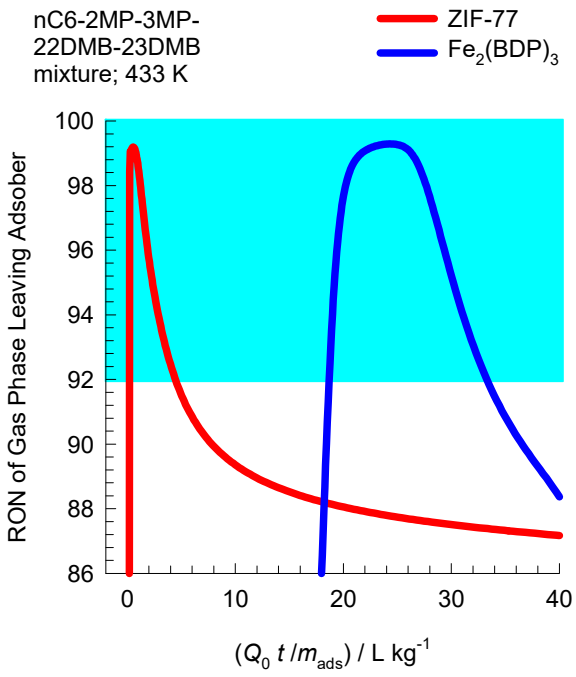

Figure S63. Plot of RON of product gas mixture exiting fixed bed adsorber packed with ZIF-77, and $Fe_2(BDP)_3$, plotted as a function of $\frac{Q_0 t}{m_{ads}}$.

14 Separation of xylene isomers

14.1 Background on xylenes separation

Aromatic hydrocarbons, that are valuable feedstocks in the petrochemical industries, are most commonly obtained from catalytic reforming of naphtha. The xylene isomers, o-xylene, m-xylene and in particular p-xylene, are important chemical intermediates. Ortho-xylene is oxidized to make phthalic anhydride which is used to make phthalate plasticizers among other things. Meta-xylene is oxidized to produce isophthalic acid, which is used in unsaturated polyester resin. However, p-xylene has the largest market of the three isomers; the demand for p-xylene is several times that of m-xylene and o-xylene. The largest use of p-xylene is in its oxidation to make terephthalic acid, that is used in turn to make polymers such as polyethylene terephthalate (PET) and polybutylene terephthalate (PBT). PET is one of the largest volume polymers in the world, and is used to produce fibers, resins, films, and blown beverage bottles.

In a commonly used separation scheme (cf. Figure S64, Figure S65, and Figure S66), the xylenes rich stream from the bottom of the reformate splitter is routed to a xylenes splitter. Here, the heavier aromatics (C9+) are removed from the bottom of the column. The overhead stream from the xylenes splitter containing o-xylene, m-xylene, p-xylene, and ethylbenzene need to be separated for recovery of p-xylene. Due to the very small differences in boiling points, p-xylene recovery form o-xylene/m-xylene/p-xylene/ethylbenzene mixtures is not possible by use of distillation technology. There are, however, significant differences in the freezing points (see Figure S67, Figure S68, and Figure S69) that allow fractional crystallization to be used for separations. The differences in the freezing points arise because of differences in the stacking efficiencies of molecules. Para-xylene has the highest freezing point because these molecules stack most efficiently; pure p-xylene crystals are the first to emerge from the solution upon cooling. However, the energy requirements for fractional crystallization are high because of the need to cool to temperatures of about 220 K. Selective adsorption of xylene isomers

within the pores of ordered crystalline micro-porous materials is an energy-efficient alternative to fractional crystallization. In currently used technology the separation is carried out using cation-exchanged Faujasite (FAU) zeolite in a Simulated Moving Bed (SMB) adsorption separation unit (see Figure S71, and Figure S72). [109-112]

An SMB unit consists of a set of interconnected columns in series; countercurrent flow of the solid and liquid phases is simulated by the periodic shifting of the inlets and outlets in the direction of the liquid flow. Commonly used SMB technologies are UOP's Parex, Axens' Eluxyl, and Toray's Aromax.[109, 113, 114] In Figure S71 the SMB process for separation of a feed mixture containing o-xylene/m-xylene/p-xylene/ethylbenzene is depicted in its (mathematically) equivalent form of true moving bed with counter-current contacting between the down-flowing adsorbent material and up-flowing desorbent (eluent) liquid.

The typical composition of a mixed xylenes feed to a simulated moving bed (SMB) adsorber is 19% ethylbenzene, 44% m-xylene, 20% o-xylene, and 17% p-xylene. Since the adsorbent particles are in contact with a mixture in the *liquid* phase, the pores of the adsorbent material are practically saturated with guest molecules. The hierarchy of adsorption strengths is dictated by molecular packing, or entropy, effects. Binding energies of guest molecules with the framework walls or non-framework cations do not solely determine the separation performance. As pointed out by Peralta et al.[115], adsorbents selective to p-xylene are desirable for high productivities; they need to adsorb only ~20% of the feed, whereas an adsorbent that rejects p-xylene would have to adsorb 80% of the feed. In current industrial practice the adsorbent used is BaX zeolite, that selectively adsorbs p-xylene.[110, 111] Typically, BaX zeolite also contains other cations such as K^+. The separation of xylenes at pore saturation is influenced also factors other than molecular packing effects. For illustration, Figure S70 shows the pure component isotherms for hydrocarbons in BaX zeolite at 453 K, plotted using the Langmuir parameters reported by Minceva and Rodrigues.[114, 116] Industrial operations are for molar concentrations exceeding about 7 mol L^{-1}, corresponding to liquid phase operations. The selectivity of BaX becomes increasingly in favor of p-xylene as pore saturation conditions are approached; the preference for p-xylene is

entropically driven because the packing of p-xylene within the supercages of FAU is less energy demanding than the packing of m-xylene within the supercages; this aspect has been explained clearly in the thesis of Costa.[112]

The desorbent used in the UOP Parex unit is p-diethylbenzene (pDEB; see Figure S69);[109] pDEB has been found to have approximately the same affinity for BaX zeolite as does p-xylene, balancing the amount of desorbent required for p-xylene desorption while not excluding the p-xylene from adsorbing in the adsorption zone. pDEB boils at 450 K while the highest - boiling xylene, o-xylene, boils at 417.6 K so there is substantial relative volatility to perform the distillative separations economically.[109]

Toluene is an alternative choice as desorbent; see Figure S69.

In the configuration depicted in Figure S71,the feed mixture containing o-xylene, m-xylene, p-xylene, and ethylbenzene is introduced at a port near the middle of the SMB unit.[113, 114] The eluent is introduced at the bottom. For a clearer appreciation of the SMB operations, Figure S72 presents typical liquid phase concentrations of o-xylene, m-xylene, p-xylene, ethylbenzene along the adsorber height. The extract phase, containing the more strongly adsorbed p-xylene, is recovered at the bottom section of the column, below the feed injection port. The raffinate phase, containing the more weakly adsorbed o-xylene, m-xylene, and ethylbenzene is tapped off at a location in the upper section above the feed injection port. Four different operation zones can be distinguished.

Zone 1: Regeneration of adsorbent,

Zone 2: Desorption of the less strongly adsorbed components o-xylene, m-xylene, and ethylbenzene,

Zone 3: Adsorption of the more strongly adsorbed p-xylene,

Zone 4: Regeneration of the eluent.

The components o-xylene, m-xylene, and ethylbenzene, contained in the rafffinate phase of the SMB unit, are sent to a xylenes isomerization unit. In the isomerization unit the xylenes mixture is re-equilibrated, and the main products are benzene, toluene, and p-xylene.

On examination of the boiling points of the C8 aromatics, we note that o-xylene has the highest boiling point (see Figure S67). A xylenes splitter, which ordinarily would separate the C9+ aromatics

from the xylenes (cf. Figure S65), can be redesigned to remove o-xylene as well; this alternative configuration is depicted in Figure S66. In this configuration, the fractionation split in the xylenes splitter is between m-xylene and o-xylene with a temperature difference of only 5 K; consequently we need a super-fractionating tower containing about 135 fractionating trays. The overhead product from the xylenes splitter, rich in ethylbenzene, p-xylene, and m-xylene is fed to a recovery unit for p-xylene. The bottoms product from the super-fractionator is routed to a further distillation column in which o-xylene is separated from C9+ aromatics and recovered as overhead product. In the configuration shown in Figure S66 both the xylenes splitter and o-xylene recovery columns are super-fractionators that have high energy demands.

There is considerable potential for use of metal-organic frameworks (MOFs) adsorbents for use in one or more of the following separation tasks.

(1) For realizing improvements in the SMB adsorber we need to discover adsorbents that have both higher uptake capacity and selectivity of p-xylene when compared to BaX zeolite, that is to be regarded as the benchmark adsorbent.

(2) Better MOF adsorbents will result in lower recirculation flows of eluent, and solids and this will result in significant economic advantages.

(3) Both the distillation columns in the processing scheme shown in Figure S66 could be replaced by an adsorption unit, perhaps operating using SMB technology, with a MOF adsorbent that is selective to o-xylene.

(4) MOFs could be used for separation of a mixture of benzene, toluene, and non-aromatics as replacement for extractive distillation depicted in Figure S64. A hybrid combination of distillation and adsorption is also another option.

(5) MOFs could be used for separation of ethylbenzene/styrene mixtures either as total, or partial, replacement of the vacuum distillation tower currently used; see Figure S64.

A common feature of all the aromatics separation is that the operation conditions are such that the pores are nearly saturated with guest molecules. Therefore, molecular packing effects are of primary

importance in the separations. Components that pack most efficiently are the ones that are selectively adsorbed. For any adsorbent material, the packing efficiencies of any aromatic molecule are dictated by a combination of two factors: (a) molecular dimensions, and (b) departures from planarity.

14.2 Screening of MOFs for separation of xylene isomers

The height and width of the C8 aromatics are: o-xylene: 8 Å × 7.4 Å; m-xylene: 8.9 Å × 7.4 Å; p-xylene: 9.3 Å × 6.7 Å; ethylbenzene: 9.5 Å × 6.7 Å; styrene: 9.3 Å × 6.7 Å; see dimensions provided in Figure S67. A further point to note is that xylene isomers are flat; these isomers can align themselves parallel to the channel walls, affording better van der Waals interactions with the framework atoms. By contrast, ethylbenzene is not a flat molecule; the ethyl branch is not in the same plane as the benzene ring; see Figure S68.

Due to the differences in the molecular dimensions of the xylene isomers, the efficiencies with which the xylene isomers stack within the channels of different dimensions are different. We can deliberately choose a material with a specified channel dimension in order to allow the optimum stacking of one or other of the xylene isomers.

Experimental data [117-119] for MIL-47 and MIL-53 with 1D rhombohedric channels of 8.5 Å show that these MOFs are selective to adsorption of o-xylene when operating at conditions close to pore saturation. The snapshots in Figure S73a obtained from CBMC simulations,[120] clearly show the optimal stacking of o-xylene within 8.5 Å channels of MIL-47.

Experimental data of Niekiel et al.[121] for adsorption isotherms for xylene isomers in CAU-13 show strong selectivity towards o-xylene that has optimal stacking within the 8.46 Å channels. Fang et al.[122] report pulse breakthrough simulations for 4-component o-xylene/m-xylene/p-xylene/ethylbenzene in MOF-CJ3 that indicate adsorption selectivity towards o-xylene. MOF-CJ3 has that has square channels of approximately 8 Å size that is adequate for commensurate stacking of o-xylene.

Clearly, MIL-47, MIL-53, CAU-13, and MOF-CJ3 are not suitable for replacement of BaX zeolite in SMB units.

Separation of xylene isomers

Torres-Knoop et al.[120] have adopted a conceptual approach, using CBMC simulations for selecting MOFs that have the desired selectivity to p-xylene. Within the one-dimensional 10 Å channels of MAF-X8, we have commensurate stacking of p-xylene; see snapshots in Figure S73b.

Co(BDP), that has 10 Å square-shaped 1D channels of Co(BDP), also allows p-xylene to stack vertically (cf. Figure S73c), resulting in selectivity in favor of p-xylene.[120]

Figure S74 presents snapshots of stacking of o-xylene, m-xylene, p-xylene, and ethylbenzene within the 1D zig-zag shaped channels of Co-CUK-1, which is comprised of cobalt(II) cations and the dianion of dicarboxylic acid $[Co_3(2,4\text{-pdc})_2(\mu 3\text{-OH})_2]$ (2,4-pdc = pyridine-2,4-dicarboxylic acid dianion); the synthesis of this MOF is described by Humphrey et al.[123, 124]The p-xylene molecules can stack vertically, and this results in a higher saturation capacity for the para-isomer, as demonstrated by the experimental data on unary isotherms in Figure S74.

Mukherjee et al.[125] have presented pure component adsorption isotherm data at 298 K for o-xylene, m-xylene, p-xylene, and ethylbenzene in a Zn(II)-based dynamic coordination framework, $[Zn_4O(L)_3]$ where the ligand L = 4, 4'- ((4-(tert-butyl) - 1,2- phenylene)bis(oxy))dibenzoate). The MOF structure gets transformed in such a manner as to allow optimal packing of p-xylene within the cavities; see Figure S75.

The production of *p*-xylene involves the separation of 4-component equimolar o-xylene(1)/m-xylene(2)/p-xylene(3)/ethylbenzene(4) mixtures.[8, 120, 126] We calculate the *gravimetric separation potential* Δq for preferential adsorption of p-xylene, and rejection of o-xylene, m-xylene, and ethylbenzene as follows [7]

$$\Delta q = \left(q_{pX}\right)\frac{y_{oX}+y_{mX}+y_{EthBz}}{1-y_{oX}-y_{mX}-y_{EthBz}} - \left(q_{oX}+q_{mX}+q_{EthBz}\right) \tag{S46}$$

In eq (S46) the *gravimetric* loadings of each of the four aromatics, q_i, expressed in mol per kg of crystalline adsorbent, are calculated using the IAST for mixture adsorption equilibrium.

Adopting the methodology described in earlier work,[8] we compare the performances of all MOFs at conditions corresponding to pore saturation. Let us compare the separation performance of BaX zeolite

with other MOFs that show selectivity towards p-xylene: DynaMOF-100 [125, 127], Co-CUK-1,[124] MAF-X8,[120] JUC-77,[128] Co(BDP),[107] and MIL-125.[129-131] The isotherm data for MAF-X8,[120] JUC-77,[128] Co(BDP), and MIL-125 are taken from Torres-Knoop et al.[120] The isotherm data for DynaMOF-100 are taken from Mukherjee et al.[125, 127] The isotherm data for Co-CUK-1 are taken from the Yoon et al.[124]

Figure S76 is a plot of Δq as a function of the gravimetric uptake of p-xylene in the mixture. A combination of high separation potential and high p-xylene capacity provides the best separation capability in a SMB adsorber. According to Figure S76, the best separation performance is realized with DynaMOF-100. The next best performance is that of Co-CUK-1. Both these MOFs offer significantly higher separation potential than the commercially used BaX zeolite

14.3 Separation of styrene/ethylbenzene mixtures

Alkylation of benzene with ethene produces ethyl benzene (cf. Figure S64), which is dehydrogenated to styrene, a monomer used in the manufacture of many commercial polymers and co-polymers The conversion of ethylbenzene to styrene is only partial, and the reactor product contains a large fraction, in the range of 20%-40%, of unreacted ethylbenzene. Due to the small, 9 K, difference in their boiling points, the distillation separation of styrene and ethylbenzene has to be carried out in tall distillation columns operating under vacuum and at high reflux ratios; the energy demands are therefore very high. Adsorptive separations using microprous metal-organic frameworks offer energy-efficient alternatives.

Maes et al.[132] and Remy et al.[133] have demonstrated that MIL-47 (V) and MIL-53 (Al) also have the potential for separation of mixtures of styrene and ethylbenzene. Styrene is a flat molecule; by contrast, ethylbenzene is not a flat molecule (cf. Figure S68); the ethyl branch is not in the same plane as the benzene ring. Due to differences in the flatness, styrene has stronger interactions with the metal framework. Being flat, styrene molecules stack more efficiently within the 1D channels of MIL-47 (V) and MIL-53 (Al). The pure component isotherm data of Maes et al.[132], measured for bulk liquid phases show that the adsorption loadings of styrene are higher than that of ethylbenzene. The experimental data of Maes et al.[132] for transient breakthroughs of ethylbenzene/styrene mixtures in MIL-47(V) and MIL-

53(Al) demonstrate that styrene is selectively adsorbed. Let us now compare the performance of MIL-47(V) and MIL-53(Al) with DynaMOF-100 that undergoes guest-induced structural changes to selectively encapsulate styrene (cf.Figure S77).

For comparing the separation performance of MIL-47(V) and MIL-53(Al) with DynaMOF-100, we adopt the concept of the separation potential: $\Delta q = q_{St} \frac{y_{EthBz}}{1 - y_{EthBz}} - q_{EthBz}$, where q_i, expressed in mol per kg of crystalline adsorbent. Figure S78 presents a plot of the separation potential, $\Delta q = q_{St} \frac{y_{EthBz}}{1 - y_{EthBz}} - q_{EthBz}$, versus the gravimetric styrene uptake capacity. The clear superiority of DynaMOF-100 for styrene/ethylbenzene separations needs, however, to be established by experiments in fixed beds.

14.4 List of Figures for Separation of xylene isomers

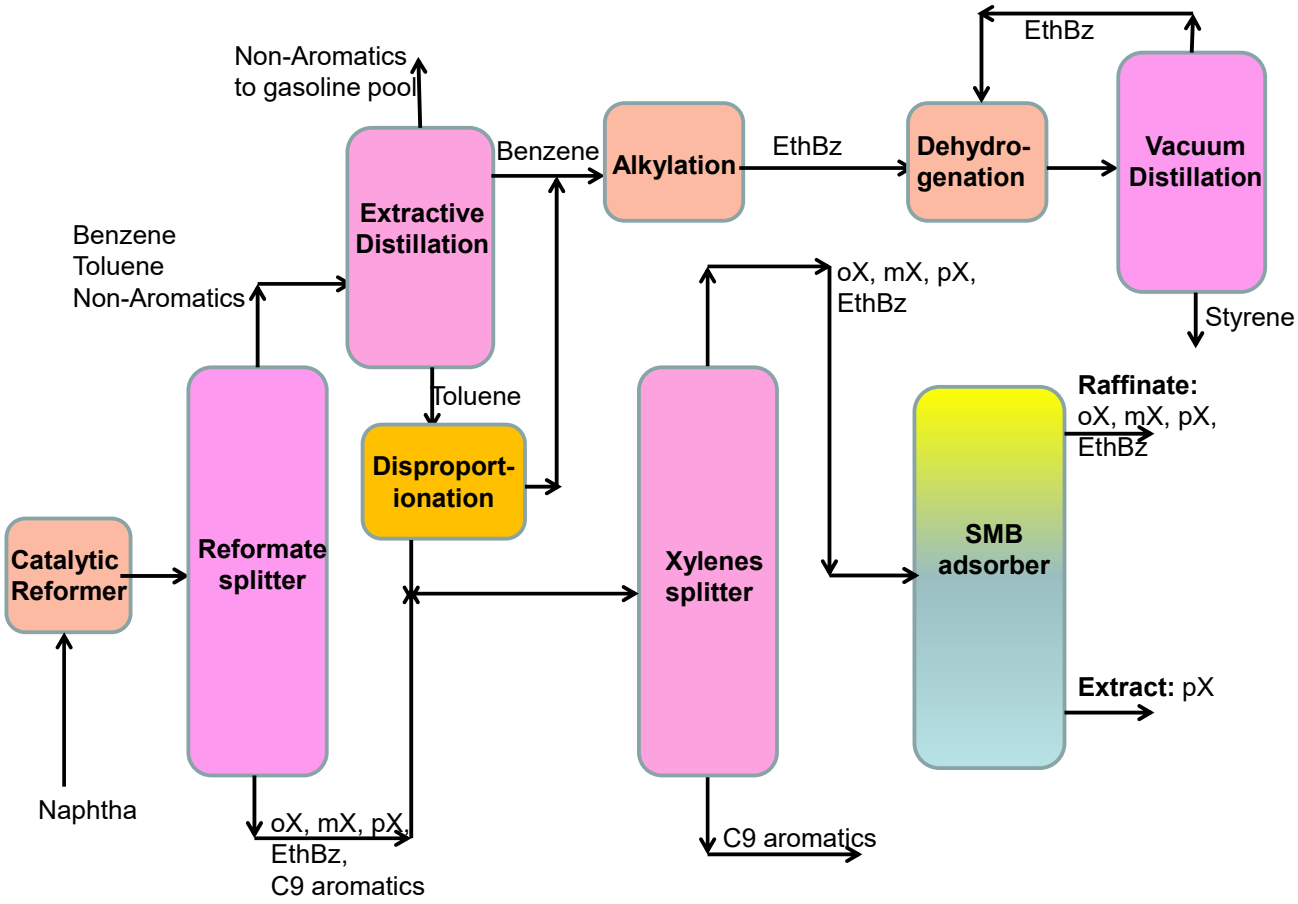

Figure S64. Schematic showing the separations of the products from a catalytic reforming unit.

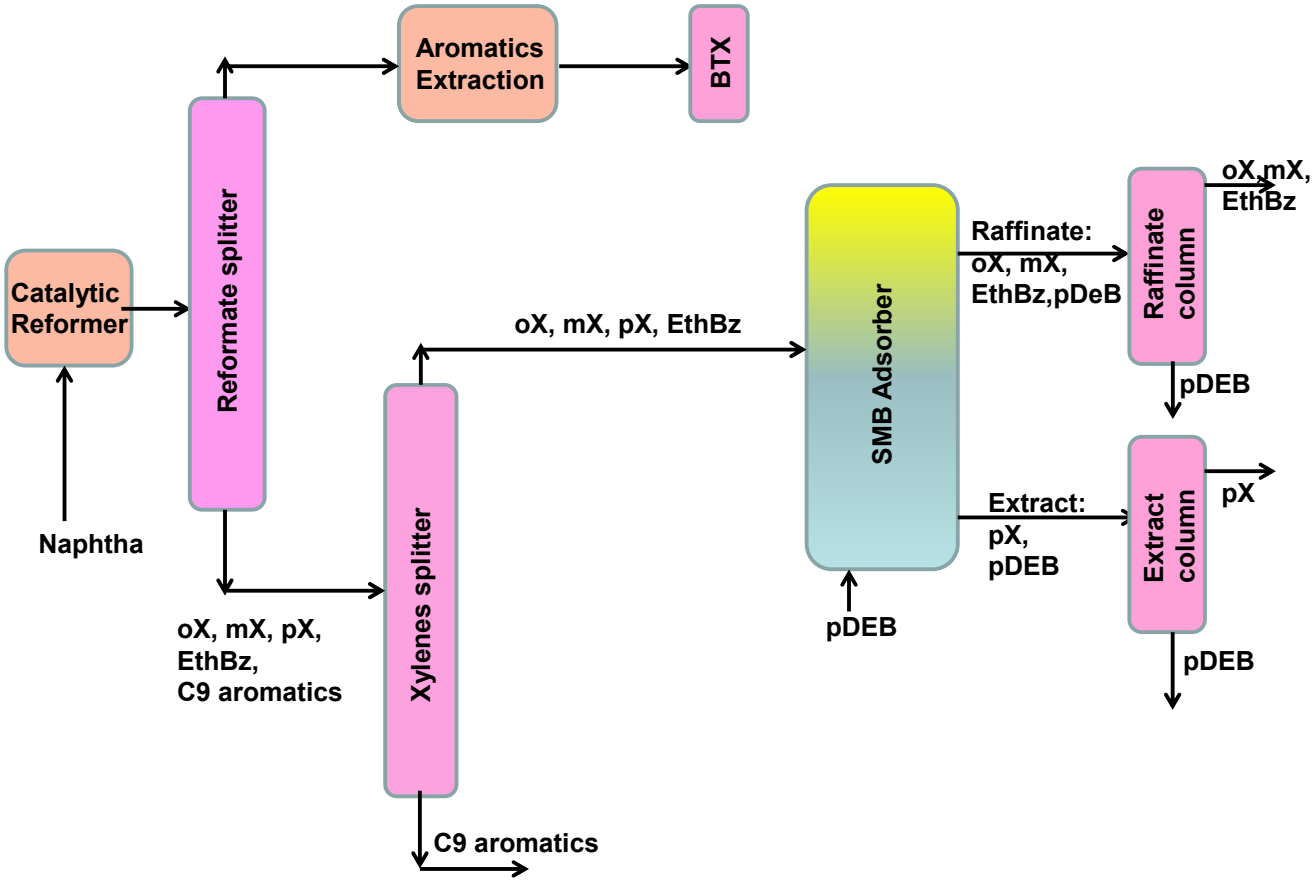

Figure S65. Schematic showing the separations of the products from a catalytic reforming unit.

Separation of xylene isomers

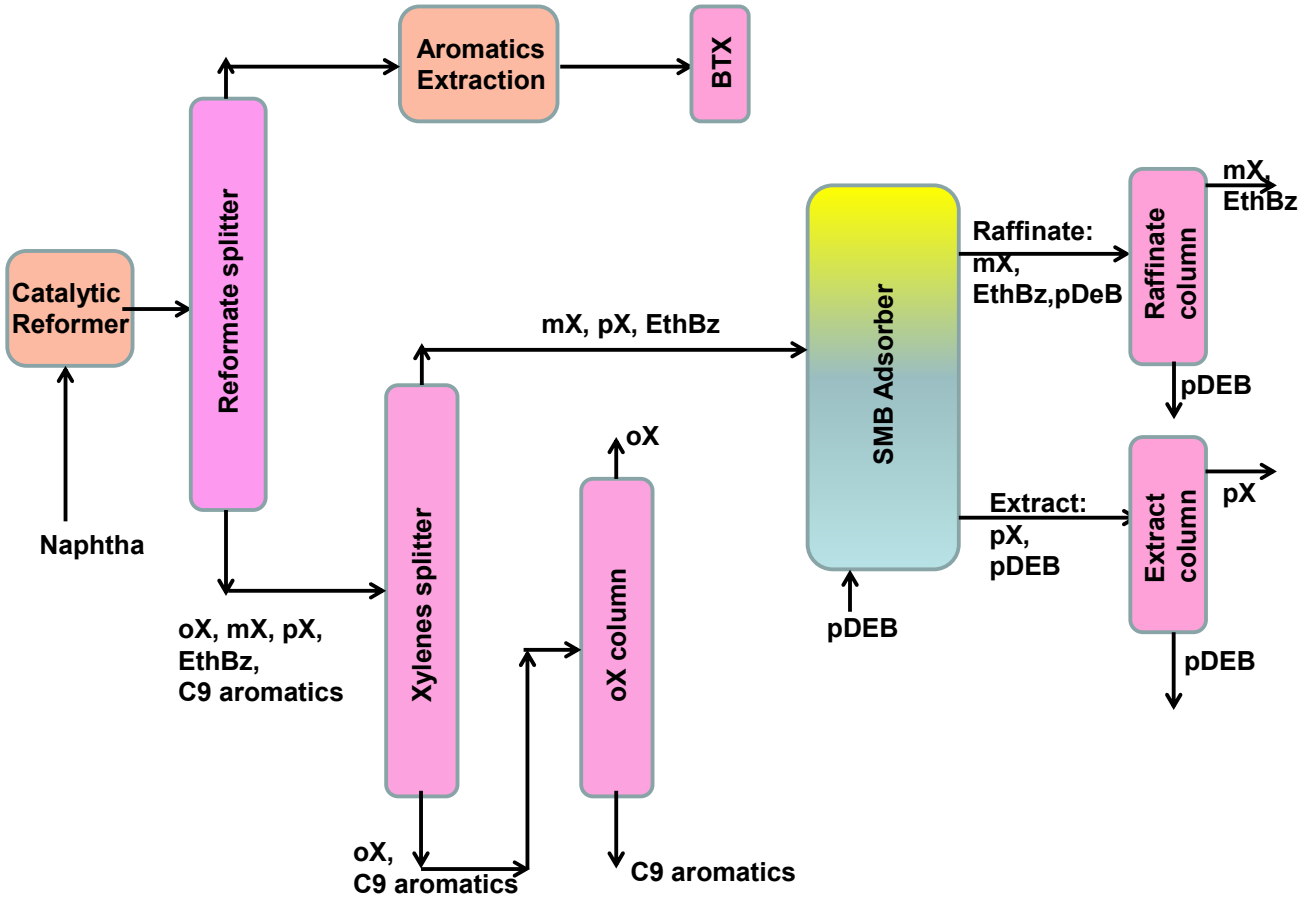

Figure S66. Schematic showing the separations of the products from a catalytic reforming unit.

Separation of xylene isomers

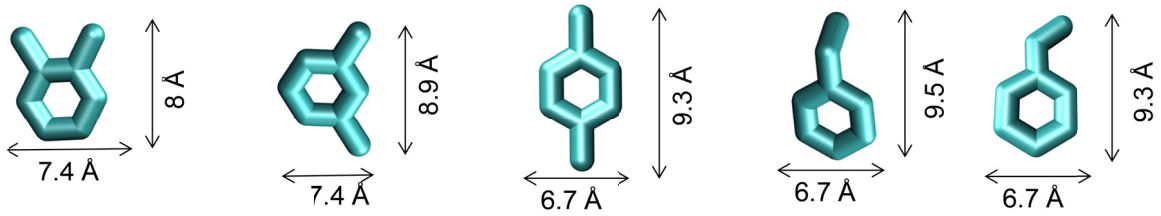

	o-xylene (oX)	m-xylene (mX)	p-xylene (pX)	Ethylbenzene (EtBz)	Styrene (St)
Boiling point	417.6 K	412.3 K	411.5 K	409 K	418.3 K
Freezing point	248 K	222 K	286 K	178 K	242.5 K

Figure S67. Boiling points, and freezing points of C8 hydrocarbons, along with the molecular dimensions, culled from Torres-Knoop et al.[120]

Separation of xylene isomers

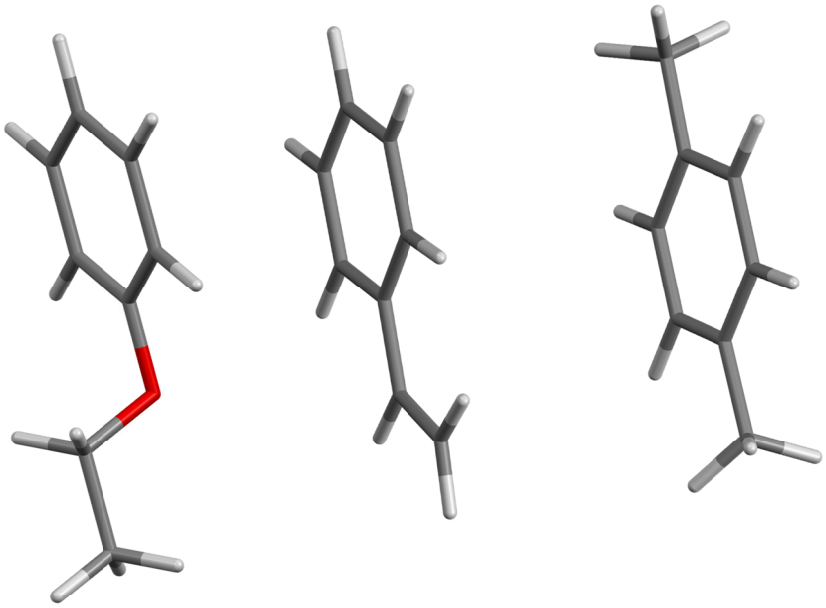

	Ethylbenzene (EtBz)	Styrene (St)	p-xylene (pX)
Boiling point / K	409.3	418.3	411.5
Freezing point / K	178.2	242.5	286.4

Figure S68. Planarity of aromatic molecules.

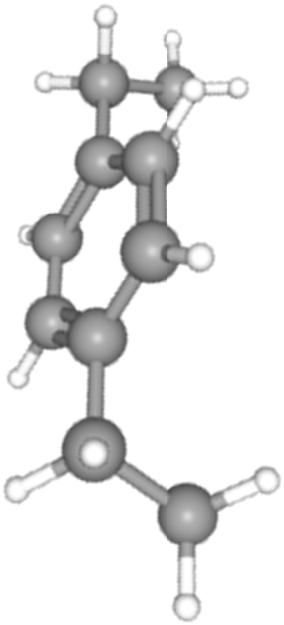

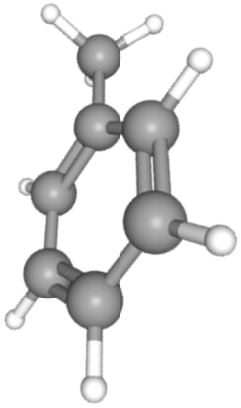

	pDEB	toluene
Boiling point	456 K	384 K
Freezing point	230 K	178 K

Figure S69. Desorbents used in SMB process for xylenes separations.

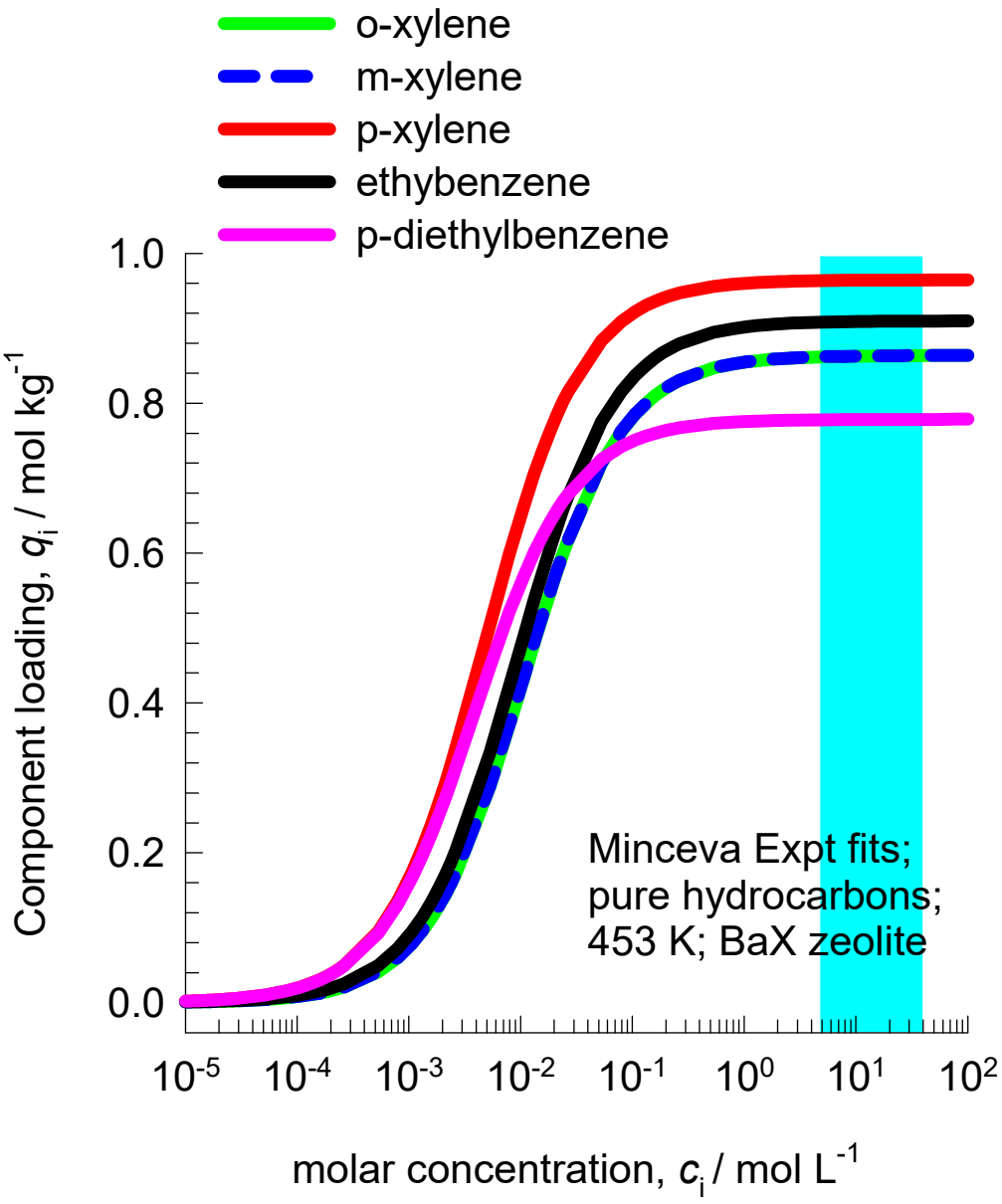

Figure S70. Pure component isotherms for hydrocarbons in BaX zeolite at 453 K, plotted using the Langmuir parameters reported by Minceva and Rodrigues.[114, 116]

Separation of xylene isomers

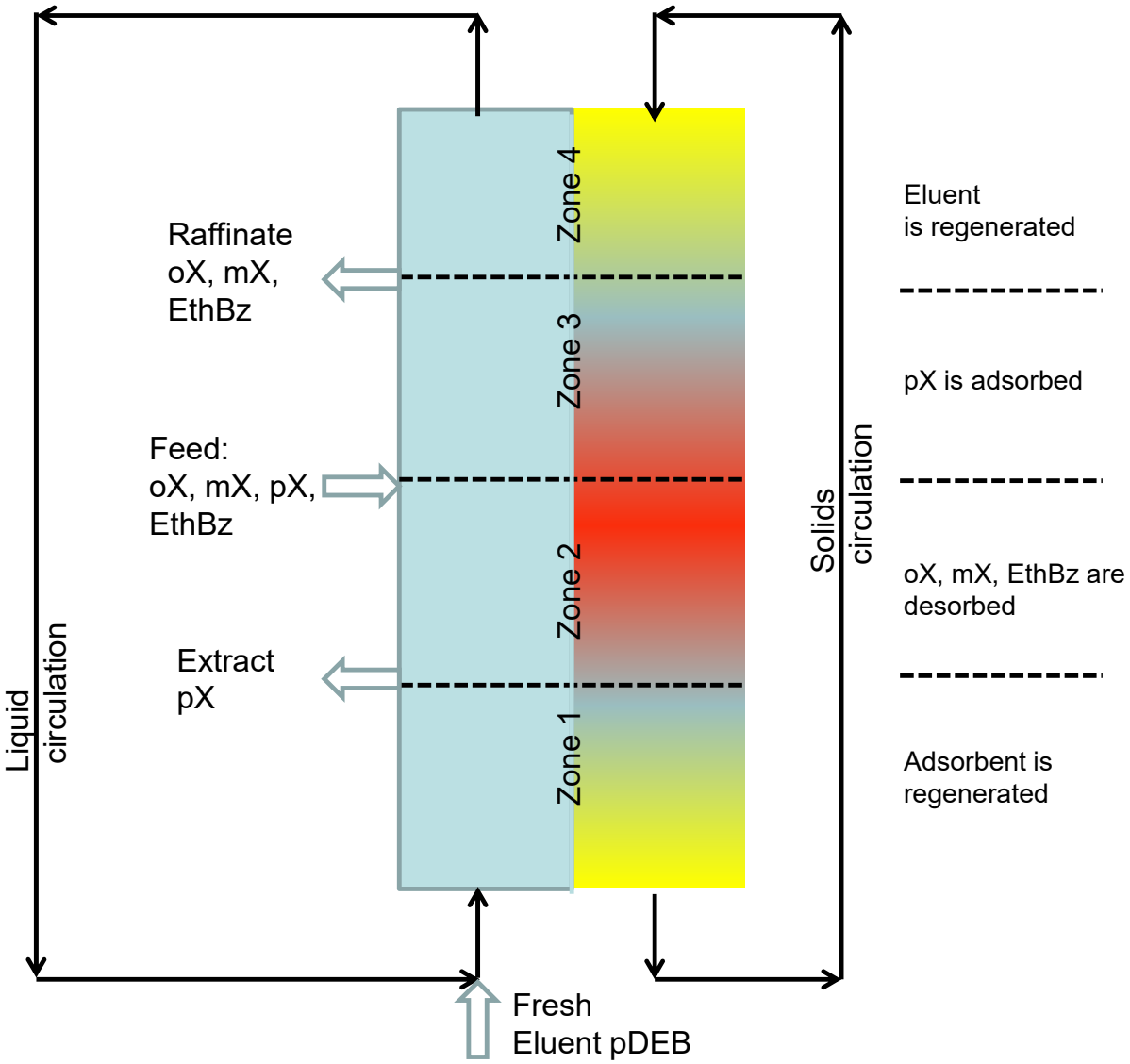

Figure S71. Moving bed adsorption technology for separation of feed mixture containing o-xylene/m-xylene/p-xylene/ethylbenzene. The simulated moving bed technology, used in industrial practice, is depicted here in its (mathematically) equivalent form of true moving bed with counter-current contacting between the downflowing adsorbent material and upflowing desorbent (eluent) liquid.

Separation of xylene isomers

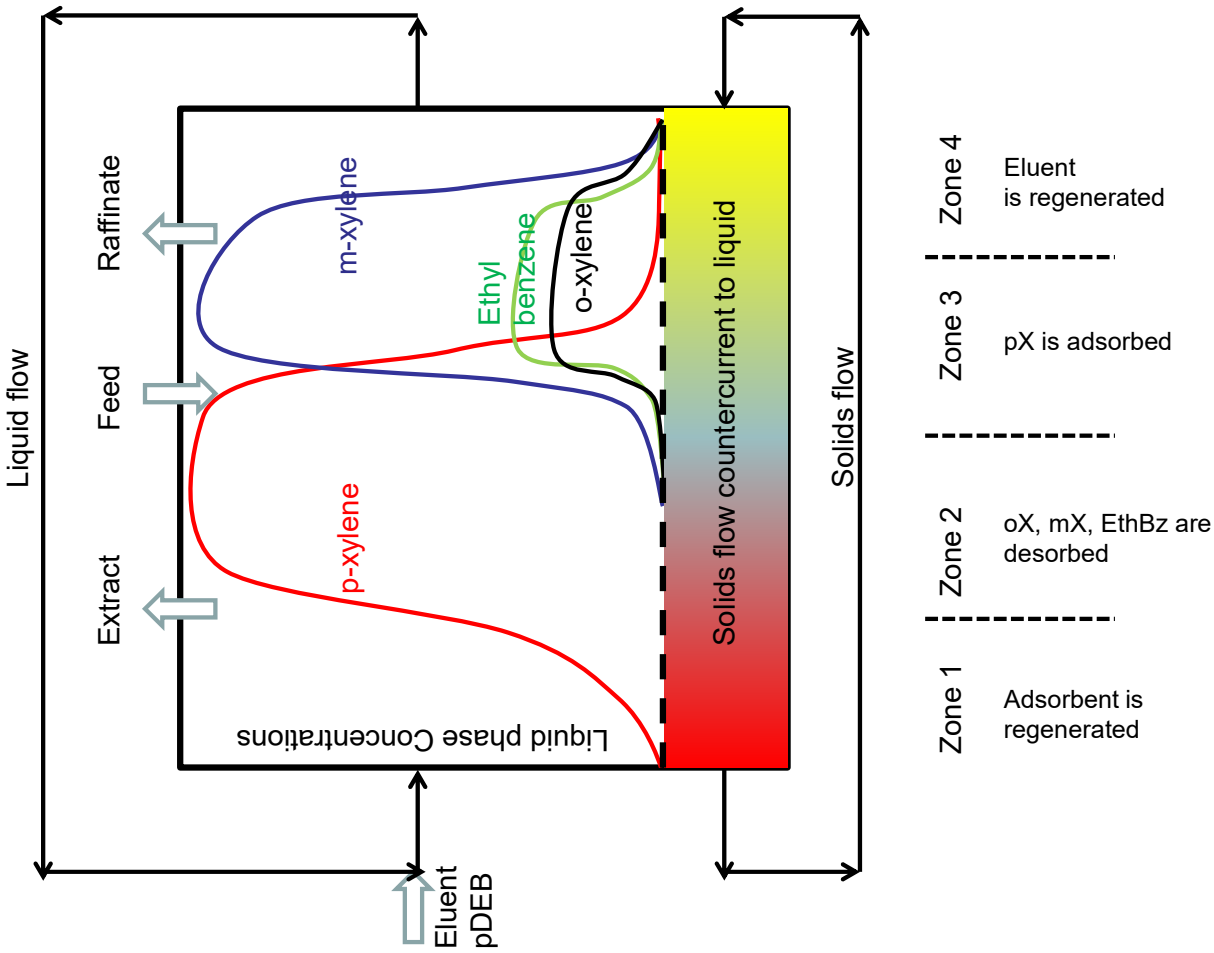

Figure S72. Qualitative representation of the liquid phase concentrations of a mixture of o-xylene/m-xylene/p-xylene/ethylbenzene in a SMB adorption unit with zeolite selective to p-xylene. The data shown are plotted using the information presented by Minceva and Rodrigues.[113]

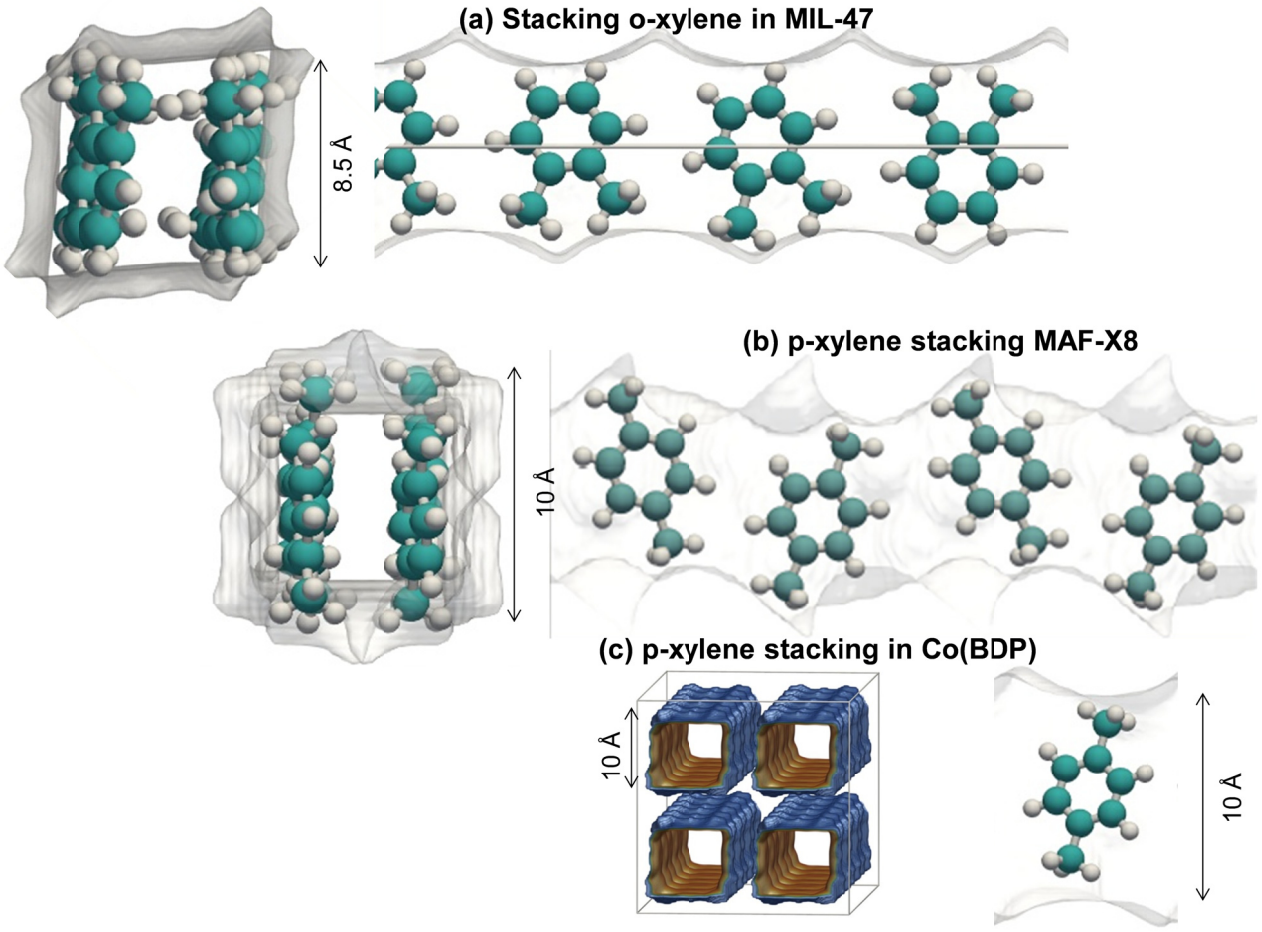

Figure S73. Snapshots, obtained from CBMC simulations [120], showing (a) stacking of o-xylene within 8.5 Å channels of MIL-47, (b) stacking of p-xylene within 10 Å channels of MAF-X8, and (c) Snapshots showing the stacking of p-xylene within 10 Å channels of Co(BDP).

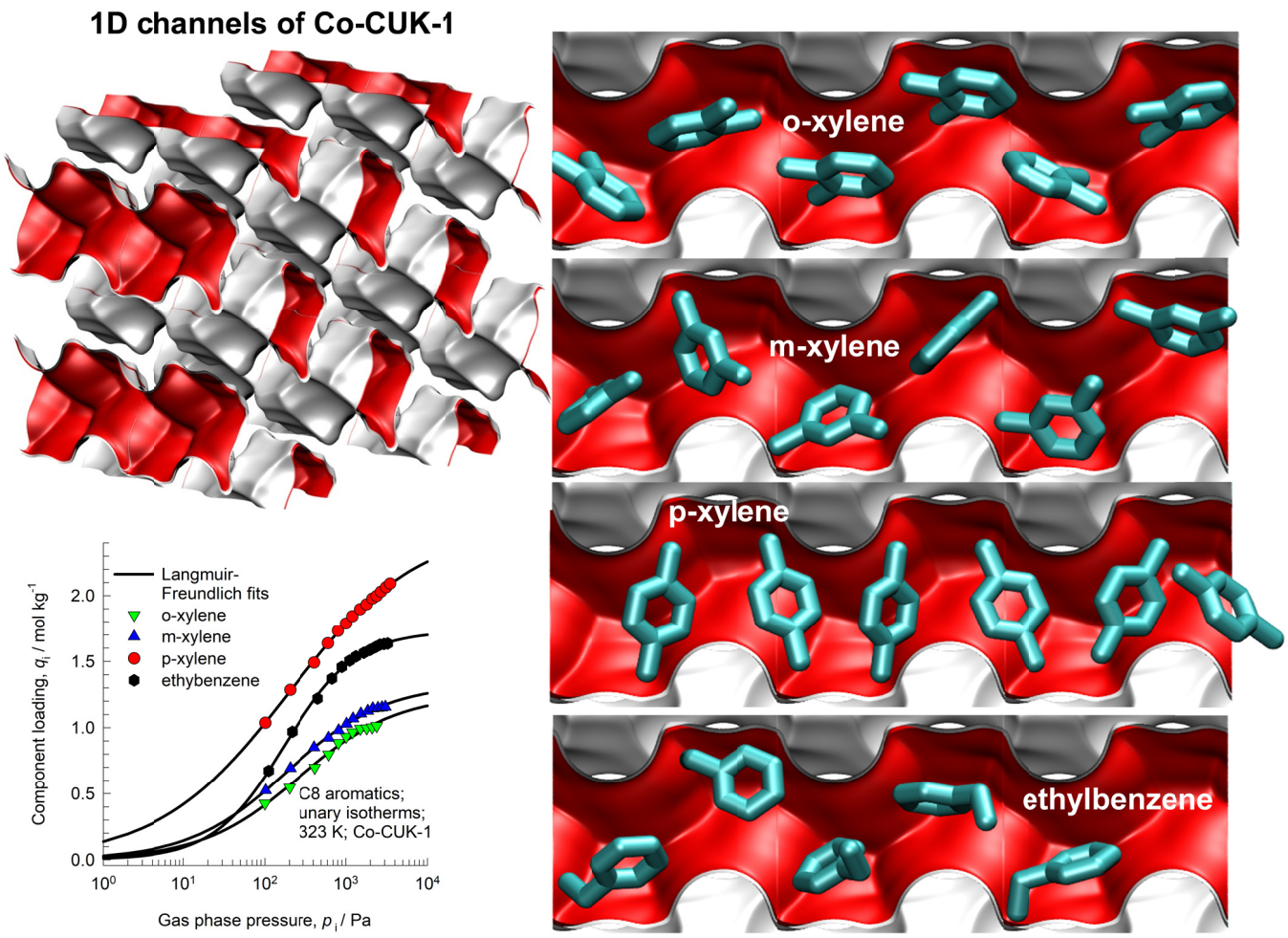

Figure S74. Snapshots, obtained from CBMC simulations, showing the stacking of o-xylene, m-xylene, p-xylene, and ethylbenzene within the 1D zig-zag shaped channels of Co-CUK-1. Also shown are the experimental data presented by Yoon et al.[124]

Separation of xylene isomers

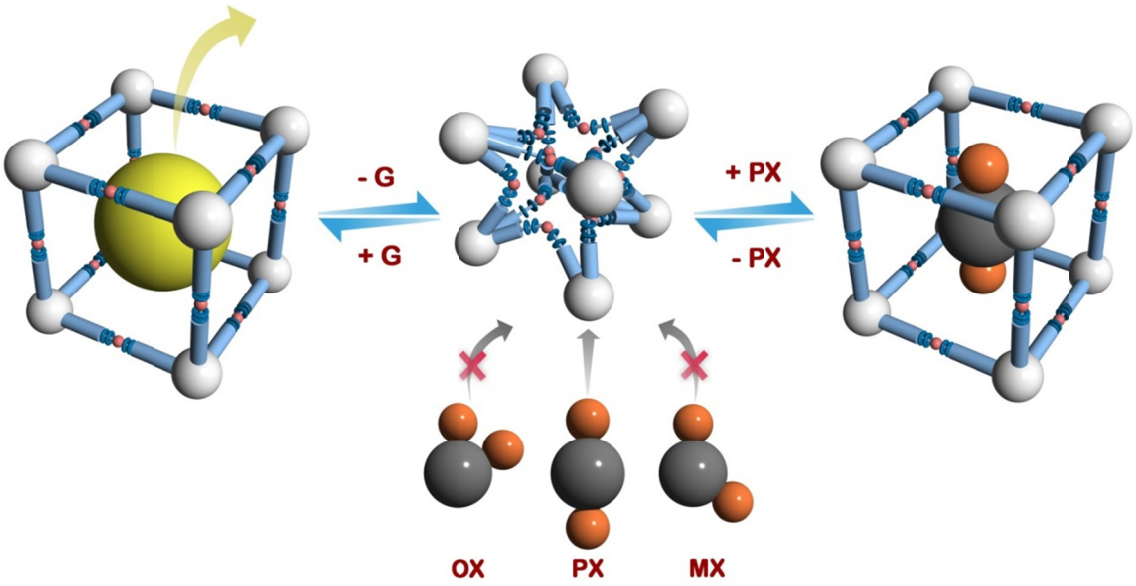

Figure S75. Schematic representation of the framework flexibility of DynaMOF-100 with selective accommodation of *p*-xylene from xylenes mixture.[125]

Separation of xylene isomers

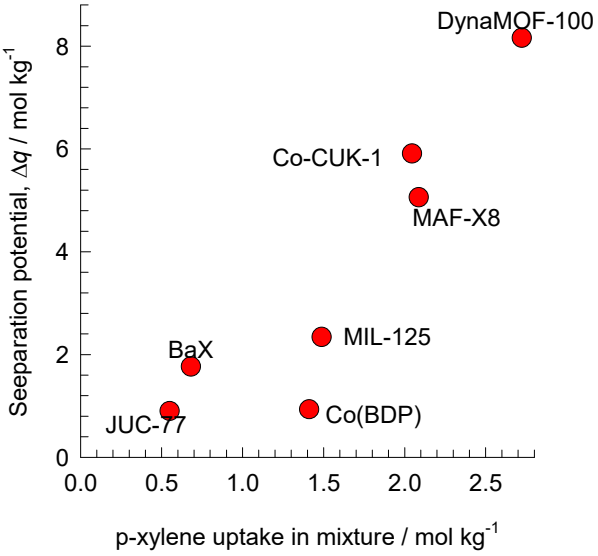

Figure S76. The separation potential, Δq for separation of equimolar 4-component o-xylene/m-xylene/p-xylene/ethylbenzene mixtures plotted against the gravimetric uptake of p-xylene. For each adsorbent, the conditions correspond to pore saturation.

Separation of xylene isomers

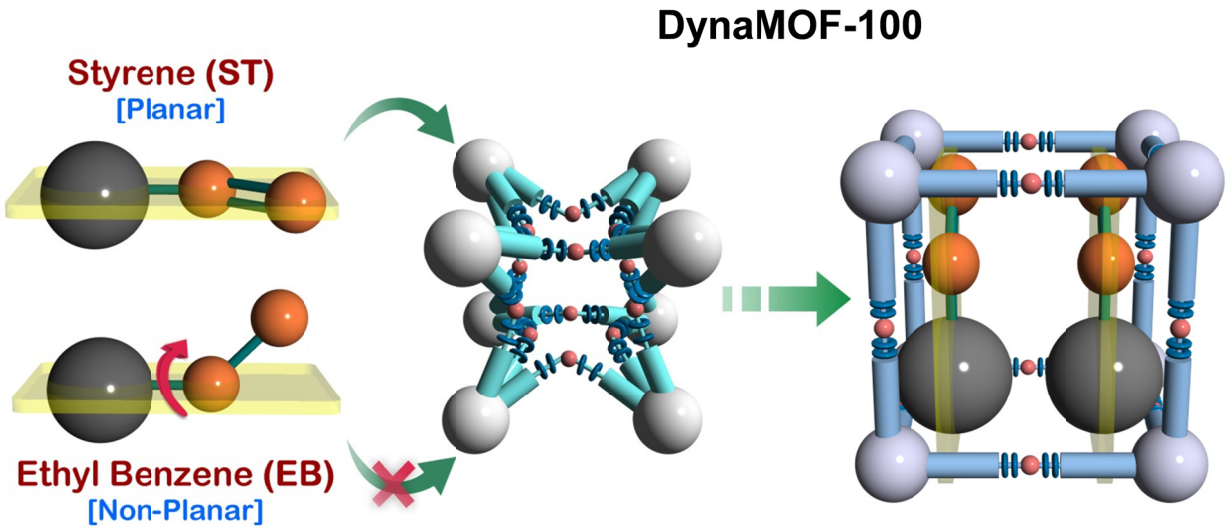

Figure S77. Schematic representation of the framework flexibility of DynaMOF-100 with selective accommodation of styrene from mixtures with ethylbenzene.[127]

Separation of xylene isomers

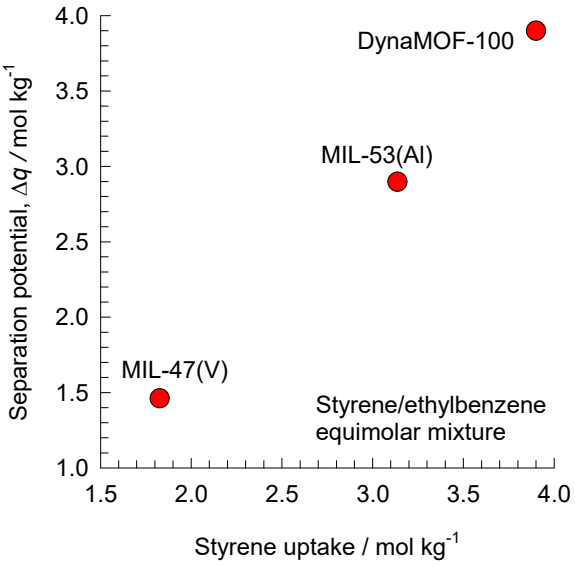

Figure S78. Plot of the separation potential, $\Delta q = q_{St} \frac{y_{EthBz}}{1 - y_{EthBz}} - q_{EthBz}$ vs styrene uptake capacity for equimolar styrene/ethylbenzene mixtures in MIL-47(V), MIL-53(Al), and DynaMOF-100. The calculations are from Krishna.[7]

15 Nomenclature

Latin alphabet

b_i	Langmuir parameter, Pa^{-1}
c_i	molar concentration of species *i*, mol m^{-3}
c_{i0}	molar concentration of species *i* in fluid mixture at inlet to adsorber, mol m^{-3}
c_t	total molar concentration in mixture, mol m^{-3}
$Đ_i$	Maxwell-Stefan diffusivity for molecule-wall interaction, m^2 s^{-1}
f_i	partial fugacity of species *i*, Pa
L	length of packed bed adsorber, m
m_{ads}	mass of adsorbent in packed bed, kg
n	number of species in the mixture, dimensionless
N_i	molar flux of species *i* with respect to framework, mol m^{-2} s^{-1}
p_i	partial pressure of species *i* in mixture, Pa
p_t	total system pressure, Pa
q_i	component molar loading of species *i*, mol kg^{-1}
$q_{i,sat}$	molar loading of species *i* at saturation, mol kg^{-1}
q_t	total molar loading in mixture, mol kg^{-1}
$\bar{q}_i(t)$	spatial-averaged component uptake of species *i*, mol kg^{-1}
Q	volumetric flow rate of gas mixture, m^3 s^{-1}
r	radial direction coordinate, m
r_c	radius of crystallite, m
R	gas constant, 8.314 J mol^{-1} K^{-1}
t	time, s
S_{ads}	adsorption selectivity, dimensionless

Nomenclature

T	absolute temperature, K
u	superficial gas velocity in packed bed, m s^{-1}
v	interstitial gas velocity in packed bed, m s^{-1}
x_i	mole fraction of species *i* in adsorbed phase, dimensionless
y_i	mole fraction of species *i* in the bulk fluid phase, dimensionless
z	distance along the adsorber, m

Greek alphabet

Γ_{ij}	thermodynamic factors, dimensionless
ε	voidage of packed bed, dimensionless
μ_i	molar chemical potential, J mol^{-1}
ρ	framework density, kg m^{-3}
τ	time, dimensionless

Subscripts

i	referring to component *i*
t	referring to total mixture
sat	referring to saturation conditions
0	referring to conditions at inlet to fixed bed*i*

16 References

(1) Materials for Separation Technologies: Energy and Emission Reduction Opportunities. U.S. Department of Energy, Energy Efficiency and Renewable Energy, 2005.

(2) Yang, R. T. *Adsorbents: Fundamentals and Applications*. John Wiley & Sons, Inc.: Hoboken, New Jersey, 2003.

(3) Ruthven, D. M. *Principles of Adsorption and Adsorption Processes*. John Wiley: New York, 1984.

(4) Sircar, S.; Myers, A. L. *Gas Separation by Zeolites, Chapter 22*. Handbook of Zeolite Science and Technology; Edited by S.M. Auerbach, K.A. Carrado and P.K. Dutta, 1063-1104, Marcel Dekker: New York, 2003.(

(5) Myers, A. L.; Prausnitz, J. M. Thermodynamics of Mixed Gas Adsorption. *A.I.Ch.E.J.* **1965**, *11*, 121-130.

(6) Siperstein, F. R.; Myers, A. L. Mixed-Gas Adsorption. *A.I.Ch.E.J.* **2001**, *47*, 1141-1159.

(7) Krishna, R. Screening Metal-Organic Frameworks for Mixture Separations in Fixed-Bed Adsorbers using a Combined Selectivity/Capacity Metric. *RSC Adv.* **2017**, *7*, 35724-35737. https://doi.org/10.1039/C7RA07363A.

(8) Krishna, R. Methodologies for Evaluation of Metal-Organic Frameworks in Separation Applications. *RSC Adv.* **2015**, *5*, 52269-52295.

(9) Krishna, R. The Maxwell-Stefan Description of Mixture Diffusion in Nanoporous Crystalline Materials. *Microporous Mesoporous Mater.* **2014**, *185*, 30-50.

(10) Krishna, R. Tracing the Origins of Transient Overshoots for Binary Mixture Diffusion in Microporous Crystalline Materials. *Phys. Chem. Chem. Phys.* **2016**, *18*, 15482-15495.

(11) Krishna, R.; Baur, R. Modelling Issues in Zeolite Based Separation Processes. *Sep. Purif. Technol.* **2003**, *33*, 213-254.

(12) Krishna, R.; Baur, R. Diffusion, Adsorption and Reaction in Zeolites: Modelling and Numerical Issues. http://krishna.amsterchem.com/zeolite/, University of Amsterdam, Amsterdam, 1 January 2015.

(13) Ruthven, D. M.; Farooq, S.; Knaebel, K. S. *Pressure swing adsorption*. VCH Publishers: New York, 1994.

(14) Krishna, R. Highlighting the Influence of Thermodynamic Coupling on Kinetic Separations with Microporous Crystalline Materials. *ACS Omega* **2019**, *4*, 3409-3419. https://doi.org/10.1021/acsomega.8b03480.

(15) Krishna, R.; van Baten, J. M.; Baur, R. Highlighting the Origins and Consequences of Thermodynamic Nonidealities in Mixture Separations using Zeolites and Metal-Organic Frameworks. *Microporous Mesoporous Mater.* **2018**, *267*, 274-292. http://dx.doi.org/10.1016/j.micromeso.2018.03.013.

(16) Krishna, R.; Van Baten, J. M. Investigating the Non-idealities in Adsorption of CO_2-bearing Mixtures in Cation-exchanged Zeolites. *Sep. Purif. Technol.* **2018**, *206*, 208-217. https://doi.org/10.1016/j.seppur.2018.06.009.

(17) Krishna, R.; Van Baten, J. M. Elucidation of Selectivity Reversals for Binary Mixture Adsorption in Microporous Adsorbents. *ACS Omega* **2020**, *5*, 9031-9040. https://doi.org/10.1021/acsomega.0c01051.

References

(18) van Zandvoort, I.; Ras, E.-J.; de Graaf, R.; Krishna, R. Using Transient Breakthrough Experiments for Screening of Adsorbents for Separation of C_2H_4/CO_2 Mixtures *Sep. Purif. Technol.* **2020**, *241*, 116706. https://doi.org/10.1016/j.seppur.2020.116706.

(19) van Zandvoort, I.; van der Waal, J. K.; Ras, E.-J.; de Graaf, R.; Krishna, R. Highlighting non-idealities in C_2H_4/CO_2 mixture adsorption in 5A zeolite. *Sep. Purif. Technol.* **2019**, *227*, 115730. https://doi.org/10.1016/j.seppur.2019.115730.

(20) Kooijman, H. A.; Taylor, R. A dynamic nonequilibrium model of tray distillation columns. *A.I.Ch.E.J.* **1995**, *41*, 1852-1863.

(21) Michelsen, M. An efficient general purpose method of integration of stiff ordinary differential equations. *A.I.Ch.E.J.* **1976**, *22*, 594-597.

(22) Bulirsch, R.; Stoer, J. Numerical treatment of ordinary differential equations by extrapolation methods. *Numer. Math.* **1966**, *8*, 1-14.

(23) Krishna, R.; van Baten, J. M. Investigating the potential of MgMOF-74 membranes for CO_2 capture. *J. Membr. Sci.* **2011**, *377*, 249-260.

(24) He, Y.; Krishna, R.; Chen, B. Metal-Organic Frameworks with Potential for Energy-Efficient Adsorptive Separation of Light Hydrocarbons. *Energy Environ. Sci.* **2012**, *5*, 9107-9120.

(25) Krishna, R.; Long, J. R. Screening metal-organic frameworks by analysis of transient breakthrough of gas mixtures in a fixed bed adsorber. *J. Phys. Chem. C* **2011**, *115*, 12941-12950.

(26) Chen, X.; Plonka, A. M.; Banerjee, D.; Krishna, R.; Schaef, H. T.; Ghose, D.; Thallapally, P. K.; Parise, J. B. Direct Observation of Xe and Kr Adsorption in a Xe-selective Microporous Metal Organic Framework. *J. Am. Chem. Soc.* **2015**, *137*, 7007-7010.

(27) Banerjee, D.; Cairns, A. J.; Liu, J.; Krishna, R.; Thallapally, P. K.; Strachan, D. M. Potential of Metal-Organic Frameworks for Capture of Noble Gases. *Acc. Chem. Res.* **2015**, *48*, 211-219.

(28) Kluge, G.; Franke, T.; Schöllner, R.; Nagel, G. Estimation of Component Loadings in Fixed-Bed Adsorption from Breakthrough Curves of Binary Gas Mixtures in Nontrace Systems. *Chem. Eng. Sci.* **1991**, *46*, 368-371.

(29) Malek, A.; Farooq, S. Effect of Velocity Variation on Equilibrium Calculations from Multicomponent Breakthrough Experiments. *Chem. Eng. Sci.* **1997**, *52*, 443-447.

(30) Sircar, S.; Golden, T. C. Purification of Hydrogen by Pressure Swing Adsorption. *Separ. Sci. Technol.* **2000**, *35*, 667-687.

(31) Ribeiro, A. M.; Grande, C. A.; Lopes, F. V. S.; Loureiro, J. M.; Rodrigues, A. E. A parametric study of layered bed PSA for hydrogen purification. *Chem. Eng. Sci.* **2008**, *63*, 5258-5273.

(32) Banu, A. M.; Friedrich, D.; Brandani, S.; Düren, T. A Multiscale Study of MOFs as Adsorbents in H_2 PSA Purification. *Ind. Eng. Chem. Res.* **2013**, *52*, 9946-9957.

(33) Majlan, E. H.; Daud, W. R. W.; Iyuke, S. E.; Mohamad, A. B.; Kadhum, A. H.; Mohammad, A. W.; Takriff, M. S.; Bahaman, N. Hydrogen purification using compact pressure swing adsorption system for fuel cell. *Int. J. Hydrogen Energy* **2009**, *34*, 2771-2777.

(34) Pakseresht, S.; Kazemeini, M.; Akbarnejad, M. M. Equilibrium isotherms for CO, CO_2, CH_4 and C_2H_4 on the 5A molecular sieve by a simple volumetric apparatus. *Sep. Purif. Technol.* **2002**, *28*, 53-60.

(35) Sircar, S. Basic research needs for design of adsorptive gas separation processes *Ind. Eng. Chem. Res.* **2006**, *45*, 5435-5448.

(36) Belmabkhout, Y.; Pirngruber, G.; Jolimaitre, E.; Methivier, A. A complete experimental approach for synthesis gas separation studies using static gravimetric and column breakthrough experiments. *Adsorption* **2007**, *13*, 341-349.

(37) Mofarahi, M.; Gholipour, F. Gas Adsorption Separation of CO_2/CH_4 System using Zeolite 5A. *Microporous Mesoporous Mater.* **2014**, *200*, 47-54.

(38) Bakhtyari, A.; Mofarahi, M. Pure and Binary Adsorption Equilibria of Methane and Nitrogen on Zeolite 5A. *J. Chem. Eng. Data* **2014**, *59*, 626-639.

(39) Jamali, S.; Mofarahi, M.; Rodrigues, A. E. Investigation of a novel combination of adsorbents for hydrogen purification using Cu-BTC and conventional adsorbents in pressure swing adsorption. *Adsorption* **2018**, *24*, 481-498. https://doi.org/10.1007/s10450-018-9955-0.

(40) Matsuda, R.; Kitaura, R.; Kitagawa, S.; Kubota, Y.; Belosludov, R. V.; Kobayashi, T. C.; Sakamoto, H.; Chiba, T.; Takata, M.; Kawazoe, Y.; Mita, Y. Highly controlled acetylene accommodation in a metal–organic microporous material. *Nature* **2005**, *436*, 238-241.

(41) Fischer, M.; Hoffmann, F.; Fröba, M. New Microporous Materials for Acetylene Storage and C_2H_2/CO_2 Separation: Insights from Molecular Simulations. *ChemPhysChem* **2010**, *11*, 2220-2229.

(42) Wang, L.; Yang, L.; Gong, L.; Krishna, R.; Gao, Z.; Tao, Y.; Yin, W.; Xu, Z.; Luo, F. Constructing redox-active microporous hydrogen-bonded organic framework by imide-functionalization: photochromism, electrochromism, and selective adsorption of C_2H_2 over CO_2. *Chem. Eng. J.* **2020**, *383*, 123117. https://dx.doi.org/10.1016/j.cej.2019.123117.

(43) Gao, J.; Qian, X.; Lin, R.-B.; Krishna, R.; Wu, H.; Zhou, W.; Chen, B. Mixed Metal-Organic Framework with Multiple Binding Sites for Efficient C_2H_2/CO_2 Separation. *Angew. Chem. Int. Ed.* **2020**, *59*, 4396-4400. https://doi.org/10.1002/anie.202000323.

(44) Liu, R.; Liu, Q.-Y.; Krishna, R.; Wang, W.; He, C.-T.; Wang, Y.-L. Water-stable Europium-1,3,6,8-tetrakis(4-carboxylphenyl)pyrene Framework for Efficient C_2H_2/CO_2 Separation. *Inorg. Chem.* **2019**, *58*, 5089-5095. https://doi.org/10.1021/acs.inorgchem.9b00169.

(45) Ye, Y.; Ma, Z.; Lin, R.-B.; Krishna, R.; Zhou, W.; Lin, Q.; Zhang, Z.; Xiang, S.; Chen, B. Pore Space Partition within a Metal-Organic Framework for Highly Efficient C_2H_2/CO_2 Separation. *J. Am. Chem. Soc.* **2019**, *141*, 4130-4136. https://doi.org/10.1021/jacs.9b00232.

(46) Wu, H. C.; Yan, C. S.; Luo, F.; Krishna, R. Beyond Crystal Engineering: Significant Enhancement of C_2H_2/CO_2 Separation by Constructing Composite Material. *Inorg. Chem.* **2018**, *57*, 3679-3682. http://dx.doi.org/doi:10.1021/acs.inorgchem.8b00341.

(47) Foo, M. L.; Matsuda, R.; Hijikata, Y.; Krishna, R.; Sato, H.; Horike, S.; Hori, A.; Duan, J.; Sato, Y.; Kubota, Y.; Takata, M.; Kitagawa, S. An Adsorbate Discriminatory Gate Effect in a Flexible Porous Coordination Polymer for Selective Adsorption of CO_2 over C_2H_2. *J. Am. Chem. Soc.* **2016**, *138*, 3022-3030.

(48) Luo, F.; Yan, C.; Dang, L.; Krishna, R.; Zhou, W.; Wu, H.; Dong, X.; Han, Y.; Hu, T.-L.; O'Keeffe, M.; Wang, L.; Luo, M.; Lin, R.-B.; Chen, B. UTSA-74: A MOF-74 Isomer with Two Accessible Binding Sites per Metal Center for Highly Selective Gas Separation. *J. Am. Chem. Soc.* **2016**, *138*, 5678-5684.

(49) Duan, J.; Jin, W.; Krishna, R. Natural Gas Purification Using a Porous Coordination Polymer with Water and Chemical Stability. *Inorg. Chem.* **2015**, *54*, 4279-4284.

(50) Li, P.; He, Y.; Zhao, Y.; Weng, L.; Wang, H.; Krishna, R.; Wu, H.; Zhou, W.; O'Keeffe, M.; Han, Y.; Chen, B. A Rod-Packing Microporous Hydrogen-Bonded Organic Framework for Highly Selective Separation of C_2H_2/CO_2 at Room Temperature. *Angew. Chem. Int. Ed.* **2015**, *54*, 574-577.

(51) Chen, K.-J.; Scott, H. S.; Madden, D. G.; Pham, T.; Kumar, A.; Bajpai, A.; Lusi, M.; Forrest, K. A.; Space, B.; Perry IV, J. J.; Zaworotko, M. J. Benchmark C_2H_2/CO_2 and CO_2/C_2H_2 Separation by Two Closely Related Hybrid Ultramicroporous Materials. *Chem* **2016**, *1*, 753-765. https://dx.doi.org/10.1016/j.chempr.2016.10.009.

(52) Lee, J.; Chuah, C. Y.; Kim, J.; Kim, Y.; Ko, N.; Seo, Y.; Kim, K.; Bae, T. H.; Lee, E. Separation of Acetylene from Carbon Dioxide and Ethylene by a Water-Stable Microporous Metal–Organic Framework with Aligned Imidazolium Groups inside the Channels. **2018**, *130*, 7995-7999. https://doi.org/10.1002/anie.201804442.

(53) Scott, H. S.; Shivanna, M.; Bajpai, A.; Madden, D. G.; Chen, K.-J.; Pham, T.; Forrest, K. A.; Hogan, A.; Space, B.; Perry IV, J. J.; Zaworotko, M. J. Highly Selective Separation of C2H2 from CO2 by a New Dichromate-Based Hybrid Ultramicroporous Material. *ACS Appl. Mater. Interfaces* **2017**, *9*, 33395-33400. http://dx.doi.org/doi:10.1021/acsami.6b15250.

(54) Qazvini, O. T.; Babarao, R.; Telfer, S. G. Multipurpose Metal−Organic Framework for the Adsorption of Acetylene: Ethylene Purification and Carbon Dioxide Removal. *Chem. Mater.* **2019**, *31*, 4919-4926. https://doi.org/10.1021/acs.chemmater.9b01691.

(55) Tagliabue, M.; Farrusseng, D.; Valencia, S.; Aguado, S.; Ravon, U.; Rizzo, C.; Corma, A.; Mirodatos, C. Natural gas treating by selective adsorption: Material science and chemical engineering interplay. *Chem. Eng. J.* **2009**, *155*, 553-566.

(56) Bhadra, S. J.; Farooq, S. Separation of MethaneNitrogen Mixture by Pressure Swing Adsorption for Natural Gas Upgrading. *Ind. Eng. Chem. Res.* **2011**, *50*, 14030-14045.

(57) Yoon, J. W.; Chang, H.; Lee, S.-J.; Hwang, Y. K.; Hong, D.-Y.; Lee, S.-K.; Lee, J. S.; Jang, S.; Yoon, T.-U.; Kwac, K.; Jung, Y.; Pillai, R. S.; Faucher, F.; Vimont, A.; Daturi, M.; Férey, G.; Serre, C.; Maurin, G.; Bae, Y.-S.; Chang, J.-S. Selective Nitrogen Capture by Porous Hybrid Materials Containing Accessible Transition Metal Ion Sites. *Nature Materials* **2017**, *16*, 526-531.

(58) Majumdar, B.; Bhadra, S. J.; Marathe, R. P.; Farooq, S. Adsorption and Diffusion of Methane and Nitrogen in Barium Exchanged ETS-4. *Ind. Eng. Chem. Res.* **2011**, *50*, 3021-3034.

(59) Jayaraman, A.; Hernandez-Maldonado, A. J.; Yang, R. T.; Chinn, D.; Munson, C. L.; Mohr, D. H. Clinoptilolites for Nitrogen/Methane Separation. *Chem. Eng. Sci.* **2004**, *59*, 2407-2417.

(60) Habgood, H. W. The Kinetics of Molecular Sieve Action. Sorption of Nitrogen-Methane Mixtures by Linde Molecular Sieve 4A. *Canad. J. Chem.* **1958**, *36*, 1384-1397.

(61) Kuznicki, S. M.; Bell, V. A.; Nair, S.; Hillhouse, H. W.; Jacubinas, R. M.; Braunbarth, C. M.; Toby, B. H.; Tsapatsis, M. A titanosilicate molecular sieve with adjustable pores for size-selective adsorption of molecules. *Nature* **2001**, *412*, 720-724.

(62) Bhadra, S. J. *Methane-Nitrogen Separation by Pressure Swing Adsorption*. Ph.D. Dissertation, National University of Singapore, Singapore, 2007.

(63) Farooq, S.; Ruthven, D. M.; Boniface, H. A. Numerical-Simulation of a Pressure Swing Adsorption Oxygen Unit. *Chem. Eng. Sci.* **1989**, *44*, 2809-2816.

(64) Rama Rao, V.; Farooq, S.; Krantz, W. B. Design of a Two-Step Pulsed Pressure-Swing Adsorption-Based Oxygen Concentrator. *A.I.Ch.E.J.* **2010**, *56*, 354-370.

(65) Rama Rao, V. *Adsorption based portable oxygen concentrator for personal medical applications*. Ph.D. Dissertation, National University of Singapore, Singapore, 2011.

(66) Ritter, J. A. Development of Pressure Swing Adsorption Technology for Spaceflight Oxygen Concentrators. http://www.dsls.usra.edu/meetings/hrp2010/pdf/Friday/Ritter.pdf, NASA Human Research Program, Houston, 2010.

(67) Ruthven, D. M.; Farooq, S. Air Separation by Pressure Swing Adsorption. *Gas Sep. Purif.* **1990**, *4*, 141-148.

(68) Yang, R. T. *Gas separation by adsorption processes*. Butterworth: Boston, 1987.

(69) Farooq, S.; Rathor, M. N.; Hidajat, K. A Predictive Model for a Kinetically Controlled Pressure Swing Adsorption Separation Process. *Chem. Eng. Sci.* **1993**, *48*, 4129-4141.

(70) Farooq, S. Sorption and Diffusion of Oxygen and Nitrogen in Molecular- Sieve RS-10. *Gas Sep. Purif.* **1995**, *9*, 205-212.

(71) Bloch, E. D.; Queen, W. L.; Krishna, R.; Zadrozny, J. M.; Brown, C. M.; Long, J. R. Hydrocarbon Separations in a Metal-Organic Framework with Open Iron(II) Coordination Sites. *Science* **2012**, *335*, 1606-1610.

(72) Khalighi, M.; Chen, Y. F.; Farooq, S.; Karimi, I. A.; Jiang, J. W. Propylene/Propane Separation Using SiCHA. *Ind. Eng. Chem. Res.* **2013**, *52*, 3877-3892.

(73) Da Silva, F. A.; Rodrigues, A. E. Vacuum swing adsorption for propylene/propane separation with 4A zeolite. *Ind. Eng. Chem. Res.* **2001**, *40*, 5758-5774.

(74) Grande, C. A.; Poplow, F.; Rodrigues, A. E. Vacuum pressure swing adsorption to produce polymer-grade polypropylene. *Separ. Sci. Technol.* **2010**, *45*, 1252-1259.

(75) Da Silva, F. A.; Rodrigues, A. E. PropylenePropane Separation by Vacuum Swing Adsorption Using 13X Zeolite. *A.I.Ch.E.J.* **2001**, *47*, 341-357.

(76) Geier, S. J.; Mason, J. A.; Bloch, E. D.; Queen, W. L.; Hudson, M. R.; Brown, C. M.; Long, J. R. Selective adsorption of ethylene over ethane and propylene over propane in the metal–organic frameworks M_2(dobdc) (M = Mg, Mn, Fe, Co, Ni, Zn). *Chem. Sci.* **2013**, *4*, 2054-2061.

(77) Yoon, J. W.; Jang, I. T.; Lee, K.-Y.; Hwang, Y. K.; Chang, J.-S. Adsorptive Separation of Propylene and Propane on a Porous Metal-Organic Framework, Copper Trimesate. *Bull. Korean Chem. Soc.* **2010**, *31*, 220-223.

(78) Khalighi, M.; Karimi, I. A.; Farooq, S. Comparing SiCHA and 4A Zeolite for Propylene/Propane Separation using a Surrogate-Based Simulation/Optimization Approach. *Ind. Eng. Chem. Res.* **2014**, *53*, 16973-16983.

(79) Olson, D. H.; Camblor, M. A.; Vallaescusa, L. A.; Kuehl, G. H. Light hydrocarbon sorption properties of pure silica Si-CHA and ITQ-3 and high silica ZSM-58. *Microporous Mesoporous Mater.* **2004**, *67*, 27-33.

(80) Hedin, N.; DeMartin, G. J.; Roth, W. J.; Strohmaier, K. G.; Reyes, S. C. PFG NMR self-diffusion of small hydrocarbons in high silica DDR, CHA and LTA structures. *Microporous Mesoporous Mater.* **2008**, *109*, 327-334.

(81) Ruthven, D. M.; Reyes, S. C. Adsorptive separation of light olefins from paraffins. *Microporous Mesoporous Mater.* **2007**, *104*, 59-66.

(82) Cadiau, A.; Adil, K.; Bhatt, P. M.; Belmabkhout, Y.; Eddaoudi, M. A Metal-Organic Framework–Based Splitter for Separating Propylene from Propane. *Science* **2016**, *353*, 137-140.

(83) Cui, X.; Chen, K.; Xing, H.; Yang, Q.; Krishna, R.; Bao, Z.; Wu, H.; Zhou, W.; Dong, X.; Han, Y.; Li, B.; Ren, Q.; Zaworotko, M. J.; Chen, B. Pore Chemistry and Size Control in Hybrid Porous Materials for Acetylene Capture from Ethylene. *Science* **2016**, *353*, 141-144.

(84) Li, L.; Lin, R.-B.; Krishna, R.; Li, H.; Xiang, S.; Wu, H.; Li, J.; Zhou, W.; Chen, B. Ethane/ethylene Separation in a Metal-Organic Framework with Iron-Peroxo Sites. *Science* **2018**, *362*, 443-446. https://doi.org/10.1126/science.aat0586.

(85) Lin, R.-B.; Wu, H.; Li, L.; Tang, X.-T.; Li, Z.; Gao, J.; Cui, H.; Zhou, W.; Chen, B. Boosting Ethane/Ethylene Separation within Isoreticular Ultramicroporous Metal−Organic Frameworks. *J. Am. Chem. Soc.* **2018**, *140*, 12940-12946.

(86) Qazvini, O. T.; Babarao, R.; Shi, Z.-L.; Zhang, Y.-B.; Telfer, S. G. A Robust Ethane-Trapping Metal−Organic Framework with a High Capacity for Ethylene Purification. *J. Am. Chem. Soc.* **2019**, *141*, 5014-5020.

(87) Chen, Y.; Qiao, Z.; Wu, H.; Lv, D.; Shi, R.; Xia, Q.; Zhou, J.; Li, Z. An Ethane-trapping MOF PCN-250 for Highly Selective Adsorption of Ethane over Ethylene. *Chem. Eng. Sci.* **2018**, *175*, 110-117. http://dx.doi.org/doi:10.1016/j.ces.2017.09.032.

(88) Gücüyener, C.; van den Bergh, J.; Gascon, J.; Kapteijn, F. Ethane/Ethene Separation Turned on Its Head: Selective Ethane Adsorption on the Metal-Organic Framework ZIF-7 through a Gate-Opening Mechanism. *J. Am. Chem. Soc.* **2010**, *132*, 17704-17706.

(89) Chen, D.-L.; Wang, N.; Xu, C.; Tu, G.; Zhu, W.; Krishna, R. A combined theoretical and experimental analysis on transient breakthroughs of C2H6/C2H4 in fixed beds packed with ZIF-7. *Microporous Mesoporous Mater.* **2015**, *208*, 55-65.

(90) Böhme, U.; Barth, B.; Paula, C.; Kuhnt, A.; Schwieger, W.; Mundstock, A.; Caro, J.; Hartmann, M. Ethene/Ethane and Propene/Propane Separation via the Olefin and Paraffin Selective Metal−Organic Framework Adsorbents CPO-27 and ZIF-8. *Langmuir* **2013**, *29*, 8592-8600.

(91) Liao, P.-Q.; Zhang, W.-X.; Zhang, J.-P.; Chen, X.-M. Efficient purification of ethene by an ethane-trapping metal-organic framework. *Nat. Commun.* **2015**, *36*, 8697. http://dx.doi.org/doi:10.1038/ncomms9697.

(92) Liang, W.; Xu, F.; Zhou, X.; Xiao, J.; Xia, Q.; Li, Y.; Li, Z. Ethane Selective Adsorbent Ni(bdc)(ted)0.5 with High Uptake and its Significance in Adsorption Separation of Ethane and Ethylene. *Chem. Eng. Sci.* **2016**, *148*, 275-281.

(93) Yang, H.; Wang, Y.; Krishna, R.; Jia, X.; Wang, Y.; Hong, A. N.; Dang, C.; Castillo, H. E.; Bu, X.; Feng, P. Pore-Space-Partition-Enabled Exceptional Ethane Uptake and Ethane-Selective

Ethane−Ethylene Separation. *J. Am. Chem. Soc.* **2020**, *142*, 2222-2227. https://doi.org/10.1021//jacs.9b12924.

(94) Andres-Garcia, E.; Oar-Arteta, L.; Gascon, J.; Kapteijn, F. ZIF-67 as Silver-Bullet in Adsorptive Propane/Propylene Separation. *Chem. Eng. J.* **2019**, *360*, 10-14. https://dx.doi.org/10.1016/j.cej.2018.11.118.

(95) Lin, Y. S. Molecular Sieves for Gas Separation. *Science* **2016**, *353*, 121-122.

(96) Divekar, S.; Nanoti, A.; Dasgupta, S.; Aarti; Chauhan, R.; Gupta, P.; Garg, M. O.; Singh, S. P.; Mishra, I. M. Adsorption Equilibria of Propylene and Propane on Zeolites and Prediction of Their Binary Adsorption with the Ideal Adsorbed Solution Theory. *J. Chem. Eng. Data* **2016**, *61*, 2629-2637.

(97) Chen, D.-L.; Shang, H.; Zhu, W.; Krishna, R. Transient Breakthroughs of CO_2/CH_4 and C_3H_6/C_3H_8 Mixtures in Fixed Beds packed with Ni-MOF-74. *Chem. Eng. Sci.* **2014**, *117*, 407-415.

(98) Yu, H.; Wang, X.; Xu, C.; Chen, D.-L.; Zhu, W.; Krishna, R. Utilizing transient breakthroughs for evaluating the potential of Kureha carbon for CO_2 capture. *Chem. Eng. J.* **2015**, *269*, 135-147.

(99) Li, L.; Yang, J.; Li, J.; Chen, Y.; Li, J. Separation of CO_2/CH_4 and CH_4/N_2 Mixtures by M/DOBDC: a Detailed Dynamic Comparison with MIL-100(Cr) and Activated Carbon. *Microporous Mesoporous Mater.* **2014**, *198*, 236-246.

(100) Herm, Z. R.; Wiers, B. M.; Van Baten, J. M.; Hudson, M. R.; Zajdel, P.; Brown, C. M.; Maschiocchi, N.; Krishna, R.; Long, J. R. Separation of Hexane Isomers in a Metal-Organic Framework with Triangular Channels *Science* **2013**, *340*, 960-964.

(101) Krishna, R.; van Baten, J. M. Screening of zeolite adsorbents for separation of hexane isomers: A molecular simulation study. *Sep. Purif. Technol.* **2007**, *55*, 246-255.

(102) Dubbeldam, D.; Krishna, R.; Calero, S.; Yazaydın, A. Ö. Computer-Assisted Screening of Ordered Crystalline Nanoporous Adsorbents for Separation of Alkane Isomers. *Angew. Chem. Int. Ed.* **2012**, *51*, 11867-11871.

(103) Dandekar, H. W.; Funk, G. A.; Gillespie, R. D.; Zinnen, H. A.; McGonegal, C. P.; Kojima, M.; Hobbs, S. H., Process for alkane isomerization using reactive chromatography. UOP, Des Plaines, Illinois, USA., *U.S. Pat.*, US 5763730, 1999.

(104) Dandekar, H. W.; Funk, G. A.; Zinnen, H. A., Process for separating and recovering multimethyl-branched alkanes. UOP LLC, Des Plaines, Illinois, USA., *U.S. Pat.*, US 6069289, 2000.

(105) Carr, R. W.; Dandekar, H. W. *Adsorption with reaction*. Reactive Separation Processes; 2nd, Edited by S. Kulprathipanja, 115-154, Taylor & Francis: New York, USA, 2001.(

(106) Krishna, R.; Smit, B.; Calero, S. Entropy effects during sorption of alkanes in zeolites. *Chem. Soc. Rev.* **2002**, *31*, 185-194.

(107) Krishna, R.; van Baten, J. M. In silico screening of metal-organic frameworks in separation applications. *Phys. Chem. Chem. Phys.* **2011**, *13*, 10593-10616.

(108) Krishna, R. Evaluation of Procedures for Estimation of the Isosteric Heat of Adsorption in Microporous Materials. *Chem. Eng. Sci.* **2015**, *123*, 191-196.

(109) Kulprathipanja, S. Zeolites in Industrial Separation and Catalysis; Wiley-VCH: Weinheim, 2010.

(110) Khabzina, Y.; Laroche, C.; Perez-Pellitero, J.; Farrusseng, D. Xylene Separation on a Diverse Library of Exchanged Faujasite Zeolites. *Microporous Mesoporous Mater.* **2017**, *247*, 52-59. http://dx.doi.org/10.1016/j.micromeso.2017.03.026.

(111) Khabzina, Y.; Laroche, C.; Perez-Pellitero, J.; Farrusseng, D. Quantitative Structure–property Relationship Approach to Predicting Xylene Separation with Diverse Exchanged Faujasites. *Phys. Chem. Chem. Phys.* **2018**, *20*, 23773--23782. http://dx.doi.org/10.1039/c8cp04042g.

(112) Costa, I. C. M. *Adsorption/diffusion Interplay in Hierarchical Zeolites: Understanding the role of External Surface and Additional Porosity*. Ph.D. thesis l'Université Claude Bernard Lyon 1, Lyon, 2019. https://tel.archives-ouvertes.fr/tel-02168674v2/document.

(113) Minceva, M.; Rodrigues, A. E. Modeling and Simulation of a Simulated Moving Bed for the Separation of *p*-Xylene. *Ind. Eng. Chem. Res.* **2002**, *41*, 3454-3461.

(114) Minceva, M.; Rodrigues, A. E. Understanding and Revamping of Industrial Scale SMB Units for p-Xylene Separation. *A.I.Ch.E.J.* **2007**, *53*, 138-149.

(115) Peralta, D.; Barthelet, K.; Pérez-Pellitero, J.; Chizallet, C.; Chaplais, G.; Simon-Masseron, A.; Pirngruber, G. D. Adsorption and Separation of Xylene Isomers: CPO-27-Ni vs HKUST-1 vs NaY. *J. Phys. Chem. C* **2012**, *116*, 21844-21855.

(116) Minceva, M.; Rodrigues, A. E. Adsorption of xylenes on Faujasite-type zeolite. Equilibrium and Kinetics in Batch Adsorber. *Chem. Eng. Res. Des.* **2004**, *82*, 667-681.

(117) El Osta, R.; Carlin-Sinclair, A.; Guillou, N.; Walton, R. I.; Vermoortele, F.; Maes, M.; De Vos, D.; Millange, F. Liquid-Phase Adsorption and Separation of Xylene Isomers by the Flexible Porous Metal−Organic Framework MIL-53(Fe). *Chem. Mater.* **2012**, *24*, 2781-2791.

(118) Finsy, V.; Verelst, H.; Alaerts, L.; De Vos, D.; Jacobs, P. A.; Baron, G. V.; Denayer, J. F. M. Pore-Filling-Dependent Selectivity Effects in the Vapor-Phase Separation of Xylene Isomers on the Metal-Organic Framework MIL-47. *J. Am. Chem. Soc.* **2008**, *130*, 7110-7118.

(119) Remy, T.; Baron, G. V.; Denayer, J. F. M. Modeling the Effect of Structural Changes during Dynamic Separation Processes on MOFs. *Langmuir* **2011**, *27*, 13064-13071.

(120) Torres-Knoop, A.; Krishna, R.; Dubbeldam, D. Separating Xylene Isomers by Commensurate Stacking of p-Xylene within Channels of MAF-X8. *Angew. Chem. Int. Ed.* **2014**, *53*, 7774-7778.

(121) Niekiel, F.; Lannoeye, J.; Reinsch, H.; Munn, A. S.; Heerwig, A.; Zizak, I.; Kaskel, S.; Walton, R. I.; de Vos, D.; Llewellyn, P.; Lieb, A.; Maurin, G.; Stock, N. Conformation-Controlled Sorption Properties and Breathing of the Aliphatic Al-MOF [Al(OH)(CDC)]. *Inorg. Chem.* **2012**, *53*, 4610-4620.

(122) Fang, Z. L.; Zheng, S. R.; Tan, J. B.; Cai, S. L.; Fan, J.; Yan, X.; Zhang, W. G. Tubular metal–organic framework-based capillary gas chromatography column for separation of alkanes and aromatic positional isomers. *J. Chromatogr. A* **2013**, *1285*, 132-138.

(123) Humphrey, S. M.; Chang, J.-S.; Jhung, S. H.; Yoon, J. W.; Wood, P. T. Porous Cobalt(II)–Organic Frameworks with Corrugated Walls: Structurally Robust Gas-Sorption Materials. *Angew. Chem. Int. Ed.* **2007**, *46*, 272-275.

(124) Yoon, J. W.; Lee, J. S.; Piburn, G. W.; Cho, K. H.; Jeon, K.; Lim, H.-K.; Kim, H.; Jun, C.-H.; Humphrey, S. M.; Krishna, R.; Chang, J.-S. Highly Selective Adsorption of p-Xylene over other C8 Aromatic Hydrocarbons by Co-CUK-1: A Combined Experimental and Theoretical Assessment. *Dalton Trans.* **2017**, *46*, 16096-16101. http://dx.doi.org/10.1039/C7DT03304D.

(125) Mukherjee, S.; Joarder, B.; Manna, B.; Desai, A. V.; Chaudhari, A. K.; Ghosh, S. K. Framework-Flexibility Driven Selective Sorption of p-Xylene over Other Isomers by a Dynamic Metal-Organic Framework. *Sci. Rep.* **2014**, *4*, 5761. http://dx.doi.org/10.1038/srep05761

(126) Krishna, R. Separating Mixtures by Exploiting Molecular Packing Effects in Microporous Materials. *Phys. Chem. Chem. Phys.* **2015**, *17*, 39-59.

(127) Mukherjee, S.; Joarder, B.; Desai, A. V.; Manna, B.; Krishna, R.; Ghosh, S. K. Exploiting Framework Flexibility of a Metal-Organic Framework for Selective Adsorption of Styrene over Ethylbenzene. *Inorg. Chem.* **2015**, *54*, 4403-4408.

(128) Jin, Z.; Zhao, H. Y.; Zhao, X. J.; Fang, Q. R.; Long, J. R.; Zhu, G. S. A novel microporous MOF with the capability of selective adsorption of xylenes. *Chem. Commun.* **2010**, *46*, 8612-8614.

(129) Moreira, M. A.; Santos, J. C.; Ferreira, A. F. P.; Loureiro, J.; Ragon, F.; Horcajada, P.; Yot, P. G.; Serre, C.; Rodrigues, A. E. Toward Understanding the Influence of Ethylbenzene in p-Xylene Selectivity of the Porous Titanium Amino Terephthalate MIL-125(Ti): Adsorption Equilibrium and Separation of Xylene Isomers. *Langmuir* **2012**, *28*, 3494-3502.

(130) Moreira, M. A.; Santos, J. C.; Ferreira, A. F. P.; Loureiro, J.; Ragon, F.; Horcajada, P.; Yot, P. G.; Serre, C.; Rodrigues, A. E. Effect of ethylbenzene in p-xylene selectivity of the porous titanium amino terephthalate MIL-125(Ti)_NH2. *Microporous Mesoporous Mater.* **2012**, *158*, 229-234.

(131) Vermoortele, F.; Maes, M.; Moghadam, P. Z.; Lennox, M. J.; Ragon, F.; Boulhout, M.; Biswas, S.; Laurier, K. G. M.; Beurroies, I.; Denoyel, R.; Roeffaers, M.; Stock, N.; Düren, T.; Serre, C.;

References

De Vos, D. E. *p*-Xylene-Selective MetalOrganic Frameworks: A Case of Topology-Directed Selectivity. *J. Am. Chem. Soc.* **2011**, *133*, 18526-18529.

(132) Maes, M.; Vermoortele, F.; Alaerts, L.; Couck, S.; Kirschhock, C. E. A.; Denayer, J. F. M.; De Vos, D. E. Separation of Styrene and Ethylbenzene on Metal-Organic Frameworks: Analogous Structures with Different Adsorption Mechanisms. *J. Am. Chem. Soc.* **2010**, *132*, 15277-15285.

(133) Remy, T.; Ma, L.; Maes, M.; De Vos, D. E.; Baron, G. V.; Denayer, J. F. M. Vapor-Phase Adsorption and Separation of Ethylbenzene and Styrene on the Metal−Organic Frameworks MIL-47 and MIL-53(Al). *Ind. Eng. Chem. Res.* **2012**, *51*, 14824-14833.